Universität Hamburg
DER FORSCHUNG | DER LEHRE | DER BILDUNG

Fachbereich
Chemie

Studienbüro Chemie

Smart RAFT Polymers and Their Versatile Use for Gold Nanoparticle Polymer–Shell Hybrids

Dissertation

In conformity with the requirements for the degree of

Doctor rerum naturalium (Dr. rer. nat.)

submitted to the University of Hamburg

–

Faculty of Mathematics, Informatics, and Natural Sciences

–

Department of Physical Chemistry

submitted by

Sascha Benedict Lemich

Hamburg 2026

Supervisor:	Prof. Dr. Volker Abetz
1st Referee:	Prof. Dr. Volker Abetz
2nd Referee:	Prof. Dr. Wolfgang Parak
Defense Committee:	Prof. Dr. Volker Abetz
	PD Dr. Tobias Kipp
	PD Dr. Christoph Wutz
Date of Oral Defense:	27.03.2026
Date of Print Release:	19.04.2026

Disclaimer

The submitted dissertation was prepared under the supervision of Prof. Dr. Volker Abetz at the Institute of Physical Chemistry (Chemistry Department, MIN Faculty) of the University of Hamburg. The work on the PhD was conducted between July 2020 and January 2026.

This work was funded by the German Research Foundation (Deutsche Forschungsgemeinschaft (DFG)) in the context of the Nanohybrid graduate school program (Grant Number: RTG 2536).

“One of the basic rules of the Universe is that nothing is perfect. Perfection simply doesn't exist without imperfection, neither you nor I would exist.” – Stephen Hawking.

Publications

Leading Authorships

1)

Synthesis of Multiresponsive Gold@Polymer-Nanohybrid Materials Using Polymer Precursors Obtained by Photoiniferter RAFT Polymerization

***Sascha Benedict Lemich**, Nils Sobania, Nils-Felix Meyer, Patrick Schütz, Birgit Hankiewicz,* and Volker Abetz**

Macromol. Chem. Phys., **2022**, 2200355.
DOI: 10.1002/macp.202200355

2)

Defining New Benchmarks of Low CTAB-Concentration-Based Gold Nanorod Synthesis: The Underestimated Potential of Polymer-Directed Anisotropic Growth

***Sascha Benedict Lemich**, Steffen Soltau, Maria Weißpflog, Verena R. Schulze, Neus Feliu, Birgit Hankiewicz,* and Volker Abetz**

Adv. Funct. Mater, **2024**, 2400995.
DOI: 10.1002/adfm.202400995

Co-Authorships

1)

Dual-Responsive PIL Films with Gold Nanoparticles: Tailoring Electrical Responses to pH and Thermal Stimuli

*Chia-Wei Chang, **Sascha Benedict Lemich**, Patrick Schütz, Siraphat Weerathaworn, Maria Weißpflog, Chia-Ti Wu, Yu-Hsuan Tseng, Chun-Ting Chang, Birgit Hankiewicz, Volker Abetz,* and Jiun-Tai Chen**

ACS Appl. Mater. Interfaces, **2024**, 16, 61096−61104.
DOI: 10.1021/acsami.4c14733

2)

Multi-responsive hydrogels based on magneto-plasmonic nanoparticles in a thermo-responsive polymer matrix

*Patrick Schütz, **Sascha Benedict Lemich**, Maria Weißpflog, Paul Körner, Volker Abetz, Birgit Hankiewicz*

Nano Trends, **2025**, 10, 100113.
DOI: 10.1016/j.nwnano.2025.100113

Table of Contents

Table of Contents i

Abbreviations v

Constants and Variables ix

1. Zusammenfassung 1

2. Abstract 5

3. The Objective of This Work 9

4. Introduction and Theoretical Background 11

4.1. Gold nanoparticles (GNPs) 11

4.1.1. History of the Development of Colloidal Gold Particles 11

4.1.2. Synthesis of GNPs 14

4.1.3. Optical Properties of GNPs 24

4.2. Smart Polymers: From the Synthesis to Responsive Behavior 33

4.2.1. RAFT Polymerization 35

4.2.2. Smart Polymers and Polymer Networks: From Thermal to pH-controlled Polymer Morphologies 41

4.3. GNP@Polymer: Core-Shell Nanohybrids 48

4.3.1. Physical Properties and Scattering Behavior of GNP@Polymer/Microgel Hybrids in Solution 52

5. Results and Discussion 57

5.1. Particle Systems: A Joint Perspective 57

5.2. *In Situ* Polymer-Assisted Synthesis of Au@P(DMAEMA) Multiresponsive Nanohybrids 59

5.2.1. Polymerization of DMAEMA: Amines are a Critical but Potent Functional Group 59

5.2.2. Responsive Properties of the pTTC-P(DMAEMA) and dTTC-P(DMAEMA) Polymer Precursors 66

5.2.3. Synthesis of pTTC-P(DMAEMA)- and dTTC-P(DMAEMA)-based Au@P(DMAEMA) Nanohybrids 71
5.3. Polymer-Assisted Anisotropic Growth of GNRs 80
5.3.1. *Grafted*-DMEAMA-based Polymers as the First Generation of Anisotropic-Growth Assisting Precursors 86
5.3.2. Block copolymer-based DMEAMA-based Polymers: The Second Generation of Anisotropic-Growth Assisting Precursors. 91
5.3.3. Additional Blind Studies and Test Reactions to Embrace the Polymer-Based GNR Synthesis Potential for Future Research 103
5.4. Tailoring Thermoresponsive Properties of Smart Au@Polymer Hybrids: A Systematic Investigation 107
5.4.1. Responsive Properties of the Au@P(DMAEMA)$_n$ and the GNR@qBCP Nanohybrids: A Comparison of Polymer Solution and Nanohybrid Suspension Behavior 108
5.4.2. Preparation and Particle Assembly of GNS Stabilized by Double Thermo-Responsive Graft-Copolymers 115
5.4.3. Addressing the Open Questions About Temperature-Responsive Behavior of GNS@Polymer Hybrids Using Stimuli-Responsive Polymer Stabilizers: A Review of this Work Advances 136
6. Achievements and Future Perspectives 145
7. Experimental Methods 151
7.1. Used Chemicals 151
7.1.1. Chemicals and Materials Used for RAFT Polymerization 151
7.1.2. Chemicals Used for Particle Preparation 152
7.2. Preparative Methods 153
7.2.1. Organic Synthesis of The RAFT Agents 153
7.2.2. Photo RAFT-Polymerization of Polymer Stabilizers 154
7.2.3. GNP Hybrid Material Preparation 164
7.3. Analytical Methods 172
7.3.1. Basic Analytical Methods 172
7.3.2. Temperature-Dependent Analytics 172

8. References 175
9. Appendix 191
9.1. Polymerization Conditions and Polymer Characterization Results 191
9.1.1. NMR-Spectroscopy 191
9.1.2. Size Exclusion chromatography (SEC) 192
9.1.3. Analytical Results and Kinetics 192
9.1.4. ATR-FTIR Spectroscopy 195
9.2. Particle Results: TEM Images, TEM Evaluation, and Thermoresponsive Properties 196
9.2.1. TEM Sample Preparation, Measurement, and Image Evaluation 196
9.2.2. Additional TEM Images and Evaluation Results 197
9.3. Additional Analytics for the Temperature-Dependent Behavior of GNP@Polymer Hybrids and Their Polymer Stabilizers 199
10. Danksagung 207
11. Eidesstattliche Erklärung 211

Abbreviations

AA	ascorbic acid
Abs	absorbance
ADC	acetone dicarboxylate
AFM	atomic force microscopy
AR	aspect ratio
ATR	attenuated total reflection
ATRP	atom transfer radical polymerization
AV	acceleration voltage
BCP	block copolymer
BHD	1-bromohexadecane
BIS	*N*,*N*'-methylene-bis(acrylamide)
BSA	bovine serum albumin
BTPEMA	2-(2-(*n*-butyltrithiocarbonate)propionate)ethyl methacrylate
CA	citric acid
CTA	chain transfer agent
CTAB	cetyltrimethylammonium bromide
cmc	critical micelle concentration
DBP	diblock copolymer
DBrP	1,5-dibromopentane
DEGMA	di(ethylenglycol) methyl ether methacrylate
DP	degree of polymerization
DLS	dynamic light scattering
DMAEMA	2-(dimethylamino) ethyl methacrylat
DTC	dithiocarbonate
DTP	2,2'-dithiodipyridine
DVB	divinylbenzene
EDX	energy dispersive X-ray
EDT	2,2'-(ethylenedioxy)diethanethiol
EM	electromagnetic
Eq	equation
FTIR	Fourier transform infrared spectroscopy
GNP	gold nanoparticle
GNR	gold nanorod

GNS	gold nanosphere
HR	high-resolution
LCST	lower critical solution temperature
LSP	localized surface plasmon
LSPR	localized surface plasmon resonance
MFP	mean free path
NiPAM	*N*-isopropyl acrylamide
NPAM	polyacrylamide
NIR	near-infrared
NP	nanoparticle
NR	nanorod
OEGMA	oligo(ethylene glycol) methacrylate (~500 g/mol)
PAA	poly(acrylamide)
PDS	pyridyl disulfide
PEG/PEO	polyethylene glycol/polyethylene oxide
photoRAFT	Photo-iniferter reversible-addition–fragmentation chain transfer
P(DEGMA)	poly(di(ethylenglycol) methyl ether methacrylate)
P(DMAEMA)	poly(2-(dimethylamino) ethyl methacrylate)
P(NiPAM)	poly(*N*-isopropyl acrylamide)
P(OEGMA)	poly(oligo(ethylene glycol) methacrylate)
PIL	polyionic liquid
PS	polystyrene
PSP	propagating surface plasmon
PTT	phase transition temperature
RAFT	reversible-addition–fragmentation chain transfer
RDRP	reversible deactivation radical polymerization
RI	refractive index
SAXS	small-angle X-ray scattering
SC	sodium citrate
SEC	size exclusion chromatography
SEM	scanning electron microscopy
SDV	standard deviation
SP	surface plasmon
TCA	trisodium citrate
TEM	transmission electron microscopy
TTC	trithiocarbonate

UCST	upper critical solution temperature
UV	ultraviolet
Vis	visible

Constants and Variables

$Đ$	Dispersity ($\overline{M}_w/\overline{M}_n$) [dimensionless]
$\alpha(pH)$	degree of protonation [dimensionless]
c	concentration [mol·L^{-1}; %(*w*/*w*)]
h	Planck's constant [6.63·10^{-34} Js]
h	fuzziness factor [dimensionless]
λ	wavelength [nm]
λ_{LSPR}	wavelength at the LSPR maximum [nm]
$\Delta\lambda_{LSPR}$	LSPR maximum wavelength shift [nm]
λ_{max}	wavelength at emission/intensity maximum (light source) [nm]
R	Radius [m]
R_H	hydrodynamic radius [µm–nm]
n_b	refractive index
p_i	Impulse
I_d	power density [mW·cm^{-2}]
$\tilde{n}$	refractive index [dimensionless]
d_c	interparticle distance (surface to surface) [nm]
d_{NP}	particle diameter [nm]
DP_D	degree of polymerization of DMAEMA-units
DP_{DEG}	degree of polymerization of DEGMA-units
DP_N	degree of polymerization of NiPAM-units
$\varnothing_{GNS}$	GNS Diameter [nm]
M	molecular weight [g/mol]
$M_{n,th}$	theoretical number average molecular weight [g/mol; kDa]
$\overline{M}_n$	number average molecular weight [g/mol; kDa]
$\overline{M}_w$	weight average molecular weight [g/mol; kDa]
n	amount of substance [mol]
p_M	monomer conversion [dimensionless]
$[CTA]_0$	CTA concentration (t = 0) [g/mol]
$[M]_0$,$[M]_t$	monomer concentration (t = 0 min,t = x min respectively) [g/mol]
V	Volume [L]
ζ	zeta potential [mV]

1. Zusammenfassung

Diese Arbeit beschäftigt sich mit dem Potenzial von Goldnanopartikeln (GNP), die mithilfe sogenannter intelligenter Polymersysteme stabilisiert werden. Im Fokus dieser Arbeit stehen verschiedene Aspekte der Herstellung und Charakterisierung dieser Nanopartikel-Polymerhybride.

Im Rahmen dieser Arbeit wurden drei Klassen von Nanohybridmaterial hergestellt und charakterisiert. Bei den ersten beiden vorgestellten Nanohybriden wird sich mit dem unterstützenden Potential von RAFT-Polymeren bei der Synthese von GNP befasst. Bei diesen Hybridmaterialien liegt der Fokus auf der Nanopartikelherstellung in Anwesenheit des späteren polymeren Stabilisators. Beim dritten Nanohybridmaterial rücken die thermoresponsiven Eigenschaften in den Fokus der Untersuchung. Anders als bei den vorherigen beiden Systemen werden hier die Polymerstabilisatoren und die GNP separat hergestellt und mittels eines Ligandenaustausches miteinander kombiniert. Allen untersuchten Hybriden gemein ist, dass die polymere Vorstufe mittels photoinitiierter *iniferter reversible addition–fragmentation chain-transfer* (photoRAFT)-Polymerisation hergestellt wurde.

Die Ergebnisse dieser Arbeit zeigen, dass RAFT-Polymere aufgrund ihrer Herstellungsmethode vielseitig als Stabilisatoren für GNP einsetzbar sind. Die für RAFT-Polymere typische Trithiocarbonatgruppe (TTC) besitzt eine natürliche Affinität zu GNP-Oberflächen. Darüber hinaus macht die große Bandbreite an polymerisierbaren Monomeren sowie die robuste Reaktionsführung die RAFT-Technologie zu einem zentralen Bestandteil dieser Arbeit. Als wiederkehrendes Thema dieser Arbeit wurde hierbei ein besonderer Fokus auf das Up-scaling der RAFT-Polymerisation gelegt um chargenbedingte Schwankungen beim späteren Nanohybrid bestmöglich zu reduzieren. Bei der Copolymerisation von Oligoethylenglycolmethacrylat (OEGMA) und 2-(2-(*n*-Butyltrithiocarbonat)propionat)-ethylmethacrylat (BTPEMA) zum statistischen Copolymers P($OEGMA_{233}$-*r*-$BTPEMA_{11}$) (B03) konnte hierbei ein Reaktionsmaßstab von knapp 450 g mit einem Feststoffanteil (RAFT-Agent und Monomere) von ~20 %(*w*/*w*) erreicht werden. Verglichen mit der Literatur[1] entspricht dies einer Maßstabserhöhung um über das 20-fache. Es konnte gezeigt werden, dass das erhaltene B03 keine signifikanten Einbußen der temperaturresponsiven Eigenschaften aufwies. Darüber hinaus konnten die doppelt temperaturresponsiven Eigenschaften der literaturbekannten[1] Graft-Copolymer-Folgestufe aus (P(OEGMA)) und Poly(*N*-Isopropylacrylamid) (P(NiPAM)) erfolgreich nachgestellt werden. Diese Ergebnisse sind sowohl für die Forschung im Bereich der

Initiator-freien photoRAFT-Polymerisation generell als auch für die Reproduzierbarkeit der GNP@Polymer-Hybridsynthesen dieser Arbeit von Bedeutung.

Eines der Ziele dieser Arbeit war die Herstellung von CO_2- und temperaturresponsiven Goldnanohybriden. Die Synthese sollte möglichst simpel und schnell durchführbar sein, weshalb sich für eine Methode nach J. Shan et al.[2] entschieden wurde. Hierbei werden die GNP in Anwesenheit des späteren Stabilisators, in diesem Fall Poly(2-(dimethylamino)ethylmethacrylat) (P(DMAEMA)), mithilfe eines starken Reduktionsmittels synthetisiert. Die gewonnenen Goldnanosphären (GNS) wiesen Partikeldurchmesser im Bereich von 3.8 – 5.2 nm auf. Nach Überführung der Hybride in eine wässrige Suspension konnte mittels temperaturabhängigen dynamischen Lichtstreuungsexperimenten (DLS) nachgewiesen werden, dass die erhaltenen Nanohybride (Au@P(DMAEMA)$_n$) temperatur-responsives Verhalten aufweisen. Zudem war eine Abhängigkeit des Löslichkeitsverhaltens der Hybride von der verwendeten RAFT-Endgruppe zu erkennen. In weiteren Experimenten konnte ebenfalls CO_2-sensitives Verhalten bestätigt werden. Die hierzu in Kapitel 5.2 zusammengefassten Daten wurden im späteren Verlauf veröffentlicht.[3]

Eine große Herausforderung in der Nanotechnologie, insbesondere im Bereich biologischer Anwendungen, ist die Toxizität von Nanopartikeln. Insbesondere die Nutzung von Goldnanostäbchen (engl. *gold nanorods*; GNR) ist aufgrund dieser Problematik stark eingeschränkt. Aus physikalischen Gesichtspunkten sind GNR eine hochinteressante Partikelklasse. Basierend auf ihrer Form reicht ihre plasmonische Absorptionsbande je nach Partikellänge bis in den Nahinfrarot-Bereich (NIR). Im Unterschied zu Wellenlängen im sichtbaren Spektrum ist NIR-Strahlung in der Lage tief in biologisches Gewebe einzudringen, wodurch eine plasmonische Anregung von GNRs auch *in vivo* möglich ist. Allerdings wird sich diese Eigenschaft mit einer eingeschränkten Biokompatibilität der GNR erkauft, welche hauptsächlich auf die Verwendung des kationischen Tensids Cetyltrimethylammoniumbromid (CTAB) bei der Synthese von GNRs zurückgeführt wird.[4–6] Um die Biokompatibilität von GNRs zu erhöhen wurde der Austausch von CTAB während der Synthese von GNRs durch speziell entworfene RAFT-Polymere geprüft. Basierend auf der Funktionalisierung von P(DMAEMA)-Kettensegmenten mit Cetylbromid wurden verschiedene Polymere als CTAB-Alternativen getestet. Basierend auf der herkömmlichen Synthese von monokristallinen GNR[7] wurde ein Verfahren entwickelt in welchem die CTAB-Konzentration während der GNR-Synthese um 99 % verringert werden konnte. Einzelne Optimierungsschritte wurden herausgearbeitet und schlussendlich konnten GNRs mit einem Aspektverhältnis von bis zu 2.2 ± 0.8 gewonnen werden. Die Ergebnisse zeigen ein zum CTAB vergleichbares Potential der polymeren Alternativen bei der Förderung von anisotropem Wachstum auf. Mithilfe von Zellkulturtests konnte zudem bewiesen werden, dass durch die Einbindung von CTAB-äquivalenten Gruppen in eine

Polymerkette die akute Zelltoxizität nur unerheblich erhöht wird und deutlich unterhalb der Toxizität von CTAB angesiedelt ist. Mit diesen Ergebnissen konnte die initiale Motivation des Themas erfüllt werden. Auch die Ergebnisse aus Kapitel 5.3 führten zu einer eigenständigen Publikation im Fachjournal *Advanced Functional Materials* des Wiley-Verlags.[8]

Sowohl die Au@P(DMAEMA)$_n$ als auch die GNR-Hybride zeigen, dass sich das temperatur-responsive Verhalten der Hybride stark von dem der verwendeten, ungebundenen Polymere unterscheidet. Allgemein lässt sich beobachten, dass die Phasenübergangstemperatur (PTT) der Polymermatrix deutlich unschärfer wird, wenn das Polymer an der Oberfläche von Nanopartikeln bindet. Die Messdaten der NP@Polymer-Hybride weisen einen flachen näherungsweise linearen Verlauf der temperatur-responsiven Reaktion. Um diesem Phänomen auf dem Grund zu gehen, wurde ein weiteres System für die strukturierte Analyse des responsiven Verhaltens von Polymerhybriden entwickelt (Kapitel 5.4).

Beim Design des Polymersystems wurde auf das bekannte doppelt temperatur-responsive Graft-Copolymersystem von J. Xu und V. Abetz zurückgegriffen.[1,9] Durch die erhöhte Ansatzgröße der B03-Synthese war es möglich mehrere Folgestufen mit unterschiedlicher P(NiPAM)-Seitenkettenlänge in ausreichender Menge zu synthetisieren. Diese Folgenstufen, ebenso wie B03 wurden anschließend erfolgreich über einen Ligandenaustausch auf Citrat-stabilisierte GNS (GNS@citrate) ($\varnothing_{GNS}\approx$13 nm) aufgebracht. Die thermoresponsiven Eigenschaften der erhaltenen Hybridsysteme wurden mit Hilfe von temperaturabhängiger UV–Vis Extinktionsspektroskopie und temperaturabhängigen dynamischen Lichtstreuungsexperimenten (DLS) untersucht. Die Ergebnisse wurden mit dem kürzlich vorgestelltem *fuzzy sphere* Modell verglichen, welches das Streuverhalten von Kern-Schale Nanohybriden beschreibt.[10–12] Es konnte gezeigt werden, dass das responsive Verhalten der Hybride mit dem NiPAM-Polymerisationsgrad (DP_N) korreliert. Je höher der eingesetzte DP_N, desto vergleichbarer wurde die Temperaturabhängigkeit des hydrodynamischen Radius (R_H) der Nanohybride mit der im *fuzzy sphere* Modell beschriebenen Abhängigkeit. Diese Beobachtung ist ebenfalls auf die mittels UV–Vis beobachteten optischen Eigenschaften der Kern-Schale-Nanohybride übertragbar. Diese Ergebnisse sind ein wichtiger Schritt für weitere Entwicklungen auf diesem Gebiet. Die simple Präparation und die verbesserte Vorhersagbarkeit des responsiven Verhaltens dieser Hybride bilden eine solide Grundlage für die Entwicklung von präzise einstellbaren Hybridmaterialien.

In Kombination mit größeren GNP unter Nutzung der Quervernetzbarkeit der verwendeten Graft-Copolymersysteme, könnten diese mittels Ligandenaustausch hergestellten Partikelhybride eine Schlüsselkomponente in Materialien mit steuerbaren optischen Eigenschaften darstellen. Die hierfür notwendige Quervernetzbarkeit der Hybridsysteme wurde bereits in einem aktuellen Projekt an magneto-plasmonischen Hybridnanopartikeln nachgewiesen.[13] Dies zeigt eine generelle Kombinationsfähigkeit dieser Kern-Schale-Nanohybride mit anderen, beispielsweise Dithiol stabilisierten Nanopartikelsystemen.

Die bereits veröffentlichten Folgeprojekte[13,14] basierend auf den Ergebnissen und Methoden dieser Arbeit und die direkt aus dieser Arbeit entstandenen veröffentlichen Projekte[3,8] verdeutlichen die wissenschaftliche Relevanz und hohe Reproduzierbarkeit der Ergebnisse dieser Arbeit.

2. Abstract

This thesis explores the potential of gold nanoparticle systems (GNPs) stabilized by so-called smart polymer systems. The focus lies on various aspects of the synthesis and characterization of nanoparticle–polymer hybrids.

In this work, three classes of nanohybrids were synthesized and characterized. During the development of the first two nanohybrids, special focus was placed on the assistance of RAFT polymers and their potential for GNP synthesis. For these projects, the synthesis of nanoparticles in the presence of the polymeric stabilizer and its effects are focused on. For the third class of nanoparticle hybrids, the focus shifts from the polymer-assisted effects during GNP synthesis to the adjustment and deeper understanding of the thermoresponsive properties of nanoparticle–polymer hybrids. Unlike the first two hybrids, the GNP and the polymer stabilizers are synthesized separately and combined via an additional ligand-exchange step. All studied hybrid systems share a common feature—the polymeric precursors were synthesized via photo-initiated iniferter reversible addition–fragmentation chain-transfer (photoRAFT) polymerization.

The findings demonstrate that RAFT polymers, owing to their controlled synthesis, serve as versatile stabilizers for GNPs. The trithiocarbonate (TTC) end groups characteristic of RAFT polymers exhibit an inherent affinity for gold surfaces. Additionally, the broad range of polymerizable monomers and the robustness of the RAFT process further emphasize its central role in this work. Particular focus is given to upscaling photoRAFT polymerization to reduce batch-based variations as much as possible. For the RAFT copolymerization of oligo(ethylene glycol) methacrylate (OEGMA) and 2-(2-(*n*-butyltrithiocarbonate)propionate)ethyl methacrylate (BTPEMA) to the random copolymer P(OEGMA$_{233}$-*r*-BTPEMA$_{11}$), a reaction scale of close to 450 g with a solid content (RAFT agent and monomers) of ~20 %(*w*/*w*) was achieved. Compared to the literature[1,9], this corresponds to a more than 20-fold increase in reaction scale. For P(OEGMA$_{233}$-*r*-BTPEMA$_{11}$), the temperature-responsive characteristics were maintained. Furthermore, the double temperature-responsive properties of the literature-known[1] follow-up graft copolymer product, consisting of the (P(OEGMA)) backbone with grafted poly(N-isopropylacrylamide) chains (P(NiPAM)), were successfully reproduced. These results are of significance both for fundamental research on initiator-free photoRAFT polymerization and for the reproducibility of the GNP@polymer hybrid syntheses presented in this thesis.

The first project addressed the synthesis of CO_2- and thermoresponsive gold nanohybrids. The chosen method had to be simple, and the final product had to be obtained quickly. Therefore, the procedure described by J. Shan et al.[2] was chosen. According to this procedure, the GNP are synthesized in the presence of the hybrid's stabilizer poly(2-(dimethylamino)ethyl methacrylate) (P(DMAEMA)), and a strong reducing agent. The gold nanospheres (GNS) showed particle diameters of 3.8–5.2 nm. After transferring the hybrids from an organic to an aqueous solution, the thermoresponsive behavior was confirmed by temperature-resolved dynamic light scattering (DLS) experiments. The solubility properties of the hybrids were shown to depend on the RAFT end group of the P(DMAEMA)$_n$ precursor used during the synthesis. Additional experiments confirmed CO_2-sensitive behavior. The respective results are described in detail in Section 5.2 and Section 5.4.1. The results are additionally published.[3]

A recent challenge in nanotechnology, particularly for biological applications, is nanoparticle toxicity. Gold nanorods (GNRs) are especially affected by this issue. From a physical perspective, GNRs are of great interest due to their anisotropic shape. This shape extends their plasmonic absorption band into the near-infrared (NIR) region, enabling deep-tissue penetration for *in vivo* applications. However, this behavior comes at the cost of limited biocompatibility, mainly attributed to the use of the cationic surfactant cetyltrimethylammonium bromide (CTAB) during GNR synthesis.[4–6] To improve biocompatibility, CTAB was replaced during GNR synthesis with RAFT polymers explicitly designed for this purpose (Chapter 5.3). Based on the functionalization of P(DMAEMA) side chains, different polymer architectures were tested as potential CTAB alternatives. Using a conventional protocol for single-crystalline GNR synthesis,[7] a process was developed that enabled a 99 % reduction in CTAB concentration. Optimization steps were identified, and GNRs with aspect ratios of up to 2.2 ± 0.8 were obtained by this advanced polymer-assisted approach. The polymer stabilizers demonstrated performance comparable to that of CTAB in promoting anisotropic growth. Cell culture experiments confirmed that embedding CTAB-equivalent moieties within a polymer backbone resulted in only minor cytotoxicity, which is significantly lower than that of free CTAB. The findings from Section 5.3 met the project's initial goal and were published in *Advanced Functional Materials* (Wiley).[8]

Both the Au@P(DMAEMA)$_n$ and the GNR hybrids showed thermoresponsive behavior that differed significantly from that of the free polymer. Generally, the polymer matrix exhibits a broader temperature-dependent response around the phase transition temperature (PTT) when bound to nanoparticle surfaces. The temperature-dependent response of NP@polymer hybrids tends to be more gradual, more linear, without a distinct PTT. To further investigate this phenomenon, an additional system was developed for the structured analysis of responsive behavior, as described in Chapter 5.4.

For the hybrid material design, the polymer system based on the well-known dual thermoresponsive graft copolymer introduced by J. Xu and V. Abetz was applied.[1,9] Due to the successful scale-up of B03's polymerization, multiple subsequent batches with varying P(NiPAM) side-chain lengths were synthesized. P(OEGMA$_{233}$-*r*-BTPEMA$_{11}$) and the subsequent graft polymers were successfully attached to citrate-stabilized GNS (GNS@citrate) ($\varnothing_{GNS}\approx$13 nm) via ligand exchange. The thermoresponsive behavior was analyzed by temperature-dependent UV–Vis extinction spectroscopy and DLS. The results were compared with the recently introduced fuzzy sphere model, which describes the scattering behavior of core–shell nanohybrids.[10–12] The data showed that the responsive behavior correlated with the degree of polymerization of the P(NiPAM) segments (DP_N). Higher DP_N values led to thermoresponsive hydrodynamic radius (R_H) behavior that closely aligned with the fuzzy sphere model. This relationship was also reflected in the optical properties of the hybrids, determined via temperature-resolved UV–Vis spectroscopy. These results are an important step in the area of thermoresponsive gold nanohybrids. The simple preparation method and the improved predictability of the responsive behavior build a solid foundation for the development of fine-tuned gold nanohybrid materials.

When combined with larger GNPs, enabled by the graft copolymer's crosslinking capability, these hybrids could serve as key components in materials with tunable optical properties. The feasibility of such crosslinking has already been demonstrated in a recent project on magneto-plasmonic hybrid nanoparticles.[13] This project shows the general compatibility of core–shell hybrids with other systems, such as dithiol-stabilized nanoparticles.

The follow-up publications[13,14] based on the methods and results of this work, along with the direct publications arising from this thesis[3,8], emphasize both the scientific relevance and the high reproducibility of the findings presented here.

3. The Objective of This Work

The idea of embedding inorganic nanoparticles inside a polymer shell has been pursued for several decades. Polymers are a reliable tool, especially when nanoparticle assemblies are required. For GNPs, the complexity of these assemblies can range from uniform assemblies, such as highly ordered nanoparticle arrays, to more complex assemblies, including chain-like[15] or ring[16] structures (see **Figure 1**). Of course, preparing these assemblies can become increasingly complex depending on the required range, structure, and quality of the final assembly. These complex protocols are usually accepted because of the fascinating properties of such assemblies.

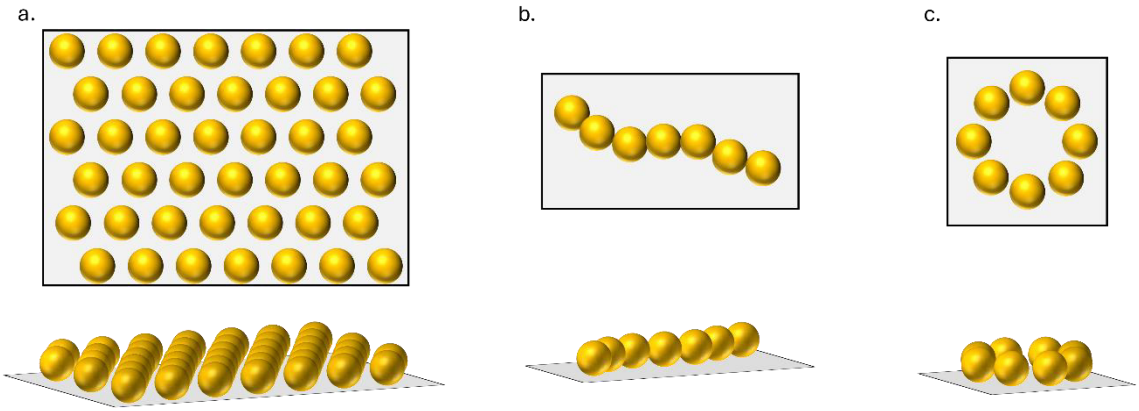


Figure 1. Exemplary assemblies of spherical GNPs into GNS-film (a.), GNS-chain (b.), and GNS-ring assimilations (c.).

It is commonly known that the localized surface plasmon resonance of GNPs strongly depends on the nature of the assembly, such as the relative orientation of two or more particles to each other and the distance between them. The first is particularly important when at least one of these particles shows an anisotropic shape. A more practical reason for assembling nanoparticles with polymers is the simplified (automated) evaluation of imaging techniques such as scanning electron microscopy (SEM) and transmission electron microscopy (TEM). These methods typically cover only a small fraction of the samples investigated. Obtaining a uniform monolayer during sample preparation can support automatic evaluation, as the number of overlapping particles decreases. This decrease increases the number of particles that can be evaluated within a short time period. One example of a polymer often used to control the assembly of GNPs is poly(ethylene glycol) (PEG).[16–18]

Another exciting field in nanoscience, and the major field of interest in this work, is preparing Au@polymer core-shell systems with tunable shell sizes. This tunability is achieved when the inorganic particle is combined with a so-called "smart" polymer shell. These polymers can react to a specific stimulus by changing their chain conformation (see sections 4.2.2 and 4.3 for more

detailed information). In this work, mostly temperature- and pH-responsive polymers were applied to various GNP systems, which are further introduced in Section 4.2 and discussed in Chapter 5.

The combination of GNP with a stimuli-responsive polymer matrix enables several advanced applications. It is of great scientific interest since the plasmonic behavior of the GNP is dependent on the interparticle distances as well as on the refractive index (n_b) of the medium around the surface of the GNP. Because of the complexity of these systems, they are not yet fully understood. However, GNP hybrids are exemplary systems for other nanoparticle hybrids, as the synthesis of most GNP morphologies is well established and therefore highly reproducible (see section 4.1.2 for more information).

This thesis provides alternative polymer-based synthesis protocols for GNPs and their hybrid systems. Simultaneously, polymer particle interactions were investigated for an advanced understanding of these structures' plasmonic behavior and scattering phenomena. The results are concluded in Chapter 5.

4. Introduction and Theoretical Background

To provide background on this work's topic, this chapter presents the basic and advanced theory needed for a deeper understanding of the results presented in Chapter 5. This work combines the leading subjects of nanoscience and polymer science. The dominant topic of this work is the combination of gold nanoparticles with tailored, smart polymers obtained via reversible addition–fragmentation chain transfer (RAFT) polymerization. This chapter is separated into two major topics, later fused into this work's objective (Section 4.3.). At the beginning of Section 4.1. and Section 4.2. the respective topic is first put into a recent perspective to highlight the relevance of the subtopics before the scientific development, and the theory is further illuminated.

4.1. Gold nanoparticles (GNPs)

4.1.1. History of the Development of Colloidal Gold Particles

Although not noticed for a long time, humans have used colloidal gold particles for centuries.[19] One of the earliest known prominent artifacts where GNPs are responsible for the unique appearance is the Lycurgus cup, dated to the 4th century AD. Its dichromatic properties kept scientists engaged, and it took them centuries to conclude that colloidal gold particles are responsible for its appearance. GNPs are also found in old glass, such as church windows [20]. Adding metals and their salts to the glass melting process was a common practice in the manufacture of colored glass. One example of such metals is gold. Together with other metals used in the glass manufacturing process, the addition of gold produced different colors in the final material. Of course, these processes involved trial-and-error development. Modern analytical methods were needed to identify the origins of these effects.

The first steps towards nanoscience were taken by M. Faraday in 1857 when he published his article about the interaction of gold with light. His article describes the synthesis of a ruby-to amethystine-colored ether suspension by adding a phosphorus solution to a gold chloride solution.[21] By investigating these suspensions, he observed that some samples tend to destabilize after a certain time, depending on the concentration of gold precursor used for the reaction. From these and other observations, he concluded that small gold particles must have been formed, which are diffused in the medium and interact with light based on their size.

In 1925, Richard Adolf Zsigmondy was awarded the Nobel Prize in Chemistry for his work in colloid chemistry. In 1902, he proved that the red color of gold-ruby glass is based on the presence of gold particles.[22] Three years later, Albert Einstein published his work on the kinetics of suspended particles in a solvent, including the Brownian molecular motion.[23] In 1908, Gustav Mie published his theory of the correlation between the absorbance of a colloidal gold particle

suspension and particle size.[24] Ludwig Lorenz presented a solution for the Maxwell equation to describe the light scattering of colloidal particles. Mie expanded this theory towards metallic particles with diameters around the wavelength of the incident light and smaller. Because of the similarity of both theories, this approach is also known as the Lorenz-Mie theory. Since then, the Lorenz-Mie theory has been applied across many scientific fields to describe the scattering of electromagnetic waves by spherical objects.[25–27] Richard Gans expanded the Mie model in 1912, making it applicable to optical soft, anisotropic nanoparticles.[28]

The next groundbreaking contribution in the field of GNPs was published by J. Turkevich in 1951. He presented a simple method for synthesizing colloidal gold particles in water by reducing gold(III) acid with citric acid.[29] Due to its well-reducibility and the benign reaction conditions, his protocol is still considered amongst the most frequently used protocols for synthesizing gold nanospheres (GNS) in today's science. Parallel to advances in electron microscopy between the 1970s and 1990s, several notable advances and milestones in gold nanoparticle synthesis have been achieved.[30–32]

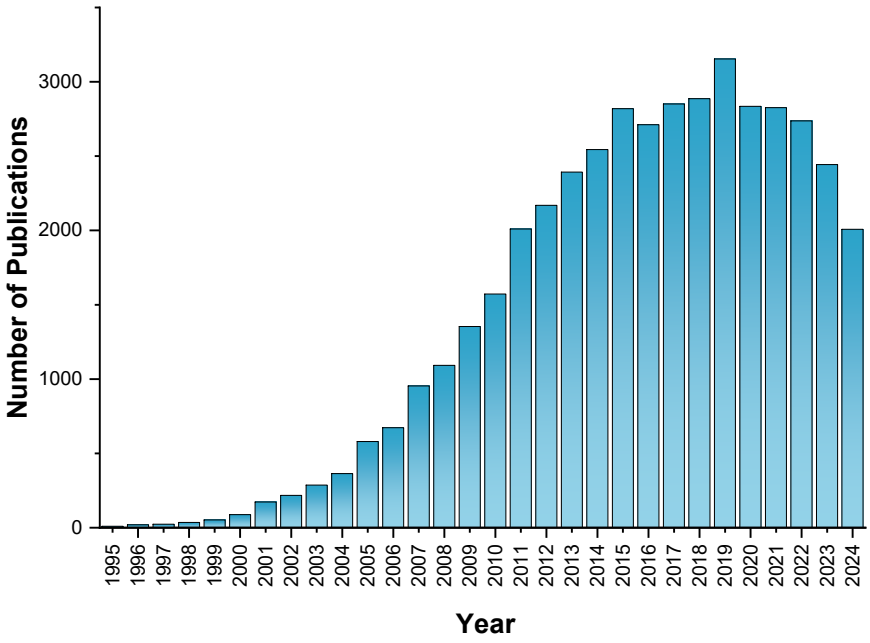


Figure 2. Number of publications with "gold nanoparticles" or "Au nanoparticles" in their title for each year since 1995 (source Web of Science; November 2024).

In the early 2000s, the focus shifted toward nanoparticle systems' application, causing a boost in the number of publications about GNPs each year (see **Figure 2**). Anisotropic particle morphologies also increased interest due to their advanced physical/plasmonic properties (Section 4.1.3). Today, GNPs are applied in many fields, including medical applications as contrast agents for cell imaging[33–35], as agents in photothermal therapy[34,36,37], or as drug carriers for enhanced drug targeting[38–40].

During the coronavirus pandemic, from 2020 to 2022, gold nanoparticles found their way into every household. Implemented as a colorimetric sensor material in lateral flow assay tests (commonly known as antigen rapid tests or corona rapid tests), GNPs, besides other NPs, represented a crucial tool in the fight against the SARS-CoV-19 virus.[41,42] Colloidal GNPs can also be found in rapid pregnancy tests and lateral flow assay tests to detect viral infections like influenza, hepatitis (a,b, and c), HIV, and several more.[43] GNPs are therefore an essential tool for rapid diagnostics in modern medicine.

Besides medical applications, GNPs are also used as catalysts[44,45], in information storage[46], in sensor arrays[18,47,48] using their unique electrical and interparticle distance-dependent properties, or as colorimetric sensors[49,50] using their adjustable plasmonic properties. They also bear great potential as supporting materials for photovoltaic cells by localizing light at the nanometer scale.[51–53]

4.1.2. Synthesis of GNPs

As described in the previous chapter, several protocols for the synthesis of GNPs are found in the literature. Depending on the application, the synthesis of GNPs can vary drastically to address the final particle system's task adequately. Due to the diverse demands for GNP systems, numerous methodologies for synthesizing various GNPs via chemical reduction are known.[54] In the context of this work, three different particle systems that address different scientific questions are presented. Therefore, this chapter will be separated into three sections covering the background of three methodologies. The first section will focus on the water-based syntheses of GNPs, following the protocol by Turkevich and recent developments in that area. Since the third GNP system studied in this work covers the seeded-growth-based synthesis of gold nanorods (GNRs), the second section of this chapter will cover the synthesis of Au seed particles, before, in the third section, the anisotropic growth of GNRs is covered.

4.1.2.1. Citrate-based GNS synthesis: Chronological development of the particle growth mechanism

The synthesis of gold nanospheres (GNS) by the reduction of $HAuCl_3$ with citric acid (CA), first described by Turkevich et al., is a robust procedure to obtain well-stabilized gold nanospheres with a diameter of around 20 nm.[29] For the synthesis, a $HAuCl_4$ (aq) solution is heated to the boiling point before a trisodium citrate (TCA) solution is added under constant stirring. Because the synthesis is highly size- and shape-selective, the resulting particles are often used without additional purification. The obtained citrate-stabilized particles are nontoxic and applicable to various biomedical applications.[55] Since the citrate-based synthesis was published, many scientists have studied it extensively to improve it. In 1973, Frens expanded the achievable particle diameter range from 12 nm to 150 nm by adjusting the amount of TCA solution.[30] In fact, using the Turkevich-Frens reduction method in D_2O, GNS with diameters down to 5 nm are achieved.[56] Both Turkevich and Frens described the characteristic color changes of the solution during the synthesis. Typically, the solution turns from colorless to grayish–blue to the often-described ruby-red. These significant color changes indicate different stages during particle growth. For a long period, a LaMer model (see **Figure 3** for more details) based process was widely accepted as the underlying mechanism for the particle growth.[57–63]

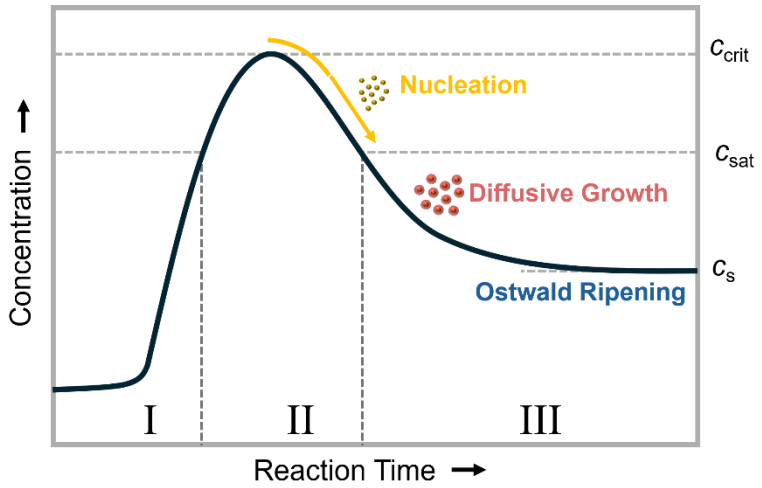
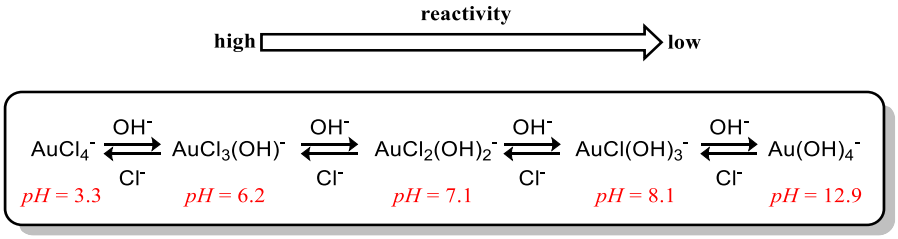


Figure 3. Schematic illustration of the particle growth mechanism according to the three stages of the LaMer model, with stage (I) as the soluble phase with a precursor concentration below the supersaturation concentration (c_{sat}), stage (II) as the nucleation phase after surpassing c_{sat}, and stage (III) where particle growth by diffusion occurs and the precursor monomer is consumed until the saturation concentration is reached.[64]

The LaMer model basically distinguishes between three phases of nanoparticle synthesis.[64] The first stage (I) describes the increase of the concentration of the monomer species until the supersaturation concentration (c_{sat}) is reached. For many NP synthesis protocols, supersaturation is usually accomplished by rapid injection of the monomer species of the respective nanoparticles. In this second phase (II), the critical supersaturation concentration (c_{crit}) is reached. After surpassing c_{crit}, the nucleation starts, and the first particle seeds (nuclei) are formed until the monomer concentration again reaches c_{sat}. If the monomer concentration falls below c_{sat}, the third stage of particle growth is entered. In stage (III), the nucleation stops, and the particle seeds grow via monomer diffusion to the particle surfaces. The monomer is consumed during this phase, and the saturation concentration (c_s) is approached. Diffusive growth becomes increasingly unfavorable as c_s is approached, and the so-called Ostwald ripening becomes more likely. However, the particle growth mechanism of the citrate reduction synthesis has been the subject of extensive discussion over the past decades. In 2007, B.-K. Pong et al.[65] reported a gold nanowire intermediate network at the early stages of the reaction, which strongly contradicted the accepted LaMer model. Similar aggregates were found and investigated by Peng and coworkers.[66] They found that the formation of these structures usually occurs at lower pH values and is caused by the formation of intermediate gold complexes at different pH values (**Scheme 1**) before nucleation begins. As a result, Peng et al. proposed two reaction pathways for synthesizing GNPs at different pH regions. They observed rapid nucleation at pH values between 3.7 and 6.5 (after < 10 s). With increased pH values between 6.5 and 7.7, the nucleation was significantly slower, with around 60 s.

Another comprehensive investigation was performed in 2011 using *in situ* small-angle X-ray scattering (SAXS) and dynamic light scattering (DLS) measurements alongside other *in situ* methods by the group around Y. Mikhlin.[60] In the SAXS measurements, in opposition to the findings of B.-K. Pong et al. and the Pengs group, no Au nanowire structures were observed in these *in situ* experiments. These results lead to the conclusion that the appearance of such structures is an effect of the TEM sample preparation. Y. Mikhlin et al.[60] observed the formation of smaller particles and the progressive growth of these particles. However, the pH value remains a dominant factor during the synthesis.[61,66] Other key parameters for the reaction are the concentration of the precursor[30,67] and the concentration of citric acid[68] as the reducing agent. Additionally, some additives can enhance the circularity of the resulting GNSs.[63,69]

Rapid nucleation followed by diffusive growth is crucial for synthesizing nanoparticles with a narrow distribution.[70] An overlap between nucleation and growth processes will broaden particle-size distributions. Therefore, it is advisable to increase the nucleation rate. Fast nucleation can be achieved by increasing the precursor's reactivity, which can be controlled by pH (**Scheme 1**).[63,66,69,71]



Scheme 1: Appearances of the Au(III) precursor at different *pH* values in water according to the developments in the field of the mechanistic studies of citrate-based GNS synthesis.

In **Figure 4**, the initial chemical processes of the reaction are displayed. Prior to nucleation, citrate is oxidized, forming acetone dicarboxylate (ADC; see **Figure 4**, top square) and carbon dioxide. The two electrons released during this process reduce the Au(III) precursor ($AuCl_3$) to Au(I) (AuCl). Besides providing electrons for the reduction of the precursor, the formation of ADC is crucial because it serves as a bidentate ligand for the AuCl. The capability of the ADC to form larger intermediate complexes with AuCl (**Figure 4**, bottom left) is considered a crucial factor in initiating the nucleation process, as it causes concentration hotspots of AuCl within the solution. Molecular modeling investigations also confirmed the formation of different intermediate gold complexes at varying pH values.[61] Within these [AuCl]-hot spots, the disproportionation of AuCl to Au^0 and $AuCl_3$ can take place (**Figure 4**, bottom right). Afterward, Au^0 can form stable Au_n-clusters leading to nucleation.

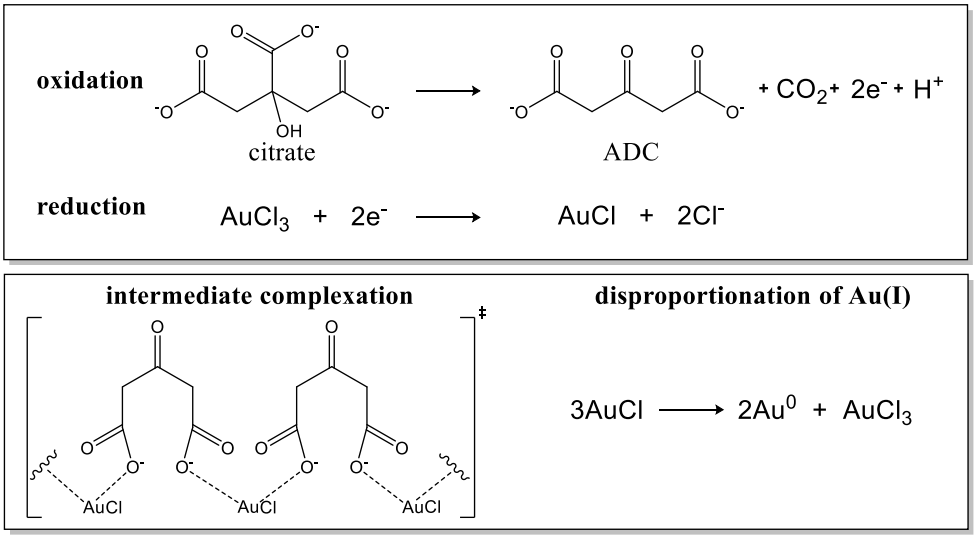


Figure 4. Redox chemistry of the citrate-based Turkevich GNS synthesis and intermediate complex formation, supporting AuCl disproportionation. The top square shows the half-reactions of the redox process of citrate to ADC and $AuCl_3$ to AuCl. The bottom square illustrates the importance of ADC as a supporting complexation agent (left) and AuCl as the GNS monomer species (right) in the Turkevich process.

Although AuCl is known to form orthogonal complexes with other AuCl molecules due to d^{10}-d^{10}-electron interactions, a higher ADC concentration [ADC] is considered to support this coordination. Therefore, increasing the initial [ADC] improves nucleation efficiency. One way to achieve a higher [ADC] is to change the reagent addition sequence by adding the Au(III) precursor solution into the boiling CA solution.[72,73] These approaches are so-called inverted Turkevich methods. Particles obtained by these protocols are slightly smaller (~5–12 nm in diameter)[63,74] than those obtained by the original sequence.

In 2014, F. Schulz et al.[63] published an improved, inverted Turkevich method using ethylenediaminetetraacetic acid (EDTA) for better particle shape control and a citric acid/sodium citrate buffer solution to obtain a constant pH. Highly uniform spherical particles with a particle diameter of 12 nm and a narrow size distribution were obtained. Due to its high reliability, this protocol was also used in this work to synthesize GNS intermediates, which were further functionalized with polymer stabilizers (see **Chapter 5**).

After forming initially stable Au seeds, particle growth takes place. Regarding the work from J. Polte and his coworkers, it becomes evident that the particle growth mechanism is seed-mediated and based on the coalescence of the initially formed particles.[59,75] Although their work disproved the theory of forming 3-dimensional Au worm-like networks during the synthesis, it also disagrees with the LaMer-based growth model because it suggests a more complex model for particle growth. In 2015, they revised the growth mechanism by unraveling the latest open questions.[74] In this work, they confirmed their proposed 4-step seed-mediated growth mechanism (**Figure 5**), which explains the formation of monodisperse GNS via a size-focusing effect during the third and fourth phases.

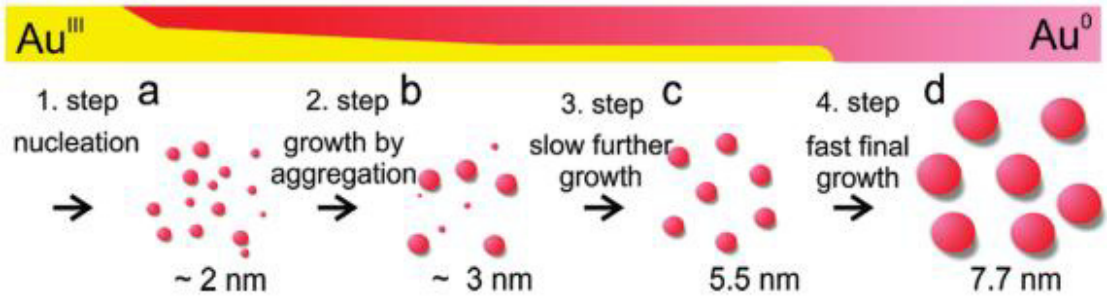


Figure 5. Schematic illustration of the GNS formation in a four-step sequence first described by Polte et al.[59] in 2010. The four different growth steps are (a) fast nucleation in the early stages of the reaction and the formation of nuclei (first 60 s), (b) formation of seed particles due to the coalescence of the Au nuclei, (c) slow continuous particle growth, and (d) final growth phase after a rapid precursor consumption. Reprinted without adaptations with permission from *J. Am. Chem. Soc.* **2010**, 132, 1296–1301. Copyright 2010 American Chemical Society.[59]

According to the results presented by Polte et al.[59,75] the nucleation starts with the reduction of a fraction (about 20 %) of the Au(III) precursor and the formation of polydisperse Au nuclei (at ~45 %). In this context, the term 'nuclei' refers to the first thermodynamically stable clusters that form during the reaction. This step is followed by an aggregative growth step (2. step) due to the coalescence of the initial gold nuclei. In this step, the first seed particles are formed. Only after entering the second step does the number of particles in the suspension remain nearly constant. In the third phase, slow diffusion-based particle growth continues, and the average size distribution narrows to about 14 % due to size-focusing effects. At the end of the third phase, a rapid precursor consumption occurs, leading into the fourth phase, where fast particle growth occurs, and the polydispersity is further narrowed down to about 10 %. Polte et al. attributed this enhancement in reaction rate to autocatalytic processes on the GNP surface after particles with a diameter of 10 nm formed. This four-step mechanism has been proven valid across a wide range of parameters, which was confirmed later with some minor adjustments.[74,76]

The development of this mechanism impressively shows the complexity of the citrate reduction and is an excellent example of how vital the development of analytical methods for nanoscience is.

4.1.2.2. The Silver-assisted synthesis of GNRs: Seed-mediated anisotropic growth

To control the anisotropic growth of GNPs, several different agents and specific reaction conditions are required. Many different reaction protocols for the syntheses of a vast number of GNPs with different sizes and morphologies, ranging from the already described spherical particles, over rod-shaped[7,77,78] to more complex structures like stars[79], hollow spheres[80], and tubes[81], are known in the literature. This work involved synthesizing GNRs using a tailor-made diblock copolymer (DBP) system to trigger anisotropic growth. For this reason, this chapter covers the mechanism of GNR synthesis and highlights some crucial conditions for conventional seeded-growth synthesis. As the previous sentence implies, GNRs can also be synthesized using various techniques, such as template-based approaches.[82,83]. Although these techniques can have several advantages over the seed-based approaches, they often lack flexibility, for example, when different particle sizes are needed. They are often fixed to a specific aspect ratio (AR) and require complex protocols, such as removing the used template.

The synthesis of GNRs via the seeded-growth approach provides higher flexibility. Small changes in the reaction conditions can easily adjust the length. Since Wang et al.[84] discovered the anisotropic growth-inducing effect of some surfactants, the GNR synthesis in solution, and its mechanism have been continuously revised.[85–91] The most commonly used surfactant in these protocols is cetyltrimethylammonium bromide (CTAB). Silver nitrate is added to the reaction to support the anisotropic growth. All these approaches are two-step processes performed in water.

GNRs can be divided into sub-classes, such as monocrystalline and pentatwinned GNRs. Both have their advantages and disadvantages. For example, pentatwinned GNRs usually have higher aspect ratios and are synthesized without additional silver, but they also come with a limited shape yield and must be purified after synthesis.[7,78] The key factor for the synthesis of both classes of GNR is to trigger the nucleation process at a specific point during the preparation. Therefore, the synthesis of GNRs usually begins with the preparation of GNS seed particles. This section will focus on the synthesis of these particles because the GNR synthesis presented in this work is adapted from the seeded-growth synthesis of monocrystalline GNRs. CTAB-stabilized GNP seeds are needed to synthesize monocrystalline GNRs. Therefore, CTAB-stabilized GNP-seed particles are synthesized in the first step by reducing the Au^{III}-precursor ($HAuCl_4$) with a potent reducing agent like sodium borohydride ($NaBH_4$). These seeds must be freshly prepared to achieve better results because seed quality (size distribution and stabilization) can suffer greatly when stored for a long time. In the second step, the precursor solution is prepared, which contains the gold precursor (usually $HAuCl_4$), CTAB as a stabilizer and facet directing agent, as well as silver nitrate ($AgNO_3$) to further support anisotropic growth, and ascorbic acid (AA) as a mild reducing agent. In **Figure 6**, the different steps of the particle synthesis are illustrated.

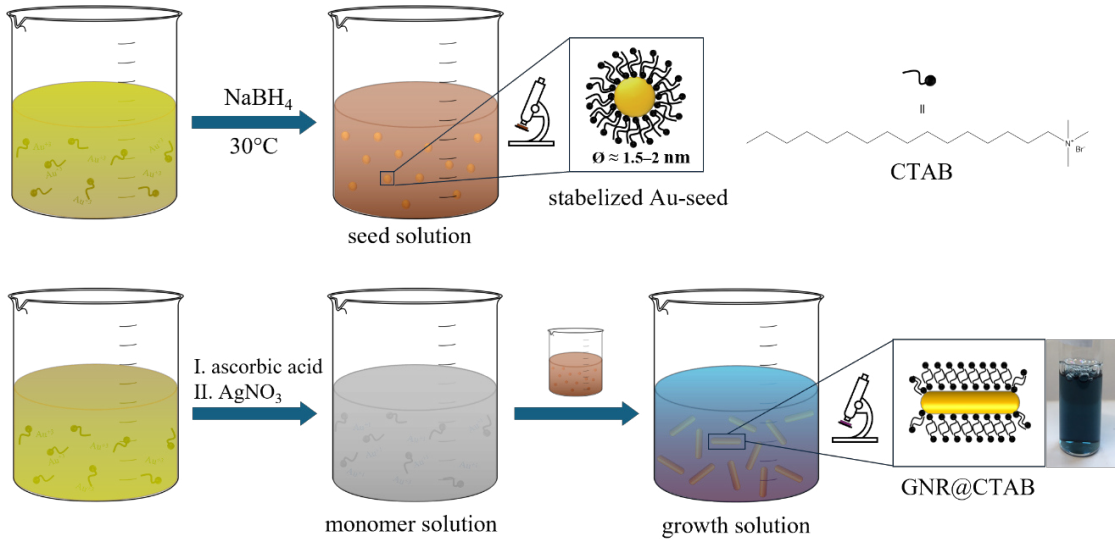


Figure 6. Illustrated silver-assisted seeded growth, GNR-synthesis, and nomenclature of the intermediate solutions, as they are used further in this work. The figure is inspired by the synthesis protocol described in Reference [7], which was used and adapted in this work to synthesize GNR.

The order in which the reactants are added is essential when preparing the precursor solution. Preparation begins by dissolving CTAB in water. Afterward, a $HAuCl_4$ solution is added. After the addition, the solution can initially appear turbid while progressively turning deep yellow and clear. It is important to wait until the solution clears again before AA is added to the next step. As a mild reducing agent, AA reduces the Au(III) precursor to the Au(I) monomer species. The solution turns from yellow to colorless due to the formation of colorless Au(I) complexes. This color change is an important indicator that the following reaction will be successful because the appearance of any color at this stage strongly indicates the formation of particles due to a secondary nucleation process. Immediately after discoloration of the solution, a freshly prepared $AgNO_3$ solution is added. This increases selective growth at the particle tips in later reaction steps due to the formation of a facet-specific Ag/CTAB complex and the underpotential deposition of Ag^0[92,93] on higher-energy facets. Finally, particle growth is initiated by adding the seed solution to the monomer solution, forcing nucleation of the monomer species on the seed surfaces. The mechanism of the GNR growth can be described as a complex interplay between thermodynamic and kinetic-controlled conditions.[7,94]

In 2015, Scarabelli et al.[7] reviewed the synthesis of GNRs in great detail by simultaneously pointing out some common mistakes before and during the execution of the synthesis, and giving helpful tricks to avoid them. By providing important knowledge regarding the chemical and physical processes during the reaction, they underlined the significance of an accurate reaction execution.

CTAB: A double-faced ally

GNRs are among the most versatile GNPs due to their unique plasmonic properties (chapter 4.1.3).[95] They are applicable in many different fields. However, driven by the urge to use CTAB as a nearly alternative-free option for seeded-growth-based approaches, GNRs are primarily inapplicable for biological and medical applications because of the inherent toxicity of CTAB.[4–6] This issue is the motivation for the second publication presented in this thesis, where a tailor-made polymer is presented capable of replacing CTAB in the monomer solution (Chapter 5). To address the question: *Why is CTAB so important and challenging to replace?* The following paragraphs are dedicated to the different tasks of CTAB and their significance for anisotropic growth in more detail.

- *Particle stabilization*. The arguably most apparent task of CTAB is its role as a surfactant and stabilizer of the GNRs. As implied in **Figure 7**, CTAB forms a bilayer on the particle's surface to stabilize GNPs in suspensions.[89,96–98] This CTAB-bilayer forms an equilibrium with excess CTAB micelles in the solution, enhancing the stability of the particle suspension.[4,89,99] To obtain this CTAB-bilayer, a CTAB concentration (c_{CTAB}) above the critical micelle concentration (*cmc*) is needed, which is between 0.081 mM and 0.94 mM[100–103] depending on the solution temperature. As a result, typical GNR protocols operate well above the *cmc* of CTAB (0.1 M[7,8]). Reducing c_{CTAB} below a specific concentration, depending on the composition of the suspension (ionic strength, temperature, etc.), will ultimately destabilize the particle suspension. Although this behavior was applied in several studies investigating the shape-selective precipitation[104] and controlled assimilation of GNRs[105,106], it ultimately limits the capacity for ligand exchanges since this destabilization happens to be irreversible[107] in many cases.

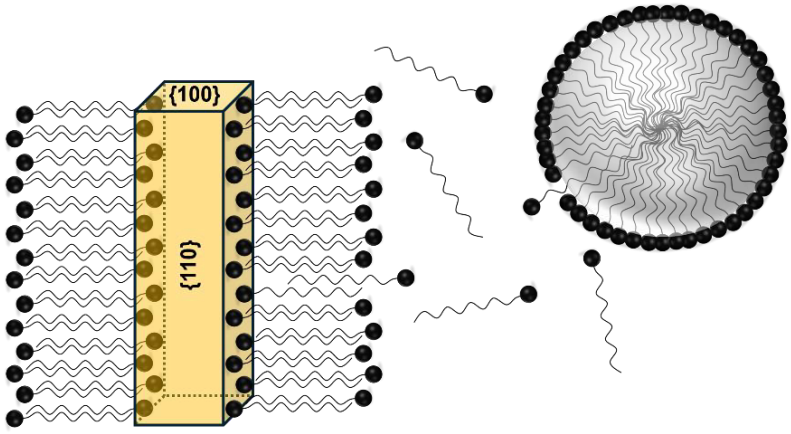


Figure 7. Simplified visualization of the facet-specific GNR (yellow) stabilization via a bilayer structure and equilibrium with the CTAB micelle in water.

- *Facet-specific capping agent.* As indicated in **Figure 7**, the cationic headgroup of CTAB preferentially coordinates to the {110}-facet surface of the GNRs due to the higher surface energy of this face.[86,90,106,108] This behavior is critical during anisotropic growth because it forces particle growth dominantly at the particle tips.[86,108] However, there has been some controversy about the exact crystallographic properties of GNRs. Therefore, the scheme shown in **Figure 7** must be taken with caution. Later investigations showed that GNRs show higher-index lateral facets than those shown in **Figure 7**.[88,109] However, the principle of facet-blocking seems reasonable because of the facet-specific binding affinity of CTAB[110] and its complexes (see "*The anion effect*" below).
- *Electric-field-directed growth.* The facet-specific capping mechanism is not the only proposed mechanism for the anisotropic growth of GNRs. In 2004, Mulvaney et al. described the theory of electric-field-directed growth of GNRs.[91] They claimed that Au(III) and Au(I) ions are quantitatively bound to the CTAB micelles in the solution. Consequently, CTAB is present at every step of the GNR synthesis, such as the reduction of Au(III) to Au(I) by ascorbic acid and the flux of the Au(I) ions to the surface of the injected Au seeds. The resulting mechanism describes a maximum flux of Au(I) ions at higher surface curvatures, driven by an increased electrical potential gradient of the double layer at higher surface curvatures. Although the authors claim that their proposed mechanism does not necessarily apply to every surfactant-based system and that there is uncertainty about the initial symmetry-breaking at the onset of the particle growth, it can still be applied to explain the formation of particles with non-equilibrium crystal characteristics.
- *The anion effect.* The above-discussed tasks of CTAB mostly focused on the effects of the cetyl trimethyl ammonium cation (CTA^+). However, the bromide anion (Br^-) also contributes significantly during particle growth in various stages. If the bromide ion concentration drops below 0.1 mM, the GNR synthesis is impacted significantly, which can be explained by the important interplay between the Ag^+- and Br^--ions described by Zhang and coworkers.[111] They identified the complex $[AgBr(CTA)]^+$ as the key for anisotropic growth and described that a Br/Ag-ratio of 1:1 or higher is needed to synthesize GNRs with sufficient shape yield (>90 %), which stands in agreement with earlier investigations.[112–114] Zhang and coworkers also found that bromide decreases the reaction time. They explained this behavior by the formation of $AuBr_2^-$ at higher Br^- concentrations and by the passivating behavior of $AuBr_2^-$, which contributes to the kinetic control of the particle growth by limiting the accessibility of the Au^I-monomers.[111]

Due to the toxicity of CTAB, the substitution of CTAB from the GNR dispersion has been the subject of several investigations.[4,5,115,116] The current challenge is that the absence of CTAB must be proven, especially for biological applications.[4]

One example of the successful quantitative replacement of CTAB for CTAB-stabilized GNRs was reported by M. Chanana and coworkers in 2015.[116] They used the protein bovine serum albumin (BSA) to coat GNRs with different aspect ratios. The full replacement of CTAB was shown by using several analytical techniques. Although the group of M. Chanana has undoubtedly achieved inspiring results, this procedure remains very complex and requires many different measures to provide CTAB-free conditions. Additionally, their protocol only applies to BSA. The quantitative functionalization of GNRs with a polymer shell, as it is aimed for in this work, remains challenging, especially for higher aspect ratio GNRs. The main reason is the increased side-to-tip surface ratio and the higher affinity, leading to stronger binding of CTAB to the lateral particle surface.[4,116] In 2014, Z. Zhang and M. Lin published their work about the fast loading of thiolate PEG (PEG-SH) on CTAB-protected GNRs. This procedure enabled the replacement of CTAB with PEG-SH within a short period (30 min). However, as the authors claim, it was impossible to rule out the presence of residual CTAB trapped inside the PEG chains.[115]

Obviously, CTAB must not be removed from the GNR product if it has never been added during the synthesis. From the information above, it should be evident that this task is not trivial and needs a deeper understanding of the reaction mechanism of particle growth because CTAB is involved in all reaction steps. Seminal work on reducing the CTAB concentration during GNR synthesis was conducted by the group of C. B. Murray, which studied the effects of several additives on silver-assisted GNR synthesis. In 2012, C. B. Murray and coworkers achieved a c_{CTAB} of 0.05 M by adding aromatic additives to modify the micellization behavior of CTAB.[117] Only one year later, in 2013, the Murray group published a GNR synthesis applying a binary surfactant mixture of CTAB and sodium oleate. This procedure showed impressive improvements in the seeded growth synthesis by simultaneously enabling very low c_{CTAB} (0.037 M).[118] Reducing the concentration of CTAB during the seeded-growth synthesis of GNRs using a stimuli-responsive tailor-made copolymer system is the topic in Chapter 5.

4.1.3. Optical Properties of GNPs

GNPs are known for their unique optical properties. These properties are explained by the collective oscillation of the conducting electrons of nanoparticles induced by an incident electromagnetic (EM) field. This induced resonance is called localized surface plasmon resonance (LSPR) and is described for different NP systems like silver, platinum, titanium nitride particles, and many more.[20,119] It is one of the great examples of the differences when the nanoscale regime is entered.[19] As mentioned in Section 4.1.1, many NP applications were invented based on these LSPR properties. In Section 4.1.3.1, the general theory of the LSPR is covered.

4.1.3.1. Surface Plasmons (SPs): General theory, dependencies, and applications

Surface plasmons (SPs) are classified as bosonic quasiparticles and can be described as the collective oscillation of the conducting electrons of a metal.[51,120] As indicated by the name, SPs are confined to the surface of the metal. There are two types of plasmons: the propagating surface plasmons (PSPs) for bulk material surfaces and, when confined in a nanoparticle, the localized surface plasmons (LSPs). Depending on the size of the NP that confines the plasmon, the plasmon can be excited by a specific frequency of an incident EM field. **Figure 8** illustrates the process of collective oscillation of the conducting electron cloud (light blue sphere) induced by an external EM field, like light.

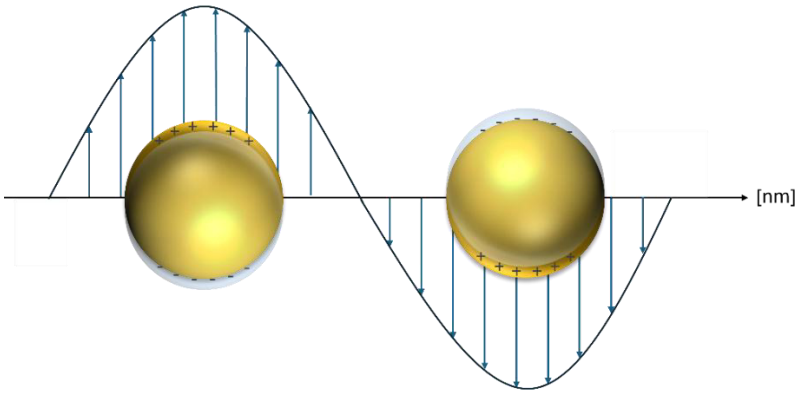


Figure 8. Generally accepted graphical concept[20,51,121–123] of the plasmonic excitation by an incident EM field for spherical GNPs with a diameter lower than the EM wavelength (λ).

The coherent displacement of the conducting electrons in the NP from their initial state leads to the formation of a dipole, with the positively charged atomic lattice serving as the countercharge. This immobilized positively charged lattice generates a restoring force to the displaced electrons that pulls the electrons back into the lattice. Due to this interaction, the plasmon in an NP can be described via a harmonic mass-spring oscillator in phase with the EM field.[19,20,52,120] This interaction leads to the absorption of the energy of the incoming photons, which is mostly efficient when the photon energy matches the LSPR.[124]

The simplified expression of the LSP via a damped oscillator driven by an EM wave, with the interaction between the positive lattice and the electronic cloud as the restoring force, allows a

deeper understanding of the LSPR and its dependencies. The frequency of the oscillation (LSP frequency) is influenced by many different factors, like the particle size and shape, the dielectric constant of the surrounding medium (ε_0), and the complex dielectric function $\varepsilon(\omega)$ with ω as the frequency of the incident light. All these parameters are combined in the Clausius-Mossotti relation to describe the magnetic polarizability (α) for spherical metal particles with a volume V_{NP} and the vacuum permittivity (ε_{vac}).[20,119,120]

$$\alpha = 3\varepsilon_0\varepsilon_{vac}V_{NP}\frac{\varepsilon(\omega) - \varepsilon_0}{\varepsilon(\omega) + 2\varepsilon_0} \tag{4.1}$$

By unraveling Equation 4.1, further dependencies of the magnetic polarizability become apparent, for instance, the dependence on ε_0 when the surrounding medium is changed. This means that changes in surface stabilization can alter the resonance frequency of GNPs. This effect would be apparent at ligand exchange on the particle surfaces.

Once the energy of a photon is absorbed by the plasmon, it can be emitted via a radiative process, by emitting another photon, or by more complex nonradiative processes. The latter is essential for photothermal processes and is based on electron-dampening effects and surface plasmon polarization (SPP).[124–126] These processes can be mathematically described by splitting the complex $\varepsilon(\omega)$ into its real ($\varepsilon_r(\omega)$) and imaginary ($\varepsilon_i(\omega)$) values. In this case, $\varepsilon_i(\omega)$ stands for the system losses.[120] To determine the efficiency of the number of photons that are removed from an incident light source, the extinction cross-section (σ_{ext}) is introduced. It is defined as the sum of the absorbing (σ_{abs}) and the scattering cross-section (σ_{sca}). For NPs significantly smaller (typically below 50 nm[19]) than the wavelength (λ) of the incident light, σ_{ext} can be derived from the dipole approximation, Equation (4.1), and by applying the solution of the Maxwell equation provided by the Mie theory.[19,127]

$$\sigma_{ext} = \frac{18\pi\varepsilon_0^{3/2}}{\lambda}V_{NP}\frac{\varepsilon_0}{(2\varepsilon_0 + \varepsilon_r(\omega))^2 + \varepsilon_i(\omega)^2} \tag{4.2}$$

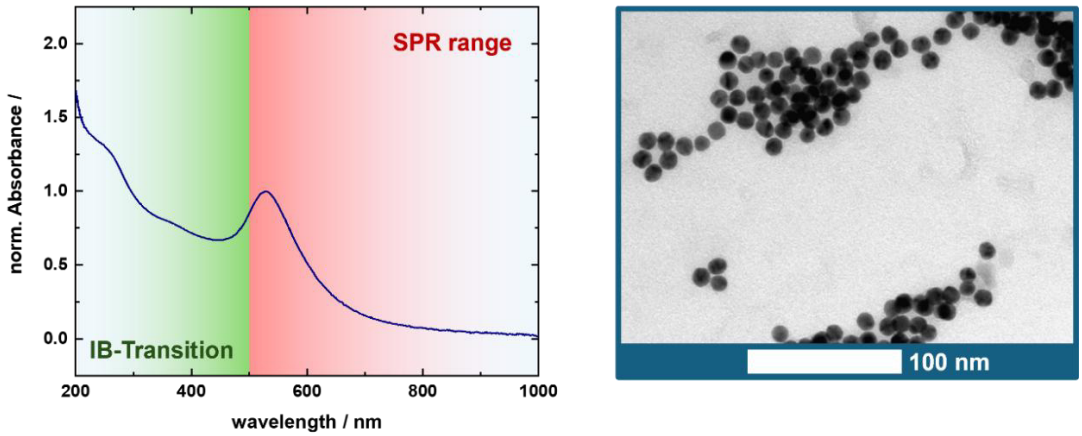


Figure 9. Normalized UV–Vis absorbance spectrum of citrate-stabilized GNS synthesized according to the inverse Turkevich method described by F. Schulz et al.[63](left) and a TEM image of the same sample after drying on a carbon film (right). Additionally, the SPR transition range (red) and the interband transition range (green) are added schematically to the spectrum.

UV–Vis extinction spectroscopy can be used to visualize the LSPR of a GNP sample. **Figure 9** shows the normalized UV–Vis extinction spectra of a GNS solution with an average diameter of (12.0 ± 0.8) nm and a TEM image of the same sample. As is typical for most GNS, the sample shows an LSPR between 520 nm and 580 nm.[120,128] In contrast to silver nanoparticles (Ag-NP), GNS shows an overlap between the plasmon signal (the SPR range) and nonradiative interband transitions corresponding to $\varepsilon_i(\omega)$ described before.

As this chapter's headline implies and as it is shown in Equations 4.1 and 4.2, the LSPR of GNS is a particle size-dependent specification. For GNS suspensions with particle sizes between 4 nm and 100 nm, a local extinction maximum in the wavelength area between 505 nm and 575 nm can be observed, depending on their size and other parameters such as the refractive index of the solvent and the stabilizing ligand.[3,127] There are specific NP sizes of special interest where different effects must be considered. One of these critical sizes is reached at a diameter of 50 nm.[129] Corresponding to the mean free path (MFP) for the free electrons in bulk, this size is the border above which multiple oscillation modes can be formed in a single particle, causing a multipolar state in the NP. It is known that larger GNPs tend to show a broadening of the plasmon band due to retardation effects and the higher modes of oscillation, which peak at lower energies and cause a redshift of the LSPR maximum for larger particles.[127,129] By decreasing the particle diameter below a specific size (~20 nm[128,129]), the oscillation is damped due to electron collisions. This causes the weakening and broadening of the plasmon band until it disappears entirely at particle diameters below 2 nm[129]. Due to the size-dependency of the LSPR, UV–Vis extinction spectroscopy has proven to be a valuable tool for the size determination of GNS.[128,130]

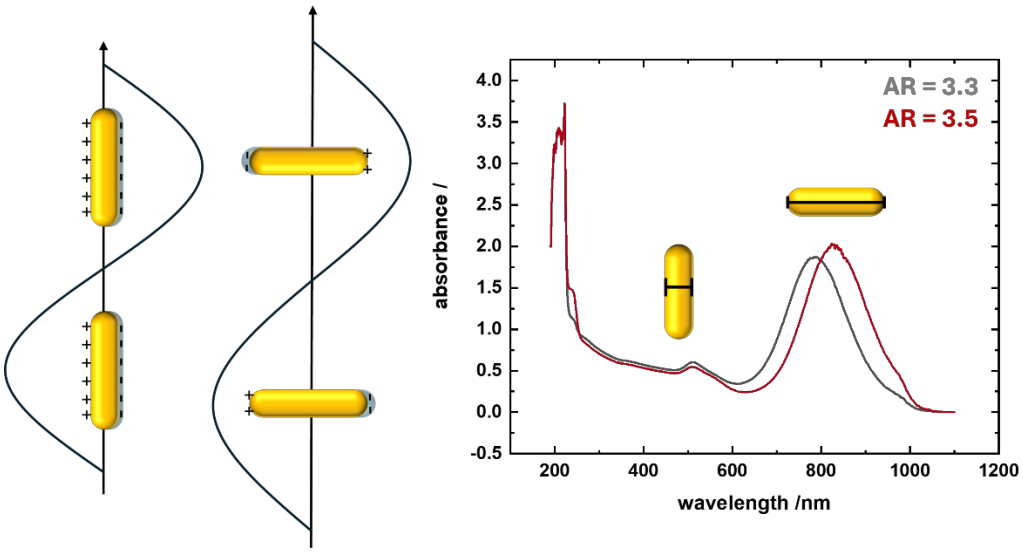


Figure 10. Plasmonic properties of a single GNR with longitudinal and transversal excitation of the collective free electron oscillation (left) and UV–vis extinction spectrum (right-hand side) of two CTAB-stabilized GNR samples (in water) with varying aspect ratios (AR).

The above-described dependencies are focused on the size dependency of the LSPR of isotropic (spherical) GNPs. Anisotropic GNPs like GNRs also show intriguing plasmonic behavior. These particles show an oscillation mode for the longitudinal (length) and the transversal (width) dimensions (**Figure 10** in the scheme on the left). This results in two distinctive plasmonic signals in the extinction spectrum. To calculate σ_{ext}, the Gans theory can be applied. This theory expands the as-discussed dipole approximation for spherical particles to elongated ellipsoids.[123,129,131,132] While the transversal mode arises from the dipole mode, the longitudinal signal in GNRs comprises multiple higher-order modes.[133,134] The plasmonic character of GNRs is strongly dependent on the aspect ratio (particle length/ particle width). **Figure 10** (right-hand side) shows the UV–vis extinction spectrum of two typical GNR samples with varying aspect ratios in a CTAB-stabilized suspension in water. The extinction spectrum impressively shows the huge impact of a higher aspect ratio on the position of the longitudinal LSPR maximum with a similar particle width (~9 nm). This dependency is well-known and is one of the reasons why GNRs are counted as the most versatile plasmonic particles.[84,95,108,129,132] The longitudinal plasmon mode of GNRs reaches into the near-infrared (NIR) regime far below the particle sizes needed for isotropic GNS.[95] In order to reach the NIR regime, GNSs must have diameters >100 nm.[135] However, particles in this size regime are impractical for biological applications because the cellular uptake of such massive particles is limited. The ideal size for an efficient cellular uptake is approximately 50 nm.[136,137] At this size, GNSs usually, depending on their stabilization, show an LSPR maximum between 500–600 nm.[135] In contrast, GNRs with a similar length show a longitudinal LSPR maximum around ~700 nm–1000 nm (strongly depending on the aspect ratio).[7,46,138] Additionally, the longitudinal signal of GNRs is separated from the energetic region where interband transitions occur in GNPs, allowing highly efficient light absorption in that area

without losses due to dampening effects like generating electron-hole pairs.[132] For biological applications, the region between 650 nm and 900 nm[33,36,139] is also known as the first biological transparent window, where an EM-wave can penetrate biological tissue more efficiently than at other wavelengths. The circumstance that the longitudinal LSPR of GNRs can be easily reached in this region makes them suitable candidates as applicants in photothermal therapy[20,34] and many other (biological) applications (see ref. [124]).

4.1.3.2. Plasmonic coupling

The versatility of the nonlinear optical properties of GNRs becomes even more evident when interparticle plasmonic coupling appears. Generally, near-field coupling of plasmons occurs at particle distances with dimensions comparable to the particle size.[140] When the interparticle distance (gap size) between two particles falls below a critical distance (d_c), the plasmons of the particles start to oscillate at a joint frequency. Plasmon coupling is usually not observed for particle distances (d) larger than d_c. In 2003, K. Su et al. observed that, for elliptical-shaped particles fixed on an indium tin oxide (ITO) substrate, the d_c depends on the diameter of the coupling nanospheres. Assuming that both particles are the same size, the dependency $d_c = 2.5 \cdot d_{np}$ applies (see **Figure 11**).[141] The coupling of plasmon modes results in a redshift of the absorbance maximum, which is taken advantage of in several applications and scientific works (see Chapter 4.3). In the same article, K. Su and coworkers reported that the intensity of the LSPR maximum shift depends on the interparticle gap size and increases as the gap size decreases.

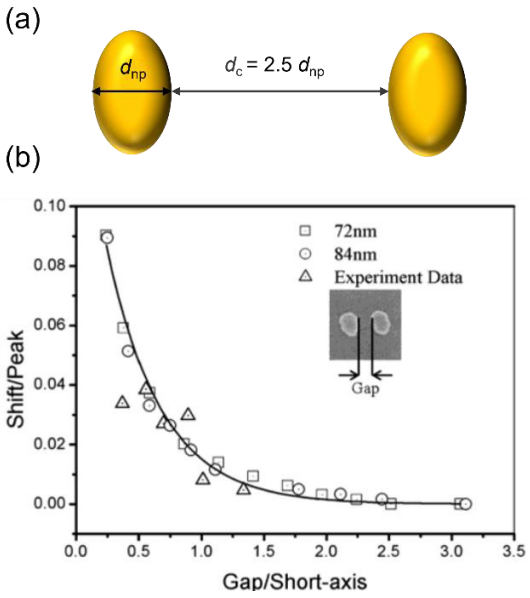


Figure 11. (a) Illustration of the maximum plasmon coupling range (d_c) of ellipsoidal particles based on the description by K. Su and coworkers[141]. The graphic (b) compares computer-simulated data (squares and circles) with experimental data (triangles) of the wavelength shift plotted against the gap size between two particles. For the simulated results, two data sets for different particle diameters (short axis) are shown. Graphic (b) was reused with permission from *Nano Letters*, Vol. 3, No. 8, **2003**. Copyright 2003 American Chemical Society.[141]

By fixing pairs of spherical nanoparticles onto a substrate and changing the polarization direction of the light, W. Rechberger et al. showed that, in addition to the gap size, the polarization direction of the incident light also significantly influences the plasmon resonance.[142] A simple way to calculate the plasmon wavelength shift ($\Delta\lambda_{LSPR}$) between two near-field-coupled, identical GNPs is to use the empirical scaling law shown in Equation (4.3).

$$\frac{\Delta\lambda_{LSPR}}{\lambda} = \beta e^{-\left(\frac{d/d_{np}}{\tau}\right)} \tag{4.3}$$

With λ being the plasmon wavelength of the individual GNP, d the distance between both particles, τ as the decay constant of the plasmon, and β the maximum fractional shift.[143–145] The latter two are usually obtained by fitting particle dimers with different particle sizes. Within specific boundaries (0 nm – d_c), Equation (4.3) can be used to reliably calculate $\Delta\lambda_{LSPR}$ for a particle dimer aligned along the polarization direction of the incident light.

Another way to describe the interaction of plasmons is by using the plasmon hybridization theory, where the conduction electrons are described as an incompressible liquid on a rigid positive charge. The advantage of this model is that it can also be used to predict the plasmonic behavior at varying polarization angles, as the hybrid orbital theory does for different molecules. In this theory, the redshift of two coupling partners is associated with the occupation of collective bonding plasmon modes. If polarized light is aligned with the interparticle axis and the particle spacing is decreased, more modes hybridize, leading to a redshift of the plasmonic resonance.[140] If the incident light stands perpendicular to the interparticle axis, a blueshift occurs, which is explained by repulsive/antisymmetric[142,145,146] forces between the induced dipoles and their coupling.

Compared with spherical particle dimers with equal particle diameters, the plasmon hybridization model becomes increasingly complicated when more complex, anisotropic particles such as GNRs are considered. As described above, aligning polarized light with the axis between particles is essential for assembled particles fixed on a substrate. However, the effect becomes negligible for particle dimers in solution since the particle dimers are in constant Brownian motion within the solution. Since for GNRs, the plasmonic properties are nonlinearly distributed within the particle, and the electrons are mainly concentrated at particle regions with high curvatures (the tips), the position of the coupling partner influences the resulting collective resonance frequency observable in the UV–Vis spectrum. The GNR product solutions investigated in this work primarily consist of spherical and rod-like structures. Therefore, the following part will focus on the interaction of these two particle classes (**Figure 12**).

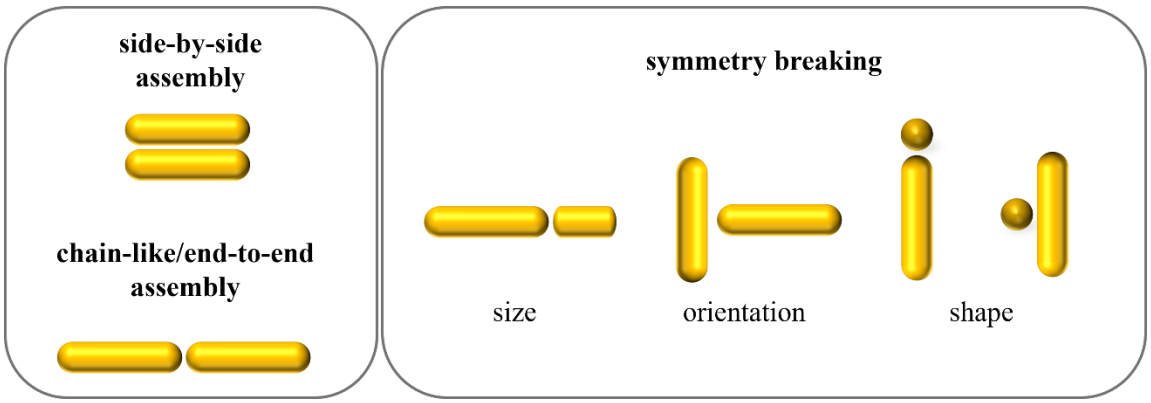


Figure 12. Relevant GNR dimers ($d > 0$ nm) with typical coupling orientations. The typical assimilations are shown, starting with the dimer assimilation of two equal GNRs (left-hand side) and symmetry-breaking particle assimilations with particles of different sizes and shapes (right-hand side).

Because of the lower surface affinities of CTAB at the particle tips, CTAB is more likely to be exchanged at these facets. This characteristic is exploited when aiming for end-to-end particle assembly.[140] The addition of sodium citrate (SC) to a CTAB-stabilized GNR solution causes side-by-side assembly of the GNRs due to the electrostatic interaction of the CA-anion with the positively charged CTAB double layer. Plasmonic coupling of GNR mostly affects the longitudinal signal, significantly shifting the maximum resonance frequency. For instance, for end-to-end particle assimilation, a bathochromic shift of the longitudinal signal of several hundred nanometers is usually observed in the extinction spectrum. Meanwhile, the transversal signal stays nearly unaffected.[147,148] The side-by-side assembly of GNRs also causes a shift of the longitudinal signal towards the blue spectrum. For the side-by-side assimilation of GNR, the transverse signal shows a redshift in the plasmon band.[106] As well as for GNS-dimers assembled, these shifts can be predicted using the plasmon hybridization theory.[149]

Additionally, for identical GNR assembled end-to-end, the shift of the longitudinal signal can be estimated using Equation (4.3), where d_{np} corresponds to the length of the GNR. By exchanging the d/d_{np} term with $(d/d_{np})^{1/3}$, Equation (4.3) becomes more accurate due to the better description of near-field interaction and Coulomb restoring forces between the dipoles of the different particles.[132]

Symmetry-breaking occurs if two coupling GNRs have different sizes and orientations, or one of the coupling partners shows another shape (GNR coupling with a GNS). This symmetry break can significantly influence the collective oscillation of the two particles. Like before, these changes are explained mainly by the hybridization model and the interaction of bonding (attractive) and antibonding (repulsive) modes. For homodimers, a dependence on the orientation angle (θ) of the nanorods relative to each other ($\theta = 0°$ for linear end-to-end assimilations) can be observed, which follows $\cos^2(\theta)$.[144,150]

When the coupling in a heterodimer (two different-sized GNRs) is present, so-called dark antibonding dimer modes are occupied and become visible in the collective spectrum. These antibonding (dark) modes are usually blue-shifted towards higher energies compared to the longitudinal signal of the smaller coupling partner. Meanwhile, the collective bonding (bright) mode is usually red-shifted compared to the longitudinal signal of the larger coupling partner.[150]

Side note: These results correspond to single-particle dimer measurements and calculations. Due to its low intensity, especially for single particles, the transversal signal is not discussed within this context. Another effect observed in such heterodimers is the appearance of asymmetric-shaped signals, especially when interacting with higher energy modes, which is commonly described by the appearance of Fano interferences.[151,152]

Symmetrical breaking also occurs when a GNR couples with a significantly smaller GNS. In this system, the positioning of the nanosphere becomes important. In 2012, L. Shao et al. published a comprehensive study that included both experimental and simulated results for this particular

heterodimer. Their results show highly sensitive plasmon coupling behavior that depends on the gap size between particles and sphere positioning.[153]

This section primarily accounts for the dimer coupling of GNPs on fixed substrates. The coupling of oligomeric particle assembly can become very complex to describe using the common theories discussed above. However, this section is considered to provide a general idea about the concept of plasmon coupling and the vast number of factors influencing the optical properties. It should provide sufficient insight into the topic to facilitate an understanding of the particle coupling discussed in this thesis.

4.2. Smart Polymers: From the Synthesis to Responsive Behavior

The following section covers the theory around the physical properties of smart polymers and their synthesis via radical polymerization using the reversible addition–fragmentation chain transfer (RAFT) polymerization technique. The development of "controlled" radical polymerization (CRP) methods, such as atom transfer radical polymerization (ATRP), nitroxide-mediated polymerization (NMP), and RAFT polymerization, has triggered interesting new developments in polymer science since they enabled control over the polymer's molecular weight and the reinitiation of polymer chains after polymerization. All three techniques belong to the reversible deactivation radical polymerizations (RDRP), which rely on an equilibrium between dormant and activated chain ends.[154–156] *Side note: Since 2009, the terminology "controlled" or "living polymerization" for RDRP methods has been outdated, since RDRP is more accurate and is the terminology recommended by IUPAC.*[157] While NMP and ATRP are based on the persistent radical effect, RAFT polymerization is based on the degenerative radical transfer. The mechanism and recent developments towards photo-initiated RAFT (photoRAFT) polymerization based on the iniferter mechanism are described in Section 4.2.1. in more detail.

Regarding the aim of this work, RAFT polymerization has one impregnable advantage over NMP and ATRP techniques, which is the sulfur-containing dithiocarbonate (DTC) or trithiocarbonate (TTC) head group on every RAFT polymer. This group can easily be transferred into a thiol functionality or used directly as a surface-active group to attach the polymer chain to Au surfaces.[158–163] Additionally, RAFT polymerization is known for its high tolerance for functional groups, enabling the controlled polymerization of most methyl acrylate and acrylate-based monomers. Since its discovery in the late 1990s[164–166], RAFT polymerization has proven itself to be a reliable tool for the controlled radical polymerization of a variety of homo- and copolymer structures. Since 1998, according to "Web of Science" (November 2024), RAFT polymerization has been the title of over 3500 publications and more than 230 patents worldwide (see **Figure 13 (A)**).

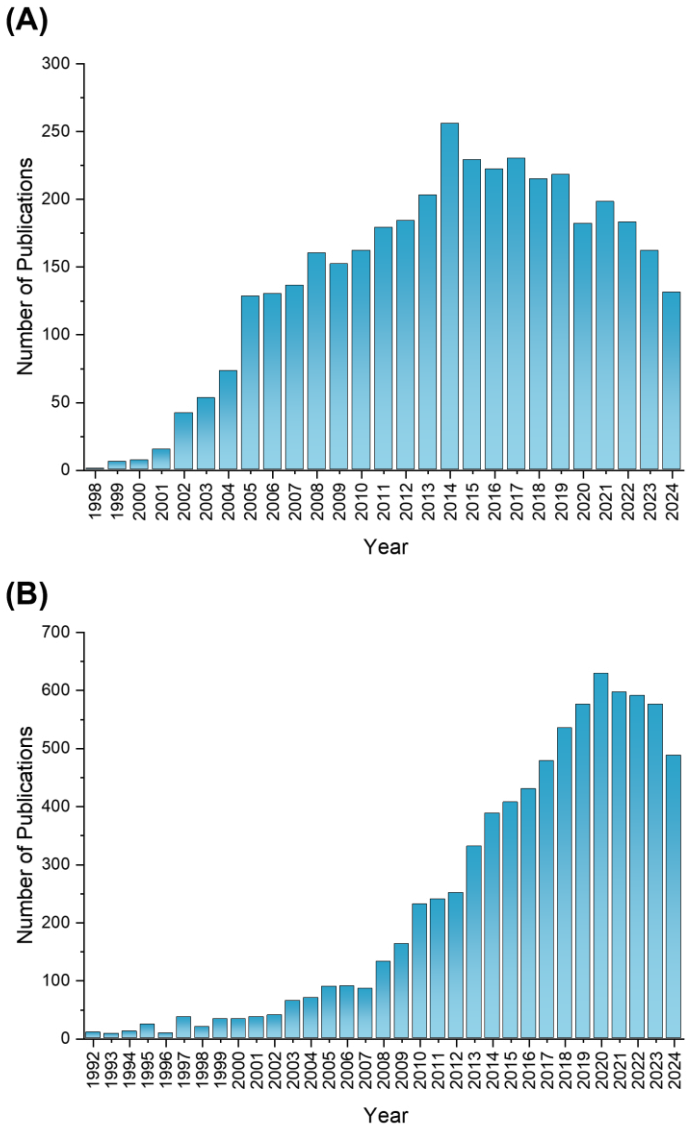
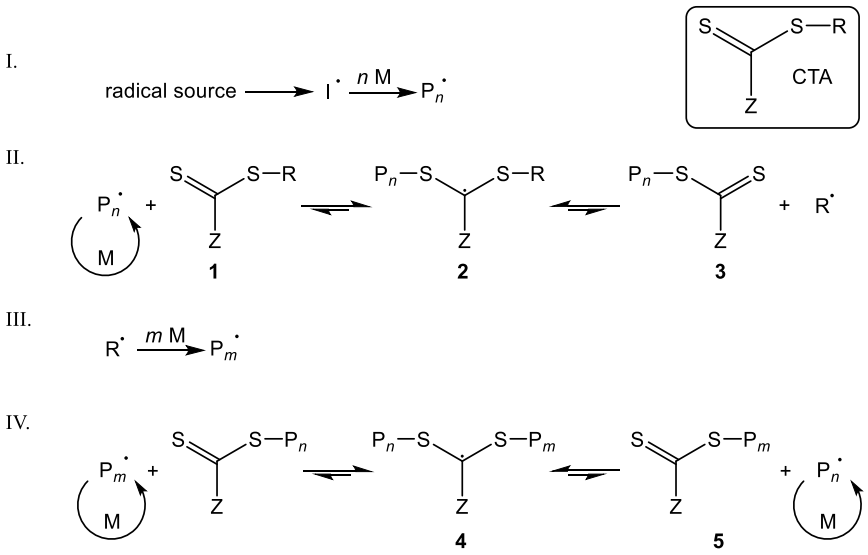


Figure 13. (A) The number of publications with "RAFT polymerization" or "reversible addition–fragmentation chain transfer polymerization" in their title from 1998 until today (source Web of Science; November 2024). **(B)** The number of publications with "smart polymers" or "responsive polymers" in their title from 1992 until today (source Web of Science; November 2024).

Section 4.2.2 covers the topic of water-soluble stimuli-responsive (co-)polymers. Stimuli-responsive polymers, also known as smart polymers, display a fascinating field within polymer science. The remarkable control over their physical properties (like their solubility in water) due to adjusting (at least) one stimulus facilitates the design of new functional polymer materials with unique properties. **Figure 13 (B)** shows the number of publications titled “stimuli-responsive” or “responsive polymers” since 1992. Typical stimuli for such polymers include changes in the system's temperature, pH, or redox potential. Besides these three, several subclasses of stimulus-responsive polymers have been reported. Although the behavior of these subclasses can yield fascinating materials with outstanding properties for several applications, their responsiveness is usually derived from the three classes mentioned earlier.

4.2.1. RAFT Polymerization

Scheme 2 shows the RAFT mechanism for conventional RAFT polymerization using an external initiator. In the first step, the initiator decays into the initiating radical, which starts the growth of the first chain (I). In the pre-equilibrium (II), the active polymer chain-end $P_n\cdot$ reacts with the chain transfer agent (CTA; see **Scheme 2**) and forms an intermediate stabilized radical species (**2**). As indicated by the reaction arrows, the formation of the radical addition product is favorable. The fragmentation of **2** can either release the active chain $P_n\cdot$, or the radical can be transferred to the R-group, forming the active radical R·. R· then initiates the growth of a second chain $P_m\cdot$ (III). In the main equilibrium (IV), $P_m\cdot$ is added to the dormant chain (**3**). At this point in the reaction, either $P_n\cdot$ or $P_m\cdot$ is released via fragmentation and performs chain growth via monomer addition. The reaction is terminated by radical-radical recombination. Because the number of active polymer chains is reduced due to the RAFT process, the radical-radical termination of two active polymer chains is less likely.



Scheme 2. RAFT mechanism with the different reaction stages, starting with the initiation of chain growth (I), followed by the RAFT pre-equilibrium (II), the reinitiation step (III), and the main equilibrium (IV). This commonly accepted mechanism for RAFT polymerization is reproduced from knowledge from different sources.[154,167–169]

For optimal reaction control by the CTA moiety, the rate of addition/fragmentation must exceed the rate of monomer propagation, ensuring that, on average, less than one monomer unit is added during the active state.[154,170] This implies that all chains have a similar degree of polymerization (DP), and a narrow molecular weight distribution (*Đ*) is obtained. However, if the fragmentation rate of **2** or **4** is too slow, the intermediate species can be consumed by side reactions.[170] This will cause less control over the polymerization and, consequently, a broader *Đ*. Additionally, the monomer conversion (p_M) can be an influencing factor. As in free radical polymerizations, the likelihood of irreversible termination events (radical-radical termination) increases as propagation becomes less likely at higher p_M. It is recommended that the polymerization be quenched before complete monomer conversion is reached to prevent irreversible termination events. As a rule of

thumb, RAFT polymerizations are quenched between 50 % and 80 %.[171–173] These values can vary depending on the polymer system—for instance, I. Oral et al.[174] showed that during the polymerization of poly(methacrylic acid), high monomer conversions (>90%), neither the achieved *Đ* nor the number of CTA-functionalized chains is significantly affected.

The CTAs Z-group significantly determines the stability of the intermediates **2** and **4**. To choose the right Z-group, the monomer class must be considered. There are two classes of monomers: the more activated monomers (MAM) and the less activated monomers (LAM). Arguably, the most popular RAFT agent class is the TTC, in which the Z-group is an alkyl thiol attached to the thiocarbonate via its sulfur atom. Due to their structure, MAMs like methyl methacrylate or styrene form relatively stable radicals. Therefore, the intermediate radical must be stabilized to become the dominant species in the pre- and the main equilibrium.[154] TTCs offer reasonable control for the polymerization of MAMs and follow simple synthetic protocols.[1,174,175] To polymerize LAMs, the Z-group has to increase the electron density at the C=S bond, which reduces its reactivity towards the active radicals.[168,176,177] An example of such CTAs are dithiocarbamates.

The right choice of the CTA is vital to ensure proper control over the polymerization process via RAFT. Therefore, several factors must be considered. An often-neglected functionality is the CTA's R-group, which is responsible for reinitiating chain growth and determines how quickly the RAFT process enters the main RAFT equilibrium. The compatibility of R· with the chosen monomer class must be ensured.[170] This consideration becomes essential for synthesizing multiblock copolymers using different monomer classes/reactivities (see **Figure 14**).[154]

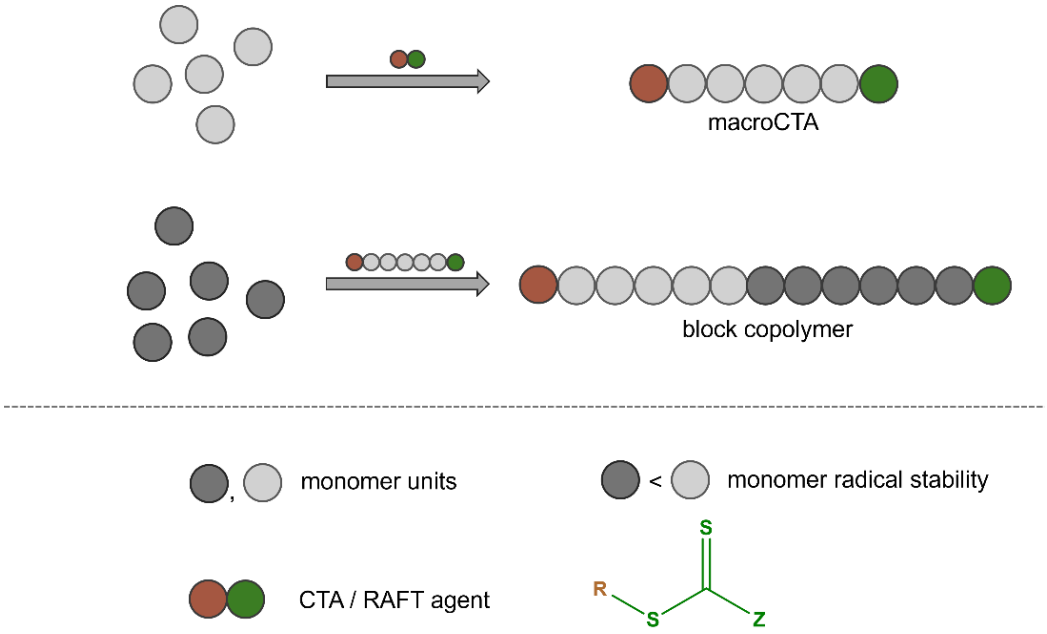


Figure 14. Illustration of a block copolymer synthesis via RAFT polymerization with different monomer reactivities in the recommended order.

Commonly, the livingness of a macroCTA is discussed as a measurement of the number of chains with a CTA end group.[178–180] As mentioned before, this terminology is outdated. From a polymer science-based point of view, the fraction of CTA-functionalized polymer chains within a polymer batch is crucial information if this polymer is further used as a macroCTA to synthesize block copolymers. For a conventional RAFT process initiated with an external radical source like a thermal initiator, the highest possible degree of functionalization is calculable with the following equation[154];

$$L = \frac{[\mathrm{CTA}]_0}{[\mathrm{CTA}]_0 + 2f[\mathrm{I}]_0(1 - \mathrm{e}^{-k_d t})(1 - {}^{f_c}/_{2})} \tag{4.4}$$

Where L is the degree of functionalization (livingness), $[CTA]_0$ is the initial CTA concentration, $[I]_0$ is the initial initiator concentration, f is the initiator efficiency, $k_{d\ is}$ the decomposition rate coefficient of the initiator, t is the reaction time, and f_c radical–radical termination factor describing the ration between the amount of termination via recombination and terminations via disproportionation. From Equation 4.4, it can be derived that to increase the "livingness" of the desired polymer product, $[I]_0$ has to be reduced.

An advanced way to reduce the initiator concentration to zero is by applying the iniferter process described by T. Otsu.[181] The photoiniferter RAFT (photoRAFT) polymerization takes advantage of the photosensitive behavior of the trithiocarbonate. If the thiocarbonyl group is irradiated with UV light, it is transferred into an excited state (π→π*-transition), and R· is released, which initiates the polymerization. Applied to the photoiniferter RAFT approach, Equation (4.4) would simplify to $[CTA]_0/[CTA]_0$, resulting in a theoretical degree of CTA functionalized chains of L=1. However, Equation (4.4) does not account for side reactions that consume the CTA group and compete with the addition-fragmentation equilibrium. For instance, prolonged UV irradiation times cause irreversible degradation by photolysis of the RAFT chain end.[182] A gentler way to initiate the polymerization is using light in the visible spectrum by exciting the spin-forbidden n→π*-transition shown in **Figure 15**. In **Scheme 3**, the widely accepted photoRAFT mechanism is illustrated.[176,183]

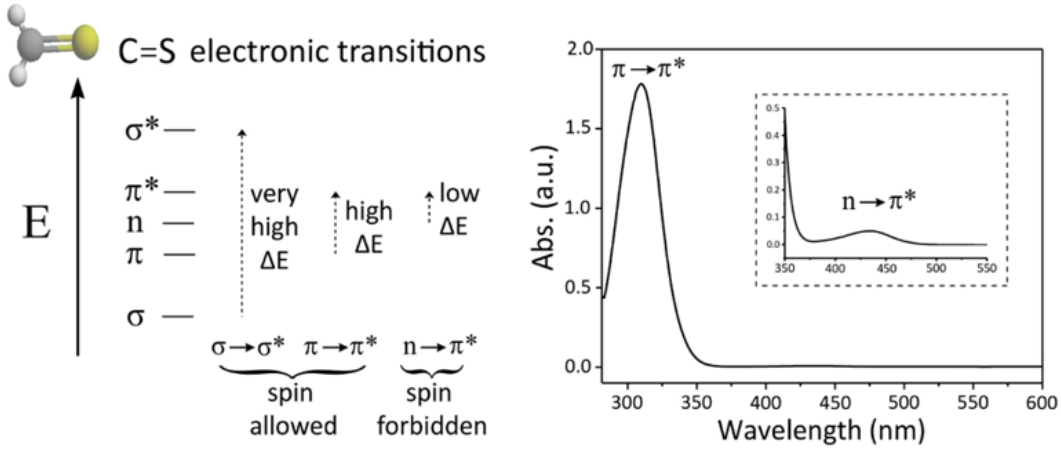
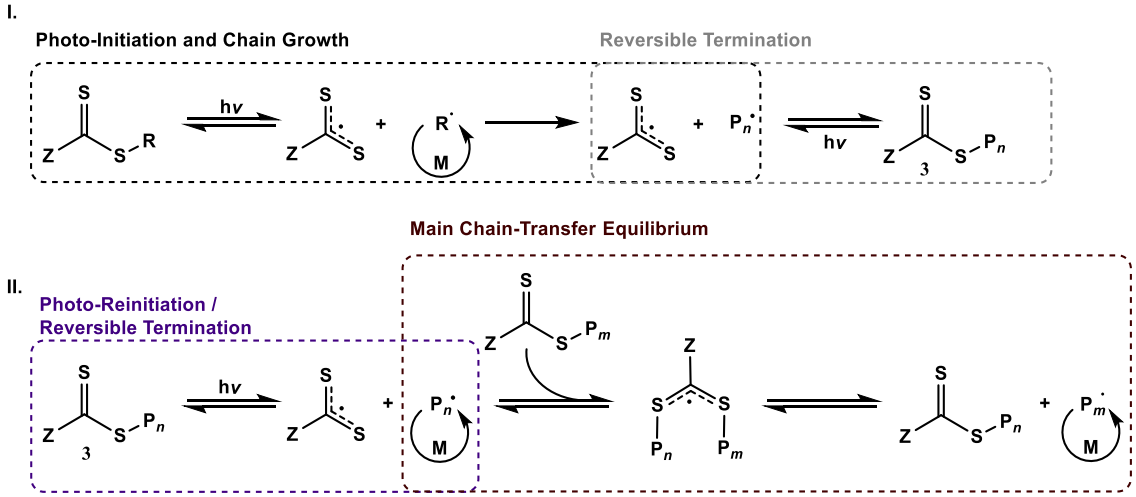


Figure 15. Energy level diagram of a thiocarbonyl compound and the respective UV–vis absorption spectrum with the assigned π→π*- and the "forbidden" n→π*-transition. Reprinted with permission from *Macromolecules* **2015**, 48, 3864−3872. Copyright 2015, American Chemical Society.[184]



Scheme 3. Schematic photo-iniferter RAFT mechanism from forming the first chain P_n (I) to the main RAFT equilibrium (II). The mechanism is adapted from the literature with slight adjustments for better visualization.[176,183,185,186]

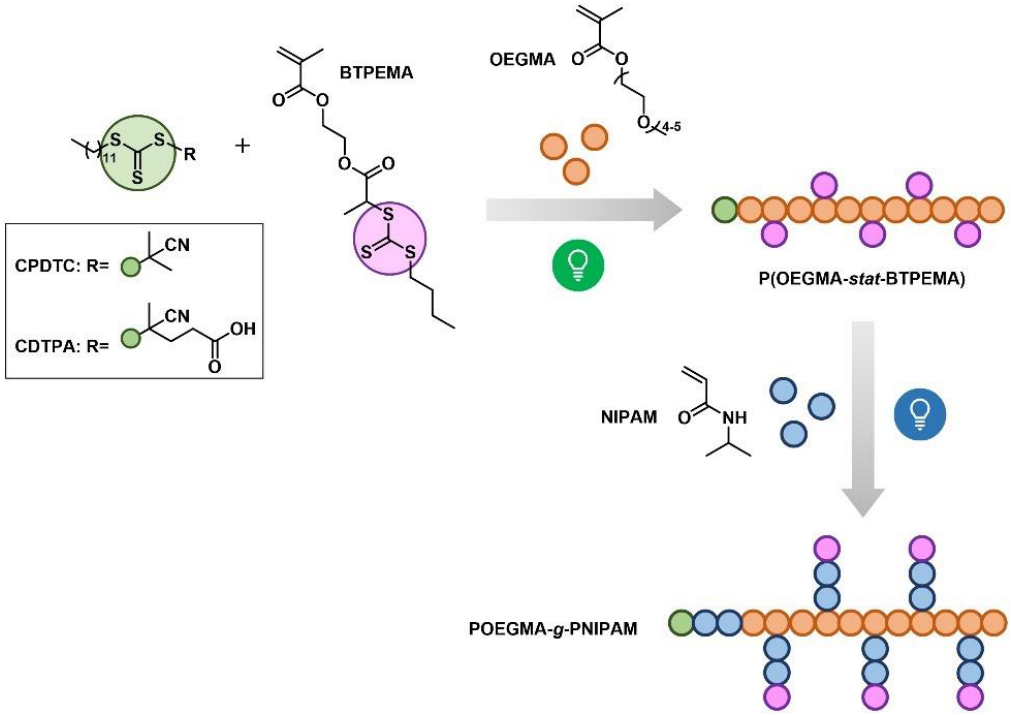
As shown in **Figure 15** and **Scheme 3**, photoRAFT polymerization is a nifty tool to synthesize RAFT polymers with a high degree of CTA end-group functionalization because all radicals in the reaction are derived from the homolytic decomposition of the RAFT agent. Therefore, every radical can, in theory, be captured via reversible termination with a CTA functionality. All RDRP methods enable control over the molecular weight of the polymerization product. However, chain growth, especially in RAFT polymerization, still follows the same rules as in conventional free-radical polymerization. Therefore, the theoretical number average molecular weight ($M_{n,th}$) for the conventional RAFT polymerizations (**Scheme 2**) can be calculated as follows;

$$M_{\mathrm{n,th}} = \frac{p[\mathrm{M}]_0 M_{\mathrm{m}}}{[\mathrm{CTA}]_0 + 2f[\mathrm{I}]_0(1 - \mathrm{e}^{-k_{\mathrm{d}}t})(1 - {}^{f_c}/_2)} + M_{\mathrm{CTA}} \qquad (4.5)$$

Where p is the monomer conversion at a specific reaction time ($t \neq 0$ s), and $[M]_0$ is the initial monomer concentration. M_m and M_{CTA} are the molecular weights of the monomer unit and CTA, respectively. Since no additional initiator is used for the discussed photoRAFT polymerization, the equation can be simplified to Equation (4.6).

$$M_{n,th} = \frac{p[M]_0 M_m}{[CTA]_0} + M_{CTA} \tag{4.6}$$

Of course, Equation 4.6 only applies if all radicals present at the polymerization are derived from the reversible photo-homolytic cleavage of the RAFT agent. Therefore, choosing the right light source is essential. In this matter, the choice of the light source wavelength is crucial. The absorbance of the RAFT agent (**Figure 15**) is one of two key factors because of the needed overlap between the visible light source's emission spectrum and the CTA group's absorbance. Because different R/Z-groups influence the C=S bond absorbance by increasing or decreasing the electron density of that bond, the wavelength at which the CTA can be transferred into an excited state is, therefore, adjustable. **Scheme 4** illustrates the selective photoinitiation of RAFT polymerization and its capabilities.



Scheme 4. Schematic pathway for the synthesis of a graft copolymer using photoRAFT polymerization. Reprinted with permission from the open-access source *Soft Matter*, **2022**, 18, 2082–2091.Copyright 2022, Royal Society of Chemistry.[1]

In this work, J. Xu and V. Abetz present a two-step synthesis of a graft copolymer using two different RAFT agents, where only one of them was activated in the first stage using a longer wavelength, and the other remained inactive while it was incorporated into the first linear polymer product as a monomer unit.[1] In the first step, the monomer oligo(ethylene glycol) methacrylate (OEGMA) is copolymerized with the CTA functionalized monomer 2-(2-(n-butyltrithiocarbonate) propionate) ethyl methacrylate (BTPEMA) to form the statistical copolymer P(OEGMA-*stat*-BTPEMA). The copolymerization of OEGMA and BTPEMA was induced by green light irradiation, which activates the used RAFT agents CDTPA/CPDTC. Since the CTA functionality of the monomer BTPEMA is not activated in the wavelength area, a linear chain is formed. In the second step, blue light initiates the polymerization of *N*-isopropyl acrylamide (NiPAM) onto the multi-functional macroRAFT agent P(OEGMA-*stat*-BTPEMA). Blue light irradiation is needed to activate the side-chain TTC functionality of the BTPEMA unit. As an essential factor for this photoselectivity, the BTPE's R-group must be named. Although the BTPE group may not be activated using green light, it can interact with the free active chain ends in the solution and form an intermediate stabilized TTC-radical. However, the fragmentation of the methacrylic radical (from OEGMA) is much more favorable than the fragmentation of the secondary, less-stable R-group radical from the BTPEMA unit.[187] As a result, BTPEMA's R-group will not reinitiate chain growth, and only linear chain growth will occur in the first step. The secondary NiPAM radical, however, shows similar stability and therefore allows the fragmentation of the secondary R·, consequently enabling the chain transfer and the formation of the main equilibrium. The double thermoresponsive (see section 4.2.2) nature and the multiple TTC functionalizations along the main chain make the graft polymer POEGMA-*g*-PNiPAM an interesting candidate for stabilizing GNP systems.

4.2.2. Smart Polymers and Polymer Networks: From Thermal to pH-controlled Polymer Morphologies

Stimuli-responsive polymers can be classified into three main classes of stimuli: physical, chemical, and biological/biochemical. Stimuli-responsive polymers, also called smart or intelligent polymers, react to a specific external stimulus by sudden, dramatic changes in their physical or chemical properties. Typical biological stimuli are concentration changes of specific biomolecules like glucose [188–190] or enzymes/proteins.[191] Changes in the pH value[192–194], the ionic strength[195–197], or the redox potential[198,199] of a solution are counted among the chemical stimuli. Physical stimuli are temperature changes,[200] light,[201–203] or electrical fields.[204–207] Categorizing certain materials into a specific class of responsive materials can be tricky because most named stimuli overlap with others. Materials where one stimulus influences the reaction of the material to other stimuli are also called multi- or dual-responsive. To deliberately trigger multi-responsive behavior, two monomers with differing or even antagonistic responsive properties are usually combined in block copolymers, where each block shows its own responsive properties. These materials, which are usually submerged in an aqueous solution, are often described as schizophrenic.[173,208–210]

The focus for the design of the polymer materials used in this work was primarily on temperature- and pH-responsive materials. Both types of responsive materials show great potential in different fields of application, such as microgel or micelle-like structures for advanced drug delivery control in medical applications[211,212], as membranes with adjustable water flux[213], or as adjustable emulsifiers in liquid applications.[214] Section 4.2.2.1 provides a closer look at thermo-responsive and pH-responsive polymers. In Section 4.2.2.2, a closer look is given at the different possibilities for post-polymerization crosslinking of different polymer materials.

4.2.2.1. Temperature and pH-Responsive Homopolymers

Temperature-responsive polymers undergo a solubility transition at a characteristic temperature. There are two classes of thermoresponsive polymers. Suppose the polymer turns from a swollen water-soluble state into a collapsed hydrophobic state while heating, the transition temperature is described as a lower critical solution temperature (LCST). If a polymer turns from a collapsed, insoluble state into a swollen, soluble state at the transition temperature, this temperature is called the upper critical solution temperature (UCST).

The type of thermos-responsive behavior, LCST or UCST, depends on the nature of the polymer-solvent interaction. If the polymer exhibits strong polymer-polymer interactions that surpass polymer-solvent interactions, it is likely to exhibit UCST behavior. This process is enthalpy (ΔH_m) controlled. Meanwhile, the LCST transition behavior relies on an entropy (ΔS_m) controlled process.[210,215] Although UCST-type polymers have intriguing characteristics that are promising for specific applications, like the delivery of hydrophobic drugs,[210,215] they are susceptible to

hydrolysis. Due to this sensitivity, this work focuses on LCST-type polymers, which are more resistant to chemical combustion of their side-chain functionalities and therefore show more reliable responsive behavior after various heating/cooling cycles in water. The classical theory that describes the dissolution of polymers in a solvent is the Flory-Huggins-Staverman theory, an extension of the regular solution theory, which is based on a two-dimensional square lattice model.[216] It shows the Gibbs free mixing energy (ΔG_m) as a function of ΔH_m and ΔS_m, as given by Equation (4.4).

$$\Delta G_m = \Delta H_m - T\Delta S_m \tag{4.4}$$

Although this theory is well applicable for the description of UCST-type behavior, it is limited when it comes to the description of LCST-like behavior because the underlying lattice model does not represent the orientation entropy of water molecules within the system. Therefore, any entropy increase caused by the release of water molecules from the polymer coil is not represented as well. A more vivid concept to describe LCST-type behavior is the model of hydrophobic hydration of a polymer chain. In this model, the polymer's hydrophobic backbone is stabilized by a layer of water molecules. When the system reaches the polymer's phase transition temperature (PTT or T_c), this layer becomes entropically unfavorable and collapses. This collapse is causing an entropy gain due to the release of water molecules (**Figure 16**).

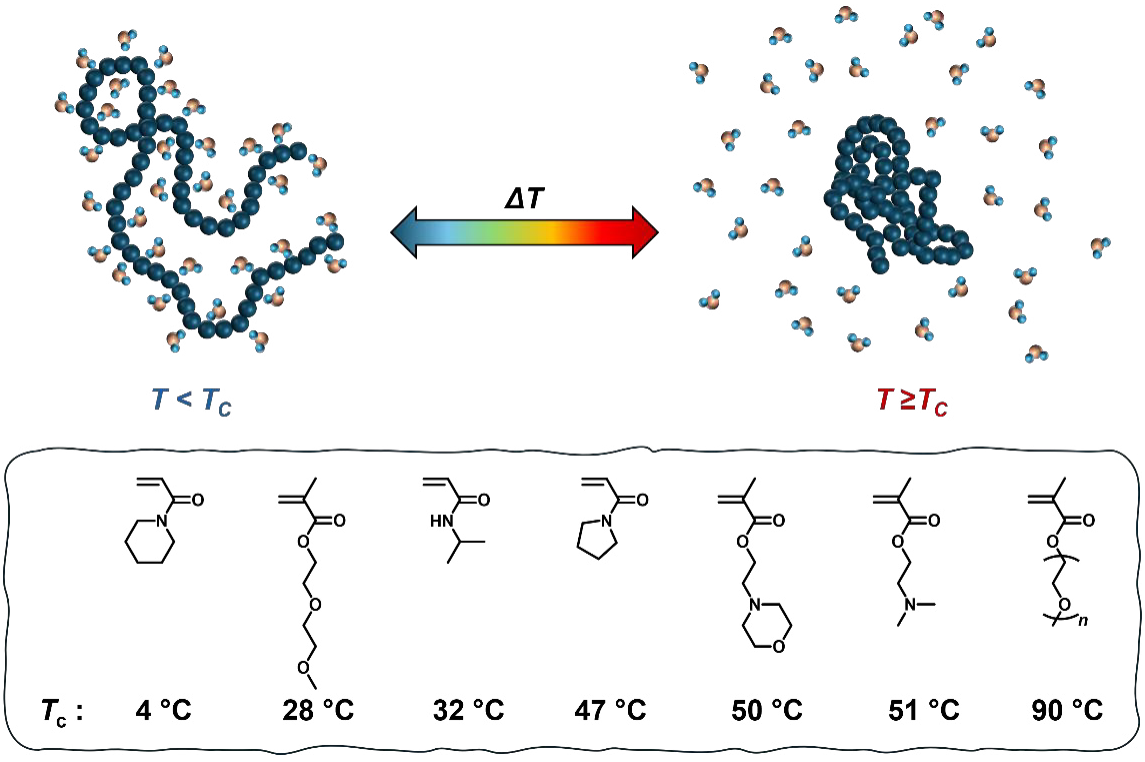


Figure 16. Illustration of the coil-to-globule transition of an LCST-type polymer (top) and typical LCST-type monomers with the corresponding (approximate) LCST of the respective homopolymer.

This work uses three classes of LCST-type polymers: P(NiPAM), P(OEGMA), and P(DMAEMA)-based polymers. As illustrated in **Figure 16**, at their PTT, LCST-type polymers

go through a rapid conformational transition from a swollen to a collapsed state. For P(NiPAM), this temperature-responsive transition has been the subject of various studies, including experimental studies[217,218] and studies via molecular dynamics simulations.[219–222] From molecular dynamic simulations, it is evident that the stabilization of P(NiPAM) in water is realized below the transition temperature by forming hydrogen bonds to the side-chain functionalities with the water molecules. The transition from a coil to a globule state becomes noticeable within these simulations only for 30-mers. Shorter chains of NiPAM units do not show this transition. S. Deshmukh and coworkers attributed this phenomenon to the reduced number of water molecules in the first hydration layer for each NiPAM unit as the chain length increases.[219] In a later article, S. Deshmukh et al. compared the behavior of proximal water when interacting with P(NiPAM) with that of water-soluble non-responsive polymers poly(acrylamide) (PAA) and poly(ethylene glycol) (PEG). They found that PAA and PEG show faster diffusion and exchange kinetics of proximal water than P(NiPAM), which enables them to maintain a higher hydration level at higher temperatures.[220] These results again show the importance of the polymer-water interaction for LCST-type polymers in water. It points out that additives, like salts, that influence the strength of hydrogen bonds will impact the thermoresponsive dynamics of such a polymer solution. It was shown that for LCST polymers like poly[2-(*N*-morpholino)ethyl methacrylate] (PMEMA)[195], P(OEGMA)[197], and P(NiPAM)[49,223], according to the Hofmeister series, the addition of salts shifts the polymers' PTT.

For LCST polymers with an amine group in their side chain, like P(DMAEMA), the PTT is also significantly influenced by the system's pH. Since P(DMAEMA) is a polybase, adding acid will cause the protonation of the side chain. This side-chain protonation increases the PTT of the polymer. The intensity of the PTT shift strongly depends on the degree of the side-chain protonation. Additionally, when protonated, the P(DMAEMA) chain is in a more stretched conformation due to the repulsion of cations in the side chain.[224] Due to the tertiary amine group of 2-(dimethylamino)ethylmethacrylate (DMAEMA), the pK_a value of DMAEMA is between 8.3 and 8.5.[225–227] The poly-base equivalent P(DMAEMA) shows a pK_a=7.0–7.8.[226–228] Due to its low toxicity, P(DMAEMA) homo- and copolymers exhibit high potential as carriers for non-viral gene-delivery vectors.[212,229,230]

However, due to the positioning of its pKa value, P(DMAEMA) is also a very efficient CO_2-responsive material.[231] When dissolved in water, CO_2 forms an H_2CO_3/HCO_3^- buffer system, causing a decreased pH value of the solution.[232–234] For P(DMAEMA), this decrease is sufficient to protonate the tertiary side-chain groups, causing a change in its PTT and a more stretched chain conformation. The advantage of using tertiary amine side groups over other CO_2-responsive functionalities is their high reversibility. For example, guanidine (pK_a≈13.5[235]) forms stable conjugated acids, complicating the deprotonation reaction. Amidines are less problematic to

deprotonate, but like guanidine functionalized polymers, synthesizing these materials can be challenging, involving several post-polymerization functionalization steps.[236]

The superior CO_2-responsive reversibility of tertiary amine-functionalized polymers has been demonstrated in numerous studies, where these compounds are incorporated into BCP structures to form breathing vesicles and micelles.[237–239] In the systems, the amine-containing chain segments are protonated by purging the polymer solution with CO_2 gas, which transfers this segment into a more soluble hydrophilic state. To reverse this protonation, the solution is usually purged with an inert gas like argon or nitrogen, which forces CO_2 out of the solution. The solution can also be heated to reduce the CO_2 solubility, accelerating this process. The benefit of using CO_2 as the responsive trigger is that, in most cases, it can be quantitatively removed (and neutralized) from the solution without any ions left. This can become important if the CO_2-responsive chain segment is, for example, used to switch the hydrophilic surface properties of a pore inside a membrane.

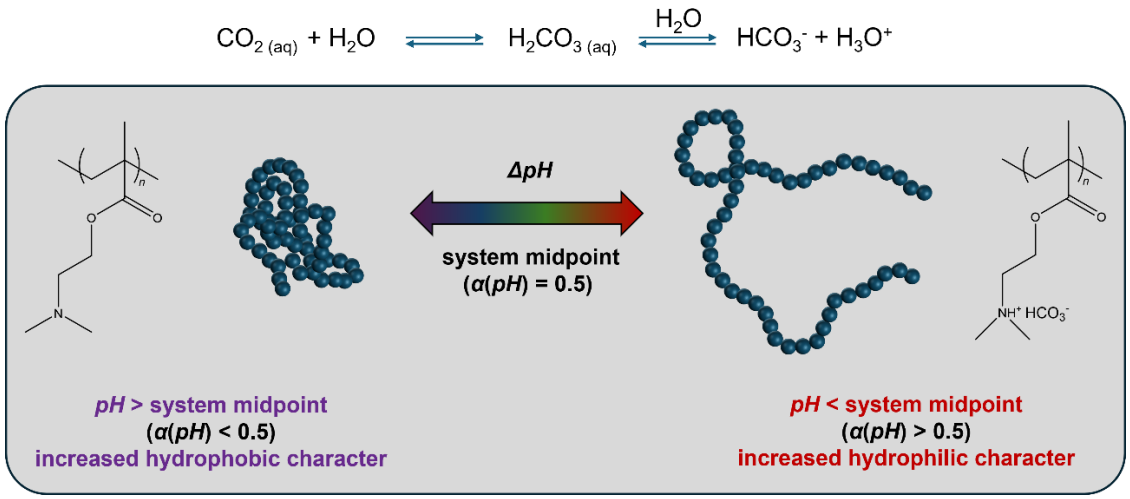
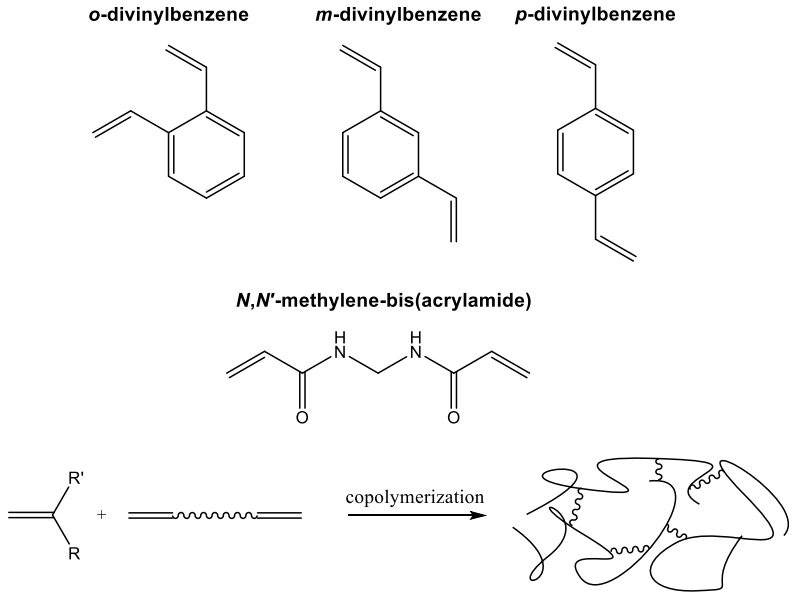


Figure 17. Representation of the CO_2-responsive character on the example of P(DMAEMA). The formation equilibrium of carbonic acid ($H_2CO_{3(aq)}$) is shown at the top. At the bottom, the pH/CO_2-responsive character of PDMAEMA is shown at different pH values above (left) and below (right) the system midpoint, defined as the pH at which the degree of protonation (α(pH)) is 50 %.[228,240]

Stimuli-responsive polymers are extraordinarily versatile and can be tailored to specific properties. Making them incredibly valuable for a nearly infinite number of highly specialized applications. However, this versatility can sometimes be challenging because one has to be aware of cross-dependencies, such as when specific stimuli overlap. For example, when developing a temperature-responsive material for drug-delivery purposes *in vitro* or *in vivo* applications, it must be considered that, depending on the polymer, the medium will impact the material's transition temperature due to the different salts in the testing environment. Due to the varying pH values in *in vivo* applications, pH/CO_2-responsive polymers face a similar challenge.

4.2.2.2. Network formation: Cross-linking and post-polymerization functionalization

Polymer gels are formed by cross-linking polymer chains to create a network. Especially for the encapsulation of metal nanoparticles, microgel formation is an essential tool. Encapsulating nanoparticles can protect them from the chemical environment, which M. Kampferbeck and coworkers showed.[241] They encapsulated iron oxide nanoparticles with a cross-linked polystyrene shell and added HCl in different concentrations. HCl is known to disassemble iron oxide nanoparticles. In their article, they provided a reliable method to verify the stability of the particles in an aqueous environment. They found a relation between the polystyrene shell thickness and the cross-linking density on the resulting particle stability in an acidic environment. To prepare the cross-linked PS shell, a grafting-from approach was chosen. They applied emulsion copolymerization of styrene and divinylbenzene (DVB) using ATRP to control the degree of polymerization. Due to the multi-functional DVB monomer, a crosslinked network was obtained. Cross-linking during the polymerization process is a common technique for forming polymer networks. For instance, M. U. Witt et al. published a preparation method for the synthesis of $CoFe_2O_4$ magnetic nanoparticles confined in a thermoresponsive P(NiPAM) network by adding the multi-functional monomer *N,N'*-methylene-bis(acrylamide) (BIS) to the polymerization process.[242,243]



Scheme 5. Common acrylic cross-linker molecules and schematic formation of a polymer network via radical copolymerization.

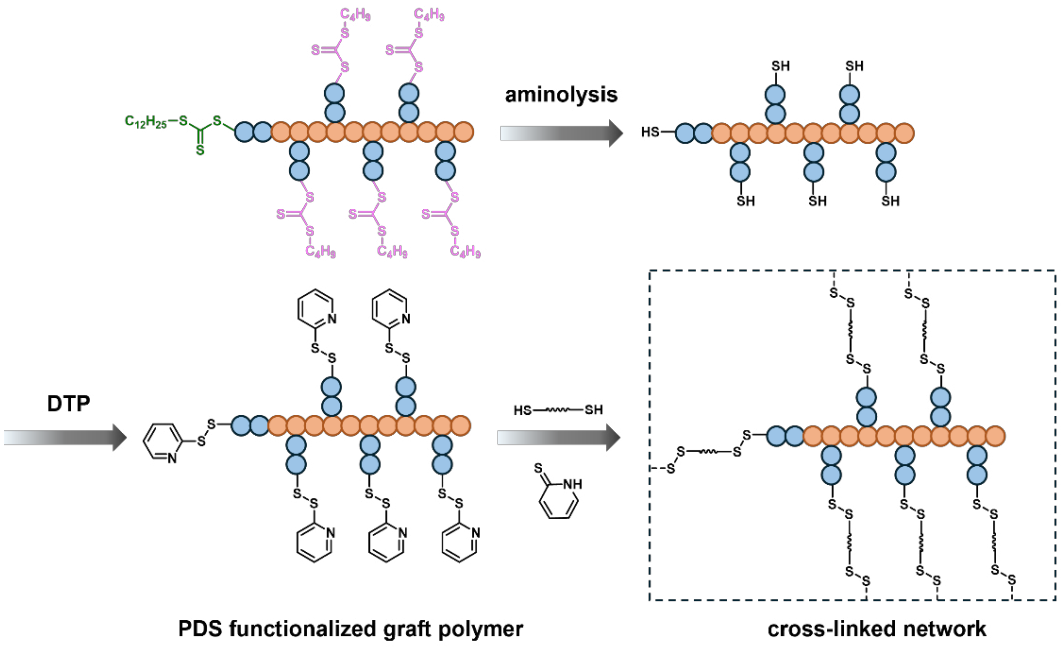
The formation of polymer networks is a broad field in economics and science. Cross-linking a polymer material significantly affects its mechanical properties by reducing chain mobility. An interesting evolving topic in cross-linked materials is the topic of dynamic networks or, more accurately, the covalent adaptable networks, where the cross-links are exchangeable and form an equilibrium. Typical examples of these networks are vitrimers. Vitrimers are an exciting new

class of cross-linked networks with mechanical properties comparable to typical thermosets but capable of thermal reprocessing/remolding. These networks are based on the reversible formation of vinylogous urea/urethane groups in the presence of excess amine functionalities.[244] The parent compound, the acetoacetate, was recently combined with different hydroxy-bearing materials, such as starch, by P. Haida et al. to achieve biodegradable materials.[245]

However, using multifunctional monomers during polymerization is not the only way to form polymer networks. Another example of the versatility of these vitrimer classes was published by S. Weerathaworn and V. Abetz.[172] They acetoacetylized different copolymer systems originated from RAFT polymerization in a post-polymerization process and later molded them into a vitrimer material in the presence of a multifunctional amine cross-linker. Due to the natural affinity of the TTC-CTA group[163,246,247] to metal nanoparticle surfaces, this material class opens an exciting new pathway for the preparation of reprocessible, highly specialized nanohybrid materials.

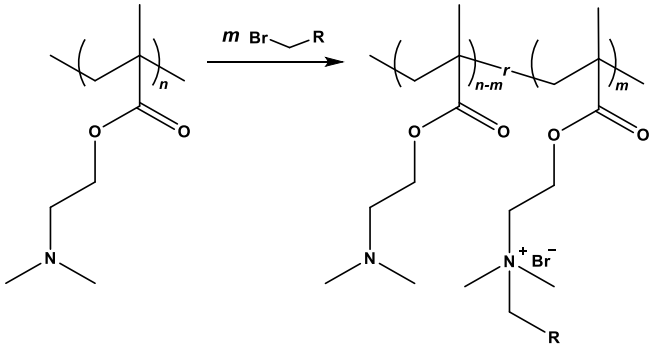
The polymer systems used in this work are based on the monomers NiPAM, DMAEMA, and methacrylates like di(ethylenglycol) methyl ether methacrylate (DEGMA) and OEGMA. The polymer architectures range from linear homopolymer chains to linear block- and statistical copolymer structures to grafted copolymer structures (like in **Scheme 4**). To achieve a crosslinked network, at least one compound of the strived polymer network must exhibit three or more functional groups (A) capable of performing the cross-linking reaction. The second component must show at least two functional groups (B) forming any connection with functional group A. Additionally, the ratio between the number of functional groups A and the number of functional groups B is of utmost importance for the network characteristics.

For the hydrogel formation, presented by J. Xu and V. Abetz, the TTC groups of the polymer were transferred into the thiol-sensitive functional group pyridyl disulfide (PDS).[1,9] In the presence of a dithiol (2,2'-(ethylenedioxy)diethanethiol; EDT), this group is exchanged, and a thioether crosslink is formed. The pathway of this procedure is presented in **Scheme 6**. In a later article, the same authors showed that the presented cross-linking pathway also shows a reversible character, which expands the potential application range of this and similar systems.[9]



Scheme 6. Multiple-step post-polymerization refunctionalization of the graft polymer end groups towards a crosslinked polymer network. This scheme is adapted with permission from the open-access source *Soft Matter*, **2022**, 18, 2082–2091, Copyright 2022 by The Royal Society of Chemistry.[1]

It is known that tertiary amine groups react with alkyl halides and form the quaternary alkyl ammonium halide. Therefore, the tertiary amine group in the side chain of P(DMAEMA) can also serve as a crosslinking vacancy. M. Semsarilar et al. used quaternary P(DMAEMA) (P(qDMAEMA)) for the stabilization of iron oxide nanoparticles in water.[248] This nanohybrid was then used to prepare membrane films with increased mechanical properties. In a later article, the group showed that by embedding magnetic iron oxide nanoparticles, the flux value of these membranes can be adjusted by an external magnetic field.[249]



Scheme 7. P(qDMAEMA) is formed via post-polymerization functionalization of P(DMAEMA) with an alkyl bromide based on a S_n2 reaction mechanism.

In the context of this work, the reactivity of the tertiary amine in the P(DMAEMA) side chain toward halogenated alkyls has proven its value several times by enabling the formation of an Au@PDMAEMA nanohybrid gel[3] and by enabling anisotropic growth of GNP[8] for a benign synthesis of GNRs. These systems are discussed in Chapter 5 in more detail.

4.3. GNP@Polymer: Core-Shell Nanohybrids

NP core-shell systems are the basis of promising multi-dimensional, multi-functional materials with a nearly infinite number of possible applications in science and applied technology. Over the last fifty years, many examples of polymer-nanoparticle hybrids have been published and reviewed.[250] The massive bandwidth of different nanoparticle systems of various materials, shapes, and sizes, combined with the at least equally massive amount of different polymer systems, including biopolymers, attachable to these nanoparticles, leads to an close to infinite amount of possible NP@polymer combinations with the potential to resolve most of the given challenges in the field, if the correct components are properly combined. Therefore, NP composites play a significant role in modern society and will most likely continue to do so.

Even if the possible combinations are restricted to only GNPs and stimuli-responsive polymers, the number of existing hybrid materials is enormous. However, this versatility also has its downsides. Due to this topic's complexity, finding a suitable system for the given task can be challenging. A precisely formulated task and knowledge about the GNPs and the polymer material are required to efficiently design suitable hybrid materials. This chapter provides an overview of the recent developments in this field and certain obstacles that must be considered when developing such hybrid materials.

There are two different ways to prepare polymer-shelled GNPs. (GNP@polymer). Both of them are schematically illustrated in **Figure 18**. They are classified by the sequence of the preparation procedure, where either the polymer is pre-synthesized and then attached to the particle surface (grafting-to) or the particle surface is functionalized and serves as a polymerization starter. In this case, the polymer is synthesized from the particle surface (grafting-from). Both approaches have their benefits. For instance, grafting-from approaches tend to have significantly higher functionalization densities of polymer chains on the particle surfaces (grafting density). Meanwhile, grafting-to approaches are naturally more flexible regarding the polymerization conditions and techniques, and therefore, more complex polymer architectures are achievable. Additionally, grafting-to approaches provide more detailed information about the polymer chain length on the particles' surfaces.

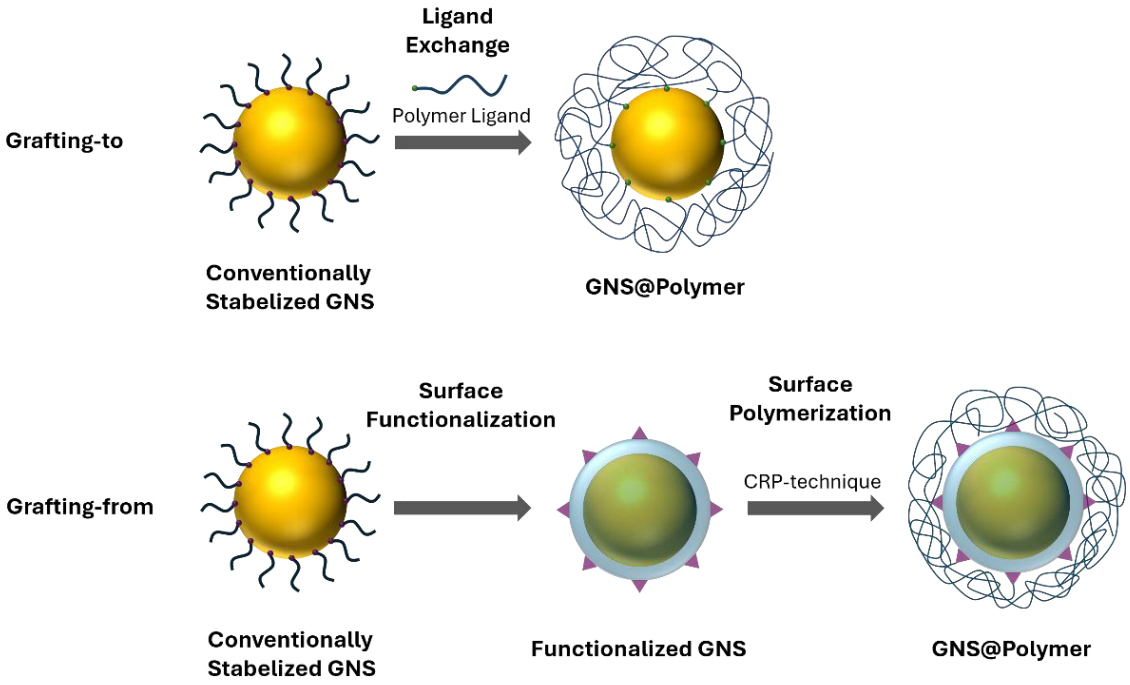


Figure 18. Illustration of the two categories (grafting-to at the top and grafting-from at the bottom) of the synthesis of GNPs covered with a polymer shell (GNP@polymer).

Another way to prepare GNP-polymer hybrids is by synthesizing GNPs in the presence of the polymer material. Typically, for such approaches, a polymer, synthesized via RAFT polymerization, is dissolved together with the Au precursor in tetrahydrofuran (THF), and the particle formation is induced by adding a strong reducing agent like sodium borohydride or other borohydride reducing agents.[2,251–255] This method allows the quick synthesis of GNP@polymer hybrids with various polymers. Also, mixtures of polymers with different polarities are used in this method to synthesize responsive amphiphilic nanohybrids.[253] This *in situ* technique is considered a subclass of the grafting-to approach and was mostly used in the early 2000s. The bandwidth of polymers is only restricted by the limits of monomers polymerizable using dithiocarbonates (DTC). DTCs are well-known CTAs in RAFT polymerization. It is commonly assumed that due to the access of a reducing agent during particle synthesis, the DTC functionality is reduced to a thiol group attached to GNP due to sulfur's naturally high affinity to Au surfaces. Usually, GNS with particle diameters between 2 nm and 8 nm are obtained by this *in situ* method. The polymers used in this method are responsive to specific stimuli to achieve multi-functional materials. The most prominent polymer used in this context is P(NiPAM). In 2007, Tenhu and coworkers published a temperature- and pH-sensitive GNP-hybrid material. They used the diblock copolymer (DBP) P(NiPAM)-*b*-PMAA with P(NiPAM) as the temperature-responsive and poly(methacrylic acid) (PMAA) as the pH-responsive component.[251]

Using the *in situ* synthesis, we published another pH- and temperature-responsive GNP-hybrid system by using poly(2-(dimethylamino)ethyl methacrylate) (P(DMAEMA)).[3] Here, the effects of different TTC groups on the particle quality and the responsive character of the hybrids in

solution were investigated. As the initial systems investigated in this work, the results are further discussed in Chapter 5. Also, additional information is given, and the results are put into perspective with the other systems studied in this thesis.

In 2011, C. Said-Mohamed et al.[252] published a work in which the interparticle distances were controlled by the thermoresponsive nature of a copolymer matrix containing NiPAM and propylacrylamide (NPAM) units, using the *in situ* approach for particle synthesis. The ability to control the interparticle distance of GNPs in a material via temperature or other stimuli is intriguing and opens many interesting applications. For instance, as shown in Section 4.1.3, the optical properties of GNPs are significantly influenced by the interparticle distance (see equation 4.2). So far, some interesting materials have been published on this behavior. For example, A. Choe et al. developed wearable colorimetric patches containing raspberry-like particles composed of a P(NiPAM) microgel as the core, decorated with GNPs on the surface. When the temperature reaches the LCST of the microgel, it collapses, and the GNPs on its surface approach each other, causing a visual change in the patches' color.[49]

Both technologies, GNP science[38] and the field of smart polymers[256,257], have already shown their capabilities of controlled drug release. Therefore, combining both as core-shell systems could enable enhanced control. For example, it can trigger the release of a drug attached to the polymer shell by increasing the local temperature above the LCST via NIR-irradiation of the plasmonic particle and the related plasmonic heating.

After casting a concentrated alkyl thiol-stabilized GNP solution onto an interdigitated electrode and drying it thoroughly, a specific Ohmic resistance can be measured after applying a current. The measured resistance depends on the interparticle distance in the casted film and will change if the particle-particle distance changes. This principle is used in chemiresistors.[47] C.-H. Su published a highly responsive humidity sensor by printing a PEG/GNP ink onto an electrode structure. A significant change in the array resistance was observed after the sensor array was exposed to a humid atmosphere, due to the hygroscopic nature of the used polymer. These changes are shown to be highly reversible.[18] Using a stimuli-responsive polymer instead of PEG, another stimulus, such as temperature or CO_2 concentration, could be added as a trigger to these sensors, potentially making them more versatile.

The group of P. Vana performed essential work regarding the preparation of RAFT polymer GNP hybrid materials. In numerous articles, they described the preparation of GNP hybrids by using a TTC functionalization as a potential anchoring point of the polymers on the surface of the GNPs. Among others, they described a reliable method to attach RAFT-polymers to the surface using a ligand exchange protocol. They further investigated the influence of the polymer architecture on particle assembly.[162] Using star-like RAFT polymers, they could synthesize planet-satellite particle assemblies like gold-core with gold-satellites[258], and mixed-material planet-satellite assemblies with a GNP core and smaller silver nanoparticle satellites.[163] These articles

investigated the influencing factors, such as molecular weight and the number of arms, on the obtained assemblies. Given the reliability of the ligand-exchange-based protocol, it was also used in this work to prepare GNS@polymer hybrids. The effect of the nature of the particle assembly on the plasmonic properties of these and similar colloidal assemblies was recently revised.[259]

4.3.1. Physical Properties and Scattering Behavior of GNP@Polymer/Microgel Hybrids in Solution

UV–Vis spectroscopy and dynamic light scattering (DLS) measurements provide a comprehensive insight into the nature of smart polymer solutions, GNPs, and their corresponding hybrid material dispersions. As mentioned before, the PTT of the polymer material is an essential value for temperature-responsive polymer solutions. A reliable and quick way to determine the transition temperature is by turbidity measurements. These measurements can be performed manually by recording the temperature at which a visual change in turbidity occurs, due to the formation of insoluble polymer clusters resulting from the coil-to-globule transition of the polymer. Another way to determine the PTT is to use automated processes, such as temperature-dependent UV–Vis extinction spectroscopy. This process provides a more detailed insight into the transition process as well. Additionally, the aggregation of polymer chains is usually accompanied by an increase in the hydrodynamic radius, which is measurable with temperature-resolved DLS. Depending on the composition of the polymer chain and the responsive material used, the temperature-dependent R_H can evolve through several stages, as shown by J. Xu and V. Abetz.[1,9]

However, the responsive behavior of free polymer chains in solution and polymer chains attached to an NP surface (GNP@polymer) hybrids significantly differs from each other. As discussed in Section 4.2.2, several factors, like the concentration of different salts or the pH value, can influence the transition temperature of responsive polymers. Molecular dynamic studies of a P(NiPAM) fixated to a surface showed that the polymer surface-interaction strength significantly influences the temperature-responsive behavior.[260] In 2009, J. Shan et al. published their work about the influence of the polymers' molar mass and the gold core size on the transition temperature of P(NiPAM) oligomers.[255] They found that the transition temperature shifts towards lower temperatures for hybrids with larger gold cores than for smaller core hybrids. This effect was negligible when the NiPAM chain length was increased. This behavior was explained by the hydrophobic nature of the GNP core, which prevents the H_2O molecules from penetrating between the densely packed P(NiPAM) chains and, therefore, increases the interchain interactions, causing a decrease in the transition temperature. This effect becomes less pronounced when the NiPAM oligomer stabilizers are larger than 2000 g/mol. Also, the grafting density of polymer chains on the particles' surface must be considered when explaining the responsive behavior. A higher grafting density is usually associated with a broadening of the polymer shell's thermal response.[261] Generally, it is suggested that the closer the chains come toward the core, the more densely packed they become, causing them to appear more stretched to avoid overlapping. A chain segment further away from the NP-core is looser packed and behaves more like its free polymer pendant. **Figure 19** illustrates the general concept of the different zones

surrounding a GNS core. Distinguishing between these two major polymer-shell regimes can explain the broader thermal response of the smart polymer forming the shell. It was observed that the inner region collapses at lower temperatures. In an earlier work, J. Shan and coworkers described a two-phase transition behavior observed via P(NiPAM) brushes grafted on the surface of GNPs.[262] This work emphasized two regimes, inner and outer, with distinct transition temperatures due to an intrinsic decrease in water accessibility near the particle surface.

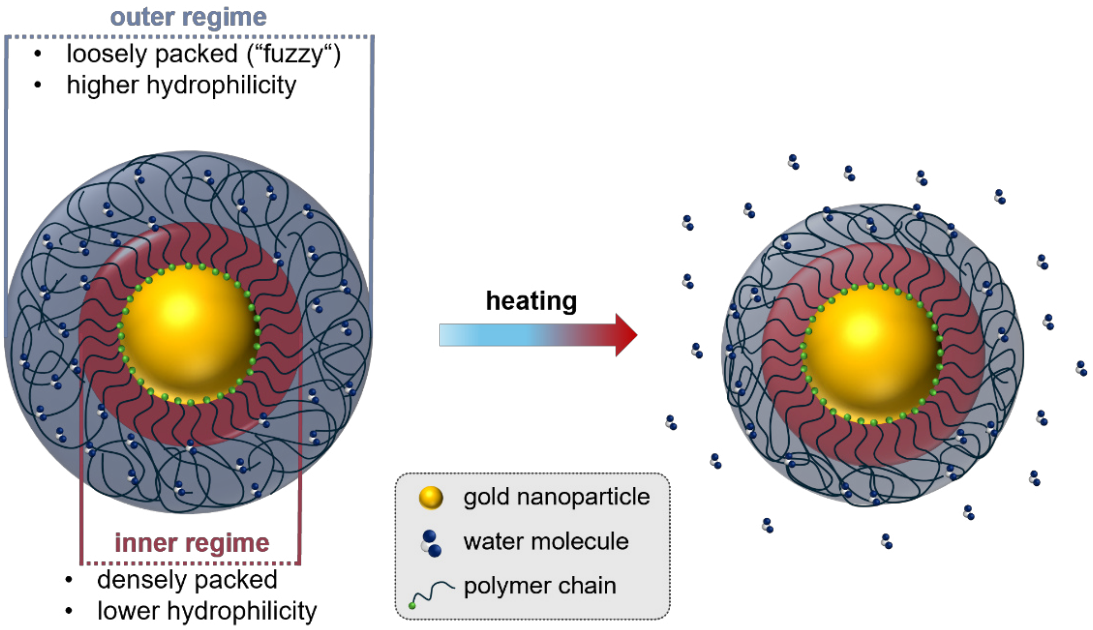


Figure 19. Illustration of the general concept of the different shell regimes and chain assemblies on a particle surface, with red as the densely packed regime with low accessibility to water molecules and blue as the loosely packed regime with higher accessibility to water molecules.

The optical properties and their dependency on the interparticle distance of GNPs (Equation 4.3) are discussed in Section 4.1.3 in detail. It was shown that adjusting the thickness of a silica shell surrounding gold nanoparticles impacts the optical appearance of the plasmonic system.[263] Several studies have shown an explicit temperature dependence of the extinction spectrum for temperature-responsive shells.[264–267] Typically observed effects are shifts of the LSPR maximum, an increased maximum absorption, or a decreased maximum absorption. All these effects result from at least one of the following effects.

- Interparticle plasmonic coupling
- Precipitation or redispersion of the Au-hybrid
- The chemical environment changes close to the NP surface

In order to obtain a shift of the maximum plasmonic resonance due to interparticle plasmonic coupling, the conditions described in Section 4.1.3.2 must be fulfilled first. Especially for well-stabilized GNP@polymer core-shell hybrids within a solution, the interparticle distances are

statistically too high to support plasmonic coupling immediately. H. Lange et al. presented an exciting example of interparticle plasmon coupling controlled by a P(NiPAM) matrix.[268] They described plasmonic coupling in GNPs with a diameter of 10 nm, well below a 7 nm interparticle distance, which aligned well with their calculations. At smaller interparticle distances, they observed a second shoulder in the extinction spectrum at wavelengths higher than the original LSPR wavelengths. Although they did not determine the interparticle distances, it is safe to say that the intense color change in the patches is due to interparticle plasmon coupling. A. Choe et al. presented another example of distance-related plasmonic coupling.[49]

From Equations (4.1) and (4.2), it is clear that the optical properties also rely on the dielectric constant of the surrounding medium (ε_0), which directly relates to the medium's refractive index. As the temperature increases and the shell transition temperature is reached, water is forced out of the shell, changing the refractive index of the shell. A shift in the LSPR maximum accompanies this change. However, compared with plasmon-plasmon coupling shifts, LSPR maximum shifts based on the collapse of the polymer shell and the related changes in the dielectricity around the particle are less intense, commonly only a few nanometers (~1 nm–10 nm).[269]

A changing extinction intensity can be described via changes in the (hybrid-)particle concentration within the observed solution via precipitation. For instance, macroscopic precipitation naturally causes a decrease in the solution's absorbance due to a decrease in the particle concentration. For thermo-responsive particles, this usually occurs when the transition temperature of the polymer precursor is surpassed. This will cause the polymer to reduce its surface energy. Due to this, the suspension becomes destabilized, causing the precipitation of the nanohybrid.

To describe an increase in a hybrid suspension's absorbance (extinction) during the collapse of the responsive shell around a particle core, another model must be taken into consideration. Recent studies showed that for a P(NiPAM) microgel-shell GNS hybrid solution with sufficiently small gold cores, the extinction increase is dominated by the scattering of the polymer compound and that the absorbance of the GNS core is negligible. The suggested fuzzy sphere model can describe and predict this effect.[10–12] This model is similar to the previous one, with two polymer regions, an inner densely packed region and an outer loosely packed region, as shown in **Figure 19**. As depicted in **Figure 19**, the core-shell hybrid's R_H decreases with increased temperature due to the phase transition of the stabilizing temperature-responsive polymer. To more efficiently describe UV–Vis spectroscopic properties of P(NiPAM) microgels, E. Ponomareva introduced the fuzzy sphere model.[10] Increased scattering intensity at smaller particle sizes, as observed in temperature-dependent optical density measurements, contradicts the R^6 relation derived from the Rayleigh–Debye–Gans approximation. The fuzzy sphere model addresses this problem by assuming that only the densely packed inner region of the polymer (**Figure 19**, red region), close to the GNP, accounts for the scattering, while the fuzzy outer region

(**Figure 19**, blue region) does not contribute significantly to the scattering. If the fuzzy region collapses and the hybrids' R_H decreases, the volume ratio of the inner dense region increases (not shown in **Figure 19**), causing the increased extinction in the visible spectrum until the fuzzy shell is fully collapsed and a homogeneously dense shell is formed due to chain rearrangements.

5. Results and Discussion

5.1. Particle Systems: A Joint Perspective

In this work, three different particle systems and their preparation have been developed and investigated. Parts of the results discussed here have already been published.[3,8] Thematically, the preparation methods developed can be separated into two groups:

1) The polymer-assisted particle synthesis and
2) The ligand exchange-based grafting process.

Although the three topics of this thesis differ in terms of their specific field of application and motivation, they are all connected by the underlying polymer design. Therefore, this section's topic is to briefly introduce the three major topics and put them into a collective perspective. Chronologically, the first topic investigated with this thesis was the polymer-assisted synthesis of P(DMAEMA) stabilized GNS particles. The motivation behind this system was to achieve a multi-responsive particle system with temperature- and pH-responsive properties, using a simple, time-efficient synthesis protocol.

Parallel to the development of the Au@P(DMAEMA) hybrid materials, Xu and Abetz published their work on the double thermoresponsive graft copolymer system. This simultaneously raised the question about their capabilities for metal NP stabilization. Due to their multiple TTC anchoring groups and intriguing responsive properties, these polymers are promising carrier matrices for nanoparticle systems. The motivation for that investigation was to determine the effects of different chain lengths, especially the P(NiPAM) side-chain lengths, focusing on the temperature-dependent optical properties and light-scattering phenomena of the obtained hybrid materials. The thermoresponsive investigations of the Au@P(DMAEMA) hybrids raised the question of whether rapid (nonlinear) thermoresponsive reactions can be achieved with the chosen polymer composition. **Figure 20** gives a quick overview of the three topics of this work.

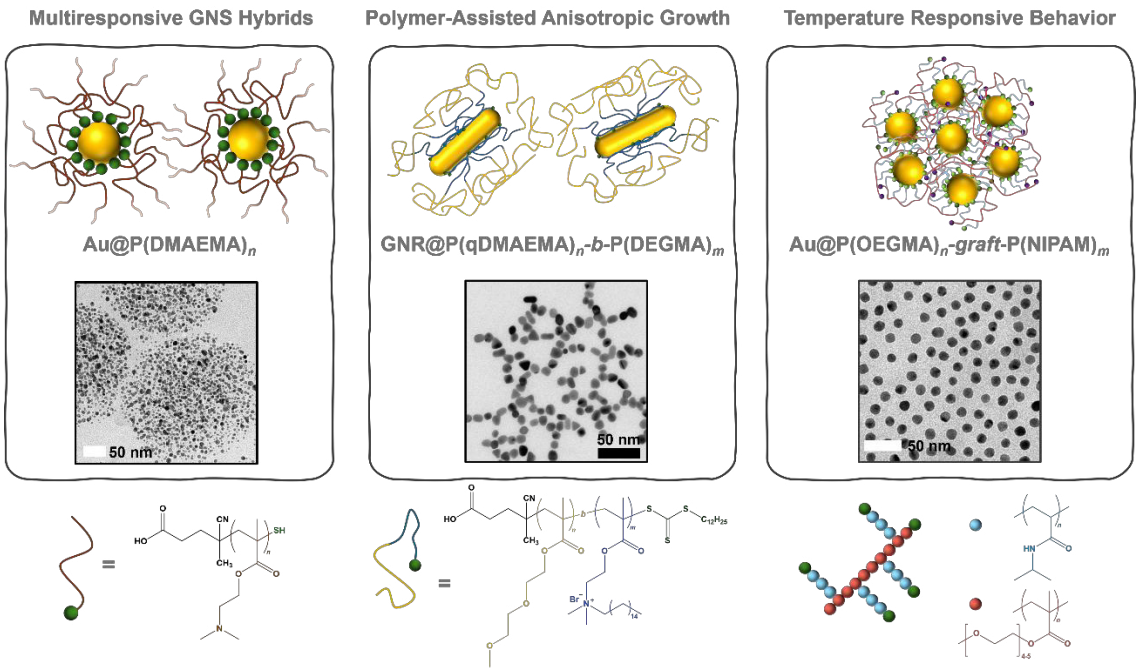


Figure 20. Illustration of the three GNP@polymer hybrids developed in this project. The two hybrids on the left-hand side and in the middle were synthesized via a polymer-assisted approach, and the GNS@graft-copolymer hybrid was prepared in a grafting-to approach using a double thermoresponsive GRAFT-copolymer (column on the right-hand side).

The results of both systems, the Au@P(DMAEMA) hybrids and the GNS@GRAFT-polymer hybrids, led to the idea of developing a polymer capable of directing anisotropic growth during particle formation. The driving force for this idea was the result obtained during the long-term stability test of the Au@P(DMAEMA) hybrids in solution. During these tests, it became evident that, if stored in THF, the Au@P(DMAEMA) hybrids exhibited aging effects similar to Ostwald ripening. Causing, among other effects, a broad particle size distribution.[3] TEM imaging revealed that spherical particles and anisotropic morphologies were formed after a few months of aging in the dark at 0 °C. These aging effects were especially evident for Au@P(DMAEMA) samples synthesized with longer P(DMAEMA)$_n$-chains. They seemed more sensitive to aging effects than their short-chain-based equivalents (see Subsection 5.2.3). The appearance of anisotropic GNPs amplified the engagement of developing a water-soluble DMAEMA-based polymer material capable of directing an isotropic growth (see Section 5.3) in a seeded growth process. In the context of this GNR hybrid system, different polymer architectures were developed and tested as anisotropic growth-directing agents with the goal of a CTAB-free GNR synthesis to reduce the inherent CTAB-based toxicity of GNR materials and enable GNR biomedical applications.

5.2. *In Situ* Polymer-Assisted Synthesis of Au@P(DMAEMA) Multiresponsive Nanohybrids

This chapter builds upon the results previously published in Reference [3] and provides additional insights into the experiences gained during the development of the Au@P(DMAEMA) hybrids synthesized during the investigation. The work can be divided into three major parts: the design and synthesis route of the P(DMAEMA) precursors (5.2.1), the characterization of the thermoresponsive nature of the P(DMAEMA) precursors (5.2.2), and the Au@P(DMAEMA) hybrid synthesis and the characterization of these nanohybrids (5.2.3).

5.2.1. Polymerization of DMAEMA: Amines are a Critical but Potent Functional Group

The basis of the P(DMAEMA) synthesis goes back to the already established photo-iniferter RAFT (photoRAFT) polymerization by former coworkers for different acrylate- and methacrylate-based thermoresponsive UCST[210,215] and LCST-type[1,9,171,175,270,271] polymer systems. The theoretical advantages of the initiator-free photoRAFT polymerization over the conventional RAFT polymerization with an additional initiator are already discussed in Subsection 4.2.1. The design of the polymerization was significantly impacted by the requirements that arose from the nanoparticle synthesis in the later steps. One of these requirements is reducing error sources along the synthetic route. Since the synthesis of nanoparticles is known to be highly sensitive to external and internal variations of the reaction parameters, such as batch-based quality changes of the ingredients, one of the main concerns during the polymer synthesis was the scale-up of the DMAEMA polymerization.

Additionally, amines inherit some special challenges due to their nucleophilic character and tendency to generate radicals when excited with higher-energy UV or blue light. Several kinetic investigations were conducted to evaluate the applicability of different light sources and ensure that all starting radicals in the polymerization are derived from the iniferter process. Therefore, different polymerization solutions were illuminated with the respective light source, including UV light (254 + 365 nm) and green light (λ_{max} = 513 nm; I_d = 0.60 mW·cm^{-2}).

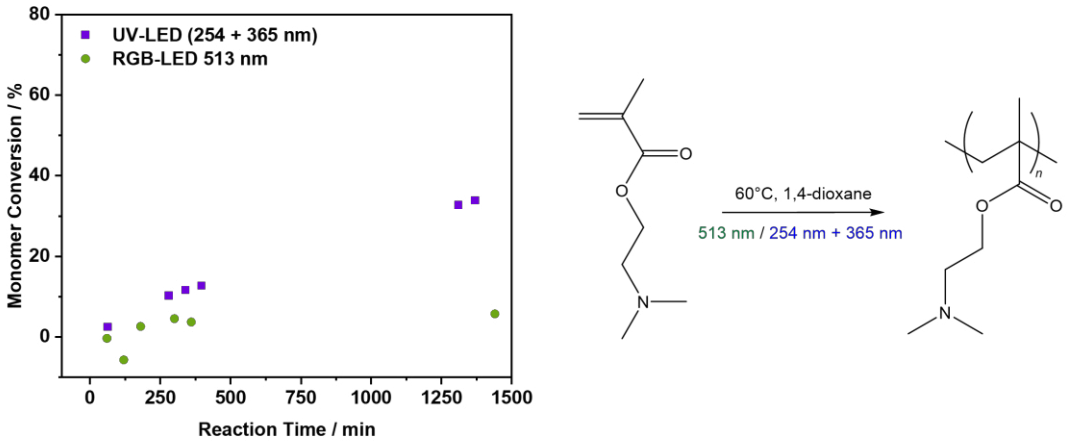


Figure 21. Kinetic plot of the monomer conversion of 1,4-dioxane/DMAEMA solutions while irradiating with light sources of different wavelengths. The green dots in the graphic show the DMAEMA conversion over several hours when exposed to a light source with an emission maximum at $\lambda = 513$ nm. The purple squares show the same setup but with a light source with emission maxima of $\lambda = 254$ nm and 365 nm. The graphic was taken with permission and minor optical adaptations from the open-access source *Macromol. Chem. Phys.* **2022**, 2200355. Copyright 2022 The Authors. Macromolecular Chemistry and Physics, published by Wiley-VCH GmbH.[3]

The graphic shown in **Figure 21** proves that DMAEMA, dissolved in 1,4-dioxane, starts polymerizing when irradiated with UV light. More importantly, after approximately 24 h, no significant monomer conversion was observed when irradiating an equally prepared DMAEMA solution with green light emitted from an RGB-LED. Based on these results, it was safe to assume that DMAEMA does not generate enough radicals to initiate radical polymerization when green light is used.

To initiate polymerization via the iniferter mechanism, an overlap between the light source's emission spectrum and the absorbance spectrum of the used CTA must be ensured. In this topic, two CTAs for the RAFT polymerization of DMAEMA were used. The chemical structure of both CTAs is shown in **Figure 22** on the left-hand side. The plot in **Figure 22** shows no overlap between the emission spectra of the green LED and the π⟶π*-transition of the used CTAs. However, the spin-forbidden σ⟶π*-transition of the TTC overlaps with the emission spectra, and the CTA can be transferred into the excited state, causing the homolytic cleavage of the CTAs' R-group, which initiates the polymerization process.

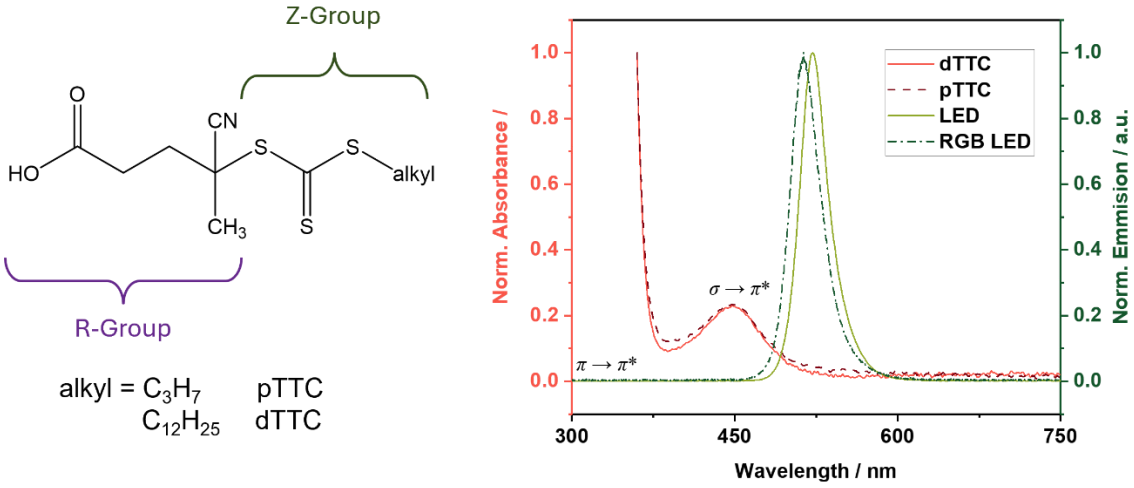


Figure 22. The left-hand side shows the chemical structure of the RAFT agents, with their respective abbreviations. The graph on the right-hand side shows the normalized emission spectra of the light sources, combined with zoomed-in normalized absorbance spectra of the CTAs pTTC and dTTC. The data shown in the graphic on the right is taken with permission from the open-access source *Macromol. Chem. Phys.* **2022**, 2200355. Copyright 2022 The Authors. Macromolecular Chemistry and Physics, published by Wiley-VCH GmbH.[3]

The second challenge in designing the polymerization was the upscaling. Therefore, a Schlenk tube was chosen to ensure homogeneous illumination of the reaction solution. The advantage of using the geometries of a Schlenk tube is the constant diameter of the reaction volume, which becomes especially important when samples are taken during the reaction for kinetic investigations. The exact reaction setup is described in the respective reference[3] and in **Figure 70** in the experimental section. With that setup, the possible polymerization volume increased from 12–20 mL in a screw capped glass vial to a possible reaction volume between 50 mL and 75 mL. Several kinetic investigations with simultaneous sampling were performed using the RAFT agents dTTC and pTTC to polymerize DMAEMA (see **Figure 23**). In these kinetic investigations, the feasibility of scale-up was shown for dTTC- and pTTC-based RAFT polymerization. Regarding the reaction kinetics, it is evident that both reactions pass through an inhibition phase in the early stages of the reaction, indicating the formation of the pre-RAFT equilibrium within the first 60 minutes of the polymerization. The dispersities ($Đ = \overline{M}_w/\overline{M}_n$) are plotted against the respective reaction time. The data indicate a well-controlled RAFT process. Additionally, the molecular weight distributions shown in **Figure 24** for the samples from both reactions exhibit a constant shift toward lower elution volume with increasing reaction time. This shift proves the progressive chain growth of the DMAEMA chains.

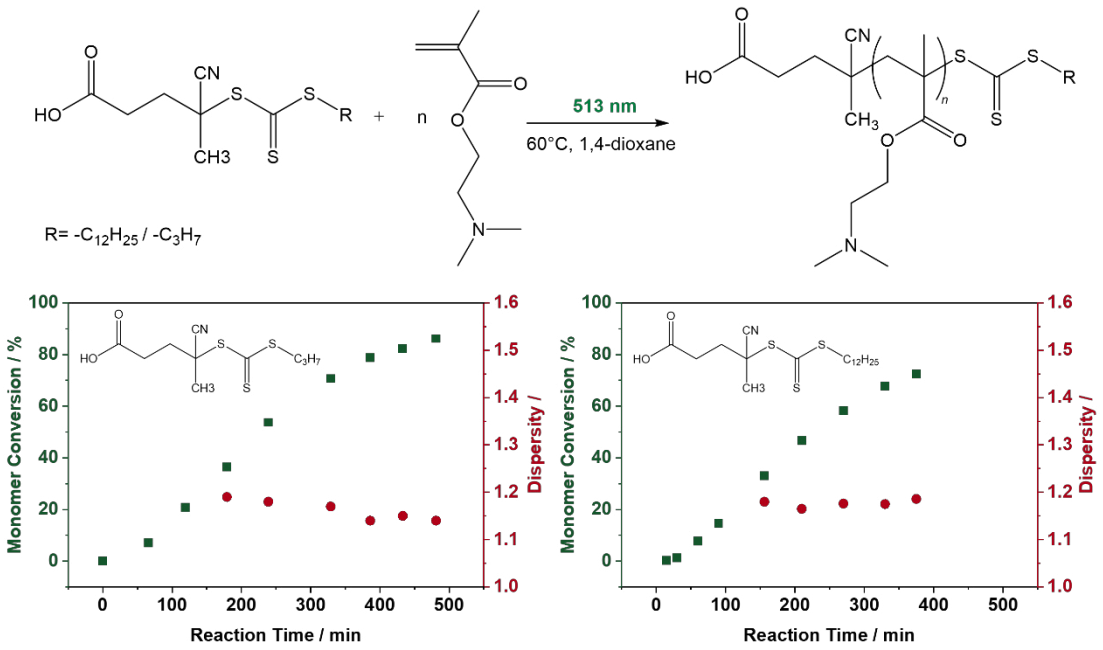


Figure 23. Kinetic data of the polymerization of DMAEMA with pTTC (left) and dTTC (right) initiated via the iniferter mechanism by using green light to excite the respective TTCs. The green squares show the DMAEMA conversion after different reaction times. The red dots represent the molecular weight distribution ($\bar{M}_w/\bar{M}_n$) of the P(DMAEMA) product at different reaction times after precipitation once in *n*-hexane. The data shown in the graphic on the right are taken with permission from *Macromol. Chem. Phys.* **2022**, 2200355. Copyright 2022 The Authors. Macromolecular Chemistry and Physics, published by Wiley-VCH GmbH.[3]

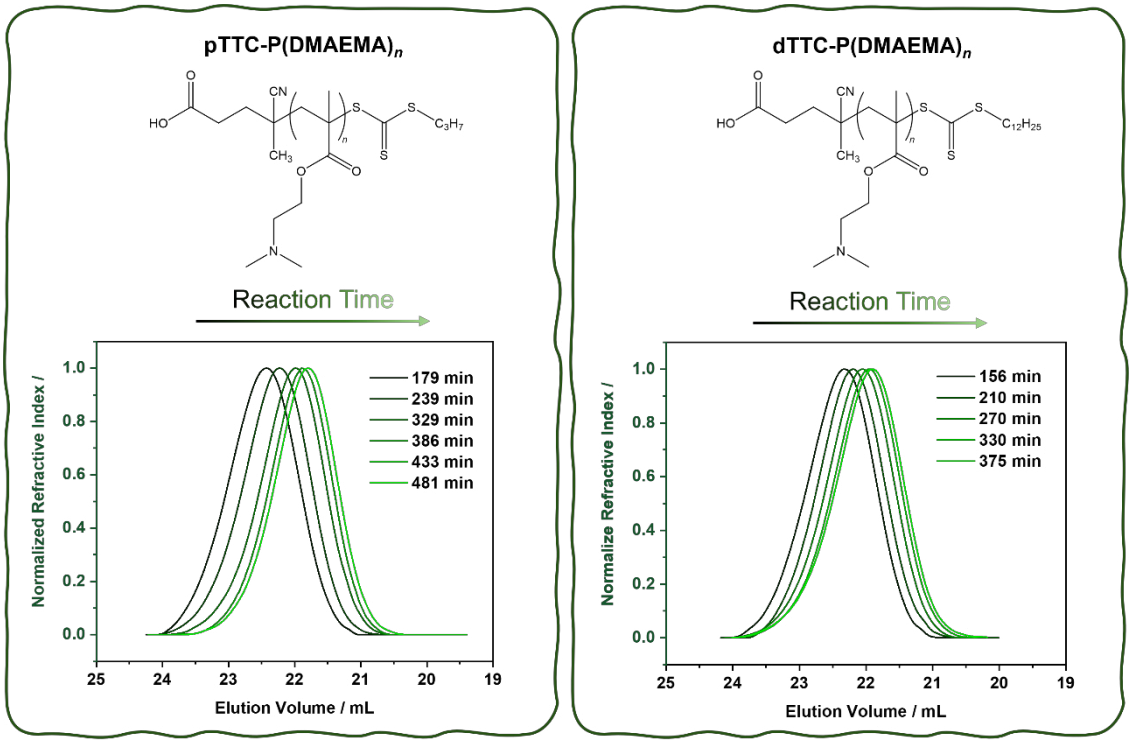


Figure 24. Plotted molecular weight distribution curves were obtained via SEC measurement of the P(DMAEMA) products at different reaction times. The data shown in the graphic on the right are taken with permission from *Macromol. Chem. Phys.* **2022**, 2200355. Copyright 2022 The Authors. Macromolecular Chemistry and Physics, published by Wiley-VCH GmbH.[3]

At monomer conversions ≥70 %, a reduced monomer addition rate is indicated by a reduced conversion gradient. This reduced conversion rate is especially pronounced for the pTTC-based reaction since the reaction was quenched later than the dTTC-based polymerization. It was concluded that polymerization should be quenched before reaching 70 % monomer conversion to prevent decomposition of the TTC moiety due to radical or nucleophilic side reactions. However, the chromatograms' symmetric shape indicates that the growth is not canceled via chain-chain recombination, which would be expressed by a shoulder formation in the respective chromatogram at lower elution volumes. In fact, the obtained chromatogram widths remain constant throughout polymerization.

In another investigation, the DMAEMA conversion limits were tested. The literature shows that some monomers allow high monomer conversions without significant drawbacks in terms of reinitiation capabilities of the obtained macroCTA for subsequent chain extensions. A great example of such a monomer is methacrylic acid (MAA), as shown by I. Oral and V. Abetz in 2021.[174] The potential of the pTTC-P(DMAEMA) macroCTA, synthesized with a DMAEMA conversion of >95%, was tested in a subsequent chain-extending polymerization step. Therefore, another kinetic investigation was performed in which the pTTC-P(DMAEMA)$_{45}$ macroCTA was synthesized, with the DMAEMA conversion pushed to its limit by prolonging the irradiation time of the polymerization solution extensively (>24 h). A second chain-extending polymerization step with DMAEMA was conducted using this polymerization product. The results of this two-step process are presented in **Figure 25**.

Again, the SEC results from the first kinetic study show no implicit broadening of the chromatograms over a reaction period of approximately 10 hours. However, a slight tailing at higher elution volumes can be observed in the elution chromatograms after a 24 h reaction time, indicating a small fraction of inactive P(DMAEMA) chains. A nearly quantitative consumption (99 %) of DMAEMA was obtained during the first consecutive polymerization step. The results of the chain-extension step of pTTC-P(DMAEMA)$_{45}$ tell a different story. The kinetic results show a strong inhibition of the polymerization after 60 % monomer conversion. Additionally, although the dispersity of the macroCTA for that polymerization was considerably narrow ($Đ$=1.2), the elution chromatogram of the chain-extended product clearly states a bimodal molecular weight distribution, with a significant fraction of inactive chains descended from the macroCTA pTTC-P(DMAEMA)$_{45}$. Because the molecular weight distribution of pTTC-P(DMAEMA)$_{45}$ does not show significant asymmetry at lower elution volumes, forming inactive chains via recombining two radical chain ends is unlikely.

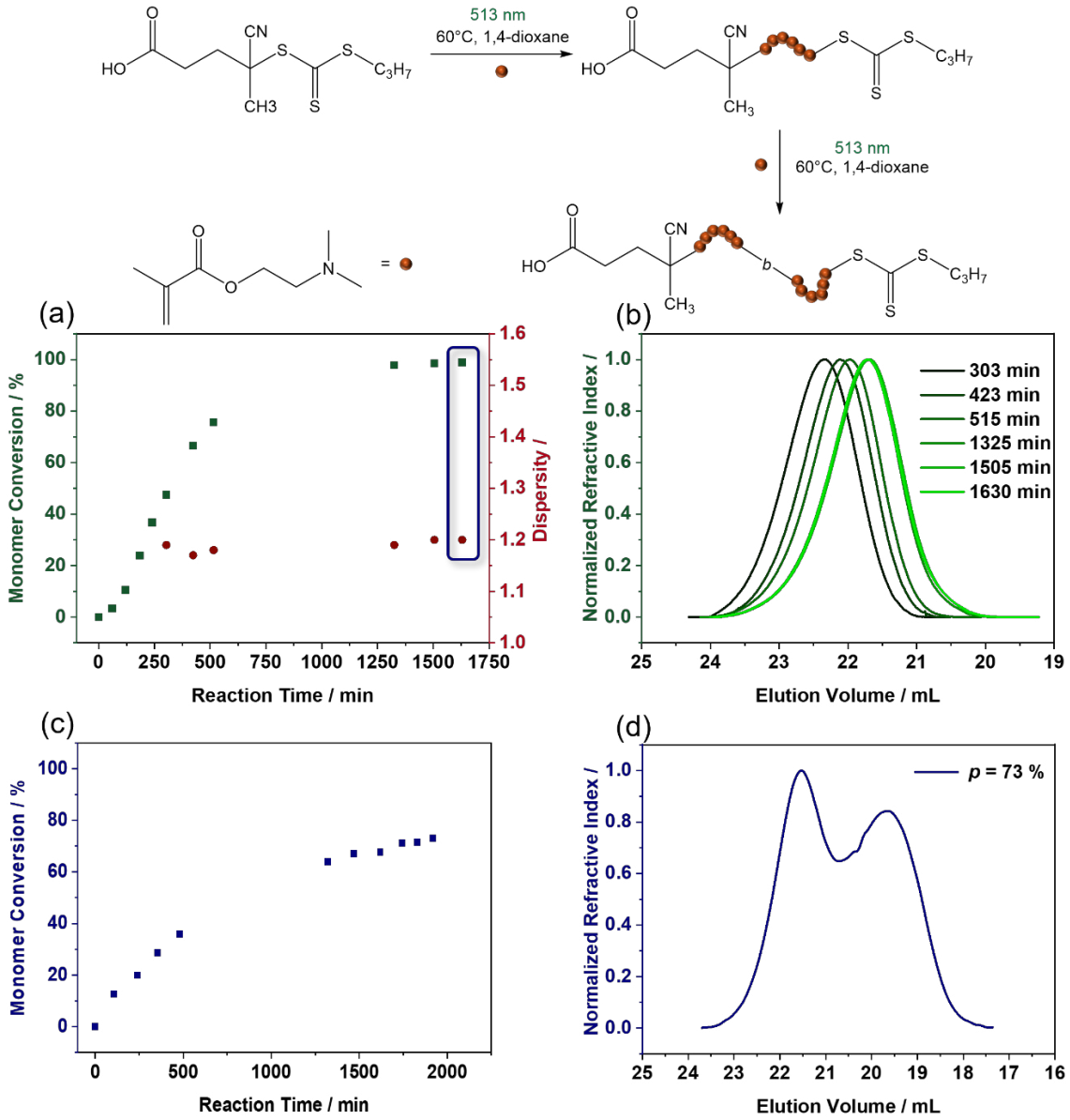


Figure 25. Photo RAFT-polymerization kinetics with nearly quantitative DMAEMA conversion in the first polymerization step. Graphic (a) shows the kinetic results of the monomer conversion (green squares) and the dispersity (red circles) relative to the reaction time. In (b), the SEC curves of the polymer at different reaction times are plotted. In (c) and (d), the polymerization results after using the product from the first reaction step as makroRAFT agent. In (c), the DMAEMA conversion is plotted as a function of reaction time. Graph (d) shows the SEC curve of the polymer after chain extension.

Such a radical-radical recombination of two active chain ends would have caused the formation of a shoulder in the elution chromatogram at lower elution volumes. Since this is not observed, other processes must be responsible for the high number of inactive chains in pTTC-P(DMAEMA)$_{45}$. The literature states that the TTC functionality can be photolytically decomposed when exposed to UV light for extended periods.[182] Since the suggested photolytic process is radical-based, it is evident that it should also be possible with a visible-light source.

Based on these results, the reaction (/green light irradiation) time was reduced to suppress the photolytic combustion of the TTC moiety during the synthesis of the TTC-P(DMAEMA) as much as possible. It was ensured that the reactions were quenched while they were still in the linear regime of the pseudo-first-order plot. However, because of possible chemical decomposition, for example, due to a nucleophilic attack at the thiocarbonyl carbon atom at the chain end, typically led to the formation of a thiol group, which is known as a suitable anchoring group for GNP surfaces, the photolytic degradation was considered to be more crucial in the context of the synthesis of the Au@P(DMAEMA) hybrids. The pTTC- and dTTC-P(DMAEMA) precursors used for the GNS synthesis all show dispersities in the range of 1.1–1.2. The chain lengths were adjusted in the range between 40 and 100 repeating units of DMAEMA. The reaction conditions of each P(DMAEMA)$_n$ polymerization are summarized in **Table 8**. The polymerization results are concluded in **Table A1**.

5.2.2. Responsive Properties of the pTTC-P(DMAEMA) and dTTC-P(DMAEMA) Polymer Precursors

P(DMAEMA) is known for its temperature and pH-responsive behavior in aqueous solutions. In accordance with Reference [3], the responsive properties were investigated. DLS measurements and UV–Vis extinction spectroscopy were predominantly used to characterize the temperature-responsive behavior. **Figure 26** depicts the results of these measurements from Reference[3]. These measurements clearly show significant differences in the responsive behavior between the pTTC- and dTTC-based P(DMAEMA) polymers. Additionally, the chain length appears to influence the value of the PTT, which can be correlated with the pH-responsive behavior typical for polybasic compounds like P(DMAEMA). Both phenomena are discussed in more detail in the following paragraphs of this section.

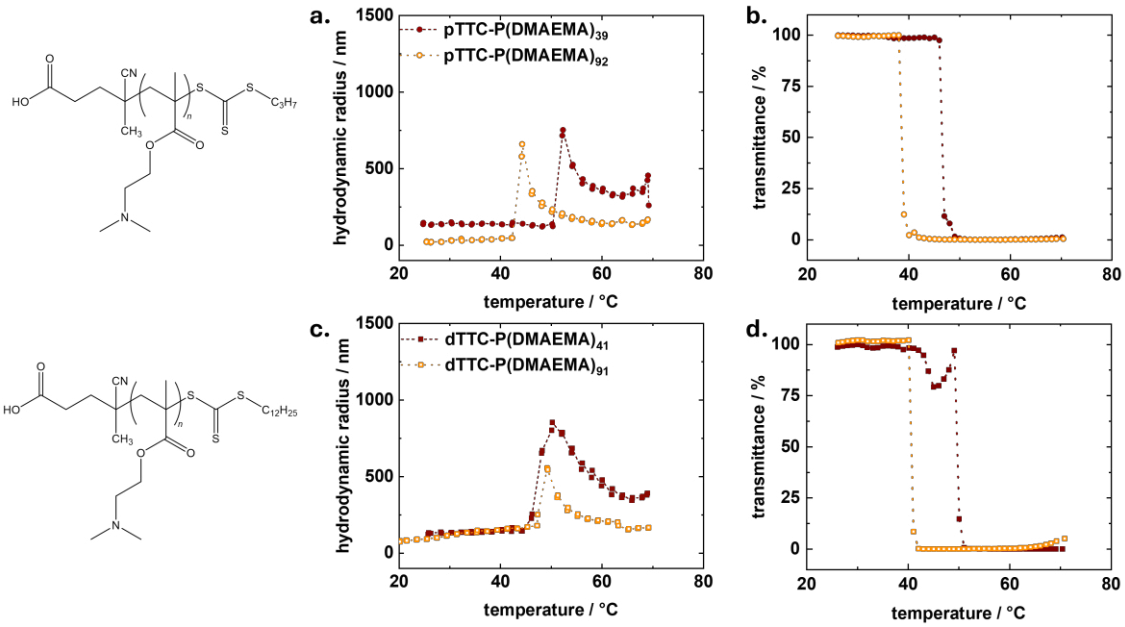


Figure 26. Representative temperature-dependent measurements DLS (a./c.) and UV–Vis transmittance measurements (b./d.) of pTTC- (top) and dTTC-P(DMAEMA) (bottom) products dissolved in water. For the DLS measurement, a 0.01 %(*w*/*w*) solution was prepared. The UV–Vis measurements were conducted on a 0.1 %(*w*/*w*) polymer solution. The data were taken with permission from the open-access source *Macromol. Chem. Phys.* **2022**, 2200355. Copyright 2022 The Authors. Macromolecular Chemistry and Physics, published by Wiley-VCH GmbH.[3]

First, it is worth noting that the measurements in **Figure 26** are from the second temperature cycle of each respective sample. It has been demonstrated that the results from the first measurement cycle differ significantly from those obtained in subsequent temperature cycles. After this first equilibration heating/cooling cycle, the responsive behavior showed excellent reproducibility over at least three further temperature cycles. Since the following cycles exhibit constant behavior, each sample was typically measured no more than four times. The temperature-responsive dependency of the R_H of the samples plotted in **Figure 26** shows self-assembling behavior around the PTT of the respective polymer in solution. This assembly is indicated by an initial increase in R_H around the turbidity point (T_{cp}) measured via UV–Vis spectroscopy. An R_H

decay follows this R_H increase. This behavior is explained best by the formation of micellar structures with the hydrophobic TTC-chain end as the core stabilized by the polar amine functionalities of the DMAEMA units as the shell material. As temperatures rise, this P(DMAEMA) shell becomes less hydrophilic, forcing water out of the shell and leading to a gradual decrease in R_H. Interestingly, the TTC group's nature significantly influences the micellization point. As visualized in **Figure 26** a., for pTTC-based P(DMAEMA) chains, the assembly temperature correlates with the chain length and is consistent with the T_{cp} measured with the UV–Vis measurements.

Meanwhile, the aggregation/micellization temperature of the dTTC-based P(DMAEMA) compounds shows some contrast compared to the turbidity temperature. Due to the dodecyl group's strong hydrophobic nature, the polymer chains are more prone to form aggregates that stabilize their hydrophobic chain ends than the propyl group. Although the pTTC-based sample shows a clear chain-length dependence of the $T_{cp,}$ the temperature where the R_H is increasing stays nearly the same when the shorter polymer chain (dTTC-P(DMAEMA)$_{41}$) is compared to the longer chain component (dTTC-P(DMAEMA)$_{91}$). For the pTTC-based polymers, the chain-length dependence of the turbidity point was investigated in greater detail. **Figure 27** shows the turbidity measurements of pTTC-P(DMAEMA)$_n$ solutions with varying molecular weights of the P(DMAEMA)$_n$ chain. The P(DMAEMA)$_n$ samples taken for this investigation were sourced from the kinetic investigation of the polymerization reaction described in **Figure 25** (a) and (b) and represent the samples after 303 min, 423 min, 515 min, and 1505 min. As in **Figure 26**, the plots show the results of the second heating/cooling-temperature cycle for better comparison. Due to the time-consuming nature of the temperature-dependent DLS measurement, the samples were pre-heated before the measurement cycle was started to save time.

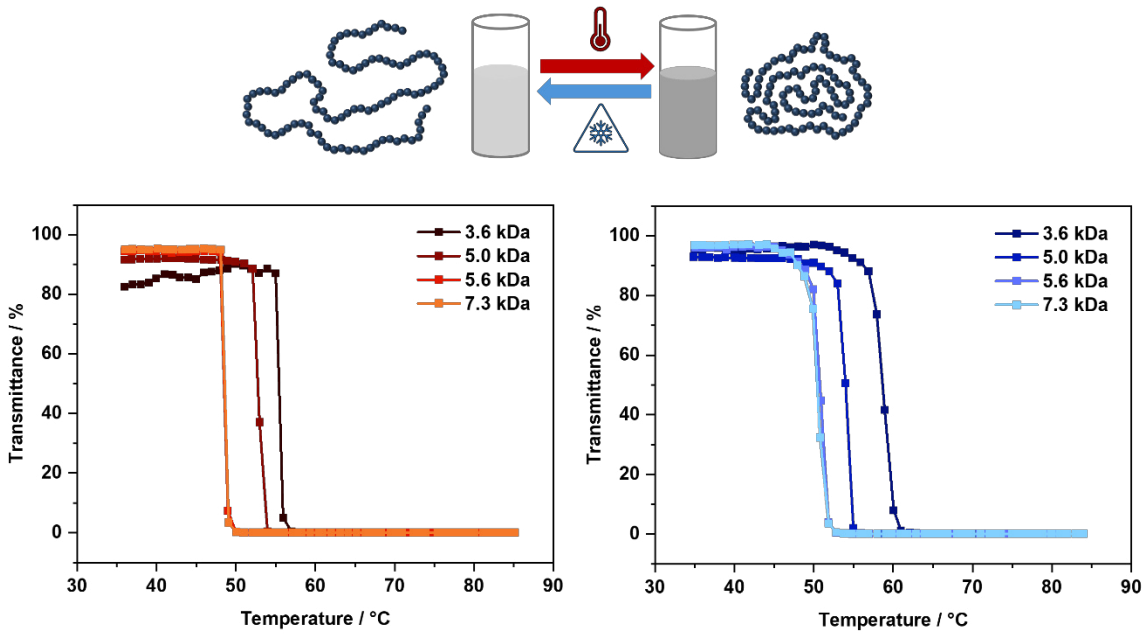


Figure 27. UV–Vis turbidity measurements of 1.0 %(*w*/*w*) pTTC-P(DMAEMA) water solutions. The heating curves (left graphic) and cooling curves (right graphic) for the respective samples are shown. The lines between the measurement points serve as optical guidance and do not represent a continuous measurement. All samples were preheated to 85 °C and cooled to room temperature prior to the temperature cycle measurement.

The heating curves in **Figure 27** indicate a dependency of the T_{cp}. This dependency is most likely attributed to more factors than the chain length alone. One well-known factor that influences the solubility of P(DMAEMA) is the pH value and the degree of the side-chain amine protonation. Therefore, acidic groups in the solution will impact the obtained value of T_{cp}. Because the R-group of the used CTA carries a carboxylic acid, the α-end of the polymer chain is also a carboxylic acid. The presence of this group explains the higher solubility of the short-chain pTTC-P(DMAEMA) components and the higher PTT in the hydrophobic state. Additionally, in **Figure 27**, due to the shorter chains, the relative ratio of acidic groups to DMAEMA units is larger than for samples with higher molecular weights. A higher amount of DMAEMA units will cause an increased pH value due to the fundamental nature of DMAEMA, which will further decrease the polymer's capability of stabilizing its hydrophobic sections. In conclusion, the chain-length dependency of the T_{cp} is primarily the consequence of the inherent pH-responsive behavior (DMAEMA). J. Xu and V. Abetz already showed that the α-end group influences the responsive nature of smart polymers in 2022.[1] The acidic R-group especially plays a crucial role in stabilizing the polymer it is attached to, even above the polymer PTT. In a side project, the RAFT agent pTTC was functionalized via esterification of the carboxylic group with (anthracene-9-yl)methanol. This functionalization was initially thought to provide photochemical crosslinking of the later Au@P(DMAEMA) hybrid materials. This approach did not prove successful. However, when comparing the temperature-responsive character of anthracene functionalized P(DMAEMA) samples (pTTC-P(DMAEMA)-AN) with the unfunctionalized counterpart (**Figure 28**), the difference becomes evident, especially for molecular weights below 10 kDa.

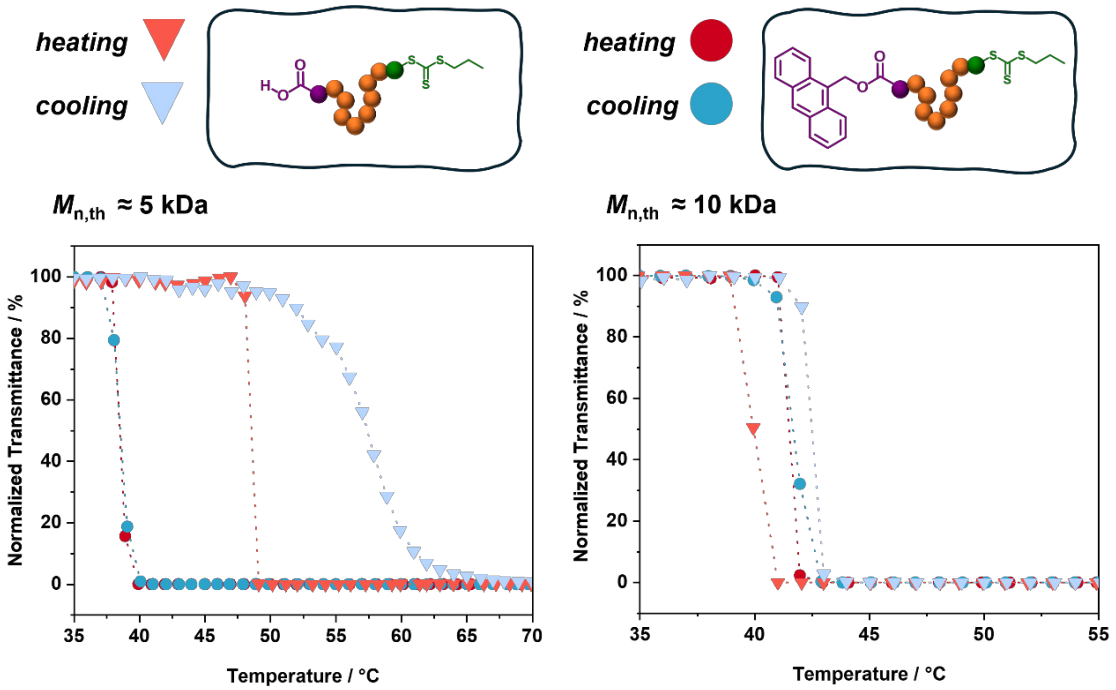


Figure 28. UV–Vis turbidity (normalized transmittance at 650 nm) measurements of 1.0 %(*w*/*w*) pTTC-P(DMAEMA) (triangles) and pTTC-P(DMAEMA)-An (circles) water solutions. Plotted is the transmittance (normalized to 0–100 % for better comparability) against the temperature after pursuing a first equilibrium temperature cycle.

Interestingly, the data for the anthracene-functionalized samples show no hysteresis between the heating and cooling curves. Additionally, the PTTs of the 5 kDa and 10 kDa samples fall within the same temperature regime, showing a temperature difference of less than 5 °C. The unfunctionalized P(DMAEMA) samples show different behavior. First, both unfunctionalized pTTC-P(DMAEMA) samples (5 kDa and 10 kDa) in **Figure 28** show a significant difference in their PTTs. This supports the assumption that carboxylic acid has an influence, as described above. Secondly, there is a noticeable difference between the heating and the cooling curves, which show hysteresis. As expected, heating both solutions caused a rapid phase transition, a typical behavior for LCST-type homopolymers. However, the redissolving process is usually kinetically hindered due to chain rearrangements. These rearrangements typically take time, leading to the redissolution of the polymer at lower temperatures than those required for the entropically driven hydrophobic phase transition. However, since the process is less pronounced at higher molecular weights and does not appear in the functional anthracene, it is a reasonable assumption that this is an α-end-based effect. Presumably, the rearrangement of the α-end onto the surface of the polymer aggregate stabilizes these aggregates until the hydration of the DMAEMA units takes over again. Since the decay of the hydrophilic shell is a rapid process, this rearrangement of the α-end is not fast enough to occur during the heating of the solution.

On the other hand, rearranging the α-end to the polymer aggregates is not temperature-related, as already described by Xu and Abetz, meaning that it will occur at temperatures above the polymers' PTT. Therefore, the aggregates should be better stabilized due to the constant hydration of the α-end, and the redissolving process is a combined effect of the temperature-responsive behavior of

the P(DMAEMA) chain and the hydrated end group. With a higher DMAEMA fraction, the difference between the heating and cooling curves becomes less pronounced, somewhat supporting the explanation of a combined effect between end-group and DMAEMA-typical behavior. At this point, it is important to note that all measurements shown in **Figure 28** were conducted at the same heating and cooling rates. Nevertheless, the observed behavior is not fully understood, and further investigation is suggested to gain a more detailed understanding of the redissolving process.

5.2.3. Synthesis of pTTC-P(DMAEMA)- and dTTC-P(DMAEMA)-based Au@P(DMAEMA) Nanohybrids

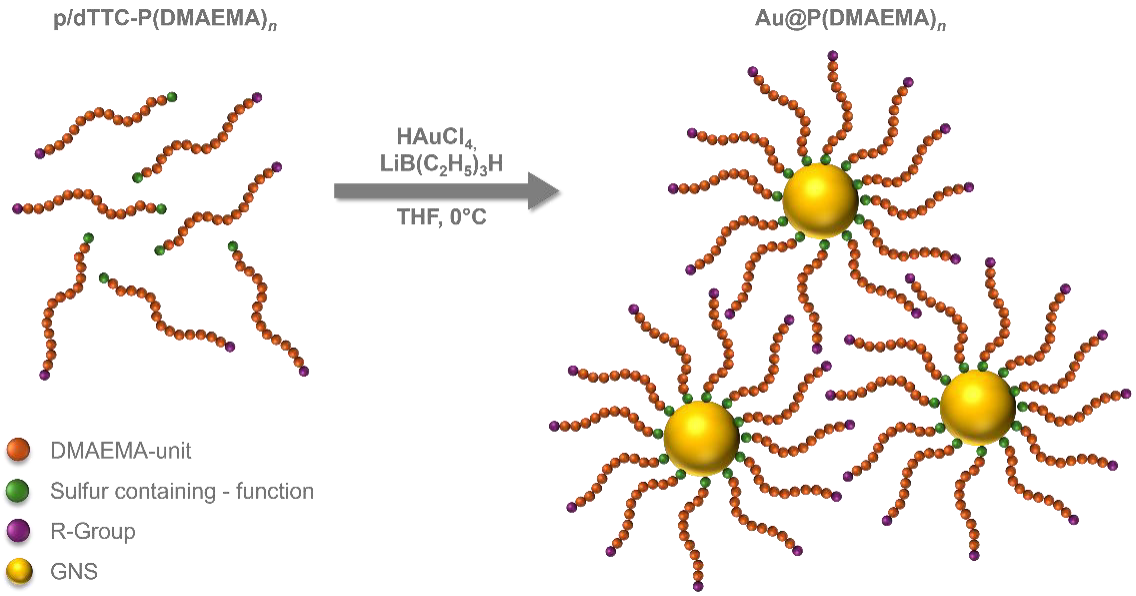


Figure 29. Illustration of the *in situ* synthesis of multi-responsive Au@P(DMAEMA) nanohybrids based on the reaction protocol presented in Reference [3].

The synthesis of Au@P(DMAEMA) nanohybrids was based on the reduction of $HAuCl_4$ using the reducing agent lithium triethyl borohydride in a THF solution (superhydrid®) with the presence of TTC-P(DMAEMA) precursors (**Figure 29**). In contrast to the hybrids known from literature, the presented nanohybrid materials are synthesized using RAFT polymers based on TTC RAFT agents. Using the P(DMAEMA) precursor, pH- and temperature-responsive properties were achieved through a simple homopolymerization. The multi-responsive nature of P(DMAEMA) enabled the use of a simple one-step polymerization and, therefore, a more detailed study of the polymerization kinetics due to its simplicity.

In this work, several factors were investigated to optimize the particle quality in terms of their size and size distribution. Aside from the results presented in Reference [3], factors like the polymer concentration, the polymer chain length, and the reaction time before quenching were varied to see whether these parameters affect the GNSs quality. The results from varying these factors are concluded in the plots shown in **Figure 30**, where the GNSs' diameter is plotted against the respective factor. These results were crucial for this work's progress because they allowed the optimization of the particle synthesis that was later published.[3] The polymers used for this investigation are listed in **Table 1**.

Table 1: Conclusion of the pTTC-P(DMAEMA) precursors used to investigate polymer concentration, polymer chain length, and reaction time for the reaction parameter optimization. Listed are the polymer names as well as their respective degree of polymerization (DP_{DMAEMA}), the theoretical number average molecular weight obtained via ^{1}H-NMR spectroscopy ($M_{n.th}$), the number average molecular weight from SEC ($\bar{M}_n$), the dispersity, and the polymer's consecutive number (CN) in the laboratory journal/data set.

Polymer	DP_{DMAEMA}	$M_{n.th}$ / kg/mol	$\bar{M}_n$ / kg/mol	$Đ$
pTTC-P(DMAEMA)$_{48}$	48	7.85	8.14	1.17
pTTC-P(DMAEMA)$_{110}$	110	17.5	16.7	1.20
pTTC-P(DMAEMA)$_{37}$	37	6.12	6.73	1.18
pTTC-P(DMAEMA)$_{72}$	72	11.4	11.7	1.11

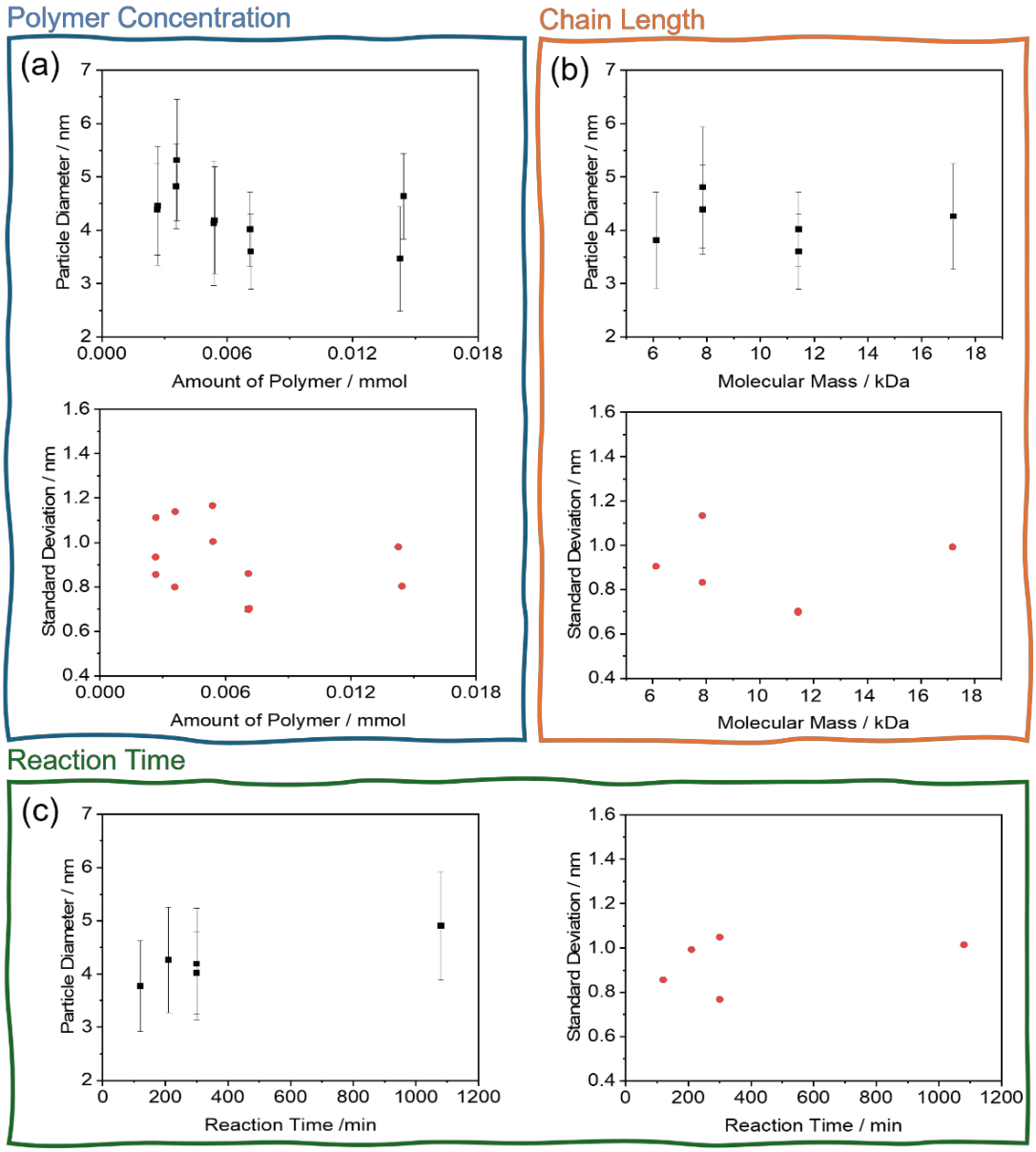


Figure 30. Influence of different reaction parameters on the GNS diameter. The investigated parameters are the amount of polymer used in the 20 mL polymer precursor solution(a), the molecular weight of the polymer precursor (b), and the reaction time (c). For the polymer concentration plot, pTTC-P(DMAEMA)$_{72}$ was used, and all reactions were quenched after 210 min. The chain-length dependency was investigated at a reaction time of 210 min. The polymer pTTC-P(DMAEMA)$_{110}$ was the precursor for the reaction time plot. The particle diameter and the standard deviation are plotted against each parameter. At least 300 particles were measured by hand for each point via the evaluation program ImageJ (version 1.51f).

The data show that none of the three parameters in the chosen borders significantly affected the average particle diameter. Also, the standard deviation (SDV) of the measured particle diameter showed no apparent dependence upon the investigated parameters. For all reactions, represented in **Figure 30**, the SDV ranged from 0.6 nm to 1.2 nm, independent of the apparent parameter. The SDV, in this case, is taken as a measure of the GNS quality in terms of particle size homogeneity. All reactions aimed at investigating the influence of polymer concentration were conducted with the same polymer precursor (pTTC-P(DMAEMA)$_{72}$) to exclude possible polymer-batch-quality-related effects. To investigate the influence of reaction time, pTTC-P(DMAEMA)$_{110}$ was used to eliminate interference from variations in polymer batch quality. Additionally, if possible, every reaction was reproduced a second time to get a feeling of how pronounced particle batch variations are. The results show that the synthesis protocol of the Au@P(DMAEMA) hybrids is highly reproducible. With an SDV below 1.2 nm for all approaches, independent of the respective parameter changes, the presented procedure is absolutely comparable to similarly prepared Au@polymer hybrids.[2,272]

Figure 31 shows some representative TEM images of the discussed samples. Typical statistical fluctuations from the synthesis and the TEM measurements explain the size variations observable in the TEM images. The hybrids published in Reference [3] are all synthesized based on the knowledge gained in the as-discussed investigations.

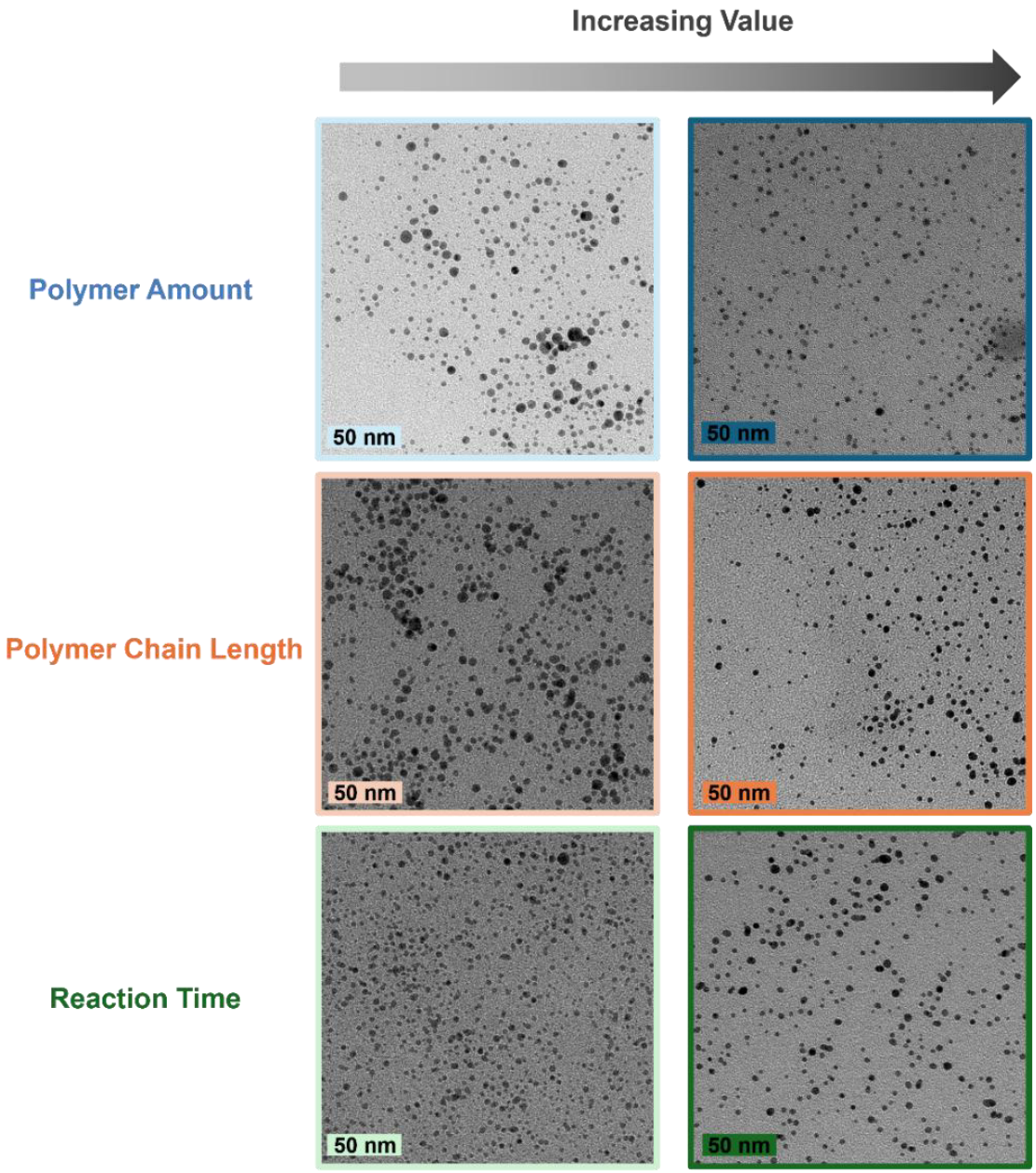


Figure 31. TEM images of the first and last sample of reaction parameters: polymer amount (top), polymer chain length (mid), and reaction time (bottom), with the lower value in the left column, and the higher value in the right column.

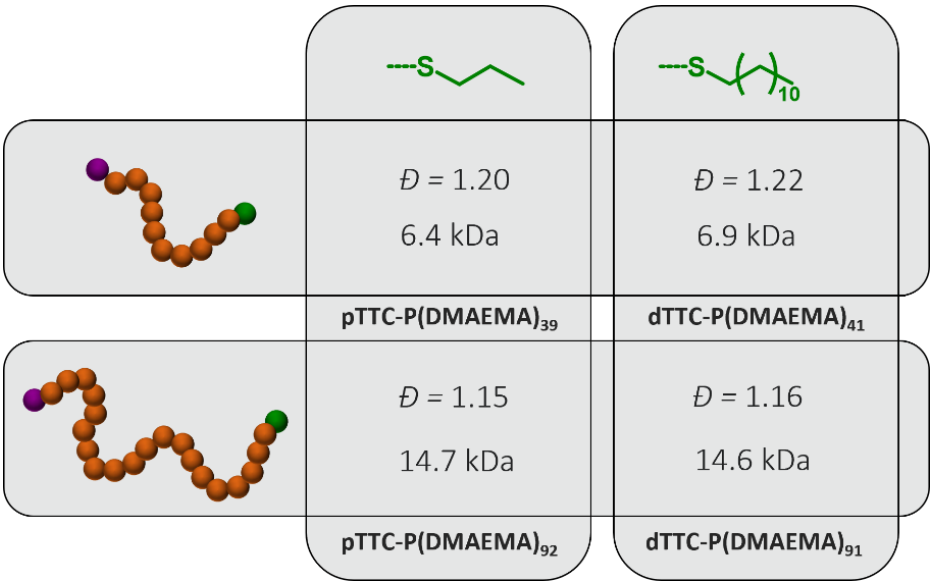


Figure 32. Overview of the P(DMAEMA)*n* precursor used for the synthesis of the published[3] Au@P(DMAEMA)*n* hybrids.

As mentioned at the beginning of this section, the RAFT-polymer precursors used for the GNS hybrid synthesis differ significantly from the RAFT-polymer precursors used in the literature for comparable GNS preparation protocols. The RAFT agents used differ from those in prior work, which predominantly used dithiocarbonyl (DTC)-based RAFT agents.[2,252,253] This difference raised the question of the influence of the end group's structure. The reducing agent is assumed to reduce the DTC group to a thiol function. When using TTC groups, the formation of two different thiols, which can bind to the gold surfaces, is possible. The successful implementation of TTC-based RAFT polymers would significantly enhance the applicability of that protocol, allowing a greater variety of different polymers and their architecture due to the versatility and easy synthesis protocols of TTC-RAFT agents.

For the publication, four different P(DMAEMA) precursors (**Figure 32**) were used for the GNS hybrid *in situ* synthesis protocol to compare the TTC polarity effect. Based on both RAFT agents, pTTC and dTTC, two P(DMAEMA precursors were synthesized, each with a longer and shorter DMAEMA chain. Each precursor was used to synthesize a corresponding Au@P(DMAEMA) hybrid suspension in THF, which was then transferred to an aqueous solution for further analytical investigations. The results of these reactions are presented in **Table 2** and **Figure 33**. To reduce the implicit statistical variations of the particle diameter, due to the inherent error of the TEM evaluation, the number of measured particles was increased for the particle diameter evaluation in the published article to at least 700 particles of each sample. While the obtained particle diameters are in a comparable region between 5.2 nm and 3.8 nm, the optical properties of the hybrids differ more significantly than the particle size implies, meaning that there must be significant differences in the particle stabilization.

Table 2: Properties of the Au@P(DMAEMA)$_n$ hybrids in aqueous solution are listed with their respective P(DMAEMA) precursor from Reference [3]. Listed are the λ_{LSPR} and the GNS particle diameters (d_{TEM}) obtained by evaluating TEM images. The data are taken with permission from Reference [3]—copyright by 2022 Wiley-VCH GmbH.

Precursors	**Au@P(DMAEMA)$_n$ Hybrid**	**HN**	**d_{TEM} / nm**	**λ_{LSPR} / nm**
pTTC-P(DMAEMA)$_{39}$	Au@P(DMAEMA)$_{39}$	H1	5.2	520
pTTC-P(DMAEMA)$_{92}$	Au@P(DMAEMA)$_{92}$	H2	4.0	505
dTTC-P(DMAEMA)$_{41}$	Au@P(DMAEMA)$_{41}$	H3	3.8	510
dTTC-P(DMAEMA)$_{91}$	Au@P(DMAEMA)$_{91}$	H4	4.1	517

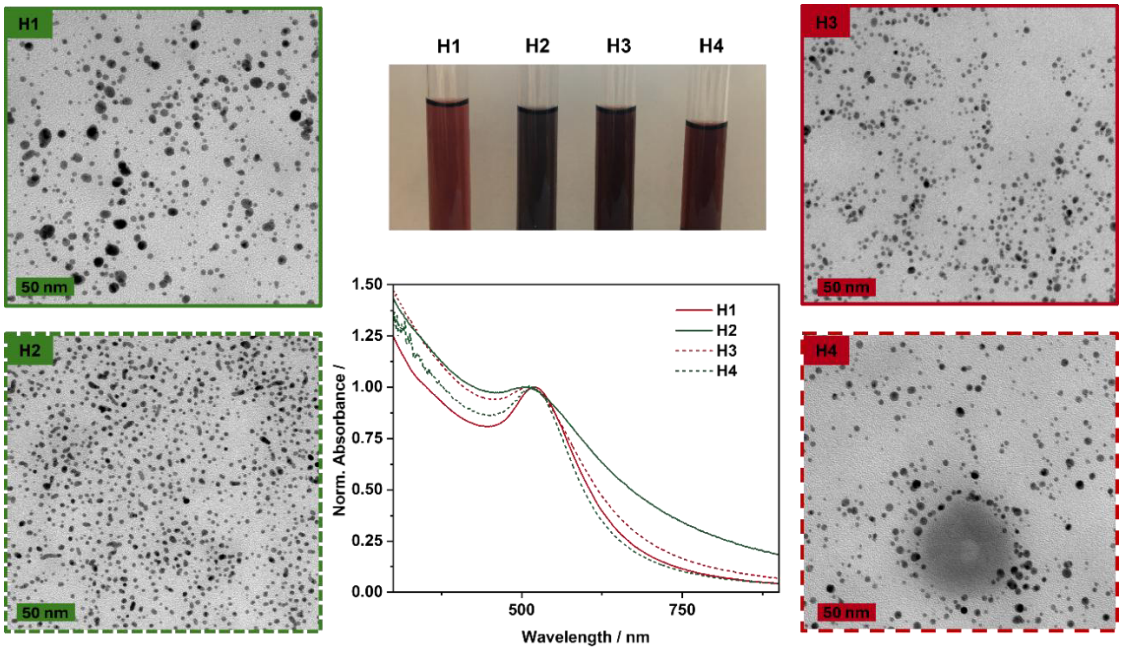


Figure 33. Collective data of the pTTC-precursor- and dTTC-precursor-based Au@P(DMAEMA) hybrids. The centered graphic shows the normalized UV–Vis absorbance spectra of the suspended Au@(PDMAEMA)$_n$ hybrids in water at 25 °C. TEM images and a photograph of the respective sample dispersed in water are provided. The photograph, the plot data, and the TEM image of the H4 are taken from the open-access source *Macromol. Chem. Phys.* **2022**, 2200355. Copyright 2022 The Authors. Macromolecular Chemistry and Physics, published by Wiley-VCH GmbH.[3]

However, the value of the obtained LSPR wavelength (λ_{LSPR}) in water and the Au-particle diameters do not follow a specific dependency. Although it appears that Au@P(DMAEMA) hybrids based on dTTC-P(DMAEMA) precursors show smaller particle diameters, these differences are most likely explained by batch-dependent variations. Nevertheless, the results show that no matter which RAFT agent is used, the particle synthesis is unaffected, which is a very positive result regarding the reproducibility of the synthesis protocol. Importantly, there are significant differences between the solubilities of pTTC- and dTTC-based nanohybrids, as discussed later in Section 5.4.1.

To show that the reduction of the gold precursor is attributed to the superhydrid® for the applied reaction conditions, the reducing potential of a THF/P(DMAEMA) solution was tested in a reduction agent-free blind reaction in the presence of $HAuCl_4$. First, the solution was kept at the

same temperature (~0 °C) at which the Au@P(DMAEMA)$_n$ hybrids were prepared. An ice bath kept the temperature constant for seven hours at 0°C. During this time, the reaction solution turned turbid without significantly changing color (**Figure 34** (a)). Afterward, the reaction was slowly heated to room temperature. At room temperature, the solution was mixed for three days. As displayed in **Figure 34** (b), the reaction significantly lost its original yellow color after this time. This decolorization indicates the reduction of the Au(III) species to the colorless Au(I)-species. Afterward, the reaction conditions were further intensified by heating the reaction to 45 °C for 23 hours. This caused a color change to blue, indicating the formation of GNPs inside the turbid suspension. Two facts can be drawn from this. First, under the reaction conditions chosen and the applied reaction time of 210 min for the *in situ* protocol, the reducing strength of P(DMAEMA) can be considered insignificant. Secondly, the reaction temperature should not be increased drastically, as this can lead to side reactions that degrade particle quality.

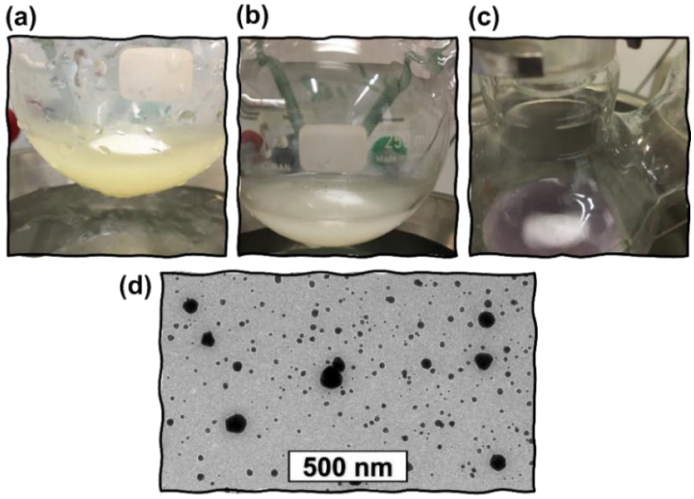


Figure 34. Images of the reaction solution of the reduction agent-free blind reaction at different points of the reaction. (a) displays the reaction solution after 7 hours under standard conditions (~0 °C). Image (b) shows the same solution at room temperature after an additional 72 hours. In (c), the reaction suspension is shown after 23 hours @45 °C. The TEM image in (d) shows the particles obtained after purification from solution (c) with a 500 nm scale bar. All images are taken from the SI of the open-access article *Macromol. Chem. Phys.* **2022**, 2200355 with minor adaptations. Copyright 2022 The Authors. Macromolecular Chemistry and Physics, published by Wiley-VCH GmbH.[3]

At this point, the question about the long-term particle stability in the THF suspensions remained unclear. Although the reducing strength of the free electron pair of DMAEMAs amine function is not noticeable under standard reaction conditions (30 min, 0 °C), according to the results of **Figure 34**, the progressive formation of GNPs can become critical when storing the particles in THF over a long period. Several THF Au@P(DMAEMA) suspensions were remeasured by TEM after storing them for a few months in THF at 0 °C in the dark to address this topic. It was found that the NPs experienced significant aging effects. Several factors have been identified as contributing to the amine content of the hybrids, which enhances aging processes. The samples investigated on the effects of aging are presented in **Figure 35**. TEM samples were prepared immediately after the particle purification and after several months of storing the hybrids suspended in THF at 0 °C in the dark.

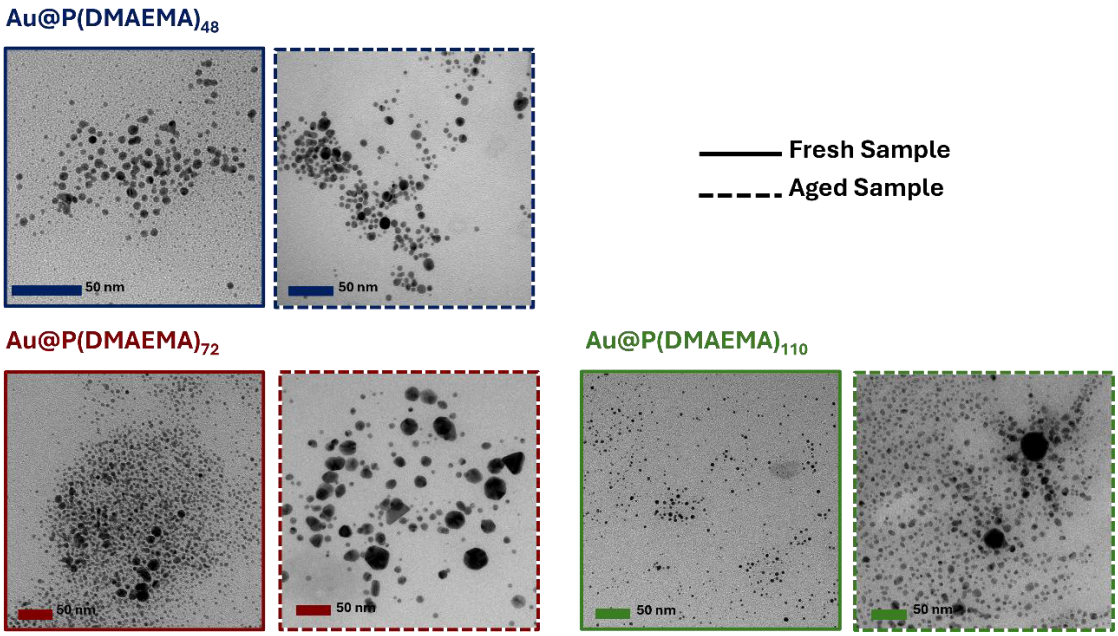


Figure 35. Aging effects of different pTTC-P(DMAEMA)$_n$-based gold hybrids after storing the THF suspensions for several months in the dark at 0 °C. Shown are TEM images of the hybrid suspension of Au@P(DMAEMA)$_{78}$ (blue frames), Au@P(DMAEMA)$_{72}$ (red frames), and Au@P(DMAEMA)$_{110}$ (green frames), before (full frame) and after (dashed frames) aging. All images are taken from the SI of the open-access article *Macromol. Chem. Phys.* **2022**, 2200355 with minor adaptations. Copyright 2022 The Authors. Macromolecular Chemistry and Physics, published by Wiley-VCH GmbH.[3]

Significant changes in the particle assimilation were observed in the literature after aging the samples.[3] The literature reports spherical assimilations of GNS within raspberry-like structures after storing the THF suspensions for six months in the dark at 0 °C. Since the formation of particle assemblies is sensitive to slight variations in the preparation procedure of the TEM sample, the observed assemblies in the literature have to be taken cautiously. In **Figure 35**, different Au@P(DMAEMA)$_n$ samples are shown. After aging, the gold nanoparticles observed by TEM exhibited inhomogeneous shapes and sizes. Indicating aging processes like Ostwald ripening. The formation of anisotropic particles after aging seeded the idea of using DMAEMA-based polymers to trigger anisotropic growth, as in Section 5.3.

Another important proof-of-principle experiment involved cross-linking the polymer and the nanohybrids, yielding a gel-like material in THF. It was shown that a bifunctional alkyl bromide like 1,5-dibrompentane (DBrP) P(DMAEMA)$_n$ can crosslink P(DMAEMA)$_n$ chains with each other, which causes the formation of a free-standing gel material. First, the crosslinking of the polymers pTTC-P(DMAEMA)$_{39}$ and pTTC-P(DMAEMA)$_{92}$ was tested. Therefore, a 1 %(*w*/*w*) THF/polymer solution was prepared, and 0.5 equivalents of DBrP (based on the amine concentration) were added to the solution. These solutions were heated to 55 °C for 72 hours without mixing. The same reaction was conducted with the Au@P(DMAEMA)$_n$ hybrids shown in **Figure 33** after using thermogravimetric analysis (TGA) of the THF hybrid suspensions to determine the amine concentration within the reaction volume. Photographs of the free-standing polymer gels are displayed in **Figure 36**.

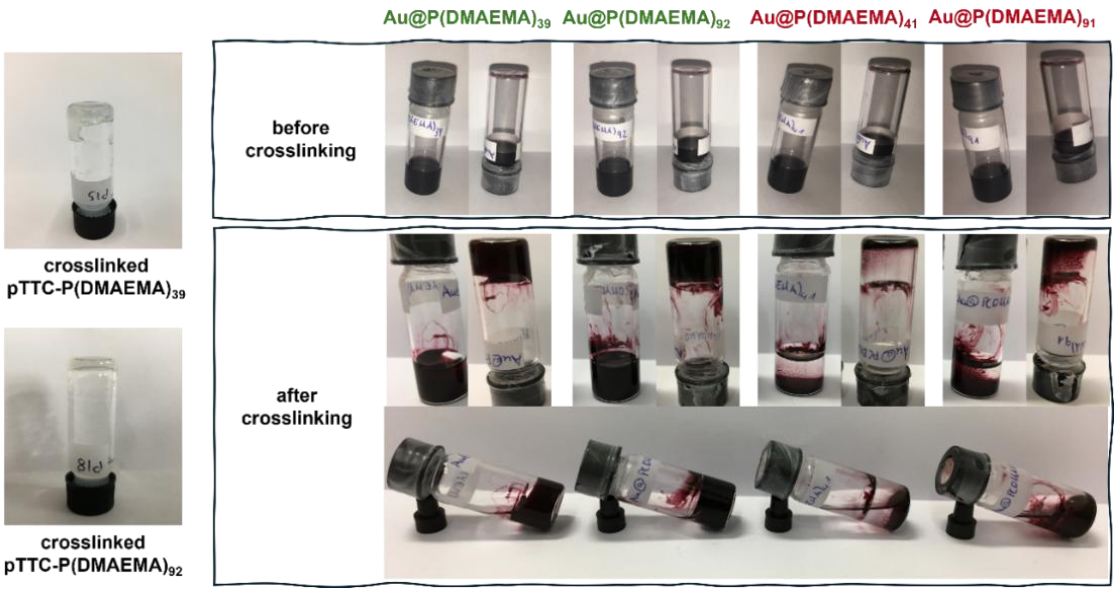


Figure 36. Photographs of the polymer precursors pTTC-P(DMAEMA)$_{39}$ and pTTC-P(DMAEMA)$_{92}$ after crosslinking with DBrP (left column), and of the THF hybrid solutions before (top row) and after (bottom row) crosslinking the P(DMAEMA) by using DBrP. The images are taken from the SI of the open-access article *Macromol. Chem. Phys.* **2022**, 2200355 with minor adaptations. Copyright 2022 The Authors. Macromolecular Chemistry and Physics, published by Wiley-VCH GmbH.[3]

Interestingly, while crosslinking the free-standing polymer samples, there was no significant difference between the pTTC-P(DMAEMA)$_n$ and the dTTC-P(DMAEMA)$_n$ distinguishable. The samples resulted in a free-standing, fragile gel structure. The Au@P(DMAEMA)$_n$, however, did show slight differences between the samples when hybrids pTTC-P(DMAEMA)$_n$ and dTTC-P(DMAEMA)$_n$ precursors were used for the synthesis. The pTTC-P(DMAEMA)$_n$-based hybrids (**Figure 36**, green) formed a gel-like structure with THF absorbed mainly by the hybrid material. The crosslinked dTTC-P(DMAEMA)$_n$-based hybrids (red) formed a more collapsed structure when the largest part of the solvent (THF) was above the crosslinked hybrids. The results indicate a first significant difference, such as the solubility of both types of Au@P(DMAEMA)$_n$ hybrids. The presented preparation method demonstrates that TTC-based polymers can be used to synthesize GNS in a direct synthetic approach and extends the method described in the literature.[2,251]

A similar functionalization was used during polymer design to trigger anisotropic growth, as discussed in Section 5.3.

5.3. Polymer-Assisted Anisotropic Growth of GNRs

Parts of this section have already been published.[8] The seeded growth method chosen for this project is a powerful tool for synthesizing GNRs and can be easily adjusted, for example, to control the particles' average aspect ratio. However, this adjustability comes at the cost of a high sensitivity toward small fluctuations in reaction conditions. As discussed in Section 4.1.2.2, factors like the ion concentration, stirring times, and the reagent addition order significantly influence the outcome of the particle synthesis.

However, the silver-assisted seeded growth procedures have been intensively studied, and many key factors that control anisotropic growth have now been revealed.[7] Due to their unique optical properties, GNRs are highly interesting for biological applications. The combination of GNRs with a stimuli-responsive polymer shell also enables photothermally regulated drug release using near-infrared (NIR) light. The longitudinal LSPR easily reaches the NIR region, where biological tissue shows its transparency windows.[33,36] This allows electromagnetic waves to penetrate biological tissue more efficiently and enables hypothermal treatment below a patient's skin, a medical field dominated by magnetic nanoparticles. This section's motivation was to reduce the inherent toxicity of seeded growth-based GNRs and provide GNRs that are more applicable for biomedical use.

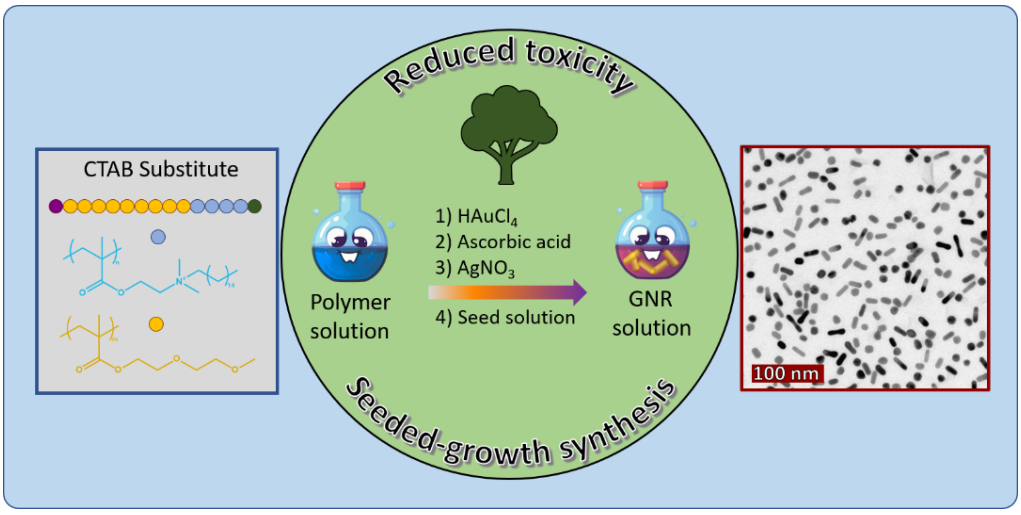


Figure 37. Topic overview of polymer-assisted anisotropic growth for toxicity reduction of the conventional silver-assisted seeded growth process used to synthesize GNRs.

The toxicity of GNRs is attributed to the stabilizing CTAB double-layer and the equilibrium-based release of CTAB molecules from that layer. However, the use of CTAB is nearly unavoidable because of its anisotropic growth-directing character. This character is mostly attributed to the nature of the tertiary amine headgroup of CTAB. The idea behind this topic was to mimic the CTAB's headgroup fixed in a polymer chain to minimize the toxicity.

Since the experience showed that the amine function of P(DMAEMA) can quickly and nearly quantitatively be functionalized into a quaternary structure, the idea of triggering anisotropic growth for GNPs was an obvious call for investigation. The supporting information of

Reference [8] includes a very detailed guideline for the polymer design. Since this thorough guideline provides an advanced outlook for the future development of polymer stabilizers in that field of research, this chapter focuses more on the synthesis and the applied, scaled-up setup for photoRAFT polymerization, as well as the challenges encountered in finding suitable anisotropic growth-supporting block copolymers.

Based on the watery-seeded growth procedure for GNR explained in Section 4.1.2.2, the basic premise for the polymer was sufficient water solubility. Later, this premise proved the most challenging to overcome. To mimic the ionic headgroups functionality of CTAB, the tertiary amine function of DMAEMA was converted to its quaternary form by reacting it with 1-bromohexadecane (BHD) (see **Figure 38**). The first approach was to functionalize P(DMAEMA) homopolymers with BHD. Since the resulting polymers were insoluble in water, they were unsuitable for GNR synthesis. In a different approach, DMAEMA was functionalized before the polymerization. In this approach, a colorless, water- and THF-insoluble powder was obtained, indicating that the qDMAEMA polymerized during functionalization. Due to this insolubility, this powder was not further investigated.

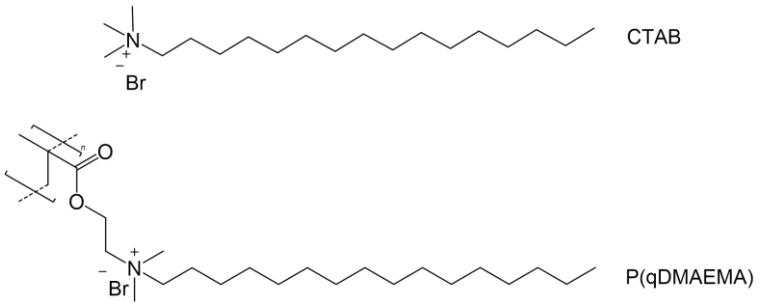


Figure 38. Comparison of the chemical structures of CTAB and the polymer substitute P(qDMAEMA).

The results indicated that a second water-soluble block is needed to stabilize the P(qDMAEMA) block in an aqueous solution. Following the premise that the CTAB substitute should improve the biocompatibility of the seeded-growth protocol, the second block should comprise bio-compatible behavior. For this purpose, the LCST polymer P(OEGMA) was chosen, which is considered biocompatible.[273] This choice was practical because the LCST-type behavior expands temperature as another parameter for the reaction. By using this responsive behavior, the polymer and particles can be removed from the solution, which could provide a valuable and benign method for purifying the product again. In parallel to this topic, the scaled-up polymerization of the P(OEGMA-*r*-BTPEMA), known from the work of Xu and Abetz[1], was just finished. Although this scale-up was initially developed for another topic (see Section 5.4.2.1), P(OEGMA-*r*-BTPEMA) was a suitable system to start. Due to its relatively high sulfur content based on the presence of copolymerized BTPEMA, additional surface stabilization effects were expected, hopefully supporting the particle synthesis. The polymerization kinetics of this scale-up photoRAFT polymerization are shown in **Figure 39**.

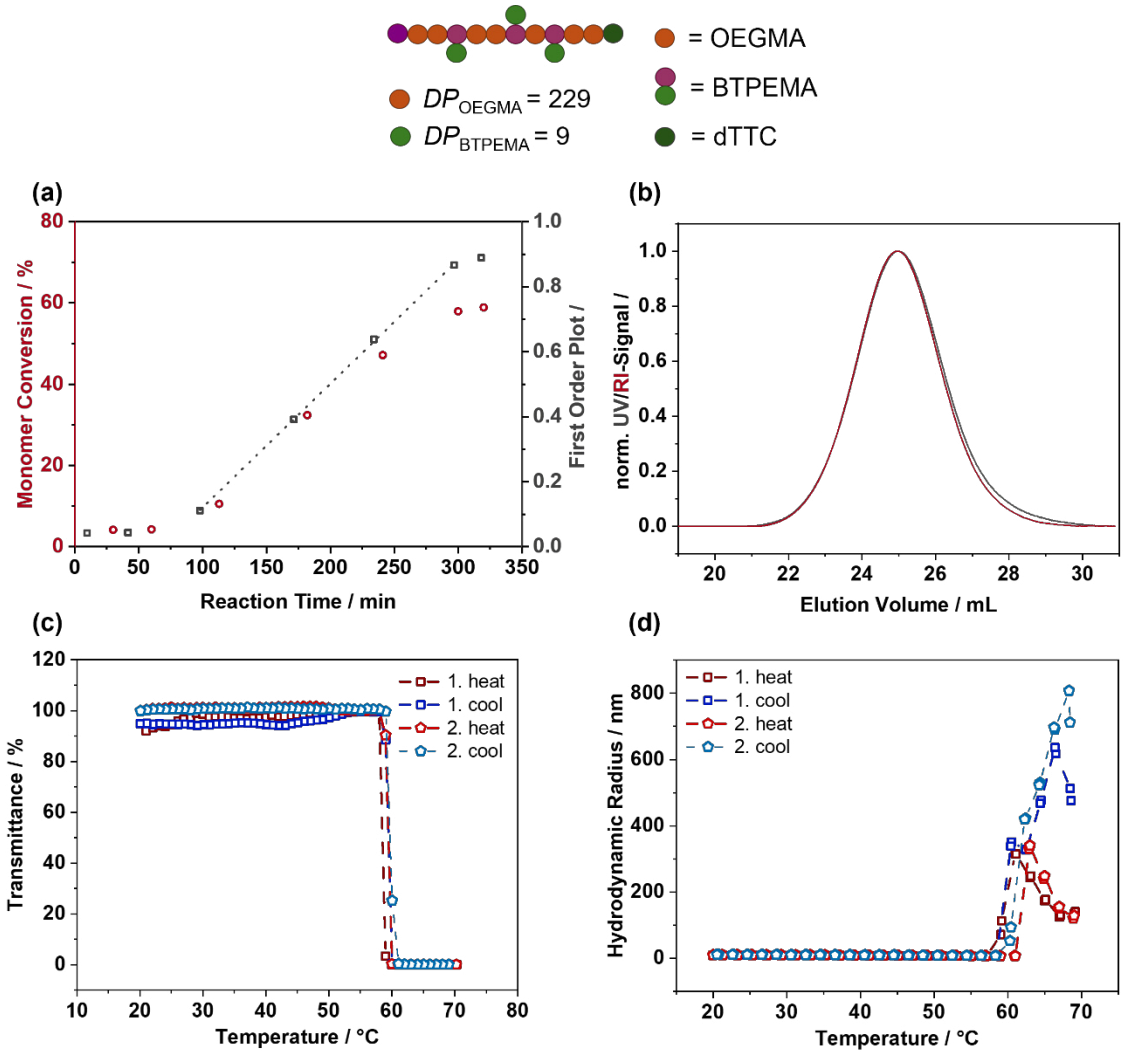


Figure 39. The results of the photoRAFT copolymerization of OEGMA and BTPEMA were obtained in a sublimation reactor setup with a reaction volume of around 250 mL. Graphic (a) shows the kinetic plots of the monomer conversion (red spheres) and the corresponding pseudo-first-order plot data (grey squares and the dashed line for the linear fit; corr. $R^2 = 0.999$) against the reaction time, respectively. In (b), the SEC of the polymer product is plotted, showing the elution chromatograms according to the normalized signal of the UV (grey) and the refractive index (RI) (red) detector. In (c) and (d), the temperature-responsive properties are characterized via UV–Vis spectroscopy (with a 1.0 %(*w*/*w*) polymer solution) and DLS measurements (with a 0.1 %(*w*/*w*) polymer solution), respectively. Two heat/cool cycles were shown after the polymer solution was pre-heated above the transition temperature.

Like in the original literature[1], a solid weight content of 20 %(*w*/*w*)was applied for the 250 mL-scaled polymerization conducted in a sublimation reactor setup. The kinetic plots show a 90-minute-long inhibition phase with a low monomer conversion rate before entering a linear first-order-like monomer conversion rate. This low conversion rate in the first phase of the polymerization is explained by the formation of the RAFT pre-equilibrium, which is surpassed after approximately 110 min reaction time. After a reaction time of 5 hours, about 60 % monomer conversion was reached, according to the ^{1}H-NMR results. Compared to smaller-scale copolymerizations of OEGMA and BTPEMA, with the same green light source (Renckforce RGB-LED stripe; λ_{max} = 513 nm; $I_d = 0.60$ mW·cm^{-2}), the 250 mL reaction displays lower monomer conversion rates. For comparison, J. Xu and V. Abetz reported a 60% monomer conversion after a three-hour reaction time for the polymer system. The reaction tracked in

Figure 39 (a) reached this conversion only after about five hours of polymerization. This behavior is explained by the reduced light intensity towards the reactor core, which corresponds to the Lambert-Beer law and causes a lower averaged light intensity referred to its complete reaction volume. Therefore, a decreased number of iniferter-based chain-activation steps are happening. In iniferter-based photoRAFT polymerizations, this inhomogeneous light-intensity distribution is a common phenomenon and becomes particularly pronounced at shorter wavelengths and in turbid reaction media.[186]

Reassuringly, graphics (b–d) in **Figure 39** show that the low polymerization rate does not significantly affect the quality of the P(OEGMA-*r*-BTPEMA). With an average of 230 OEGMA units and nine BTPEMA units in each chain, (B01) shows a narrow molecular weight distribution of $Đ$ = 1.43 for the UV-detector signal and 1.38 for the refractive index (RI) detector signal. *Side note: The DP of BTPEMA (DP_B) in B01 was recalculated using the method described by Xu and Abetz*[1]*, where the C-H signal of the BTPEMA unit adjacent to its carbonyl group is put into reference with the terminal methylene group of OEGMA. This calculation provided a DP_B=6.* Additionally, the temperature-responsive behavior of B01 with a PTT around 60 °C matches the result from the literature.[1] These results excellently prove the scalability of P(OEGMA-*r*-BTPEMA) without any significant drawbacks concerning the polymer composition, dispersity, or thermoresponsive behavior. Moreover, the enhanced scale allows more systematic investigations of side-chain length effects when extended with NiPAM (See Section 5.4.). For the development of anisotropic growth-directing polymer stabilizers for the GNR synthesis, different copolymers that originated from the P(OEGMA-r-BTPEMA) batch were synthesized using DMAEMA for the chain extension.

The first few polymerization approaches of DMAEMA aimed at a higher content of DMAEMA within the polymer and a grafted copolymer structure. Therefore, blue light (λ_{max} = 467 nm; I_d = 0.60 mW cm^{-2}) was used to initiate the polymerization of DMAEMA. As described in section 4.2.1, blue light activates all the TTC functions of B01. ^{1}H-NMR measurements were performed to track the reaction and the DMAEMA conversion (**Figure 40** on the left). The polymerization rate was very low compared with other photoRAFT polymerizations performed with DMAEMA, as described in Section 5.2.1. To achieve adequate monomer conversions of around 40 %, the reaction solution had to be irradiated for at least 300 minutes. Furthermore, during the synthesis of GD01, the monomer conversion rate decreased significantly after approximately 40 % conversion, indicating premature termination of the polymerization. These circumstances indicate issues with the underlying RAFT process. The SEC results obtained from these polymerizations are shown in **Figure 40** in the right graphic. **Table 3** concludes the product information about the two DMAEMA graft polymers and the DMAEMA-copolymers from later experiments after optimizing the system (Section 5.3.2). The underlying problem of the RAFT process is also supported by the broad molecular weight distribution shown by the SEC

measurement results in the right graph in **Figure 40** and the *Đ* values (>1.60). The radical stability mismatch of the secondary BTPEMA radical and the tertiary DMAEMA radical gives a reasonable explanation. This mismatch prolongs the reinitiation process significantly. This causes uneven chain growth because the assumption that all chains start to grow simultaneously does not hold, which is why a larger *Đ* is obtained.

However, at this stage of this work, the increased *Đ* was accepted because this project focused on the applicability of the GNR synthesis. The idea of using blue light was based on the goal of obtaining grafted copolymer precursors to increase the atom efficiency of the polymer-based GNR synthesis by increasing the DMAEMA content within the polymer.

Table 3: Conclusion of the polymer DMAEMA-precursors synthesized and used in the GNR synthesis. Listed are the polymers as well as their respective degree of DMAEMA polymerization (DP_D), the theoretical number average molecular weight obtained via ^{1}H-NMR spectroscopy ($M_{n.th}$), and the number average molecular weight from SEC ($\bar{M}_n$), the dispersity (*Đ*), and the consecutive number (*CN*) of the polymer in the laboratory journal/data set.

Polymer	*PN*	DP_D	$M_{n.th}$ / kg/mol	$\bar{M}_n$ / kg/mol	*Đ*	Light source
$P(OEGMA)_{230}$-*r*-$P(BTPEMA)_6$	B01	-	72.0	50.0	1.4;1.4	Green
$P(O_{229}$-*g*-$(D_{38})_6)$-*b*-$P(D)_{38}$	GD01	34	109	85	2.2;1.7	Blue
$P(O_{229}$-*g*-$(D_{14})_6)$-*b*-$P(D)_{14}$	GD02	14	86.5	103	2.4;2.3	Blue
$P(O_{229}$-*r*-$B_6)$-*b*-$P(D)_{61}$	BCP01	61	82.0	67.2	1.6;1.6	Green
$P(DEGMA)_{244}$	B02	-	46.4	23.3	1.7;1.5	Green
$P(DEGMA)_{244}$-b-$P(D)_{65}$	BCP02	65	56.7	25.9	1.2;1.6	Green

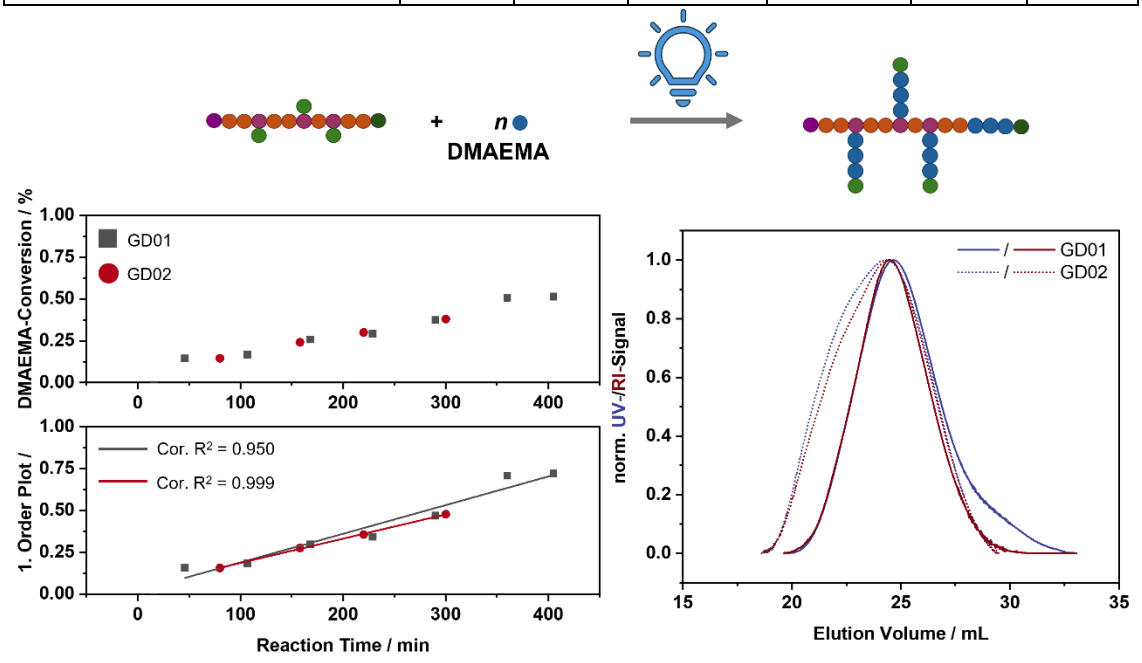


Figure 40. On the left-hand side, ^{1}H-NMR spectroscopy polymerization kinetic results from the DMAEMA polymerization using B01 as a multivalent macroRAFT agent (top scheme) under blue light irradiation are shown. The plot on the right-hand side shows the SECs of the polymers GD01 and GD02.

To obtain the targeted CTAB-equivalent polymer, all DMAEMA polymerization products (**Table 3**) were functionalized with BHD. The functionalization was conducted in DMF at 70 °C for four days. From the functionalization of GD01, a colorless precipitate was obtained (qGD01) after redissolving the product in DCM and precipitating it in *n*-hexane twice. The quantitative functionalization was tested with ^{1}H-NMR spectroscopy. The analytics for the functionalization of GD01 are shown in **Figure 41**.

The recorded ^{1}H-NMR spectra confirm that the dimethylamine function is attributed to the reaction. This can be stated due to two main factors. First and most evident is the disappearance of the methylene proton signal at 2.2 ppm, which is caused by the drastic change due to the cation formation of the nitrogen atom during the reaction. Secondly, in the ^{1}H-NMR spectrum, a sharp signal in the chemical shift region of alkyl functionalities is assigned to the CH_2-alkyl chain of BHD after functionalization. According to these results and the significant change in the solubility of the product, a quantitative conversion of the tertiary amine groups to the quaternary ammonia groups was assumed for the calculations of the proceeding work.

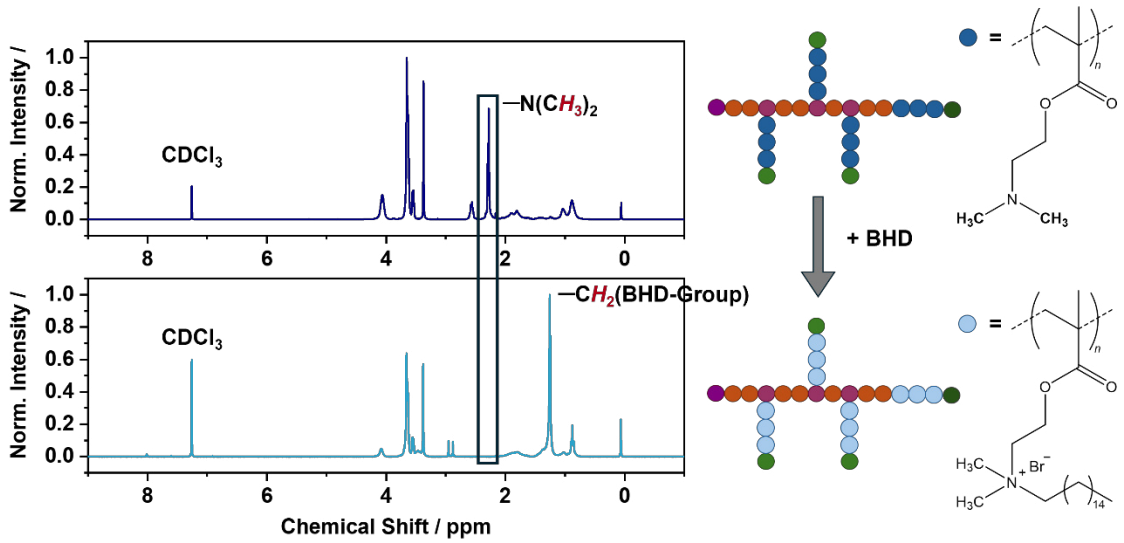


Figure 41. ^{1}H-NMR spectra of GD01 before (top) and after the functionalization (bottom) with BHD (qGD01) dissolved in chloroform-d_1, with the reaction scheme on the right-hand side. Both measurements were conducted on a Bruker FourierHD 300 MHz spectrometer. Both spectra were normalized by dividing by the maximum intensity.

5.3.1. *Grafted*-DMEAMA-based Polymers as the First Generation of Anisotropic-Growth Assisting Precursors

For the design of the polymer-assisted GNR synthesis protocol, a reliable CTAB-based protocol for the GNR synthesis had to be established in our laboratory as a benchmark reaction. After testing some exemplary protocols, a synthesis was chosen based on the protocol first described by B. Nikoobakht and El-Sayed, refined by L. Scarabelli and coworkers in 2015.[7,90] This silver-assisted seeded growth approach gave GNRs an average particle aspect ratio of 3.5 and a longitudinal absorbance peak of around 800 nm (**Figure 10** in Chapter 4.1.3.1). As schematically shown in **Figure 6** (in Chapter 4.1.2.2), this protocol includes a CTAB-based preparation of a seed solution, which was later added to the monomer solution to form the growth solution. To avoid confusion, the terminologies, seed solution, monomer solution, and growth solution defined in **Figure 6** are kept constant throughout this section. Commonly in literature, the terms monomer solution and growth solution are often not distinguished, because no value is added if done otherwise. However, since this work focuses on removing CTAB from the monomer solution, it becomes important to distinguish between the growth and the monomer solution. As described in Section 4.1.2.2, the quality of the seed solution can significantly affect the outcome of the anisotropic growth. Given their limited stability, the seeds had to be freshly prepared for the GNR synthesis. These circumstances are making the seed solution a crucial factor in this investigation. To maintain comparability between different batches and other polymer precursors, every polymer-assisted GNR synthesis was accompanied by a conventionally CTAB-based GNR synthesis. The comparability with other systems is one of the main reasons why the seed synthesis was kept CTAB-based.

While preparing the first CTAB-free, polymer-based monomer solution for the GNR synthesis, the limited water solubility of the BHD-functionalized becomes evident. In order to disperse as much polymer as possible in the monomer solution, the dispersion was treated for 30 minutes in the ultrasonic sound bath at room temperature. Additionally, the solution temperature was reduced by cooling with an ice bath to increase the solubility of the LSCT-responsive B01-based backbone. With the achieved colorless turbid suspension, the preparation of the monomer solution proceeded according to the refined procedure from L. Scarabelli and L. M. Liz-Marzan, as shown in **Figure 6** in Chapter 4.1.2.2.[7] Three different GNR syntheses using qGD01 were conducted in parallel using the same Au@CTAB seed solution. The particle growth for these three reactions was quenched after 30 min, 60 min, and 120 min to investigate potential effects of varying growth times. From the reaction solutions, a UV–vis absorbance spectrum was measured immediately after the particle purification due to several centrifugation cycles. **Figure 42** and **Table 4** conclude the results obtained by these investigations.

Table 4: Concluded results obtained by TEM image evaluation. Listed are the GNR batch number (BN), the corresponding ligand, the average particle width (*w*), length (*l*), aspect ratio (*AR*), the number of particles counted for the evaluation ($N_{Particles}$), and the reaction time after the addition of the seed solution (t_{gr}).

Particle BN	*Ligand*	*w* / nm	*l* / nm	*AR* /	$N_{particles}$ /	t_{gr} / min
NR1-CTAB	CTAB	10 ± 3	34 ± 6	3.4		30
NR1-30	qGD01	11 ± 2	18 ± 3	1.7	431	30
NR1-60	qGD01	10 ± 2	18 ± 3	1.8	605	60
NR1-120	qGD01	11 ± 2	18 ± 3	1.7	514	120

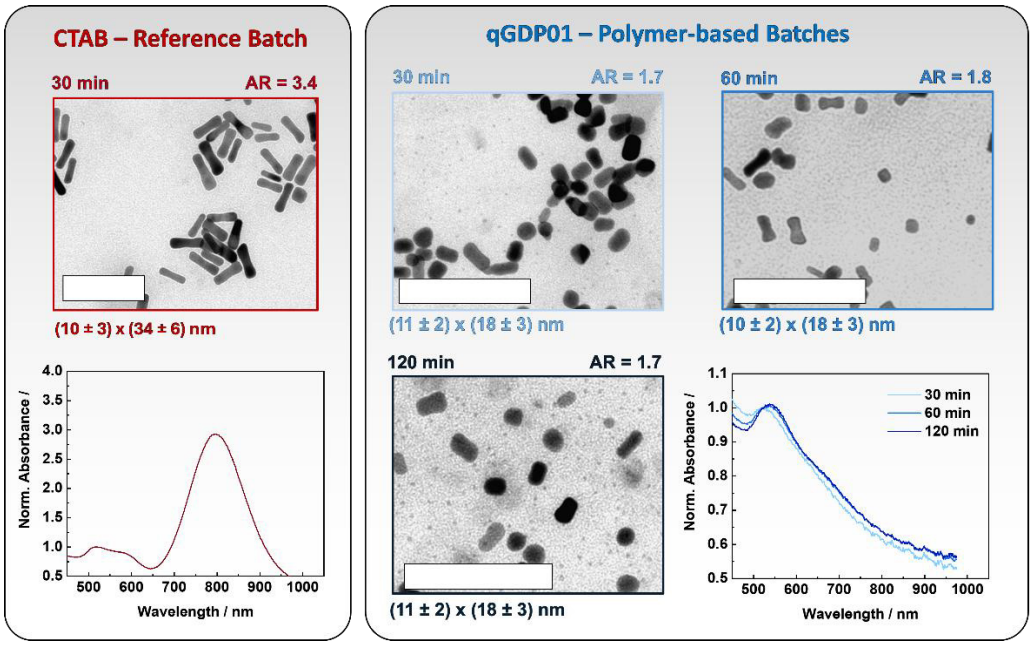


Figure 42. Results of the qGDP01-based GNRs synthesis batches with varying particle growth times compared with a CTAB reference batch using the same Au@CTAB seed solution. A TEM image from each GNR product is displayed with 100 nm scale bars. After purification, the UV–vis absorbance spectra were recorded from each GNR solution, and the absorbance was normalized to the transversal LSPR maximum. The data are taken with permission from the open-access source *Adv. Funct. Mater.* **2024**, 2400995, with adaptation.[8] Copyright 2024 The Authors. Advanced Functional Materials, published by Wiley-VCH GmbH.

The TEM measurement of the samples clearly shows that anisotropic growth was achieved during the reaction. To support the assumption that the obtained GNRs are stabilized by the polymer and not by residual CTAB, higher resolution (HR) TEM measurements coupled with an energy dispersive X-ray detector (EDX) were done with the 120 min GNR@qGD01 sample. The obtained images are shown in **Figure 43**. The EDX images show the presence of nitrogen and sulfur at the GNP surfaces. The presence of nitrogen at the particle surface was expected because it is present in CTAB and qGDP01, which provide the foundation for anisotropic growth. However, the presence of sulfur at the particle surface is an exciting result because it proves that the designed CTAB substitute qGDP01 contributes to the stabilization of the NP, since it is the only component in the reaction containing sulfur. These encouraging results lead to further investigation of this topic to address the rising challenges. The NR1 particle synthesis series is the second one conducted with qGDP01.

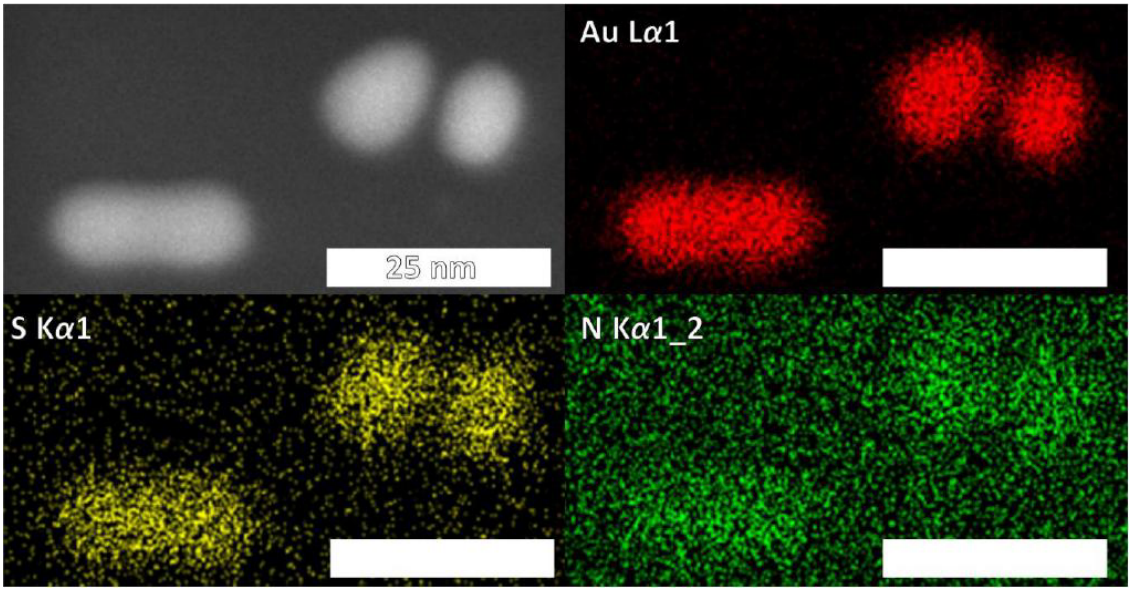


Figure 43. HR-TEM coupled EDX measurement results for GNR@qGDP01 with a growth time of 120 min after purification. The top left image shows the investigated particle. The other pictures show the identical particles studied for gold (red), sulfur (yellow), and nitrogen (green). The scale bars are 25 nm. The images shown are taken with permission from the open-access source *Adv. Funct. Mater*. **2024**, 2400995, without adaptation.[8] Copyright 2024 The Authors. Advanced Functional Materials, published by Wiley-VCH GmbH.

The results show that increasing the reaction time does not increase the average particle aspect ratio or particle size above the statistical variation between different batches. This means that the longitudinal particle growth is most likely quenched in the earlier stages of the reaction. Compared with CTAB-based protocols, the average particle aspect ratio in polymer-based GNR synthesis is significantly lower. The CTAB-based control reaction showed an aspect ratio of 3.4. The qGD01-assisted synthesis yielded an aspect ratio between 1.7 and 1.8 when performed under the same conditions.

A deeper understanding of the polymer's role during anisotropic growth is necessary to adjust the reaction parameters more effectively and achieve higher average particle aspect ratios. Therefore, the most urgent issue for the optimization of the polymer-assisted GNR synthesis was to increase the solubility of the qDMAEMA copolymer surfactant to reach higher concentrations of CTAB-equivalent functional groups that are closer to the regular CTAB concentration (0.1 mol/L). The suspension formed by qGDP01 in water favors the formation of local amine concentration (c_{amine}) peaks, especially in the vicinity of dispersed polymer particles. Different particle growth mechanisms are likely favored at these concentration peaks compared to regions with a lower local c_{amine}. Another practical benefit of a soluble polymer surfactant is that the GNR purification is simplified. Since the purification of GNRs is usually done by consecutive centrifugation cycles, the GNRs are precipitated, and the supernatant, filled with excess surfactant molecules, is removed. If the surfactant is insoluble in water, this method does not apply, and impurities attached to these molecules remain within the particle mixtures and can later be found in the product fraction (e.g., see TEM image in **Figure 42** for the 120-minute sample). To avoid these particle contaminations, the particles must first be transferred into another medium in which

qGD01 is soluble, such as chloroform. This, however, strongly contradicts the goal of reducing the toxicity of the GNR synthesis and is therefore not applicable.

There are several ways to approach this optimization. Most of these principles have in common that they reduce the hydrophobic segment content of the polymer. Substituting BHD with alkyl bromides with shorter alkyl chains during the post-polymerization functionalization would positively impact the polymers' hydrophilicity. For the following reasons, this approach was not pursued in this work. First, BHD shows low toxicity, which blends in well with the other polymer components, P(OEGMA), P(DEGMA), and P(DMAEMA), which are also known for their biocompatibility.[230,273,274] Short-chained alkyl bromides, in particular, can become more problematic in terms of their inherent toxicity. Changing from BHD to another alkyl bromide would also change the polymer's anisotropic growth-directing amine group, which reduces the comparability with CTAB. This change was considered dramatic in the early stages of the project. Due to this and other practical considerations, such as the availability of 1-bromalkanes, it was decided first to decrease the DP_D of the polymer precursor to reduce the resulting hydrophobic content in the final polymer, as was done for GDP02 (see **Table 3**). According to the ^{1}H-NMR kinetic results for the polymerization of GDP02, the weight content of qDMAEMA in qGDP02 is reduced to 37 %(*w*/*w*) from 60 %(*w*/*w*) for qGDP01.

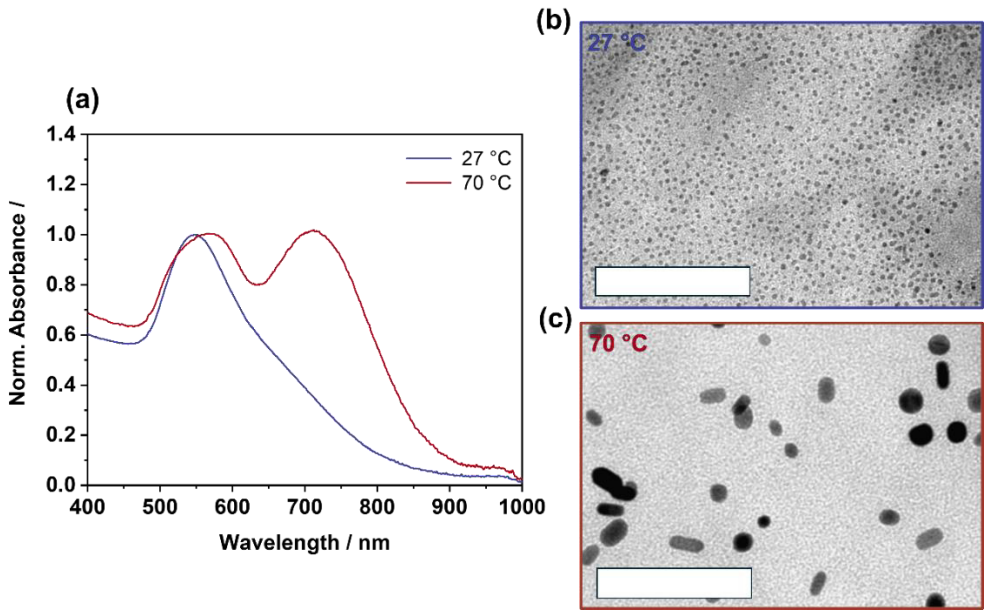


Figure 44. Analytical results of the GNP@qGDP02 synthesis at different growth solution temperatures. In graphic (a), the normalized UV–vis absorbance spectra of the product solutions for the particles synthesized at 27 °C (blue curve) and 70 °C (red curve) are plotted. The TEM images (b) and (c) present the particles obtained by each reaction. The TEM image (b) shows the particle product synthesized at 27 °C, and (c) shows the particle obtained at a growth solution temperature of 70 °C. The scale bars shown in (b) and (c) are 100 nm.

Following the standard CTAB procedure, the first reaction using qGDP02 was performed at 27 °C. The UV–Vis absorbance spectrum measured from the reaction showed no formation of a longitudinal LSPR signal, implying that no anisotropic growth had happened under the chosen reaction conditions. This implication was later supported by TEM (**Figure 44** (b)) for the respective product fraction. This reaction was also the initial reason why not every reaction was investigated via TEM, if there was no sign of a longitudinal LSPR signal formation.

In silver-assisted, seeded-growth CTAB protocols, the CTAB *cmc* is critical for GNR synthesis. Around this concentration, the formation of the CTAB bilayer can be assured, which is essential for GNR stabilization. The formation of a bilayer is the only way to stabilize particles and the hydrophobic tail of CTAB simultaneously. The formation of free CTAB micelles also leaves the quaternary ammonia function accessible at the micelles' surface. Due to the hydrophilic character of the P(OEGMA) backbone below its PTT, the qDMAEMA functionalities are likely to be partially concealed by the backbone EG units. This could explain the missing anisotropic growth during the reaction at 27 °C. A second batch of reactions with qGDP02 was performed to test this hypothesis. In this batch, two reactions are conducted simultaneously, one at 27 °C and a second above the backbone's LCST at 70 °C.

The difference between the 27 °C reaction and the 70 °C reaction results from the first qGD02 batch, shown in **Figure 44**, is impressive. The UV–Vis extinction spectrum exhibited clear transverse and longitudinal LSPR band formation. TEM images taken from the 70 °C product (**Figure 44** (c)) fraction showed the formation of GNRs with an average width of (9 ± 2) nm and length of (15 ± 3) nm (at 342 evaluated particles (AR = 1.8 ± 0.4)). In contrast to the first reaction performed at 27 °C, the 27 °C reaction from the second batch shows a significant shoulder formation in the UV–vis absorbance spectra at higher wavelengths, indicating the formation of GNR. Unfortunately, this batch was not investigated further because this shoulder was discovered after the product solution had been deposited. However, this mistake was later compensated for by performing the same test with the next generation of polymer surfactants, as discussed in the following paragraph (5.3.2).

5.3.2. Block copolymer-based DMEAMA-based Polymers: The Second Generation of Anisotropic-Growth Assisting Precursors.

The reason for using a copolymer precursor with BTPEMA copolymerized in the thermoresponsive backbone was, besides the higher affinity to gold surfaces, the probability of forming a polymer gel material, as described by J. Xu and V. Abetz.[1,9] However, with the limited control over DMAEMA-grafting polymerization and the hydrophobic character of the qDMAEMA-units, the formation of a hydrogel shifted out of this topic's focus. One reason for this shift was the unpredictable DMAEMA grafting when using blue light for the polymerization. The variation caused by the radical mismatch of the RAFT polymerization increased the uncertainty of the influence of factors like molecular weight distribution and the exact polymer morphology on the GNR product quality. The synthesis of BCP01 (**Table 3**) was pursued to reduce the uncertainty of these factors. Using the 513 nm light source to initiate the DMAEMA polymerization with B01 as the macroRAFT agent, the polymer product's weight distribution (Đ=1.6) significantly decreased for BCP01 compared to qGDP01 and qGDP02. With a correlated R^2=0.999 for the first-order plot of the monomer conversion, the reaction control was also significantly improved (Figure A4).

Additionally, the reduced complexity from a brush-like structure to a diblock copolymer (DBP) structure further simplifies the synthesis route, which can become an important factor when it comes to future upscaling of the procedure, which can reduce the synthesis costs. BCP01 was functionalized with BHD by heating to 70 °C in DMF for two hours. The product was precipitated three times in *n*-hexane and once in diethyl ether.

With qBCP01, an amine concentration (c_{amine}) of up to 0.01 mol·L^{-1} was achieved without requiring ultrasonic treatment or storing the solution for multiple days in the fridge. Therefore, using qBCP01 improved the reproducibility of the polymer-assisted GNR synthesis. The temperature dependence of the GNR synthesis was tested for qBCP01 as well. It was found that this dependency also applies to the BCP polymer. When operating the synthesis above the backbones' LCST, significantly increased particle aspect ratios are observed. In contrast to the reaction with qGDP02, the synthesis using qBCP01, conducted below the LCST at 30 °C, also provided GNRs. The results (**Figure 45**) show that for the GNR synthesis, qBCP01 behaves similarly to qGDP02.

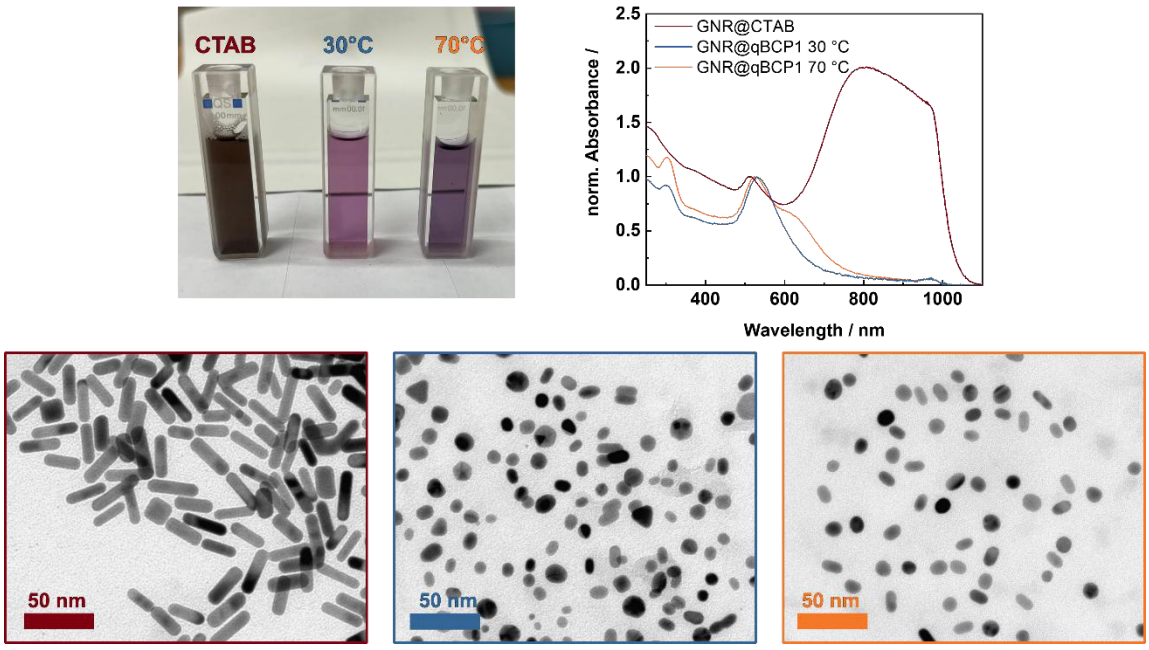


Figure 45. Photograph (top left) of the GNR particle solutions after purification and analytical result from the NR4 particle batch with the results from the qBCP01-based reaction at 30 °C (blue), the qBCP01-based reaction at 70 °C (orange), and the CTAB-based reaction at 30 °C using the same Au@seed solution as for the first two reactions (red). The graphic at the top right shows the normalized UV–vis absorbance spectra of the GNR suspensions of the three reactions. The TEM images show the particles after purification. The UV–Vis spectra data and the TEM images of the two polymer-based reactions were taken with permission from the open-access source *Adv. Funct. Mater.* **2024**, 2400995, with optical adaptations. Copyright 2024 The Authors. Advanced Functional Materials, published by Wiley-VCH GmbH.[8]

Important information can be taken from these results. First, the initial bottle-brushed polymer structure is unnecessary to support anisotropic GNR growth. Both reactions, below and above the LCST of the backbone, produced GNRs. The GNPs obtained from the reaction at 30 °C show an increased variety of particle morphologies besides the NR morphology. The average particle width of the GNRs was determined to be (9 ± 2) nm. The particle length amounts to (13 ± 3) nm, and the average aspect ratio was 1.4 ± 0.3. For the evaluation, 698 particles were measured manually from the TEM images. From the 70 °C reaction, GNRs with an average width of (9 ± 1) nm and a length of (14 ± 2) nm were obtained. The average aspect ratio of 1.7 ± 0.4 was obtained. 600 particles were measured from TEM images for this evaluation. The CTAB-based GNR synthesis delivered GNRs with an average aspect ratio of 3.0 ± 0.7, an average particle length of (26 ± 5) nm, and an average particle width of (9 ± 1) nm.[8] Without additional information, the difference in aspect ratio between the products at different reaction temperatures is insignificant. However, in combination with a shoulder in the normalized absorbance spectrum at higher wavelengths for the 70 °C product, the differing aspect ratio can be considered significant. This difference, along with the lower amount of particle-side products observed in the 70 °C sample during TEM, pointed toward an LCST-dependent effect on the reaction's selectivity.

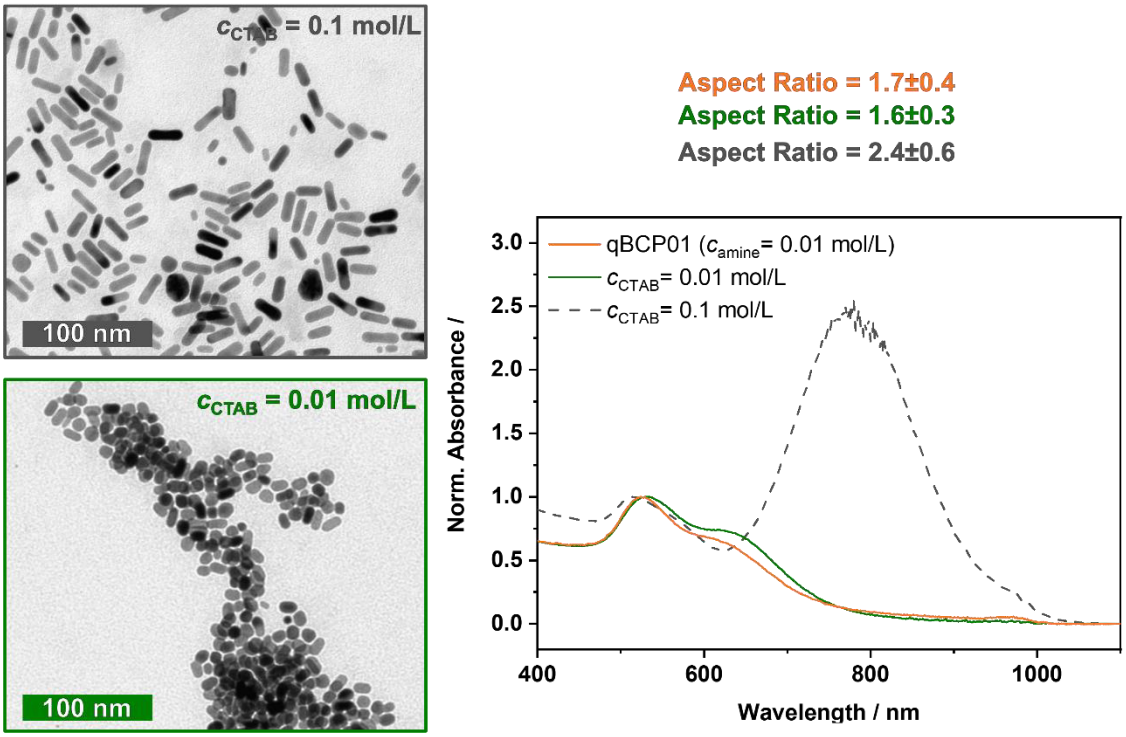


Figure 46. Results of reduced CTAB concentrations' influence on the GNR particles compared with the qBCP01-based GNR synthesized at 70 °C. The TEM images show the sample synthesized with the regular CTAB concentration of 0.1 mol/L (grey-framed image) and the reduced CTAB concentration of 0.01 mol/L (green-framed image). The same color code was used for the UV–Vis extinction spectra shown in the graphic on the right-hand side. For comparison, the extinction spectrum of the GNRs synthesized with qBCP01 (orange line) was added to the graphic. The UV–vis spectra data and the TEM images of the two polymer-based reactions were taken with permission from the SI of the open-access article *Adv. Funct. Mater*. **2024**, 2400995, with optical adaptations. Copyright 2024 The Authors. Advanced Functional Materials, published by Wiley-VCH GmbH.[8]

Using qBCP01, an amine concentration of 0.01 mol·L^{-1} was established for the polymer-based GNR synthesis. To gain insight into how the c_{amine} affects the particle quality, two GNR samples were prepared to compare the standard CTAB concentration (c_{amine}=c_{CTAB}=0.1 mol·L^{-1}) with a reduced CTAB concentration equal to the established concentration (c_{amine}=0.01 mol·L^{-1}) used with qBCP01. The results presented in **Figure 46** impressively demonstrate the high potential of the designed polymer for use in GNR synthesis. In fact, when operating the reaction at a comparable amine concentration, qBCP01 shows an anisotropic growth-directing potential that is nearly equal to that of CTAB. The obtained particles synthesized with the reduced amount of CTAB show a comparable average aspect ratio with the respective qBCP01-based GNRs, and their absorbance behavior in the UV–Vis extinction spectroscopy is also very similar (see **Figure 46**, orange and green curves). With a transversal maximum at 534 nm and the shoulder formation for the longitudinal LSPR signal with an estimated maximum of around 630 nm, the CTAB-based GNR compares well with the 70 °C qBCP01-based GNR with a transversal maximum at 524 nm and a similar shoulder formation for the longitudinal LSPR at 620 nm. This test proves that qBCP01 has comparable potential for directing anisotropic growth like CTAB when used at equal amine concentrations.

Based on these findings, two urgent optimization tasks emerged: improving polymers' solubility and adjusting their LCST. Because many subsequent processes during the GNR formation are temperature-dependent, such as the formation and stability of intermediate metal complexes (see Section 4.1.2), the adjustment of the LCST is a significant milestone of the polymer-directed anisotropic growth, especially when it comes to a closer comparison with CTAB-based protocols. Using the same polymerization setup as for B01, two other LCST polymers with lower LCSTs were polymerized. Therefore, diethylene glycol methacrylate (DEGMA) was used as a monomer for the polymerization. DEGMA is known to form polymers with an LCST around 20 °C, which is well below the operation temperature for the standard CTAB-GNR synthesis. This should allow polymer-based GNR synthesis to be conducted above the transition temperature of the hydrophilic block while operating at temperatures comparable to those used in standard CTAB protocols. First, DEGMA was copolymerized with BTPEMA. The results of the kinetic investigation of that polymerization are presented in Figure A2 in the appendix. In principle, the polymerization showed well-controlled characteristics. The molecular weight distribution ($Đ$=1.6) of the final P((DEGMA)-*r*-(BTPEMA)) product supports this statement.

However, this polymer was not used in the subsequent reaction steps towards GNR synthesis for the following reasons. First, due to resolution issues with the respective signals in the ^{1}H-NMR spectra of the kinetic investigation, a homogeneous, statistical distribution of BTPEMA units along the polymer chain could not be confirmed. Secondly, BTPEMA combined with DEGMA in one polymer caused a very low T_{cp} of the polymer product (~17 °C). This T_{cp} was too low for the requirements of the GNR synthesis (the reaction temperature is 27 – 30 °C). Due to these reasons, it was decided to polymerize DEGMA into a homopolymer. This also significantly simplifies the obtained polymer system and is a potential factor for the cost reduction of the polymerization and the synthesis route.

The polymerization kinetics for the DEGMA homopolymerization are shown in the appendix in Figure A3. Combined with the results of the DEGMA/BTPEMA copolymerization, the 250 mL polymerization setup is shown to be a suitable tool for the photoRAFT polymerization of different methacrylate esters, delivering reliable results at higher scales. From the perspective of polymer science, this is promising progress for the field of photoinitiated RAFT polymerization. The photoRAFT polymerization of DEGMA provided a P(DEGMA) homopolymer (B02) with a transition temperature of T_{cp} = 22 °C to 23 °C, a molecular weight distribution of $Đ$ = 1.5, and a degree of polymerization of DEGMA of DP_{DEG} = 244. In the second step, B02 was used as a macroRAFT agent to synthesize the diblock copolymer P(DEGMA)$_{244}$-*b*-P(DMAEMA)$_{65}$ (BCP02). At T_{cp} = 25 °C, the transition temperature is 2 °C higher than the T_{cp} for B02, which is plausible given the presence of the DMAEMA block in the chain.

According to the previous quaternization reactions, BCP02 was functionalized using BHD. The qBCP02 product was characterized and compared using IR spectroscopy (**Figure A5**) in addition to the ^{1}H-NMR investigation. With the scaled polymerization of B02 and the subsequent polymerization of the diblock copolymer BCP02, enough substance was provided to conduct several GNR syntheses and test different parameter influences on the anisotropic growth. Since the LCST is lower than the temperature of the growth solution, the influence of the polymer conformation is taken out of the equation. However, to support the theory of higher accessibility of the quaternary amine group when the polymer solution's temperature increases above the LCST, the polymer solutions' zeta potential was measured at different temperatures. The results and the corresponding model are shown in **Figure 47**.

The plot of the ζ-potential clearly shows a temperature dependence. The data show that for qBCP02 solutions with a quaternary amine concentration of 5.0 mmol·L^{-1} and 10 mmol·L^{-1}, the zeta potential increases significantly at a solution temperature of 25 °C. This increase continues until a constant value is reached around 35 °C. The onset of this increase is coherent with the polymer's transition temperature, determined by UV–Vis spectroscopy. The temperature-dependent transmittance measurements in Figure 48 show that the T_{cp} is reproducible around 25 °C and highly reversible among several heat/cool cycles. Temperature-dependent DLS experiments of qBCP02 solutions (**Figure A8**) have shown that increasing the temperature above the T_{cp} causes the formation of polymer clusters with a R_H of 400 nm. Heating the suspension further decreases the observed cluster size. As expected, the formation of polymer clusters was reversible after cooling the polymer solution below 25 °C. Interestingly, after every measured temperature cycle, the onset temperature of cluster formation significantly shifted to lower temperatures, and the maximum R_H formed in these temperature cycles did not exceed 200 nm. Meanwhile, the temperature-dependent UV–Vis turbidity showed no changes within the temperature-responsive behavior. This behavior is probably explained by the hydrolysis of the di(ethylene glycol) group from the backbone.

Additionally, the cluster formed in the following cycles showed a constant R_H at 200 nm even as the solution temperature continued to increase. Due to this time-dependent adjustment of the R_H, it is advisable to keep the polymer solution above the T_{cp} for some time to allow the polymer chains to reach an equilibrium morphology with a high positive surface charge for optimal reproducibility. The positioning of qBCP02's T_{cp} allowed for the straightforward preparation of polymer solutions with well-defined polymer concentrations. The lower T_{cp} of qBCP02 DEGMA-block enables the GNR preparation above the polymers T_{cp}, which has proven itself to be more efficient and made it possible to conduct the GNR synthesis in temperature regions closer to the original CTAB-procedures (27 °C–30 °C), simultaneously taking advantage of the higher accessibility of the quaternary amine groups (**Figure 47**, left graphic).

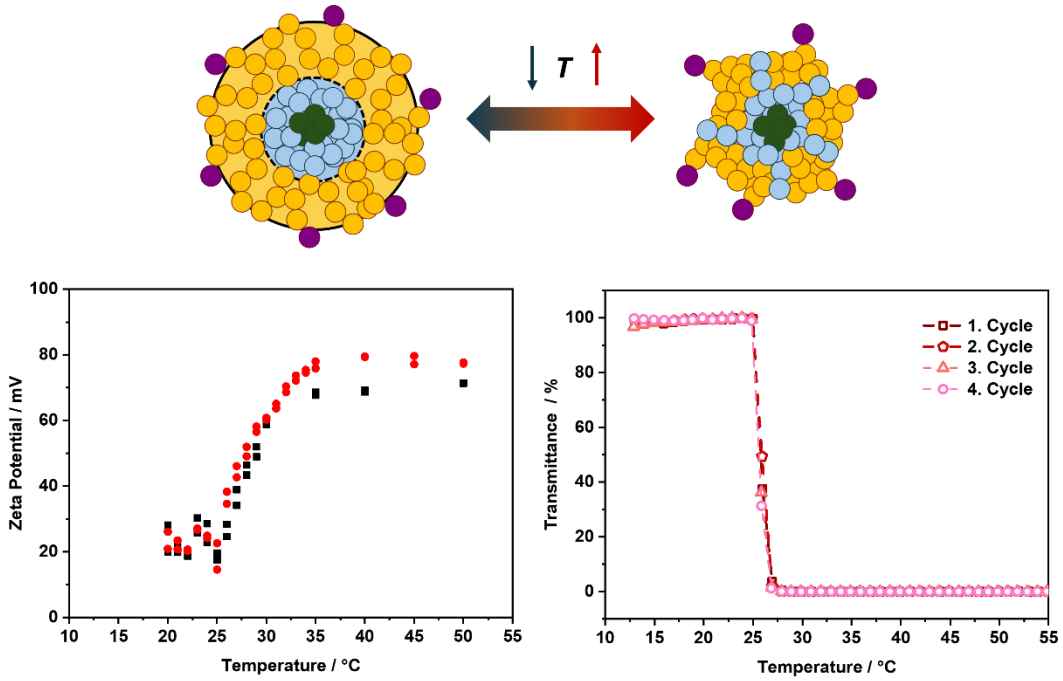


Figure 47. The scheme on the top represents the assumed morphology change of the qBCP2 and related polymers like qBCP01 and qGDP02 below (left) and above (right) the polymers T_{cp}. In the bottom left graphic, the ζ-potential is plotted as a function of the temperature for different quaternary amine concentrations, namely 5.0 mmol·L^{-1} (black squares) and 10 mmol·L^{-1} (red circles). On the right is the temperature-dependent transmission of a 0.1 %(w/w) solution of qBCP2 at repeating temperature cycles. The data are taken with permission from the open-access source *Adv. Funct. Mater*. **2024**, 2400995, with optical adaptations. Copyright 2024 The Authors. Advanced Functional Materials, published by Wiley-VCH GmbH.[8]

One final adjustment was made before setting up the qBCP02-based GNR syntheses for further investigations. The amount of silver ions in the monomer solution was doubled from 5.0 mM to 10 mM to increase the particle aspect ratio. In the conventional CTAB-based protocols, this increased silver concentration benefits the formation of the anisotropic growth-directing silver complex $[AgBr(CTA)]^+$, causing a higher particle aspect ratio due to more efficient facet blocking, noticeable by a red-shifted longitudinal LSPR (see **Figure 10** in Section 4.1.3).

With that minor adjustment, the synthesis of GNR@qBCP02 hybrids was tested. The monomer solution was synthesized using different amine concentrations to find the optimal reaction conditions. In the first trial, monomer solutions with a c_{amine} of 0.01 mM and 0.02 mM were prepared. After preparing the growth solution, samples were taken at 30 minutes, 60 minutes, and 130 minutes. Using a water bath, the growth solution temperature was kept constant at 27 °C during the reaction. No influence of different growth times was observed in the absorbance spectra and the TEM image evaluation (Figure A6 and **Table A3**). **Figure 48** shows exemplary TEM images of the two batches after 30 min of growth and the extinction spectra of the respective GNR products after purification.

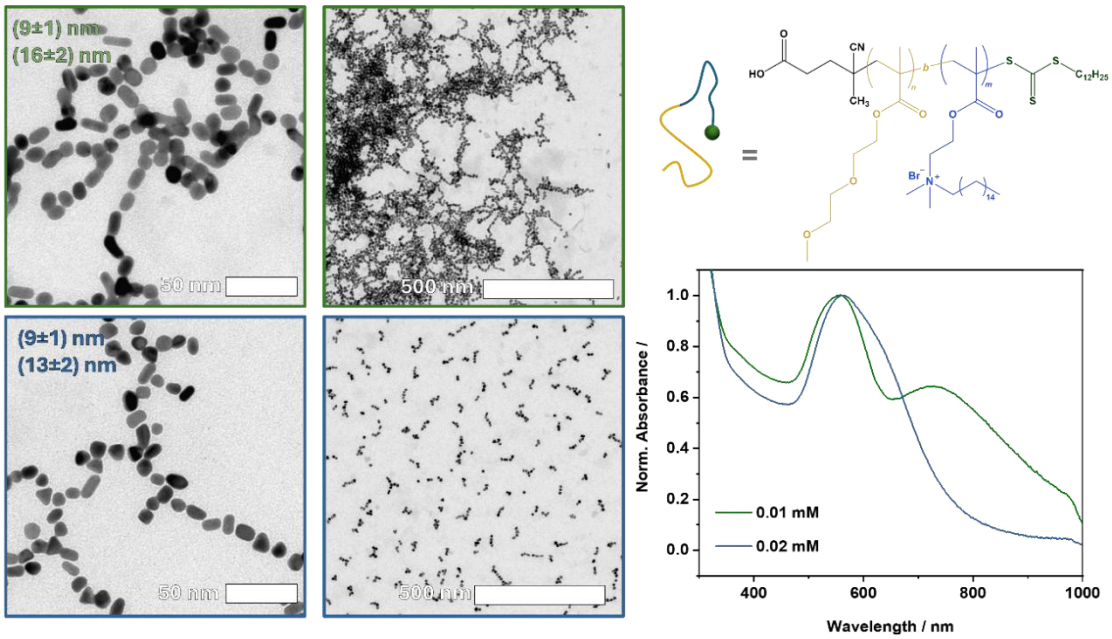


Figure 48. TEM images of the purified GNR@qBCP02 product obtained by the synthesis with c_{amine} = 0.01mM (green frame) and c_{amine} = 0.02 mM (blue frame) for the preparation of the monomer solution after a particle growth time of 30 minutes. The graphic on the bottom right shows the normalized absorbance of the diluted reaction solutions after purification. The data are taken with permission from the open-access source *Adv. Funct. Mater*. **2024**, 2400995, with minor optical adaptations. Copyright 2024 The Authors. Advanced Functional Materials, published by Wiley-VCH GmbH.[8]

As evident from the absorbance behavior of the GNR@qBCP02 solution with a higher c_{amine}, increasing the polymer concentration does not necessarily increase the facet-selective growth of GNRs. When comparing both amine concentrations, the GNR suspension with the lower c_{amine} (0.01 mM) shows two distinctive maxima in the absorbance spectra. The evaluation of TEM images gave the particle dimensions. For the evaluation of the c_{amine} = 0.01 mM suspension, 876 particles were measured manually. To obtain the particle dimensions of the c_{amine} = 0.02 mM product, 817 particles were measured manually. For both samples, the GNRs show an average particle width of 9 ± 1 nm. Interestingly, the particle length obtained from the lower-concentration reaction was 16 ± 3 nm. The GNRs obtained from the monomer solution with the higher polymer concentration showed a lower average particle length of 13 ± 2 nm. The average aspect ratios are 1.9 ± 0.5 and 1.5 ± 0.3 for the lower and the higher polymer concentrations, respectively. Combined with the obtained absorbance spectra, shown in **Figure 48** at the bottom right, size differences can be interpreted as significant effects.

Intuitively, a higher c_{amine} should cause a higher synthesis selectivity, which contradicts the just-described results. However, these results were not entirely unexpected, given observations made during particle synthesis. For 10 mL of a polymer solution with a c_{amine} = 0.01 mM, a solution with a mass concentration of qBCP02 of 11.7 %(*w*/*w*) had to be prepared. Obviously, the amount of qBCP02 is doubled for c_{amine} = 0.02 mM. The high polymer weight content significantly increased the solution's viscosity. This increased viscosity complicated the preparation of a homogeneous distribution of all compounds. While preparing the monomer solution, the increased viscosity was

a manageable challenge because the time to dissolve the single compounds is still adjustable if needed. Adding the seed solution is the most critical step in the GNR synthesis. With increasing viscosity, dispersing the seeds evenly within the reaction volume becomes challenging. In the literature, it is repeatedly pointed out that a quick injection and dispersion of seeds in the solution are essential for the success of the reaction.[7] In the conventional CTAB-based process, after seed injection, the solution is vigorously mixed for a short period and then stored without mixing to avoid disturbing the particles' anisotropic growth. Within this short mixing period, the seed must be dispersed homogenously in the suspension to avoid agglomeration and other side processes that reduce the reaction's shape selectivity. In the case of the higher polymer concentration-based GNR synthesis, the higher viscosity caused the formation of seed streaks and macroscopic clusters of brownish color, indicating an insufficient seed distribution throughout the solution. Keeping that in mind, it is not surprising that the GNRs that are obtained from the reaction are significantly shorter because the Au(I) monomer species is not only consumed by the well-submerged seeds. An undefined amount of the Au(I) monomer species is consumed within these macroscopic clusters of particles, which are removed during the sample purification. This leaves fewer monomer species for the growth of the well-dispersed seeds in the growth solution, which ultimately produces smaller particles.

One interesting phenomenon observed during TEM measurements in both batches, and more pronounced in the GNR synthesized with the higher qBCP02 concentration, is particle assembly on the TEM grid. Using qBCP02 as the stabilizer, the particles form a chain-like assembly with end-to-end orientation. This observed assembly is another feature that supports the facet-selective polymer–particle surface connection assumption. Overall, both samples showed well-stabilized behavior with nearly no formation of huge particle clusters in the TEM samples. Superficially, the number of particles in the observed particle assimilations also decreases with increasing polymer concentration at equally prepared TEM samples (**Figure A7**).

Since the higher polymer concentration negatively impacted the obtained aspect ratio, the question arose as to what effect a lower polymer/amine concentration would have on the synthesis results. Using c_{amine} = 0.005 mM monomer solution with qBCP02, another GNR synthesis was conducted (**Figure 49**). This test indicates that using qBCP02 as an anisotropic growth-driving agent, a polymer concentration around 10 %(*w*/*w*) (c_{amine} = 0.01 mM), yields the most efficient GNR growth, since the lower-concentrated reaction solution does not provide the same particle quality as the other two reactions do. The average particle dimensions provided by this reaction (for 620 evaluated particles) are 16 ± 3 nm for the particle length and 13 ± 3 nm for the particle width. The obtained average aspect ratio accounts for 1.3 ± 0.3, which shows that the obtained particle anisotropy is very limited.

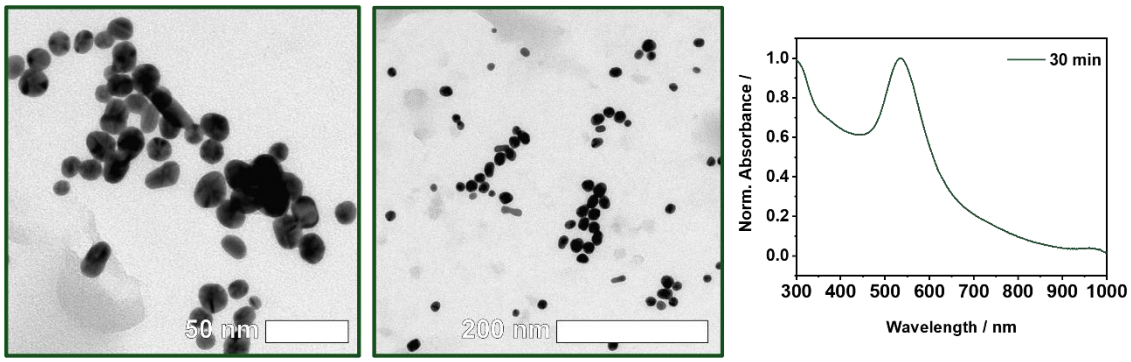


Figure 49. TEM images of the purified GNR@qBCP02 product obtained by the synthesis with c_{amine} = 0.005 mM for the preparation of the monomer solution after a particle growth time of 30 minutes. The figure shows two TEM images at different scales (left and mid) and the obtained normalized UV–Vis absorbance spectrum of the diluted reaction solutions after a 30-minute growth time. The data are taken with permission from the open-access source *Adv. Funct. Mater.* **2024**, 2400995, with minor optical adaptations. Copyright 2024 The Authors. Advanced Functional Materials, published by Wiley-VCH GmbH.[8]

In conclusion, especially the reaction conducted with an amine concentration of 0.01 mol·L^{-1} proves that the decreased T_{cp} of qBCP02 temperature-responsive backbone simplifies the synthesis protocol by providing comparable anisotropic growth control like for the particle synthesis using qBCP01 at 70 °C. Nevertheless, investigating the result from the temperature dependency of the ζ-potential of the qBCP02 solution in water shows that the reaction temperature (27 °C) chosen for the synthesis is not the temperature at which qBCP02 shows its maximum surface charge.

Therefore, a last adjustment of the GNR synthesis was made by setting the reaction temperature to 45 °C. Additionally, a polymer concentration of 12 %(*w*/*w*) (equivalent to c_{amine} = 0.01 mM) was used to prepare the monomer solution, as enhanced reaction control was observed at a similar qBCP02 concentration. A glance over the diluted reaction solution's UV–Vis absorbance spectrum (before the particle purification via consecutive centrifugation steps) indicated a promising result. The evolution of the TEM measurements confirmed this prediction. After the manual evaluation of 800 particles, the average particle dimensions obtained from the growth solution were 8 ± 1 nm for the average GNR width and 15 ± 4 nm for the particle length. The obtained average aspect ratio was 1.9 ± 0.7. After purifying the sample by two centrifugation cycles for 30 minutes at 10,000xG and 10 °C to keep qBCP02 in its soluble state, the GNRs collected from the precipitate showed an average aspect ratio of 2.2 ± 0.8. The average particle length and width were 17 ± 4 nm and 8 ± 2 nm, respectively. For this evaluation, 740 particles were measured manually. **Figure 50** summarizes the results of the optimized qBCP02-based GNR synthesis.

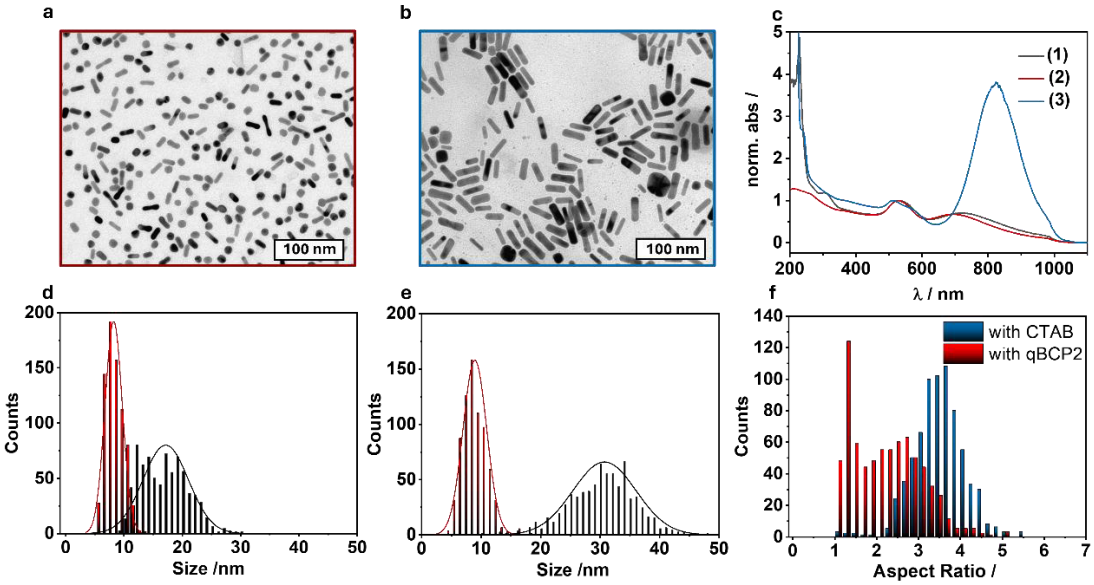


Figure 50. This figure concludes the results of the optimized qBCP02-based GNR synthesis with a growth solution temperature at 45 °C and the CTAB reference reaction (at 30 °C). In (a), an exemplary TEM image of the GRN@qBCP02 polymer hybrid product is shown. The GNR@CTAB particles are shown in the TEM image (b). In (c), the UV–Vis spectra of the samples are shown with (1) and (2) representing the spectra of the GNR@qBCP02 before and after purification, respectively, and (3) as the purified GNR@CTAB particles. The size distribution histograms obtained by manual TEM evaluation of the qBCP02- and CTAB-based samples are shown in (d) and (e), respectively, with the particle widths (red) and particle lengths (black). The distribution of aspect ratios is shown in the graphic (f). This figure is taken with permission from the open-access source *Adv. Funct. Mater.* **2024**, 2400995, without adaptation. Copyright 2024 The Authors. Advanced Functional Materials, published by Wiley-VCH GmbH.[8]

The adjusted reaction conditions delivered a well-controlled anisotropic growth of GNRs. Combined with the adjusted purification protocol, which complies with the lower LCST of qBCP02 and the hybrid, the GNRs are well separated from unreacted Au seeds. The efficient removal of seeds from the product particles is a crucial improvement compared to the grafted-polymer structures in section 5.3.1. It is safe to say that the results so far have proven the capability of the functionalized P(DMAEMA) block incorporated into a copolymer to support the growth of anisotropic rod-shaped particles. Of course, there is still room for improvement in the synthesis by redesigning the polymer structure to address the viscosity-based limited amine concentration or by further adjusting the reaction conditions.

Before the results were published, some open investigations had to be covered first. To this point of the investigation, the work was conducted on the premises that the used single compounds P(DEMGA)/P(OEGMA)[273], and P(DMAEMA)[230,274] are biocompatible, and therefore, the expected toxicity of the copolymer structure was lower than the toxicity of CTAB. However, to demonstrate that the designed copolymers meet those expectations, even after functionalization with BHD, cell viability tests were performed with BHD-functionalized and unfunctionalized polymers (see **Figure 51**). Therefore, different cell cultures were exposed to a cell medium with varying polymer concentrations. Thus, the following discussion will focus more on the polymer part of these tests. The precise test protocol is referred to in Reference [8].

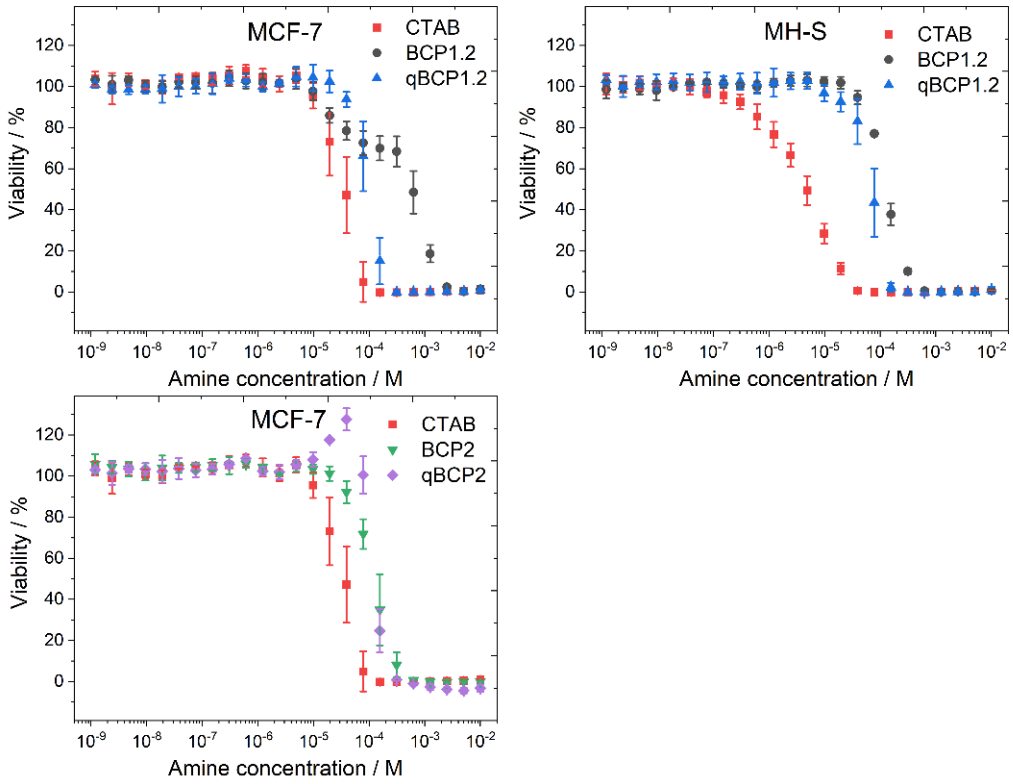


Figure 51. Cell culture viability test results reviewing the toxicity of the designed diblock copolymers BCP1.2 and qBCP1.2 in the top two graphs for the cell cultures MCF-7 (left) and MH-S (right), and for BCP02 and qBCP02 at the bottom graphic using the cell culture MCF-7. Plotted is the cell viability against the concentration of amine groups within the polymer/cell medium solution. The data are taken with permission from the open-access source *Adv. Funct. Mater*. **2024**, 2400995. Copyright 2024 The Authors. Advanced Functional Materials, published by Wiley-VCH GmbH.[8]

The block copolymers tested for their toxicity were qBCP1.2 and qBCP02. The reason why qBCP1.2 was tested is that BCP01 and qBCP01 were depleted during the particle synthesis tests and other analytical measurements. Therefore, BCP1.2 was synthesized according to the conditions of BCP01 and functionalized with BHD to obtain qBCP1.2 for toxicity evaluation. For the toxicity tests of qBCP1.2, the cell cultures of the murine alveolar macrophage cell line (MH-S) and the breast cancer cell line MCF-7 were used. The cell viability was tested at different concentrations. Parallel to the viability tests of qBCP1.2 and BCP1.2, CTAB was also tested for better comparison. For qBCP02 and BCP02, the viability tests were only conducted with the MCF-7 cell line culture. The reason for this was the low solubility of qBCP02 at the test conditions (T = 37 °C), which had already shown problematic behavior during the tests using the MCF-7 cell line (discussed below). Due to the solubility issues of qGDP01 and qGDP02, they were not considered for the toxicity tests.

The graphics in **Figure 51** show the viability plotted against c_{amine} to achieve comparability between the CTAB and the polymer substitutes. A logarithmic scale is applied to the amine concentration. All plots account for the fact that, compared to CTAB, the decline in cell viability starts at higher magnitudes of amine concentrations for the investigated unfunctionalized

polymers. This result proves that the polymer basis already shows higher biocompatibility than CTAB.

The difference between the cell-dying onset concentrations for BCP1.2 and CTAB for the MS-H cell line is even more pronounced, with a concentration that is several orders of magnitude higher for BCP1.2. With the MS-H line, qBCP1.2 and BCP1.2 behave similarly, proving that the amine functionalization using BHD does not increase the toxicity of the polymer for this cell line. However, cell viability is decreasing more rapidly for all polymer samples after surpassing a critical value of c_{amine}. The CTAB samples show a flatter decrease in the cell viability curve, but with an earlier onset. The suffocation of the cell can explain this behavior, which is caused by the possible formation of a polymer film on the cell surfaces.

The color indicator resazurin was used to evaluate the cells' viability. This measurement is based on the fluorescence change in each cell culture, which is based on reducing resazurin to resorufin when the cells are dying.[8] This method was reported previously in the literature for other nanoparticle systems.[275,276] For the B01-based polymers, this method applies well. However, due to the lower transition temperature of the B02-based polymers, the results for this measurement are falsified to a certain degree, which must be considered when evaluating the results for qBCP02 at the bottom of **Figure 51**. As for the measurement of BCP1.2, the viability using BCP02 starts to decline later at higher amine concentrations than for CTAB, indicating a higher biocompatibility of BCP02. Before the fluorescence measurement, the cell assays are incubated at 37 °C for 24 hours with a CO_2 concentration of 5 % in the atmosphere. As described earlier, functionalizing P(DMAEMA) with BHD drastically changes its solubility and removes the responsive behavior, which leaves the P(DEGMA) block as the only remaining stabilizing block. Since the sample preparation is conducted at 37 °C, the polymer loses most of its hydrophilic properties, increasing the probability of precipitation. This precipitation influences the fluorescence measurements due to the scattering phenomena caused by the polymer's phase separation and the related turbidity increase. As seen for the qBCP02 measurement at increased amine/polymer concentrations, the viability increases above 120 % before rapidly dropping. The most logical explanation for the increased viability is the sample's phase-transfer-based light scattering, which should not be confused with an increase in the number of living cells at any given time. Due to this effect, an exact lethal concentration for the MCF-7 cells cannot be determined solely from this measurement. However, when combined with the results shown for qBCP1.2, it becomes evident that the BHD functionalization does not significantly influence the polymer’s toxicity. It was concluded that the chemical toxicity of qBCP02 most likely does not significantly differ from the unfunctionalized BCP02.

5.3.3. Additional Blind Studies and Test Reactions to Embrace the Polymer-Based GNR Synthesis Potential for Future Research

Similar to the test reactions described in **Figure 46**, several tests were conducted alongside the polymer-based reactions to demonstrate the polymer's contribution indirectly. In the spirit of the test shown in **Figure 46**, the influence of the CTAB concentration in the monomer solution was tested. **Figure 52** now shows the results of a reaction with a CTAB- and polymer-free monomer solution. This test was done to exclude the possibility of a CTAB-dependent particle growth based on the CTAB dissolved in the Au-seed suspension. During the process, the question arose whether it is possible to synthesize GNR without any CTAB present in the growth solution, for example, by using a CTAB-free Au-seed solution for the synthesis (**Figure 53** and **Figure 54**).

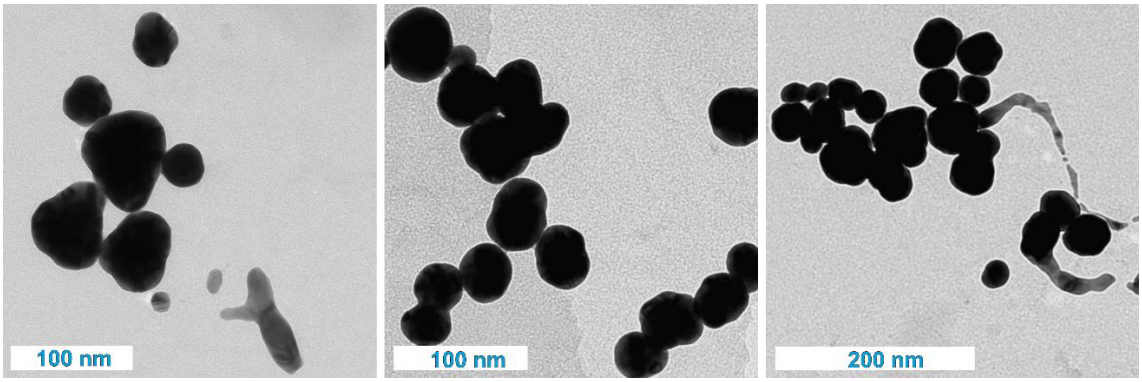


Figure 52. Different TEM images of the Au particles were obtained from the GNP synthesis, without CTAB or other stabilizing components added to the monomer solution in the conventional GNR synthesis protocol. TEM images are taken with permission from the open-access source *Adv. Funct. Mater*. **2024**, 2400995, without adaptation.[8] Copyright 2024 The Authors. Advanced Functional Materials, published by Wiley-VCH GmbH.

As evidenced by the particles shown in the exemplary TEM images in **Figure 52**, not using CTAB or one of the functionalized copolymers within the monomer solution leads, as expected, to uncontrolled growth of GNPs. The particles in this sample show that without CTAB added to the monomer solution, no shape control is given during the reaction. The particle shape shows a spherical tendency. The particle diameters are somewhere between 30 nm and 100 nm. As expected, the residual CTAB in the growth solution, coming from the addition of the seed solution, is neither sufficient to support anisotropic growth nor does it provide proper stabilization of the particle product. The latter was evident due to the formation of a dark precipitate observed during the reaction. The precipitate was not investigated further. For the reaction, the same Au-seed solution was used to synthesize the GNRs referred to in **Figure 10** in Section 4.1.3. These results show that the residual CTAB alone does not contribute to anisotropic growth. It indicates that additional directing stabilizers are required to induce anisotropic growth.

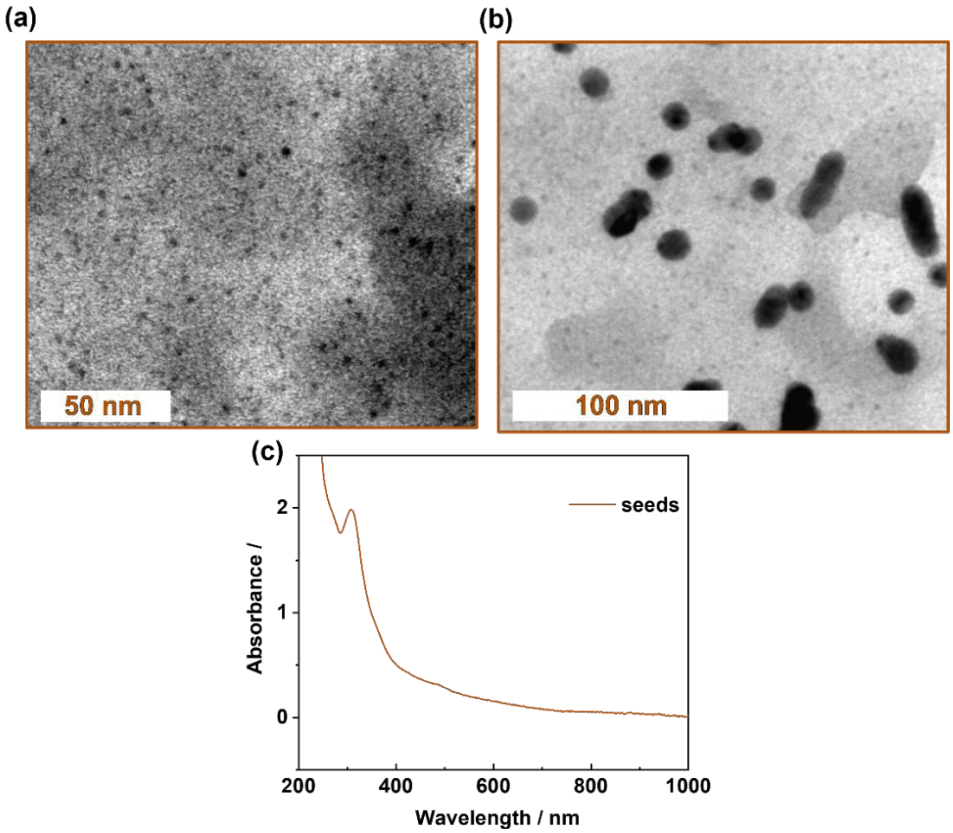


Figure 53. Synthesis results from a CTAB-free qBCP02-based seed preparation. In (a and b), exemplary TEM images of the Au seed product solution are provided. Graphic (c) shows the data for the UV–Vis extinction plots of the CTAB-free Au seeds. The data from this figure was obtained with permission from the open-access source *Adv. Funct. Mater.* **2024**, 2400995, without adaptation. Copyright 2024 The Authors. Advanced Functional Materials, published by Wiley-VCH GmbH. [8]

To address the question of whether CTAB can be obliterated from the GNR preparation, several systems based on qBCP02 were tested. From the GNS@P(DMAEMA) direct synthesis, described in Section 5.2, we knew that the synthesis of seed-sized particles by using TTC-containing polymer stabilizers is generally possible. In **Figure 53**, the results of the seed preparation using qBCP02 are shown.

For the synthesis of CTAB-free Au seeds, the original synthesis protocol of the CTAB-stabilized seeds was refined using qBCP02 instead of CTAB as the stabilizing surfactant. **Figure 53** (a) and (b) show TEM images from the obtained particle suspension. On the positive side, the TEM investigation and the distinctive color of the reaction solution indicate a successful synthesis of GNS in the desired size range of 2.2 ± 0.7 nm. The normalized UV–Vis extinction spectrum of the brownish qBCP02-based seed solution is added in **Figure 53 (c)**. However, the particle product solution also showed impurities of particles with larger diameters (**Figure 53 (b)**).

In contrast to the CTAB-stabilized seeds, some purification steps are required before the qBCP02-based seeds can be applied for a reliably controlled GNR synthesis. An additional open question is whether sufficient accessibility of the critical facets on the Au-seed surfaces is provided, since, for example, the TTC functionality is not known for facet-specific binding. The steric blocking of these crucial facets could impede the facet-specific Au(I)-monomer addition.

The qBCP02-based seed suspension presented in **Figure 53** was added to two monomer solutions. The first solution was prepared according to the conventional CTAB procedure. To test the general applicability of the Au-seed suspension, the second monomer solution was prepared using qBCP02 as the stabilizer, as developed in the polymer-assisted GNR synthesis. The resulting reactions showed signs of GNP growth due to significant color changes. **Figure 54** concludes the analytical results from both reactions.

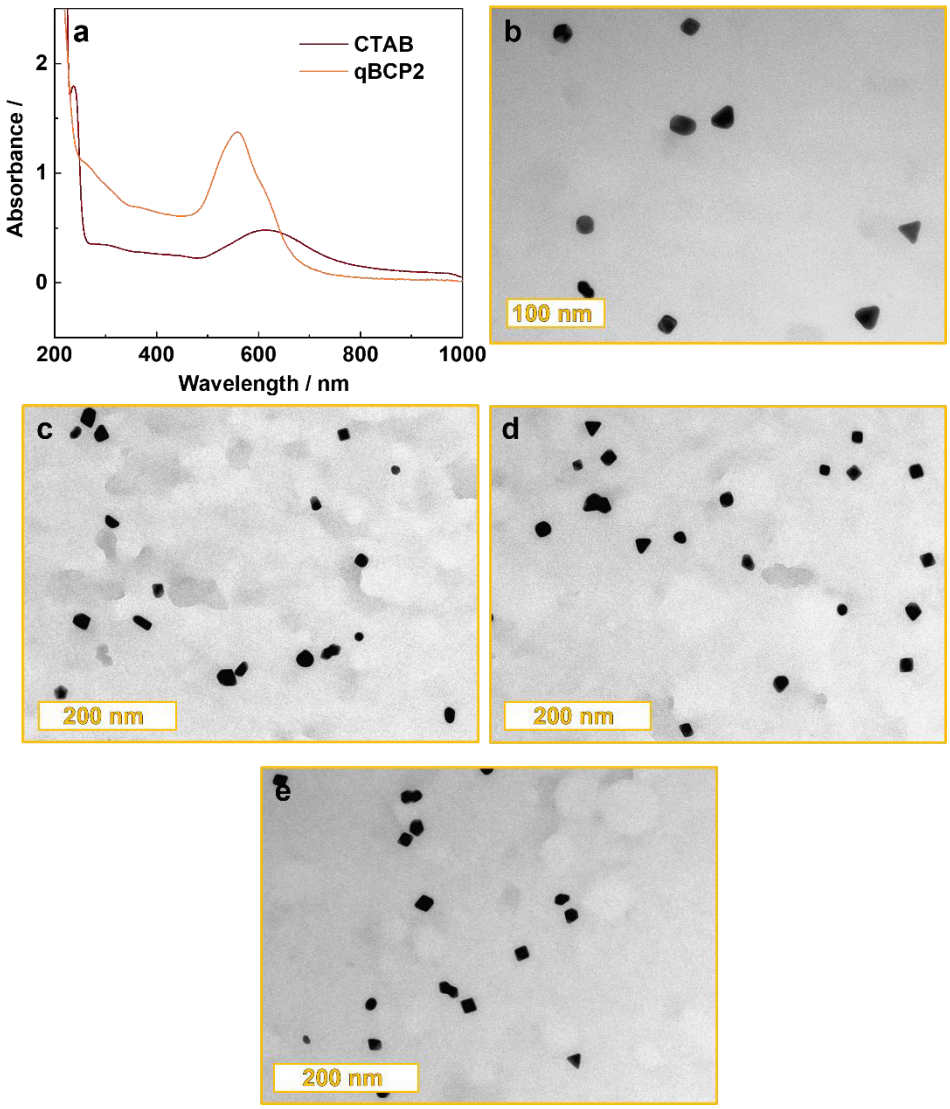


Figure 54. This figure concludes the results of the CTAB-free seed-particle trials for the GNR synthesis. In (a), the resulting particle products' UV–Vis extinction spectra are shown after purification. In the TEM images shown in b–e, a representative overview of the particle product obtained with the qBCP02-based approach is presented. The data for both the UV–vis spectra shown in (a) and the TEM image (c) were taken with permission from the open-access source *Adv. Funct. Mater*. **2024**, 2400995. Copyright 2024 The Authors. Advanced Functional Materials, published by Wiley-VCH GmbH.[8]

Because the particle suspension's UV–Vis extinction spectrum, conducted with the CTAB-based monomer solution (**Figure 54 (a)** red curve), did not show signs of anisotropic growth, the suspension was not further investigated. The extinction spectrum of particle suspension obtained from the CTAB-free qBCP2-based growth solution did show a shoulder in the LSPR signal, indicating particles that underwent anisotropic growth. Based on this finding, the sample was investigated using TEM. Exemplary TEM images obtained from this investigation are shown in **Figure 54 (b–e)**. As shown in these images, the obtained particles do not have a uniform shape. The particle morphologies range from spherical to triangular, square, and rectangular. These findings show that under the chosen conditions, qBCP02 promotes anisotropic growth, which indicates facet-specific surface blocking during the reaction. However, a sufficient shape-yield, concerning rod-like structures, is not provided under the chosen reaction conditions.

Nevertheless, the fact that the obtained particle morphologies show mostly anisotropic particles and nearly no isotropic GNS proves that qBCP02 is generally a suitable candidate for synthesizing anisotropic particles and, for that matter, rod-like particles if the conditions are appropriately chosen. There are several probable reasons why the shape-yield of the reaction is insufficient. Since the CTAB-based monomer solution also did not provide sufficient anisotropic nanoparticle structures, the qBCP02 is likely blocking the relevant surface area due to steric hindrance, which would impede the facet-specific monomer addition during the particle growth. One possibility to prevent this could be to choose a shorter, chained stabilizer. Additionally, the role of the TTC functionality is unclear, which could be another limiting factor in the applicability of qBCP02-like polymers for the synthesis of Au seeds. Assuming that the TTC group is not binding specifically at the respective facets would also reduce the shape yield.

5.4. Tailoring Thermoresponsive Properties of Smart Au@Polymer Hybrids: A Systematic Investigation

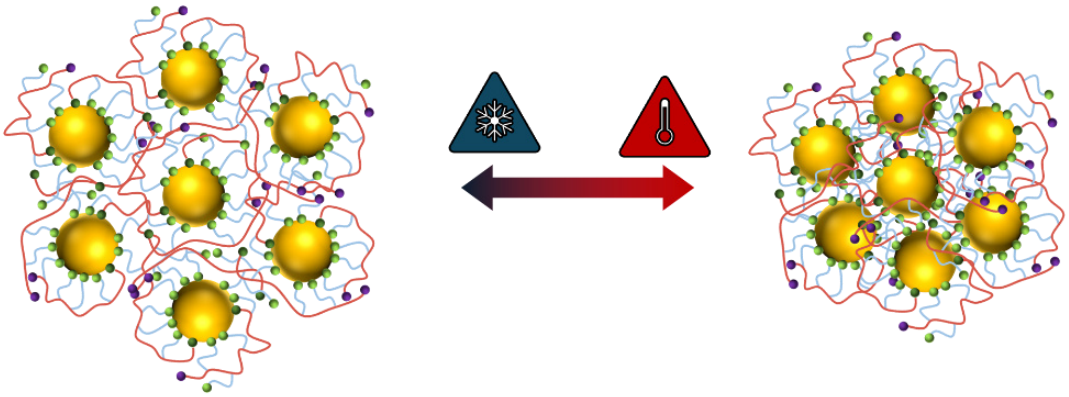


Figure 55. Illustration of the principle of interparticle space adjustment between GNS (yellow spheres) using a stimuli-responsive graft copolymer shell (orange and blue threads) to stabilize the particle surfaces.

A significant portion of this work focused on the synthesis of temperature-responsive polymers. The intriguing perspective behind the combination of GNP with a responsive polymer shell is the possibility of controlling the interparticle distances in such hybrid materials by using the respective stimuli to trigger the swelling and the collapse of the polymer shell. This behavior is indicated in **Figure 55**. As described in Section 4.1.3.2, particle characteristics like the LSPR of two particles can form a collective resonance frequency, which becomes evident by a shift of λ_{LSPR} in the UV–Vis extinction spectrum. Another intriguing characteristic that can be adjusted by the gap size between GNPs is the electrical resistance when GNPs are cast into a film. This behavior is used in many different sensor materials for gas-sensing applications.[18,48,277–279] In her recent work, K. Schaefer showed the dynamics behind the resistance changes of such films on a molecular level via force field simulation and compared these results with experimental data from the literature.[280] Using a flexible, stimuli-responsive polymer for particle crosslinking promises bigger changes in the hybrid film resistance at the transition point of the polymer and, therefore, provides a very sensitive sensor material.

However, as described in Section 4.3, responsive polymers behave significantly differently when confined on a particle surface than free polymer chains do. This section looks at the behavior of the Au@nanohybrids in aqueous solutions developed during this project. A special focus is put on the hybrids' thermoresponsive behavior compared to the solutions of free polymer precursors. First, the responsive properties of the two hybrid materials are discussed, and the properties of the GNS-free polymer precursors are compared. In this section's second subsection, the preparation of the third and last hybrid material of this work is introduced. For this material, a grafting-to method for preparing Au@polymer hybrid material is followed, which is based on the procedure published by C. Rossner et al. in 2013.[247]

5.4.1. Responsive Properties of the Au@P(DMAEMA)$_n$ and the GNR@qBCP Nanohybrids: A Comparison of Polymer Solution and Nanohybrid Suspension Behavior

A big fraction of the publications about the Au@P(DMAEMA)$_n$ hybrids described in Section 5.2 and Ref. [3] is the investigation of the hybrids' responsive properties compared with their respective P(DMAEMA)$_n$ precursor. Characterizing the temperature-responsive properties of the P(DMAEMA)$_n$ precursors was very straightforward. Especially, the heating curves of each characterized polymer precursor show a sharp transition from a hydrophilic to a hydrophobic state (see **Figure 26** in Section 5.2.2). The same characterization methods (DLS and UV–Vis) for the temperature-dependent polymer characterization were applied to the Au@P(DMAEMA)$_n$ hybrids after suspending them in water.

During the redispersion of the Au@P(DMAEMA)$_n$ hybrids in water, differences in their solubility based on the used P(DMAEMA) precursor became evident. The dTTC-based P(DMAEMA)$_{41}$ showed complications during the suspension in water under normal conditions. To prepare a homogeneous suspension in water, the Au-hybrid/THF suspensions were mixed with water. After forming a homogeneous suspension, THF was removed under reduced pressure, and the particle content was adjusted with water using the LSPR signal in the UV–Vis extinction spectroscopy as a reference. For the two pTTC-P(DMAEMA)$_n$-based hybrids, the time needed to form a macroscopically homogeneous suspension was significantly longer (several minutes) when polymer precursors with a higher DP_D were used. This behavior was expected as dissolving polymers is a kinetic process dependent on the polymer chain length. However, after removing the THF from the solution at reduced pressure, both pTTC-based hybrids formed stable suspensions under normal conditions. The hybrids synthesized using a dTTC-P(DMAEMA)$_n$ precursor showed a different behavior. A two-phase system was formed after adding the THF/hybrid stock suspension to water. For the long-chained dTTC-P(DMEAMA)$_{92}$-based gold hybrid, the two-phase system eventually formed a homogeneous single-phase system after a fair amount of mixing time. The short-chained equivalent hybrid Au@P(DMAEMA)$_{41}$ stayed in this two-phase state even after mixing for several minutes. This two-phase state persisted even after removing the THF from the system under reduced pressure; a homogeneous particle suspension formed only after purging the solution with CO_2 gas. To remove the CO_2 from the solution, the suspension was heated to 60 °C for 30 min. Interestingly, the suspension remained stable after the temperature treatment, indicating that the increased solubility of the DMAEMA chains due to CO_2 addition served only as an initiating trigger for the formation of a more stable suspension. However, these significant differences in the solubility behavior between the dTTC- and pTTC-based GNS hybrids were a clear indication of the presence of these groups in the final hybrids, significantly influencing their hydrophilic characteristics.

After preparing stable Au@P(DMAEMA) suspensions in water, they were tested for their temperature-responsive behavior using temperature-dependent DLS measurements. Based on the rapid changes observed while measuring the polymer solutions (**Figure 26** in Section 5.2.2), a rapid R_H transition around the polymer's PTT was expected for the hybrids, too. However, the results of the temperature-dependent DLS investigations of the hybrid suspensions did not match this expectation. As shown in **Figure 56**, most samples show a gradual decrease in the R_H throughout the heating period of the measurement. It is essential to note that the data in **Figure 56** show the R_H results obtained from the second temperature cycle of the respective hybrid suspension. The results obtained from the first temperature cycle (see **Figure A9**) do not show the reversible behavior of the R_H. However, most samples equilibrate during the first temperature cycle and show the expected reversibility of the R_H at varying solution temperatures. This equilibration behavior is also observed in the temperature-dependent transmittance values of the same samples shown in the Appendix in **Figure A10**.

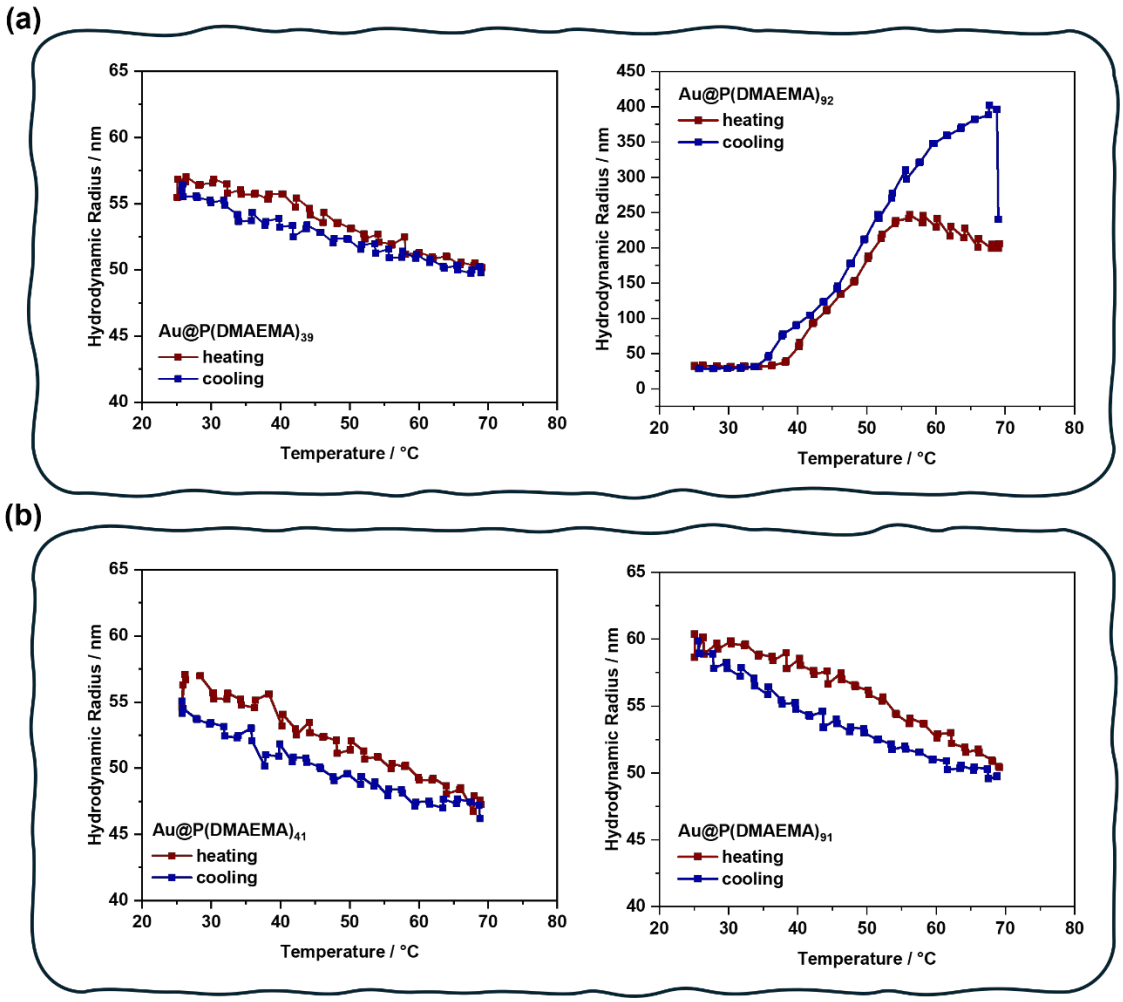


Figure 56. Temperature-dependent DLS measurements of different Au@P(DMAEMA)$_n$ hybrids dispersed in water. In (a), the R_H of pTTC-polymer precursor-based Au@P(DMAEMA)$_n$ hybrids is plotted against the solution temperature. In (b), the temperature-dependent behavior of dTTC-polymer precursor-based Au@P(DMAEMA)$_n$ hybrids with comparable DP_D is shown. The data from the four plots are taken with permission from the open-access source *Macromol. Chem. Phys.* **2022**, 2200355, with minor adaptations. Copyright 2022 The Authors. Macromolecular Chemistry and Physics, published by Wiley-VCH GmbH.[3]

In contrast to the other samples shown in **Figure 56**, the R_H of the pTTC-P(DMAEMA)$_{92}$-based hybrid (**Figure 56** (a) right plot) increases with the solution temperature. This increase starts around T_{cp} of the polymer precursor pTTC-P(DMAEMA)$_{92}$ (compare **Figure 26**). This behavior can be assigned to free-polymer chains in solution and indicates the formation of particle aggregates.[3,281] Both types of behavior are observed in other pTTC-P(DMAEMA)$_n$-based Au hybrids with no clear dependencies except the molecular weight of the used pTTC-P(DMAEMA)$_n$-precursor (see **Figure A11**). A possible explanation for that behavior is given in Section 5.4.3.

While the Au@P(DMAEMA) hybrids were developed for their responsive behavior, the scientific focus of the topic on the polymer-assisted GNR synthesis aimed to find a less toxic alternative for CTAB and to reduce the toxicity of the GNR synthesis.[8] Nevertheless, due to the use of a stimuli-responsive hydrophilic block, the obtained GNR hybrids also exhibit significant temperature-dependent responsiveness, as shown in **Figure 57** by the UV–Vis investigation of the GNR@qBCP02 sample.

The left plot shown in **Figure 57** illustrates the hybrid's normalized UV–Vis extinction spectra at different solution temperatures while heating. The two plots on the right side of **Figure 57** show the LSPR maximum wavelength for the longitudinal (top) and transversal nanorod signal. The two plots show that the temperature response is not reversible. Additionally, there are distinct differences in the LSPR shifts of the two signals. As described in Subsection 4.1.3.2, a certain difference between the obtained responses is expected because of the differing distance-dependent sensitivities toward particle-particle LSPR coupling. A significant decrease in signal intensity is observed for both signals, as shown in the left plot. Interestingly, the onset temperature of this decrease is different for each of the two particle dimensions. For the transversal particle signal, a redshift in the LSPR is first observed, with a range of 20–25 °C according to the bottom-right plot. Around 35 °C, this redshift slowly approaches a constant value of around 540 nm. Above this temperature, the transversal signal intensity drops. Overall, the transversal signal shifts irreversibly from originally 530 nm to an LSPR wavelength of 540 nm.

In contrast to that stands the longitudinal assigned signal, which, appealingly, is more affected by the temperature change. In the temperature range of 10 °C – 25 °C, the LSPR frequency exhibits a slight redshift with increasing temperatures. With the sample reaching 25 °C, the signal intensity starts to drop significantly (a 10 % relative intensity drop from 25 °C to 30 °C). Additionally, at this point, the LSPR blue shifts linearly with increasing temperature.

With the temperature-responsive nature of qBCP02 and a T_{cp} around 25 °C (see **Figure 47**), the changes can be described as a function of the qBCP02 stabilizer. Based on the knowledge gained in nanoparticle/polymer hybrids, some statements can be made to provide insight into the process observed in **Figure 57**.

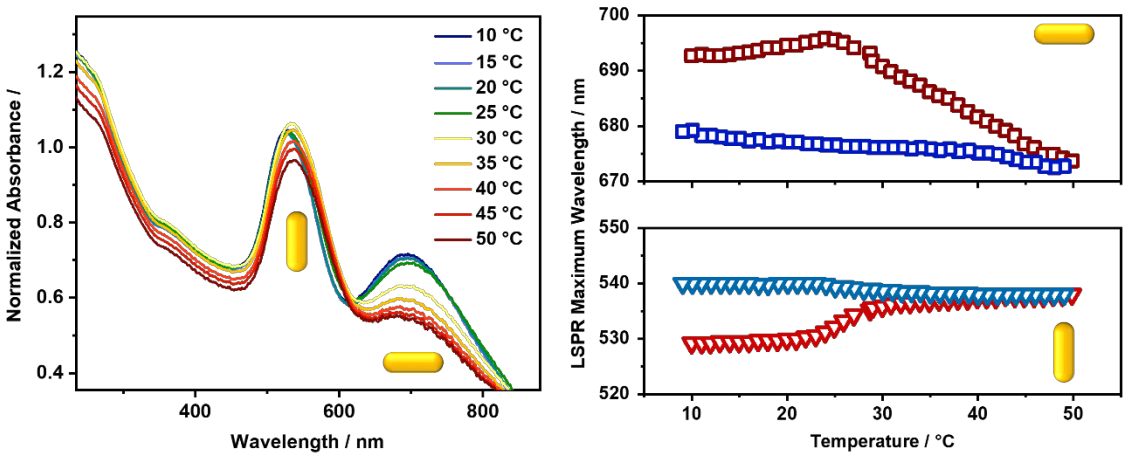


Figure 57. Temperature-dependent UV–Vis extinction spectroscopy investigation of the GNR@qBCP02. The plot on the left shows exemplary UV–Vis spectra of the GNR@BCP02 dispersed in water measured at different sample temperatures. The two plots on the right-hand side show the LSPR wavelength of the transversal (top) and the longitudinal LSPR absorbance maximum. This figure is taken with permission from the open-access source *Adv. Funct. Mater*. **2024**, 2400995, with minor adaptations. Copyright 2024 The Authors. Advanced Functional Materials, published by Wiley-VCH GmbH.[8]

With the shift of qBCP02s' P(DEGMA) block from a hydrophilic state into its hydrophobic state, the cationic amine functions must stabilize the polymer in water. This type of stabilization would require rearranging the polymer chains with the cationic amine functionalities at the intersection between water and the hydrophobic polymer coil, serving as the core of the rearranged structure. The rearrangement would require a certain amount of conformational freedom of the polymer chains and, more importantly, of the amine functions. This completely ignores the fact that even a free qBCP02 chain is insufficiently stabilized by its amine functions. In this case, the amine cations are additionally bound on the surface of the GNPs, which contradicts this type of chain arrangement. Due to these reasons, one dominant and undeniable factor that influences the optical properties is particle precipitation induced by the destabilization of the P(DEGMA) block above 25 °C. The precipitation of the destabilized particles is the main reason for the decreased absorbance of the extinction spectrum. It was observed that the solution appeared colorless, and a dark precipitate was formed at the bottom of the quartz cuvette after it was stored for 24 hours at room temperature. This precipitation was reversed by intensive mixing for most of the precipitate. Due to the differing temperature-dependent behavior in the band intensities, based on two dimensions of the GNRs, one of the first ideas was that the precipitation of each particle is dependent on its respective stabilization. It is known that particle stabilization in a suspension becomes more complex for a suspension of larger particles. When separating GNRs by size, size-dependent crystallization behavior is used to purify different aspect ratios from a polydisperse GNR suspension.[104] In the observed case shown in **Figure 57**, both effects are possible scenarios that explain the temperature-induced changes in the optical behavior. For instance, when increasing the suspension temperature above the LCST of P(DEGMA)-blocks, the formation of nanoscopic ordered GNR clusters is more likely due to the preferred side-by-side stacking based

on the anisotropic shape compared to spherical particles within the sample (compare **Figure 47** (a)). Combined with the fact that the transversal particle signal in the extinction spectrum of the rod-like particle species overlaps with the LSPR signal of spherical particles, it is logical that the longitudinal signal is more affected by the precipitation of the rod-like species.

Another possible explanation for the results shown can be given by symmetry-breaking LSPR coupling due to reduced particle-particle distances. As described in Subsection 4.1.3.2, symmetry breaking can cause different effects when it comes to LSPR coupling because of particle-particle distances decreased below the critical coupling distance. The literature shows that forming GNR particle di- and oligomers in side-by-side assembly can explain the transverse LSPR's redshift and the longitudinal LSPR's blueshift. Another explanation for this optical behavior could be the formation of isotropic particle clusters above the transition temperature of the stabilizing PDEGMA block.[8] For comparison, K. Shimoda and coworkers showed a similar behavior.[282] The investigated GNRs coated with poly(*N*-isopropyl acrylamide) (P(NiPAM)) reported a blueshift of the longitudinal band in the UV–Vis extinction spectra. Their results also showed that the extinction of this signal above the LCST of the P(NiPAM) shell decreased significantly and showed polymer chain length-dependence.

All these effects can explain the optical behavior. However, no further investigations were conducted to define the contribution of each effect more accurately because it would have exceeded the scope of the original topic, which was to prove the applicability of modified DMAEMA-based polymers for the synthesis of anisotropic GNPs. This question was picked up later as a topic.

From the introduced temperature-responsive nature of the two stimuli-responsive hybrid systems discussed so far, some general questions about the underlying process remained unresolved:

1) Is there a model that can reliably describe the underlying temperature-responsive process of such particle hybrid systems?
2) Why is the temperature-induced reaction of the polymer changing from a rapid response at a distinct transition temperature to a gradual response with no significant transition temperature when it is fixed on a particle surface?
3) Is it possible to regain that rapid hydrophilic/hydrophobic transition by increasing the molecular weight of the stabilizing polymer?
4) Is it possible to control interparticle distances in the area of the critical coupling distance by using a responsive polymer shell? And if so, is this process reversible?

Another GNP@Polymer hybrid model was developed to serve as a modeling system that shows distinctive similarities to the already presented GNP hybrids and to address some of those open questions. For this study, the previously introduced double thermoresponsive graft polymer, developed by J. Xu and V. Abetz[1,9] (see also Section 4.2), was combined with GNS obtained by using the citrate-reduction-based synthesis as described by F. Schulz and coworkers.[63]

As a well-investigated polymer system with several TTC functionalities in its side chains, the double thermoresponsive graft copolymer is a fascinating material for the synthesis of GNP@polymer shell hybrids with unique responsive properties. Like the other two systems in this work, the first major aspect before synthesizing the Au@polymer hybrid material was increasing the scale of the photoRAFT polymerization process to reduce the effects of varying polymer quality across synthesis batches. The procedure presented by F. Schulz has proven several times to provide GNS with reliable particle quality in terms of particle size distribution and shape selectivity. It is therefore chosen as the method for the GNS synthesis. This procedure provides particles with an average particle diameter of 12 nm. In a subsequent step, the particles and the temperature-responsive polymers are combined using the grafting-to protocol described by B. Ebeling and P. Vana.[162]

The convenient natural attraction between the TTC groups, which are statistically distributed along the OEGMA backbone, and gold surfaces, makes this polymer a suitable model for describing the interactions of the P(DMAEMA) chains when attached to GNS surfaces. For instance, the theory describing the thermoresponsive behavior of the Au@P(DMAEMA) hybrids assumes the P(DMAEMA) shell to be a strongly crosslinked network with increasing crosslink density toward the GNP's surface. Amines are known to show attractive interaction with positively charged GNP surfaces. Therefore, a d/pTTC-P(DMAEMA) chain can be attached to the particle's surface at several additional anchoring points besides the TTC end-functionality. The naturally strong confinement of the polymer chains near the particle surface limits the chains' flexibility, which causes a lower accessibility of these polymer segments to water and results in a decreased swelling of the polymer within that region. This results in a lower swollen-to-unswollen ratio of the polymer, which causes a less pronounced change in the, for example, R_h below and above the phase transition temperature.

In the following two sections, one of the working hypotheses is that due to the TTC-functionalities within the side chain of P(OEGMA-*r*-BTPEMA), GNS@P(OEGMA-*r*-BTPEMA) hybrids should behave like the Au@P(DMAEMA)$_n$ hybrids, which means that the temperature-dependent changes of the GNS@P(OEGMA-*r*-BTPEMA) hybrid's R_h should decay approximately linearly with increasing temperature of the aqueous suspension. To further describe this behavior, the fuzzy sphere model introduced by P. Mulvaney and coworkers in 2022 [8–10] is tested for its applicability to the particle hybrids described in this thesis. Their model is based on a crosslinked P(NiPAM)-shell (see Section 4.3.1). The question is whether this fuzzy-sphere model is also

suitable for describing the behavior of the particle hybrids investigated in this work. If this model proves suitable for predicting the thermoresponsive behavior of NP hybrids, designing the responsivity could become much more straightforward in the future. Based on their findings, P. Mulvaney and coworkers used the following equation to describe the temperature-dependency of the R_H of their P(NiPAM)-based hybrid material:

$$R_H(T) = R_{H,min} + \frac{R_{H,max} - R_{H,min}}{1 + \exp\left(\frac{T - T_c}{h}\right)} \quad (5.1)$$

In this equation, the factor h describes the sharpness of the hybrids' transition temperature based on the system's fuzziness.[11,12] Using the simple controlled chain extension of P(OEGMA-*r*-BTPEMEA) with NiPAM, the fuzziness of the hybrid material aimed for should be increased, which, if the equation holds, should cause a better-resolved transition temperature with increasing side chain length. Additionally, in terms of the material properties, adjusting the molecular weight of the polymer stabilizer should further allow the adjustment of interparticle spacing within films cast from such a material.

In Section 5.4.2, the development of the model system based on GNS and the graft-copolymer system is described to the point where the first reliable and well-reproducible results were obtained for temperature-responsive behavior. Section 5.4.3 presents a conclusion of this topic, focusing on the responsiveness of GNP@polymer hybrids.

5.4.2. Preparation and Particle Assembly of GNS Stabilized by Double Thermo-Responsive Graft-Copolymers

As the name of this section already suggests, this section is about synthesizing a GNS polymer hybrid system using a double thermo-responsive graft-copolymer to stabilize GNPs in water, as illustrated in **Figure 55** (page 107). Since the other two materials, described in the previous sections, showed a loss of their rapid, responsive behavior, the question was, what would happen if a material is chosen for the particle stabilization that has two distinct transition temperatures, and how this characteristic affects the corresponding hybrids' thermoresponsivity. Moreover, does the stabilizing material maintain at least one of its distinct transitions, and what conclusion can be drawn from these results in terms of chain assembly, chain mobility, and the influence of polymer chain configuration?

Besides the changes in temperature-responsive behavior, we were curious to identify similarities with the other described hybrid systems to better understand the nature of such hybrids in general. The aim is to use this knowledge to assign specific general characteristics to a global model for a simplified design of such responsive nanoparticle hybrids in the future.

To maintain general clarity, this topic is separated into two subsections. Subsection 5.4.2.1 explains why this graft copolymer structure was chosen and covers the applied polymerization scale-up and the analytics required to demonstrate successful scaling, including kinetic results and polymer-specific characterization of its responsive nature. In addition to that, Subsection 5.4.2.1 provides a first conclusion of the achievements regarding the scaling up of the photoRAFT polymerization reached in this work and classifies this achievement based on the results from recent literature.

In the second part of this section, Subsection 5.4.2.2, the synthesis of GNS@citrate is discussed, following the inverse Turkevich procedure described by F. Schulz and coworkers.[63] Subsection 5.4.2.2 also emphasizes the methods used to combine GNS@citrate with the as-synthesized double thermoresponsive graft copolymers. The section also sheds light on the challenges encountered in developing a reliable and reproducible procedure for preparing GNS@polymer hybrids and on why a procedure closely related to that described by the group of P. Vana was chosen as the preferred method.[247]

5.4.2.1. Photo Iniferter RAFT Polymerization: Final Scale-up and Resume of the Achievements in Comparison With Recent Research

A multiple-step reaction pathway was developed and described in this section to synthesize the desired particle hybrids. This section focuses on the first step of this procedure: the synthesis and scale-up of the double thermoresponsive graft copolymers, which are later used to stabilize GNS. J. Xu and V. Abetz reported that synthesizing the double thermoresponsive graft copolymer first involves copolymerizing OEGMA with the TTC-inimer BTPEMA. As in the literature, this polymerization is conducted under the irradiation from a green LED-light source, which causes the growth of a linear thermoresponsive copolymer P(OEGMA-*r*-BTPEMEA). In contrast to the polymerization of the P(OEGMA-*r*-BTPEMEA) backbone B01 described in Section 5.3, the reaction scale was increased again. Therefore, a 500 mL double-walled glass reactor purchased from Schmizo AG was used. The inner diameter of the reactor amounts to 8.5 cm. Hot water was pumped through the reactor mantle to heat the reaction solution continuously. The multivalent macroRAFT agent P($OEGMA_{233}$-*r*-$BTPEMA_{11}$) (B03) was obtained using the described reaction setup.

Starting from B03 as the macroRAFT agent, NiPAM was polymerized using the sublimation reactor setup described in Section 5.3. In contrast to the literature and to B01, the synthesis of B03 aimed for a higher BTPEMA weight content and a slightly shorter chain length to maximize the attractiveness of the resulting polymers for the following grafting-to approach to prepare the desired GNS@polymer hybrids.

Based on the B03 copolymer, the polymerization of PNiPAM was initialized using the blue light source. Two graft copolymers were synthesized with differing P(NiPAM) chain lengths. The results of the polymerizations of B03 are presented in **Figure 58**. The results of the two following NiPAM polymerizations using B03 as the macroRAFT agent are shown in **Figure 59**.

The described polymerization scale-up of the procedure is a recurring topic in this thesis and is finalized with the described setup. It touches the limits of the allowed laboratory scale (especially for the synthesis of B03). The results shown in **Figure 58** and **Figure 59** indicate a successful transformation of the graft-copolymer synthesis into a larger reaction scale. Because it was planned to investigate the influence of the polymer stabilizer's DP_N on the thermoresponsive nature of the nanohybrid, having the same basis (in this case, B03) was important for the systematic comparison of the resulting hybrids. A reliable RAFT process was essential to achieve comparable quality across the three polymers, B03, GN01, and GN02.

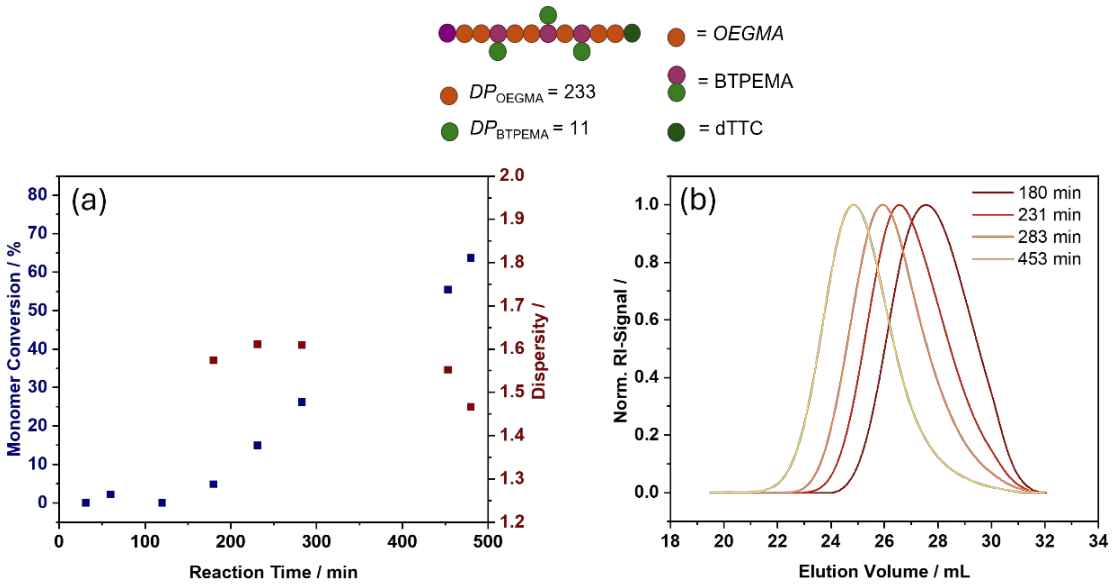


Figure 58. Conclusion of the polymerization results of the synthesis of the B03 macroRAFT agent. The picogram at the top represents the schematic composition of B03. In (a), the kinetic results are shown, concluding the progressing monomer conversion (blue squares) and the evolution of the polymers' dispersity (dark-red squares). In graph (b), the chromatograms of the intermediate polymer products at different reaction times are shown. These chromatograms represent the molecular weight distribution at different reaction times based on the detected RI signal during the SEC measurement.

Apart from a prolonged initiation phase for the B03 polymerization, all three polymerizations show a linear dependency in their kinetic pseudo-first-order plot of the monomer conversion (top graphs in **Figure 58**) with a correlated $R^2 > 0.99$ when the initiation phases are excluded. This linear behavior is a sign of a constant radical concentration during the chain growth phase, indicating a controlled RAFT process.

As reasons for the prolonged initiation phase (compared to B01 in **Figure 39**), a higher concentration of TTC functionalities and a lower intensity of the initiation light within the solution, due to multiple scattering sources arising from the reactor construction, can be identified. Due to the higher TTC concentration compared to the concentration used for the synthesis of B01 in Section 5.3, radicals are more likely to be transferred into a dormant state, which causes the reaction to slow down and increases the time needed to surpass the RAFT pre-equilibrium state of the polymerization and enter the main equilibrium. The nature of the chosen reactor setup must be named as a plausible explanation for the low conversion rate. Before entering the reaction solution, the light must surpass the reactor's heating mantle, which is filled with hot water as the heat source for the reaction. Due to the need to penetrate multiple media, the light can be scattered several times on its way into the reaction solution. This instance also made it impossible to estimate the light intensity inside the reactor because there was no equipment to measure the intensity inside the closed reaction setup.

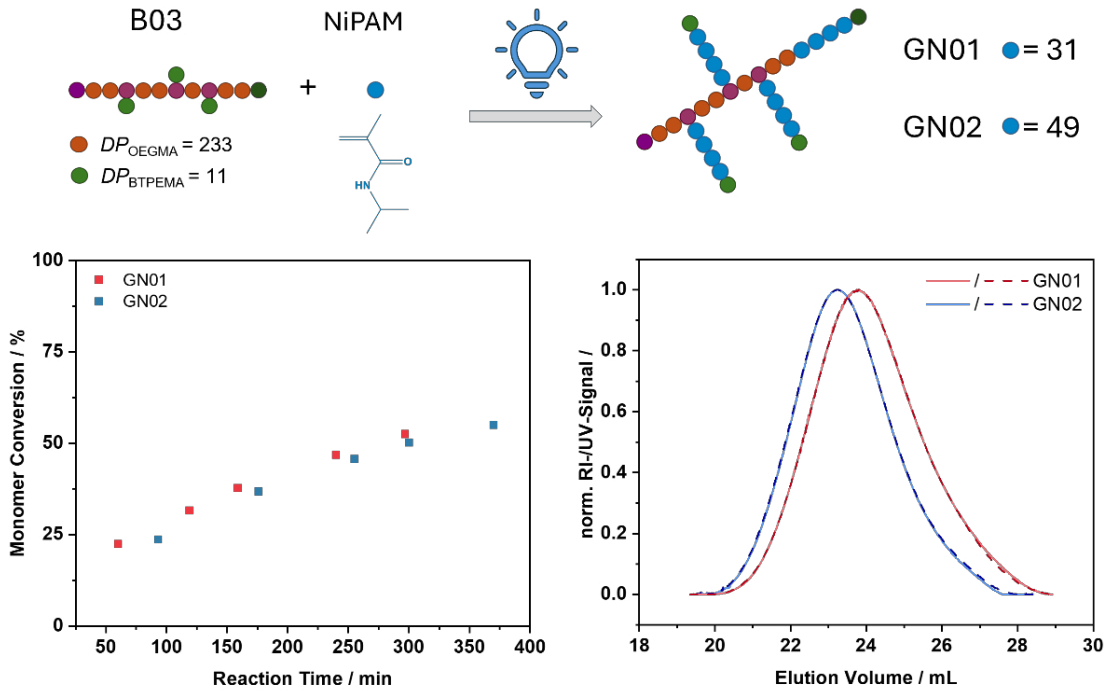


Figure 59. Scheme of the graft polymerization of GN01 and GN02 using B03 as a multi-functional macroRAFT agent and NiPAM as monomer for the second LCST-type fraction of the resulting graft polymers and blue LED light to initiate the photoRAFT polymerization process. Additionally, in the bottom-left panel, the NiPAM conversion is plotted against reaction time for the polymerization of GN01 (red) and GN02 (blue). The graphic on the bottom right shows the chromatogram results from the SEC measurements of both products. Here, the dashed lines represent the normalized signal from the UV detector. The solid lines show the normalized RI-detector signal.

However, the linear behavior in the pseudo-first-order plot indicates a controlled RAFT process, but it must not be taken as proof on its own. This common misconception is very well pointed out and discussed in the review by M. H. Stenzel and C. Barner-Kowollik.[283] Therefore, SEC measurements were conducted on all three polymer samples as a standard procedure. The resulting chromatograms show a Poisson-like distribution. More importantly, the SEC chromatograms obtained from measurements of the intermediate polymer products from the B03 polymerization display a progressive increase in the molecular weight, as shown by the shift of the elution maximum to lower elution volumes. The dispersity B03 is 1.47, which is a little higher than the dispersity reported in the literature for related copolymers ($Đ$ = 1.31–1.37[1,9]). Nevertheless, this dispersity is still within the acceptable range ($Đ$ < 1.60) to assume controlled reaction conditions.

A blue LED light source was used to initiate all TTC functions for the polymerization of NiPAM. Because NiPAM forms secondary radicals during radical polymerization, no mismatch between the NiPAM and the BTPEMA radicals, like for the polymerization of DMAEMA with B01, which hindered the formation of the main RAFT equilibrium. Using B03, the graft copolymers ($POEGMA_{233}$-*r*-$P(NiPAM_{34})_{11}$)-*b*-$PNiPAM_{34}$ (GN01), and ($POEGMA_{233}$-*r*-$P(NiPAM_{49})_{11}$)-*b*-$PNiPAM_{49}$ (GN02) were synthesized. The difference between the polymers relies on the varying PNiPAM side chain length. With Đ = 1.50 for GN01 and Đ = 1.45 for GN02, the results are

comparable to the dispersity reported in the literature (Đ = 1.42 [1]). J. Xu and V. Abetz reported a dispersity of 1.31 for their backbone structure and 1.42 for the graft copolymer. Similar dispersities were reported when the R-group of the initial RAFT agent was changed from an ACVA-based derivative to an AIBN-based derivative.[1] Given the consistency of the results with the literature, it was concluded that the assigned scale-up was successful and applicable to the investigated polymer.

The photoRAFT copolymerization of OEGMA and BTPEMA was subsequently increased by roughly 40 times the initial reaction volume, reaching the limits possible within the laboratory scale. When polymerizing at different scales, it became clear that larger reaction scales are, in fact, beneficial for the robustness of the reaction against air exposure. It is known that RAFT polymerization is sensitive to oxygen, which is why oxygen is removed from the polymerization solution before the polymerization is initiated. This procedure is a common practice that is independent of the nature of the initiation mechanism.[9,154,174,175,215,284]

Due to the lower surface-to-volume ratio at larger reaction scales and the higher volume of inert gas above the solution, handling the reaction becomes much easier. Due to the sensitivity of the RAFT process to oxygen, quenching of the polymerization was observed regularly. Especially in the case of a kinetic investigation, every sample taken was a potential risk of inserting a critical amount of oxygen into the solution, either by insufficient conditioning of the used syringe or due to the perforation of the screw cap of the flask. Quenching of the reaction while sampling was not observed for the sublimation setup. Even if the used syringe was not conditioned in advance, the amount of inserted oxygen did not noticeably change the reactions' kinetics.

However, since the 250 mL setup was built initially for sublimation reactions, sampling the polymerization solution was very impractical due to the limited accessibility of the solution in this setup. With the double-walled 500 mL glass reactor, this issue was addressed by adding an outlet for the solution at the bottom of the reactor. This outlet enabled noninvasive sampling and significantly improved the practicability of the setup. Due to the integrated adjustable mixing unit, higher polymer mass concentrations in the reaction solution can be considered. This efficient mixing process is another advantage over the previous sublimation reactor setup, which used a conventional magnetic stirring bar.

The polymerization results shown in **Figure 58** and **Figure 59** prove the great potential of the photoRAFT polymerization and show that conducting the polymerization in a batch setup is a considerable and reliable technique for synthesizing highly specialized polymers. Other techniques, like continuous-flow setups, have already been successfully tested for the iniferter RAFT polymerization.[270] The polymers obtained from a continuous setup also show a considerably low molecular weight distribution with a very high polymerization rate. However, this setup faces a critical challenge due to the product's dwell-time distribution within the flow setup. This distribution causes the reaction time to vary among the chains passing through the

flow channel. Although this effect is negligible in polymerizations, especially at lower mass concentrations in the reaction solution, it becomes critical in multi-phase systems, such as emulsion polymerization, where the solid product can clog the flow channel. Additionally, this setup is expensive (especially regarding further scale-up by number-up) and requires highly specialized equipment and knowledge. With the described 500 mL reactor setup and the adjustable mixing unit, another promising scale-up method for synthesizing advanced polymer structures in technical amounts is a considerable next step in the future development of this kind of photo-initiated RAFT polymerization.

Nevertheless, the scale-up of the described polymerization was necessary to develop reliable techniques for synthesizing Au@polymer hybrids. Therefore, it was never the primary focus of the presented work. The primary focus remained on preparing GNP hybrids, which made it necessary to prove that the synthesized polymers are of similar quality to those reported in the literature. For this purpose, the thermoresponsive properties of the polymers B03, GN01, and GN02 were further characterized. The results of this characterization are concluded in **Figure 60**. Here, the thermoresponsive properties of B03, GN01, and GN02 are characterized by temperature-dependent UV–Vis transmittance measurements and DLS experiments in aqueous solutions of the respective polymers. The results prove that the scale-up did not significantly affect the temperature. All three polymers exhibit the same aggregation behavior described in the literature across varying solution temperatures.

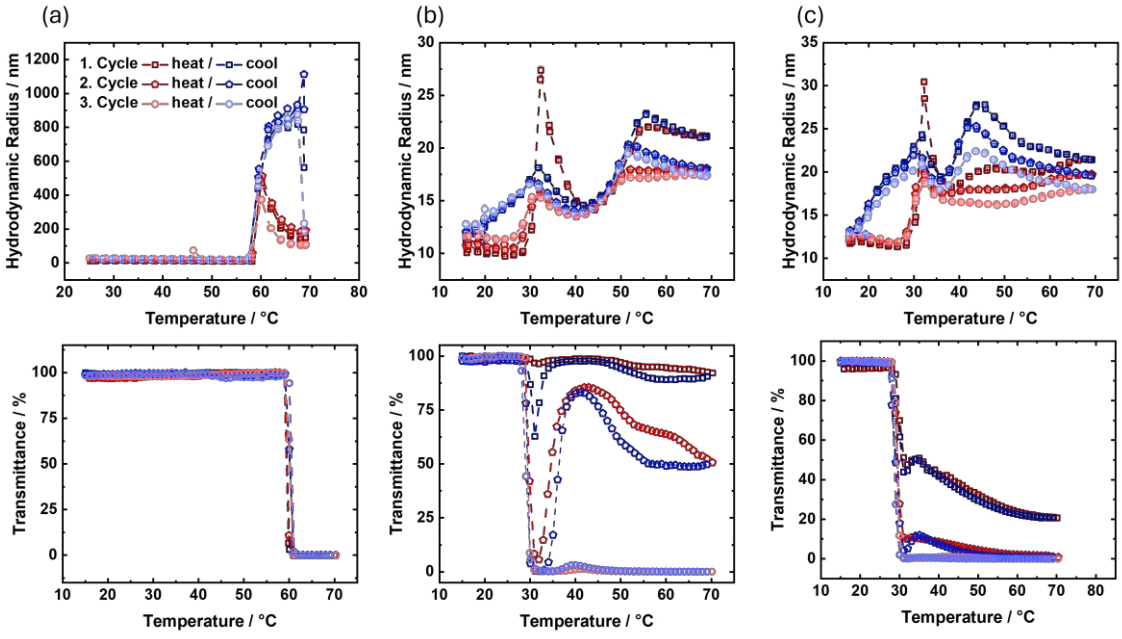


Figure 60. Temperature-responsive analytics of B03 (a), GN01 (b), and GN02 (c). The top row shows the hydrodynamic radius plotted against the solution temperature. The bottom row shows the transmittance of the respective polymer solution at a wavelength of 800 nm and varying temperatures. The DLS measurements of the hydrodynamic radius were conducted with a polymer concentration of 0.1 %(*w*/*w*). The UV-Vis measurements were performed at a polymer concentration of 1.0 %(*w*/*w*).

The reported transition temperature for a comparable P(OEGMA-*r*-BTPEMA) copolymer is around 60 °C.[1] This behavior was confirmed by temperature-dependent DLS experiments and UV–Vis transmittance measurements of B03 (**Figure 60** (a)). However, while cooling, one difference in the literature results appeared in the DLS experiments. In the literature comparing the heating and cooling curves, the measured R_H showed the same behavior with a slight shift toward lower temperatures when the sample was cooled. This behavior is logical because in order to redissolve, the polymer must first swell again, and the stabilizing hydrate shell must be formed again, which is kinetically slower than the collapse of the polymer coil and the hydrate shell. When looking at the R_H measured in this work (**Figure 60** (a) top graphic) while cooling the sample, the R_H jumps to four or five times the initial value. This behavior indicates the formation of clusters of the as-formed aggregates. However, these clusters redissolve upon further cooling, and the original state is rapidly regained when the solution temperature falls below 60 °C. A similar behavior was observed for PDMAEMA homopolymers and was referred to as an effect of the HOOC-chain end for these polymers. Since the general mechanism of the thermos-responsive behavior of POEGMA and PDMAEMA is the same, it is likely that these results are also a result of the hydration of the COOH-chain end. The difference between these results and those reported in the literature by J. Xu and V. Abetz is due to the shorter POEGMA chain length and the higher BTPEMA content in B03, consistent with the findings for the P(DMAEMA) precursors as well.

The double temperature-responsive behavior of the POEGMA-*g*-PNiPAM copolymer species was already well described by J. Xu and V. Abetz in the literature.[1] They categorized this behavior of the polymer into three different stages, illustrated in **Figure 61**. In stage I, where the solution temperature is below the transition temperature of both polymer components, the polymer is dissolved, and each polymer chain exists individually in solution. The second stage was defined as the temperature region between the transition temperature of the PNiPAM component and the PTT of the POEMA component. In this region, the polymer chains assemble into a specific core-shell structure, with the collapsed PNiPAM forming the hydrophobic core, stabilized by the POEGMA backbone. This structure is additionally stabilized by the hydration of the hydrophilic carboxylic acid chain end. The authors described the assembly of about three individual polymer chains into one aggregate as a flower-like assembly. The beginning of the second stage is defined by a rapid increase in the hydrodynamic radius observed via DLS experiments due to the formation of the aggregates described above. Increasing the solution temperature decreases the observed radius. This is explained by the progressive collapse of the PNiPAM core of the structure, where residual water molecules that are bonded in the PNiPAM core are forced out of the structure. The third stage is initiated around the transition temperature of the POEGMA backbone, as indicated by a second rapid increase in the R_H. At this stage, the flower-like structures form larger agglomerates to reduce the increasingly unfavorable surface

area between the POEGMA shell and water. The authors described two classes of POEGMA-*g*-PNiPAM copolymers based on the group used in the backbone. They observed a distinct difference in the responsive behavior when using end groups with different hydrophilicity. They found that the formed agglomerates can be stabilized in solution due to the carboxylic acid's maintained hydration. The same three stages are observed for the P(OEGMA)-*g*-P(NiPAM) copolymers analyzed in **Figure 60**, with slight variations at different P(NiPAM) chain lengths.

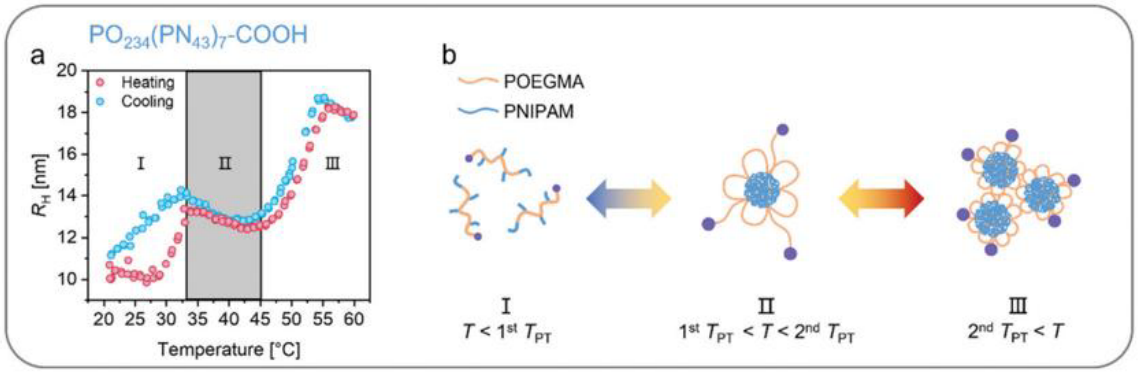


Figure 61. Temperature-dependent plot of the R_H (a) and illustration of the three stages of polymer chain assembly for P(OEGMA)/P(NiPAM) graft copolymers (b) with carboxylic acid as the chain end-group. Reprinted with permission from the open-access source *Soft Matter*, **2022**, 18, 2082–2091.Copyright 2022, Royal Society of Chemistry.[1]

In addition to the DLS experiments, temperature-dependent transmittance measurements were conducted using a polymer content of 1.0 %(*w*/*w*). For the UV–Vis temperature-dependent transmittance investigations described in the literature, a 0.5 %(*w*/*w*) polymer concentration was used. Their results supported the theory of forming larger aggregates stabilized by the hydration of the carboxylic acid group. They confirmed their assumption by noting that the solution's transmittance only dropped slightly after reaching the second transition temperature of the polymer.

The reason why, in this work, a polymer content of 1.0 %(*w*/*w*) was chosen instead of 0.5 %(*w*/*w*) was to achieve comparability with the other polymer species described in the previous sections. Because of that, slight differences between the results observed in the literature and this work are plausible. For the DLS experiments, each solution was heated and cooled in three cycles.

Compared to the literature, GN01 shows a similar molecular weight and a similar NiPAM weight fraction embedded within the chain. Interestingly, especially for the first temperature cycle, the transmittance curve (**Figure 60** b at the bottom) indicates a sufficient stabilization of the polymer within the solution at a temperature above the polymer's second transition temperature, as observed in the literature. However, this stabilization fails when lower heating/cooling rates are applied during the second and third cycles. This is most probably caused by the higher polymer concentration. The decreased heating rates were applied to rule out the possibility that a premature sample measurement masked a slower reassembly effect of the chains after reaching a specific

temperature. Therefore (in the first temperature cycle), the measurement at each temperature was taken five minutes after the sample reached the next temperature step.

In contrast to the first cycle, a 300-second (10-fold increase) waiting period was applied after reaching each subsequent temperature step. After evaluating the measurement results, a kinetic effect was ruled out primarily based on several similar observations. It appears that temperature-responsive polymers need at least one cycle to show reproducible temperature-responsive behavior. The COOH-terminated polymers are especially prone to such unexpected behavior at times (also compared to **Figure 29**). Since the second and the third temperature cycles shown in **Figure 60** (b) and (c) at the bottom are conducted with the same procedure and show differences in their behavior, it was assumed that the rate at which the solution was heated is not causing the observed drop in the transmittance based on the destabilization of the polymers. It is also safe to assume that the results observed are, in fact, end-group effects. This statement is supported by the more rapid behavior in the transmittance measurement of GN02.

Since the molecular weight of GN02 is higher than that of GN01, a decreased end-group effect is expected, causing a substantial decrease in the solution transmittance at the transition temperature of the NiPAM component in the material. After this first drop, the polymer shows nearly no redissolving caused by the reorganization of the polymer chain. This stands in great contrast to the behavior of GN01. In the first cycle, the polymer only showed minor changes around the PNiPAM transition. In the second cycle, a more pronounced transmittance drop was observed at the PNiPAM transition temperature, which was compensated mainly by the polymer's reorganization. The fact that, for hydrophobic chain ends, as investigated in the related publication, the transmittance does not increase again after surpassing the transition of PNiPAM indicates that a COOH-chain end is supporting the polymer's reorganization process in a manner that the polymer can compensate for the hydrophilic to hydrophobic transition of PNiPAM up to a certain extent. This compensation effect is decreasing with the number of cycles. As a temporary explanation, the shielding of the carboxylic acid by other chain components is assumed, prohibiting the chain end's hydration. The idea is that this shielding effect arises from hydrogen bonding between the carboxylic acid and the amide of the NiPAM units. This would also explain why the polymer's stabilization effect is much weaker at higher PNiPAM contents. The suggestions remain to be proven in future research.

5.4.2.2. Preparation of Au nanosphere (GNS) hybrids using a double temperature-responsive graft copolymer as a stabilizing particle shell

Before B03, GN01, and GN02 were synthesized and used for the stabilization of GNS, several tests were conducted prior to related grafted copolymer structures to find a proper reproducible protocol for the preparation of GNS@polymer hybrids with a predictable temperature-responsive nature. In parallel with the first grafting approaches based on the procedure described by P. Vana's group[247], another preparation protocol was tested for synthesizing the hybrid structures. All polymers used for the stabilization of GNS are presented in **Table 5**.

Table 5: Concluded polymer characteristics that were used for GNS stabilization. The table concludes the degree of polymerization of OEGMA (DP_O), the degree of polymerization of BTPEMA copolymerized with OEGMA (DP_B), the degree of polymerization of NiPAM in each chain-branch ($DP_{N/chain}$), the theoretical number average molecular weight calculated from the polymerization kinetic results ($M_{n,th}$), and the number average obtained via SEC measurements ($\bar{M}_n$). Additionally the molecular weight dispersity ($Đ$) and the batch size volume of the polymerization are provided for better transparency.

Stabilizing Polymer	DP_O	DP_B*	$DP_{N/chain}$	$M_{n,th}$ kDa	$\bar{M}_n$ kDa	$Đ$	**Batch size**
TB-GN1	233	12	40	134	134	1.9	12ml
TB-GN2	273	6	46	122	88.4	1.5	12ml
B03	233	11	-	69.9	35.6	1.6	460 mL
GN01	233	11	34	115	108	1.5	50 mL
GN02	233	11	49	138	147	1.5	50 mL

*Does not equal the number of TTC functionalities N_{TTC} (=1+DP_B).

First, homogeneous GNS were synthesized using the high-shape-and-size-selective inverse Turkevich GNP synthesis described by F. Schulz and coworkers. Several batches of citrate-stabilized GNS (GNS@citrate) were obtained using this method. **Figure 62** provides different examples of the analytical results of the GNS@citrate suspensions. The average diameter of all successfully synthesized samples varied in the 11.9 nm to 13.7 nm range and showed a λ_{LSPR} around 520 nm. These results agree with those reported for the original synthesis.[63] The particle diameter was additionally confirmed via SAXS measurement of T01, where an average particle radius of 6.35 ± 1.46 nm was found (**Figure 62 (c)**). To develop a reliable routine to synthesize GNS hybrids with the polymers from **Table 5**, only particle batches that show particle diameters within the range mentioned above were chosen. For quality assurance, every sample was first investigated visually after cooling. Secondly, a UV–Vis absorbance spectrum was taken to check if the LSPR is within the 515–520 nm range. If a sample met these two criteria, the sample was investigated via TEM, and the particle diameter was determined.

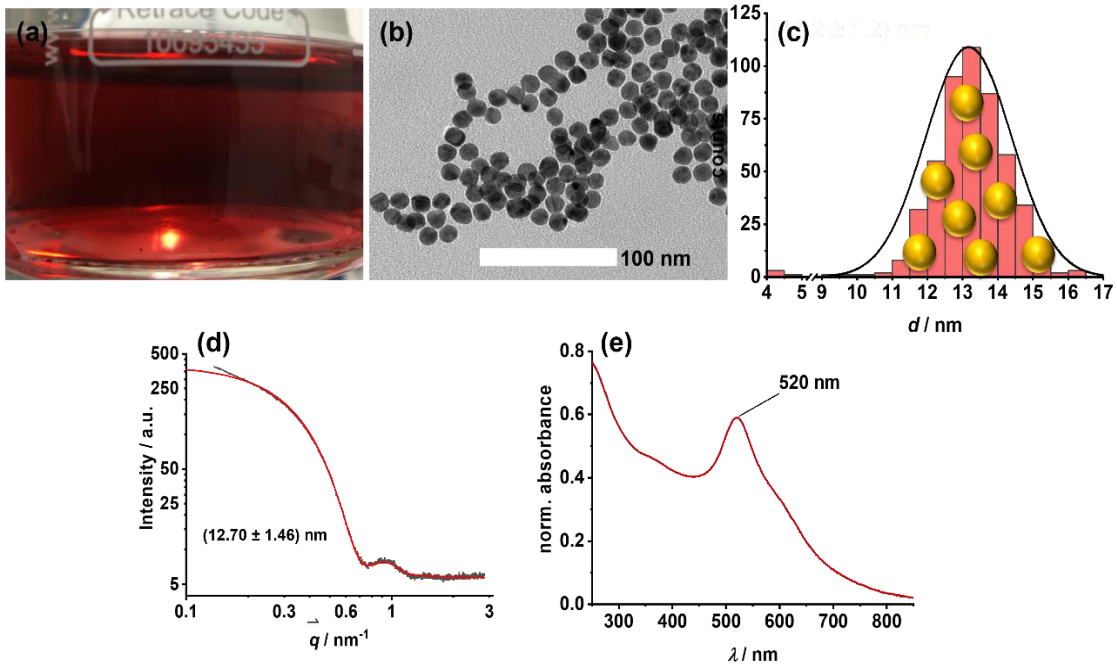


Figure 62. Analytical results of a representative citrate-stabilized GNS sample synthesized via the optimized inverse Turkevich synthesis from F. Schulz and coworkers.[63] This figure provides an image of the particle suspension with the characteristic red color (a), a TEM image of the obtained GNPs (b), and the particle diameter distribution obtained from the TEM evaluation is plotted in a histogram (c). Furthermore, SAXS results (grey) and the corresponding data fit (red) are shown in the graphic (d). In (e), the UV–Vis extinction spectrum of a representative GNS@citrate sample is plotted.

Regarding applicability, the first tests of the hybrid preparation using a grafting-to approach used several graft polymers based on different P(OEGMA-*r*-BTPEMA) base polymers. Since the general pathway for the topic was not fully set at this point, finding a reliable, straightforward way to prepare the GNS@polymer hybrids was the first challenge. During these tests, it became clear that the preparation method plays an essential role in the later found temperature-responsive properties of the obtained hybrids.

Two preparation approaches were tested in comparison to each other. **Figure 63** provides exemplary TEM images of the particle hybrids obtained by the two preparation methods. Both approaches started the same way by adding a solution with a defined volume and polymer concentration to the GNS@citrate suspension. After that, the prepared mixtures were purified either by several centrifugation cycles or by dialysis in a water bath for seven days.

For the dialysis-based preparation, after adding the aqueous polymer solution to the GNS@citrate suspension, the mixture was placed directly into a dialysis tube. An exchange of the excess citrate was ensured by frequently exchanging the water bath, in which the dialysis tube filled with the sample was stored. A dialysis tube with a molecular weight cutoff of 6–8 kDa was chosen for the dialysis.

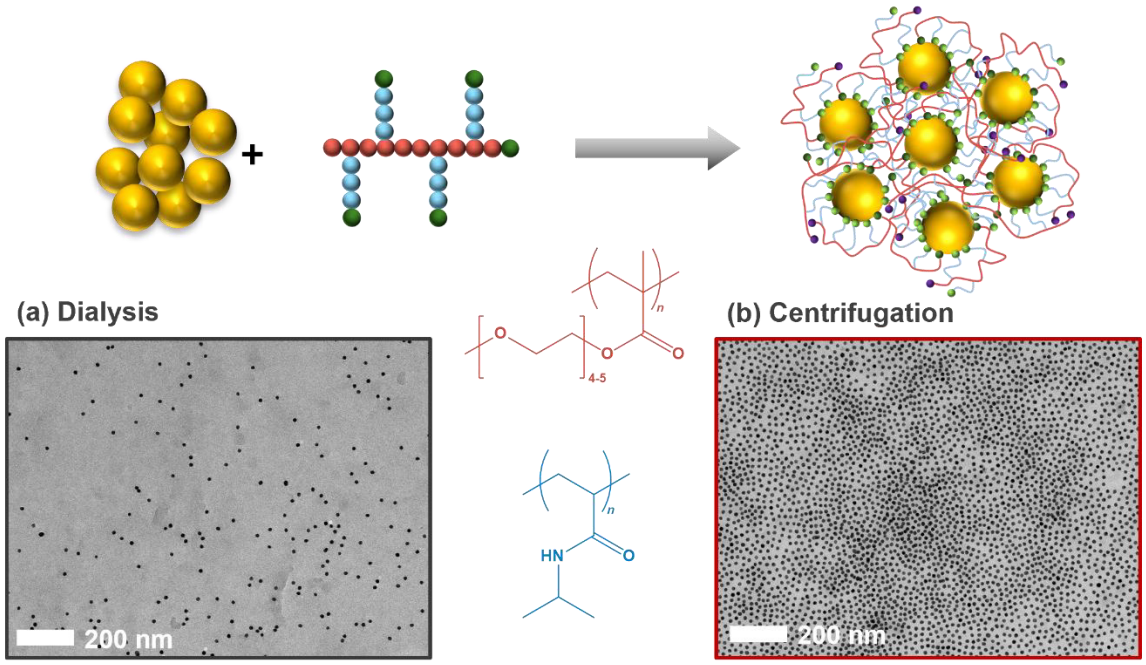


Figure 63. Preparation scheme of the GNS@polymer hybrid material and representative TEM images of the particle hybrids obtained by the dialysis-based grafting to approach (a) and the hybrids obtained by the procedure closely following the protocol described by P. Vana and coworkers (b). To prepare the TEM measurements, the samples were drop-cast onto a TEM copper grid, dried under air, and covered with a watch glass to prevent contamination by dust.

Before removing the excess free citrate and polymer from the sample via several centrifugation and redispersion steps, the polymer/GNS mixture was stored between 24 and 48 hours in the dark at 0 °C to provide sufficient time for the ligand exchange. This preparation method is grounded in and closely related to the preparation described by P. Vana and coworkers.[247]

The exact procedure of both preparation methods can be found in Section 7.2.3.3. The TEM images in **Figure 63** (a) and (b) show a clear difference in the preferred particle assimilation between the hybrids obtained from the differing preparation methods. Both methods made it possible to resolve particle clusters (compare with **Figure 62** (b)) and isolate the particles from each other. Additionally, the samples that underwent the centrifugation treatment frequently showed organized particle assimilations over large areas of the TEM grid. These long-range particle assemblies are characteristic only of this kind of hybrid preparation. Due to the fragility of the carbon film, the exact extent of these long-range assimilations is hard to estimate.

During the TEM measurements, it was observed that the sample caused the carbon film to break, especially at regions where assimilations, like in **Figure 63** (b), are present, leaving only the corners of each grid intact. It was assumed that this phenomenon was caused by the shrinking of the polymer shell due to the removal of residual water in the hybrid film, caused by the high vacuum in the sample chamber of the TEM. The corners of the grid's holes are not affected much by the force caused by the shrinking because the grid's bars are close enough to compensate for these forces.

Despite the distinct differences between the preferred particle assembly of the two samples on the TEM grid, no differences in the particle quality or other sample impurities were observed via TEM. The ordered structures observed in the centrifuged sample can be explained by the increased forces acting on the sample during centrifugation. An additional observation for some samples during preparation was the formation of clusters that were only partially redispersed and required ultrasonic irradiation. Later, these fractions are found to be mainly composed of the assembled structures shown in **Figure 63** (b).

During the experiments, special interest was given to the plasmonic behavior. The polymer shell was expected to serve as a temperature-responsive spacer between the particles, which could later be used to reversibly control interparticle coupling. Such systems are interesting materials for multiple purposes. For example, they can serve as colorimetric temperature sensors. For a GNS hybrid to be qualified as a sensor material, a high degree of reversibility is beneficial. Therefore, the samples were tested throughout several heating cycles, and the UV–vis absorbance spectra were measured at defined temperature steps. For evaluating the LSPR shift, every absorbance spectrum was fitted around the absorbance maximum (475 nm – 600 nm) with a 9^{th}-order polynomial fit (**Figure 64**, top graph). The maximum was determined from that fit, and the corresponding wavelength at this maximum was plotted against the respective temperature. The results are presented in **Figure 64** (a) and (b) for the selected samples described earlier.

Logically, the sample preparation can alter the nature of the resulting product, as already discussed and shown by the TEM images in **Figure 63**. However, the difference between the two hybrids' responsive behaviors was still surprising. In fact, both systems exhibit opposite behavior when examining the temperature-dependent LSPR shifts. The particle diameters were not affected by the performed ligand exchanges. As a result, a ′gold-core-based explanation′ for the difference between the two preparation methods can be excluded.

As a baseline for the description of both systems, it was assumed that, due to the exchange of citrate by the double-temperature-responsive graft copolymer, the particle shell should collapse as the medium temperature increases. This collapse can cause a cascade of different events. As mentioned in the introduction, many factors can cause a shift in the absorbance maximum of stabilized GNP suspensions. To explain the observed shifts of the two hybrids in **Figure 63** and **Figure 64**, many of the named reasons must be considered simultaneously. Most important are the effects like particle-particle plasmon coupling after falling under the GNP size-specific critical interparticle distances (d_c) and changes in the refractive index near the particle surface.

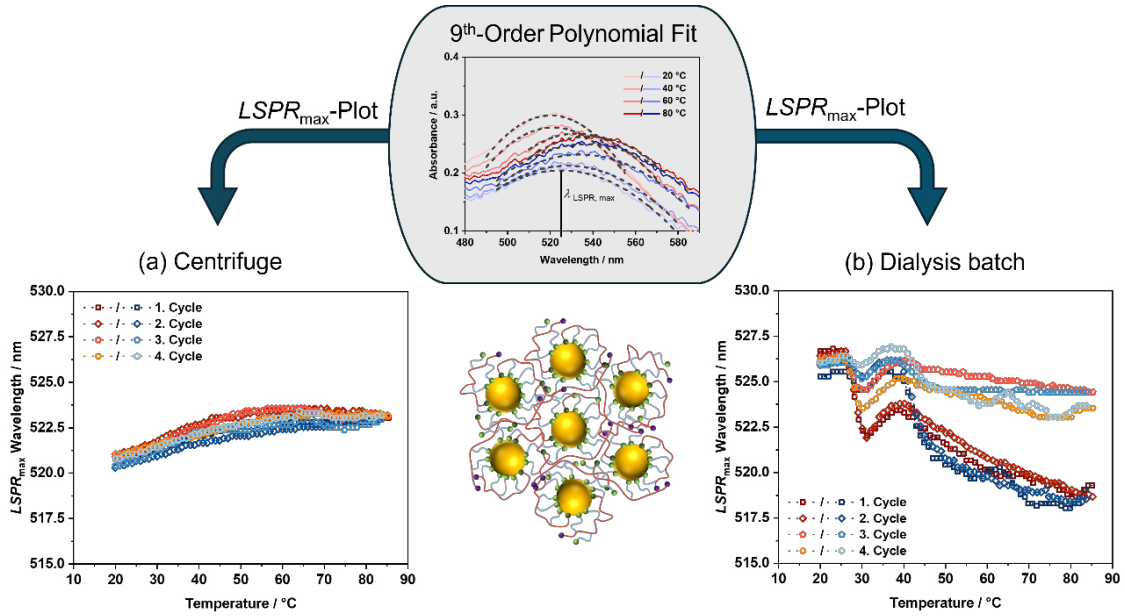


Figure 64. An example of the temperature-dependent LSPR shifts of two exemplary GNS@Polymer hybrids prepared using different methods, but the same GNS suspension and double temperature-responsive PNiPAM-graft copolymer (TB-GN1). The top graphic shows the principle applied to obtain the results in plots (a) and (b). In (a), the obtained temperature-dependent LSPR maximum wavelength of the hybrid prepared after the method of P. Vana et al. is shown.[247] The same is plotted in (b) for the hybrid material isolated via dialysis.

The change of the local dielectric constant in the proximity of the particle surface and interparticle coupling is of special importance in this consideration. As a rule of thumb, it can be stated that small shifts (≤10 nm) of the absorbance maximum are derived from changes in the surrounding dielectric constant. Meanwhile, big changes (≥10 nm) are more likely to be caused by interparticle plasmonic coupling. For instance, depending on the direction, the dielectric constant changes, allowing a blue- or red-shift of the LSPR frequency. Both LSPR shifts described in **Figure 64** (a) and (b) fall under this range. Both samples were measured using the same temperature protocols. First, the sample temperature was set to 20 °C, and the first extinction spectrum was measured. After that, the samples were heated in 1 °C-steps. When the respective temperature was reached, an equilibration time of 30 s began, after which the next spectrum was measured. This procedure was repeated until a final suspension temperature of 85 °C was reached, at which point the cooling cycle began. The same equilibration time was set for every temperature step for the cooling cycle before performing the subsequent measurement. After the first cycle was completed, the following heat/cool cycle was started. After the first cycle, an equilibration time of 5 minutes was applied to the following heating/cooling cycles to exclude the kinetic effects that influence the results.

Like the DMAEMA samples from the in-situ approaches (Section 5.4.1), the graft copolymer-based GNS hybrids were prepared by following P. Vana et al.'s approach does not show rapid temperature-dependent behavior. Throughout the temperature region of the measurement, the LSPR maximum redshifts from ~521 nm to ~523 nm, depending on the respective heating cycle.

The shift follows a quasi-linear dependency within the region between 20 °C and 40 °C. Above this temperature region, the shift slowly approaches a constant value.

The sample prepared in the dialysis tube (**Figure 64** (b)) shows contrary behavior. The shift observed for that sample clearly shows double temperature-responsiveness. Other than expected initially, the LSPR of that sample is blueshifting. The sample first shows a significant shift around the transition temperature of the NiPAM segments of the used polymer. Around a suspension temperature of 30 °C, the λ_{LSPR} shifts to 522 nm as an intermediate state. With increasing temperatures, λ_{LSPR} redshifts of about 2 nm until 35 °C are surpassed. After this intermediate maximum, the LSPR blueshifts gradually. When the maximum suspension temperature of 85 °C was reached, the LSPR maximum shifted to 518 nm. While cooling, this whole process was reversed. The second temperature cycle shows behavior similar to the first. The dependency of the LSPR maximum observed reminds one of the three stages described for the temperature-dependent nature of the free polymer's assimilation process (compared with **Figure 60** (b) and (c), bottom graphics). Because decreasing the average particle-particle distances should cause a redshift in the obtained LSPR absorbance maximum, they do not explain the obtained results. Increasing the average interparticle distances would at least explain the observed blueshift. However, this is also an improbable scenario because this would mean that the particles are already within the critical coupling distance and that this distance is increasing simultaneously with a collapse of their stabilizing shell. The expected LSPR change would be much more substantial than the observed blueshift. When looking at the initial λ_{LSPR} (@20 °C), (b) is already redshifted with λ_{LSPR} = 527 nm. Sample (a) has λ_{LSPR} = 521 nm. Considering the low reproducibility of the dialysis sample, it is likely that an incomplete ligand exchange is the cause of this behavior. For this sample, groups other than the TTC functionalities may stabilize the particles' surface, which are slowly exchanged by the TTC functions of the polymer. This would explain the changing temperature-responsive nature of the sample because the attachment of the polymer to the particle's surface is still changing, altering the polymer shell morphology.

However, mainly because of the similarity of the observed shift with the temperature-dependent absorbance behavior of the pure polymer solutions, it is more likely that scattering effects caused by free-polymer chains of the suspension are the explanation for the observed temperature dependency of the λ_{LSPR} of the sample (b) prepared by the dialysis protocol. However, the optical behavior of the dialysis-protocol-based sample is interesting. Due to the long preparation protocol and the lack of reversibility in the temperature-dependent behavior, this preparation method was dropped, and the focus shifted to the more time-efficient centrifugation-based hybrid preparation. **Figure 65** shows the optical behavior of another sample prepared by the centrifugation method, comparable to the sample (a) from **Figure 64**.

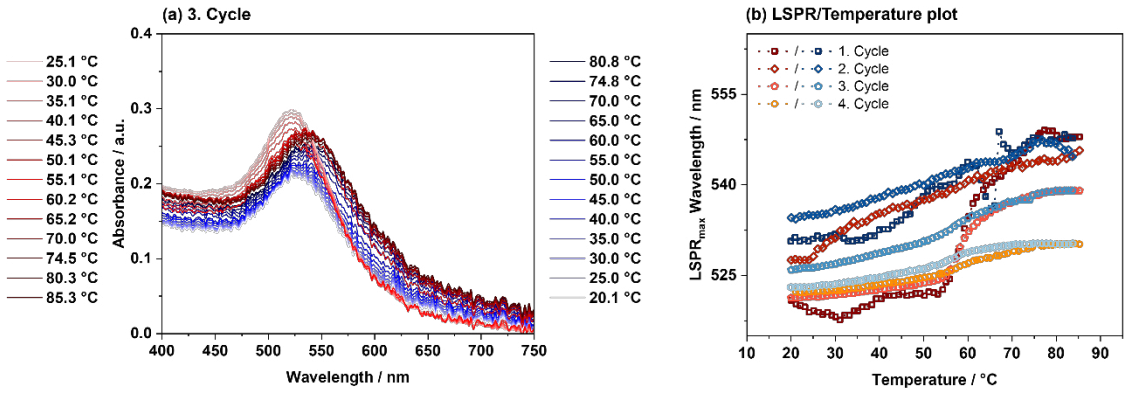


Figure 65. Temperature-dependent properties of a TB-GN2-based GNS@copolymer hybrid (GNS@TB-GN2) prepared and purified by the centrifugation protocol. Graphic (a) represents the absorbance spectra of the hybrids measured during the particle suspension's third heating/cooling cycle around λ_{LSPR} every 5 °C. Graphic (b) shows the λ_{LSPR} from each UV–Vis extinction spectrum during the different temperature cycles of the measurements.

An advantage of the centrifugation method based on P. Vanas' and his coworkers' procedure above, the preparation via dialysis, is that it allows the reliable removal of excess polymer from the sample, leaving only the GNS-hybrid particles in the product suspension if appropriately prepared. The sample shown in **Figure 65** was also prepared using this method. In contrast to the sample discussed in the previous figure, this sample was prepared with another graft copolymer (TB-GN2). According to the ^{1}H-NMR results, TB-GN2 has an $M_{n,th}$ = 122 kDa, with a PNiPAM mass content of 30 % and six PNiPAM side chains. Compared to that, TB-GN1 has an $M_{n,th}$ of 134 kDa, a PNiPAM mass content of 44 %, and 12 NiPAM-side chains. The strong LSPR redshift of the sample occurring upon heating is particularly interesting. Like the other samples shown in **Figure 64**, the sample from **Figure 65** underwent four temperature cycles of the UV–Vis extinction measurements. However, the first two measurements are shown only for completeness. While undoubtedly impressive, the measurements showed an unexpected absorbance, most likely due to the use of the wrong blank sample, as indicated by the strong LSPR shifts. The absorbance spectra showed the expected shape for the third and fourth temperature cycles. Therefore, the results from the third cycle are the first reliable results for that sample. When following the λ_{LSPR} at different temperatures of that third cycle, it first shows a flat redshift at increasing temperatures between 20 °C and approximately 55 °C. In this area, the shift is approximately linear. In the temperature region around the P(OEGMA)-backbone, this redshift rapidly increases from a λ_{LSPR} ≈ 525 nm at 55 °C to a λ_{LSPR} ≈ 539 nm at 85 °C.

While the plasmonic shift usually becomes noticeable after fitting the respective region of the extinction spectrum, for the TB-GN2-based hybrid suspension, the redshift of the LSPR band illustrated in **Figure 65** (a) is well noticeable. The red curves in this graphic represent the extinction spectra obtained during the heating in the third cycle. The blue-colored curves show the original extinction spectra obtained while cooling the aqueous NP suspension. The observed strong maximum shift described in **Figure 65** gradually dampens with every temperature cycle until, in the fourth cycle, only an overall redshift of 9 nm was observed.

By using temperature-dependent SAXS (**Figure A12**) measurements, it was found that this shift is likely to be caused by the formation of particle assemblies in which the interparticle distances had surpassed the critical particle-to-particle distance, and LSPR coupling was enabled. This observation was an important milestone in this topic. Because particle assemblies are more likely to precipitate from the suspension, the formation of these assemblies can explain the limited reversibility of the optical behavior. This precipitation is also indicated by a decrease in the plasmonic signal's absorbance intensity during the measurement cycle in the extinction spectra shown in **Figure 65** (a). At the time of this measurement, it was fascinating to observe such a significant redshift. Further investigations aimed to reproduce these results as accurately as possible, seeking a balance between a substantial plasmon shift and a reproducible temperature-dependent plasmonic nature. Improving the reversibility of the temperature-dependent shift was one of the main topics during these tests.

Several experiments were conducted using the same graft copolymer. For these experiments, different polymer concentrations were tested for the ligand exchange reaction. When preparing the previous samples, it was observed that the aqueous supernatant after the first centrifugation contained significant amounts of polymer, which was associated with an occasional pale-yellow appearance of the remaining solution. Aside from that, the first supernatant showed no optical signs of residual particles. This was assured by leaving a small amount of the supernatant (<0.5 mL) in each centrifugal tube. Because the idea was to trigger plasmonic coupling by adjusting the interparticle spacings by means of the double temperature-responsive copolymer structure, and because the results indicated that the particle stabilization plays an essential role within the process, the goal was to reduce the amount of polymer surrounding each particle by reducing the amount of polymer used for the ligand exchange. The idea was that reducing the amount of polymer would decrease the minimum interparticle distances, which would cause stronger interparticle coupling. By finding a sweet spot between polymer-stabilized particle surface area and surface area not stabilized by the used copolymer, it was assumed that a particle system should show relatively strong temperature-dependent $\Delta\lambda_{LSPR}$ and maintain better reversible optical behavior. However, the observed temperature-responsive optical behavior did not correlate with the amount of polymer used for ligand exchange.

The precipitate formed during the centrifugation was usually redispersed in methanol before the second centrifugation cycle at -5 °C was started. This precipitate was significantly harder to redisperse when using lower amounts of polymer for particle stabilization. The original idea was that, using lower amounts of polymer, the particles' surface areas not stabilized by the copolymer should still be stabilized by residual citrate. Following the observed results, this mixed stabilization is either not obtained in the first place or behaves differently from what was hoped. After rethinking this approach, this behavior is not surprising because, to achieve such mixed stabilization, citrate should have been added to the suspension during the purification protocol to capture free surface vacancies. Of course, if less polymer stabilizes the particles and no additional ligand is present to compensate for this unstable surface area, the GNS particle hybrid is less likely to form a stable suspension.

Additionally, even if a mixed stabilization was obtained at some point, this does not automatically mean that the hybrid system must show the desired reversible optical behavior. Because ligand-based particle stabilization is a dynamic process where exchanges happen regularly, it is possible that the polymer still displaces the residual citrate at the particle surface and keeps it from reattaching to the surface by sterically blocking the volume around the particles. If this theory applies to the TB-GN2 stabilized sample, it will explain (aside from the evident precipitation) the observed dampening of the LSPR shift. Long story short, reducing the polymer amount was neither effective in targeting better reversible behavior, nor did this investigation give any specific insights into how stronger $\Delta\lambda_{LSPR}$ can be obtained using the centrifugation protocol.

At this point, the polymers from the previous Subsection 5.4.2.1 came into play. Rather than focusing on a strong LSPR shift, the focus shifted toward reversibility and a deeper understanding of the nature of the stabilization. Since reducing the polymer concentration was ineffective, a higher polymer concentration of 0.5 %(*w*/*w*) was used for the ligand-exchange suspension. Also, thanks to the higher-scaled polymerization, the scale of the ligand exchange was increased. This scale-up enabled easier handling of the manual steps between centrifugations and reduced batch-to-batch variation caused by manual supernatant removal. For all preparations, it was usual that the supernatant could not be entirely removed after centrifugation without a significant loss of the precipitate caused by the manual handling of the samples. Especially after the second centrifugation, where methanol was used as the liquid medium to redisperse the particle precipitate, the loss of particles appeared frequently. To minimize particle losses during preparation, a specific amount of solvent was retained in the centrifugal tube.

The results of this scaled-up hybrid preparation are concluded in **Figure 66**. The figure shows representative TEM images of the original GNS@citrate particles (a) and TEM images of the resulting hybrids from this GNS@citrate batch using the polymers B03 (b), GN01 (c), and GN02 (d).

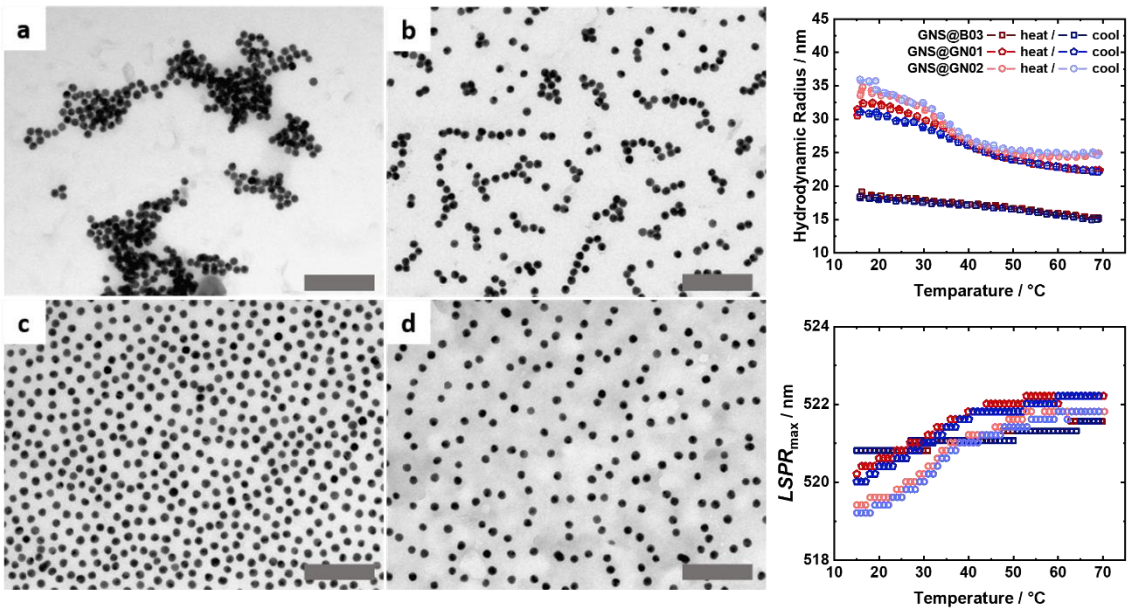


Figure 66. Result of the optimized preparation procedure of GNS@polymer hybrids using a stepwise centrifugation protocol for particle purification. In (a–d), TEM images are provided from the GNS systems drop-cast on a copper TEM grid stabilized by citrate, B03, GN01, and GN02, respectively. The scale bars in the TEM images are 100 nm. The plots on the right show the temperature-responsive behavior of the three polymer-stabilized samples dispersed in water, with the R_H plotted against the suspension temperature (top graphic) and the λ_{LSPR} at different suspension temperatures (bottom graphic).

The larger scale enabled a more reproducible procedure. In general, the supernatant was carefully removed by using a pipette. However, after removing most of the supernatant, a significant amount of the precipitate tended to redisperse due to vibrations caused by handling the samples. Using a larger volume for the ligand exchange, the total amount of solvent left was better adjusted to a defined volume because the sample was separated into several centrifugal tubes, and statistical variations were mostly balanced. This balance made defining a fixed volume of remaining supernatant transferred into the next centrifugal cycle easier.

As shown in **Figure 66**, the original GNS@citrate particles tend to form unordered agglomerates when drop-cast and slowly dried on the carbon film of the TEM grid. This formation was not observed during the TEM measurements for the polymer-stabilized samples. The particles are mostly isolated from each other, especially for the GN01 and GN02 stabilized particles. Interestingly, the particles stabilized by the P(OEGMA-*r*-BTPEMA) backbone B03 tend to form short chain-like structures after drying on the TEM grid.

Meanwhile, the GNS@GN01 sample shows no such assemblies. In this sample, the particles are closely packed (compared to the other samples) on the TEM grid. Due to the higher molecular weight of GN02, GNS@GN02 is not as closely packed as GNS@GN01. However, the difference between GNS@GN01 and GNS@GN02 may also be caused by residual water dissolved in the GN02 shell, resulting from incomplete sample drying. The hybrid GNS@GN02 also shows signs of linear particle assemblies. Of course, particle assemblies are always tricky, and the dried sample does not necessarily represent the sample dispersed in water. The TEM results strongly

indicate a successful citrate exchange with the respective polymer. The difference between the GNS@citrate (**Figure 66** (a)) sample and the TEM images from the other samples, as well as the formation of ordered structures, indicates a successful formation of a polymer shell around the particles.

The advanced purification protocol delivered well-reproducible temperature-dependent results. The samples withstood three temperature cycles and only showed statistically insignificant variations (Appendix **Figure A13** and **Figure A14**). The achieved reversibility of temperature-dependent behavior was an important milestone for this topic. Due to this reversibility, a more detailed study of the polymer influence on the temperature-responsive behavior of GNP@polymer hybrids was possible. As in the Au@P(DMAEMA) hybrids observed before for most samples, the temperature-responsive behavior of the hybrids described in the two graphics on the right of **Figure 66** shows no specific transition point of the two characterized physical values. This is interesting, especially for the hybrid GNS@GN01 and GNS@GN02, because the stabilizing polymer shell has two well-resolved transitional states.

Comparing the responses of the three samples, a polymer-dependent dependency of the R_H becomes evident. With initial R_H-values (@15 °C) of 19 nm, 31 nm, and 36 nm for the hybrids GNA@B03, GNS@GN01, and GNS@GN02, respectively, the R_H shows a distinct dependency on the molecular weight of the stabilizing polymer.

All three hybrids have in common that the R_H decreases upon heating due to the temperature-dependent collapse of the respective polymer shells. As expected in the previous sections, the R_H temperature dependency of GNS@B03 does not indicate a specific transition temperature at the PTT of B03 (60 °C). Like the Au@P(DMAEMA) hybrids, the dependency of the R_H on the medium temperature had a nearly linear character (corr. $R^2 = 0.96$ for the second cycle) in the measured temperature range. Due to the TTC functionalities on B03s' side chain, the polymer has several attachment points. These attachments to the gold surface significantly reduce the mobility of the polymer segments between the BTPEMA segments. In the case of P(DMAEMA) attached to the nanoparticles' surface, the additional attachment vacancies are provided by the amine functionalities in the side chain.

This type of connectivity is also comparable to the polymer-stabilized GNR hybrids described in Section 5.3. These polymers are designed to attach to gold surfaces with their face-selective quaternary amine groups. These similarities make the polymers described in this chapter, especially B03, ideal candidates for characterizing the responsive nature of the hybrids in this work.

With the initial goal of increasing the responsive nature of the system, the hybrids GNS@GN01 and GNS@GN02 show an intriguing character. For these systems, the additional responsive character of the P(NiPAM) component comes into play. With increasing P(NiPAM) weight content in the polymer, the influence of the NiPAM-based PTT becomes noticeable in the R_H curves and the temperature-dependent λ_{LSPR}. For both samples, the R_H decreases significantly faster after reaching 30 °C, the PTT of the first block of both GN01 and GN02 (compare **Figure 60** on Page 120). Naturally, this P(NiPAm)-based behavior is more pronounced in the GNS@GN02 sample.

Recently, P. Mulvaney and coworkers published several studies regarding the optical behavior of GNS stabilized with a crosslinked P(NiPAM) shell.[10–12] Among these studies, they formulated the dependencies described in Equation 5.1 and worked out the fuzzy sphere theory to explain the optical behavior of their particle system. An apparent similarity can be observed when comparing the shape of the temperature dependencies for the R_H form in **Figure 66** with the dependencies published for the fuzzy sphere model. This leads to the assumption that the present hybrid materials must be organized similarly on a nanoscopic level. Due to the observed behavior, the hybrid polymer shells can be approximated as a crosslinked structure. In Section 5.4.3, this issue is discussed in more detail.

In conclusion, it was possible to adapt the purification protocol described by C. Rossner et al.[247] in a way that provided well-stabilized GNS@polymer hybrids with reversible temperature-dependent behavior. It can be said that the preparation method discussed here, when applied correctly, is an excellent technique for synthesizing GNS@polymer hybrids.

5.4.3. Addressing the Open Questions About Temperature-Responsive Behavior of GNS@Polymer Hybrids Using Stimuli-Responsive Polymer Stabilizers: A Review of this Work Advances

The questions formulated in Section 5.4.2 (Page 106) are reconsidered based on the observed temperature-responsive characteristics from the GNS@copolymer hybrids discussed in the previous section. The results presented in **Figure 66** are discussed in more detail and combined with recent theoretical insights. A closer investigation of the responsive behavior shown in **Figure 66** reveals a close similarity to the temperature-dependent behavior described in the context of the mentioned fuzzy-sphere model. This similarity directly corresponds to the first question formulated in 5.4.2:

Is there a model that can reliably describe the underlying temperature-responsive process of such particle hybrid systems?

The similarities in the observed responsive behavior suggest that the responsive polymer matrix, with several possible anchoring groups along the polymer chain and side chains, can be described as a crosslinked network. The described fuzzy sphere model, initially developed for crosslinked GNS@P(NiPAM) core-shell hydrogels, provides a detailed description of the light scattering behavior of the GNS@polymer hybrid.[10–12] The temperature dependency of the R_H described in Equation (5.1) was applied to the hybrids in **Figure 66**. It can be shown that the obtained temperature-dependent R_H for all three samples converges with Equation (5.1). The fitting results for the second temperature cycle from each sample are shown in **Figure 67** and summarized in **Table 6**.

As a reminder, the weight content of P(NiPAM) increases from B03 with 0 % to 37 % for GN01 and 46 % for GN02. With increasing NiPAM content, the molecular weight of the polymer increases, and the number of repeating units between the TTC anchoring functions increases. This means that, when assuming the gold particle core as a crosslinker for the polymer, the theoretical crosslinking density decreases when the chain length of the P(NiPAM) segments increases.

In Equation (5.1), the term T_c can be described as the center temperature of the fitting function around which the curve evolves. For the GNS@B03 hybrid, no coherent center temperature was obtained by fitting the data, which was not surprising, given that the curve is more similar to a linear-like decay within the measured temperature range. For this hybrid, the values for T_c in the obtained fitting functions varied from 70 °C to 230 °C. For some measurements, the fit did not converge without adding some restrictions. Interestingly, when setting a fixed value for $T_C = 60$ °C (the PTT of B03), the factor h was determined between 17.6 °C and 23.1 °C, and the fitting function converged with reasonable results.

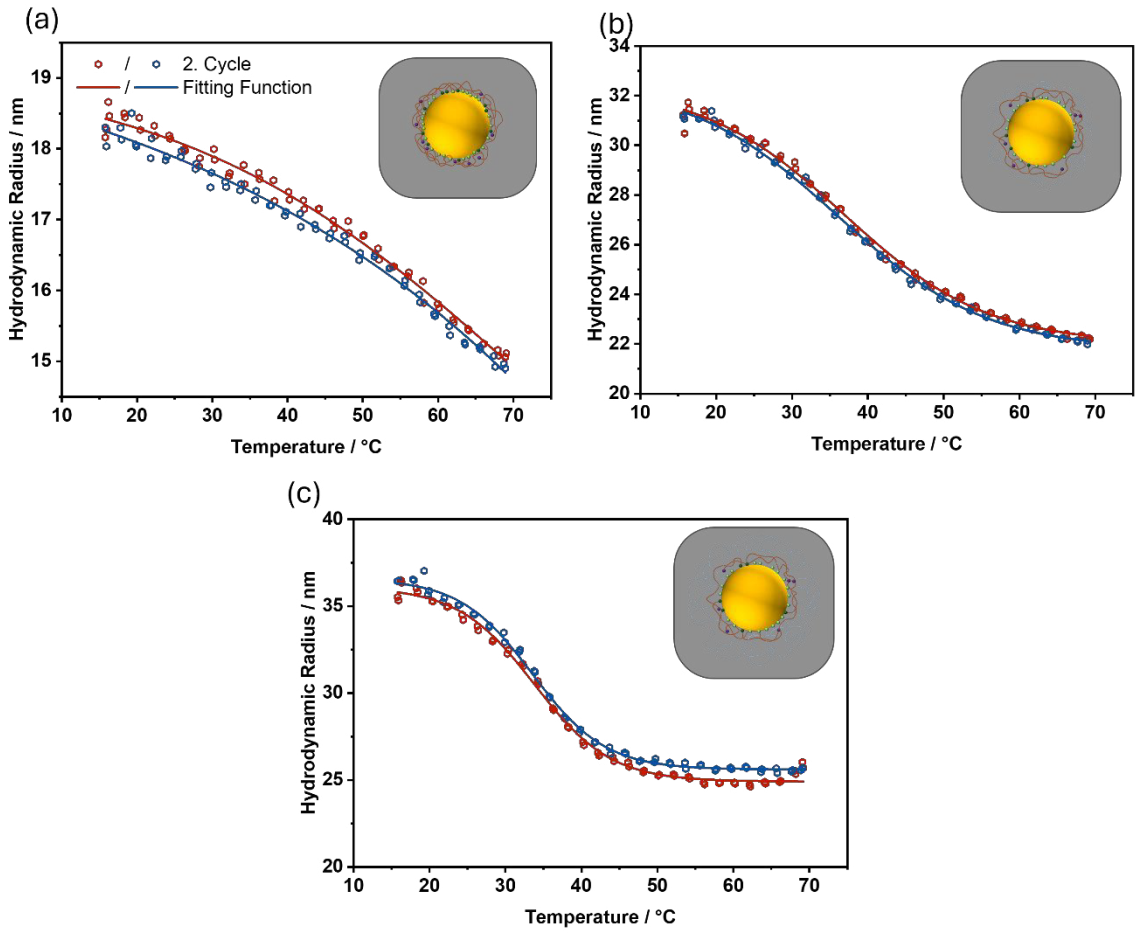


Figure 67. Temperature-dependent DLS measurements of the nanohybrids GNS@B03 fitted with the fuzzy sphere model (EQ 5.1) (a), GNS@GN01, and GNS@GN02 suspended in water. Plotted is the R_H obtained from the second temperature cycle against the respective suspension temperature for each hybrid system. The R_H values are fitted using the shown equation. The colors are coded with red for the heating curve and blue for the cooling curve.

Table 6: Concluded values obtained from the non-linear fits shown in **Figure 67**. This table includes the theoretical molecular weight-average of the stabilizing polymer used in the hybrid ($M_{n,th}$) and the percentage weight content of P(NiPAM) ($\%_{NiPAM}$) in the polymer. This table includes the fitting values for the heating and cooling curve of the second temperature cycle. The fitted values for the maximum ($R_{H,max}$) and minimum ($R_{H,min}$) hydrodynamic radius, the center temperature (T_c), the transition stepness h, and the reduced R^2 of the respective fits are provided in this table.

hybrid	$M_{n,th}$ **/ kDa**	$\%_{NiPAM}$ **(*w/w*)**	**curve**	$R_{H,max}$ **/ nm**	$R_{H,min}$ **/ nm**	T_c **/ °C**	***h*** **/ °C**	***red.*** R^2
GNS@B03	69.9	-	heat	18.8 ± 0.1	12.8 ± 0.1	60[a]	17.6 ± 0.6	0.989
			cool	18.7 ± 0.1	12.6 ± 0.1	60[a]	18.5 ± 0.7	0.991
GNS@GN01	115	37	heat	32.4 ± 0.1	22.0 ± (<0.1)	36.9 ± 0.1	9.4 ± 0.1	0.997
			cool	32.6 ± 0.1	21.8 ± (<0.1)	36.0 ± 0.1	9.8 ± 0.1	0.998
GNS@GN02	138	46	heat	36.1 ± (<0.1)	24.9 ± (<0.1)	33.8 ± 0.1	5.0 ± 0.1	0.995
			cool	36.6 ± (<0.1)	25.6 ± (<0.1)	33.6 ± 0.1	4.8 ± 0.1	0.996

[a]This value was fixed for the non-linear (Boltzmann) fit.

Fitting the R_H results from GNS@GN01 and GNS@GN02 was possible without fixing T_c to a specific value in advance. The specific fitting values are listed in **Table 6**. Interestingly, the T_c obtained from these fits was close to the NiPAM-based transition temperature of the stabilizing polymer. With the higher DP_N in GN02, the hybrid's T_c shifted further towards the NiPAM-based transition temperature. With increasing NiPAM content, the *h*-value also decreases. As described in the literature, the *h*-value can be taken as a measure of the system's fuzziness. A lower *h* corresponds to stronger responsive behavior in a hybrid material and correlates with increased fuzziness. Transferred to this system, the polymer's P(NiPAM) segments are more likely to form slopes loosely packed in the outer region of the hybrid structure.

Since no significant transition of the P(OEGMA) segment is observed, it is plausible that it is closely packed within the inner region of the polymer shell around the GNS in all three hybrids investigated. **Figure 68** illustrates the assumed hybrid structures. For clarity, the illustration shown is not true to scale. The carboxylic end-groups, illustrated with the purple spheres, are not placed at any specific area within the given illustration. Due to their high affinity for hydration, it is also possible that these groups are located at the outer surface of the polymer shell. However, because no specific effects were observed that can be definitively assigned to these groups, it is also likely that they are embedded within the shell structure and, therefore, shielded from the solvent. Additionally, due to the low weight content of these groups within the core-shell structure, the expected stabilizing effect of these groups was considered to be negligibly small. The amount of stabilizing carboxylic groups on the hybrid's surface is even more decreased compared to the copolymer precursor because they are also capable of binding to the GNP surface. The detection of the effect of these groups is therefore very complex. Experiments like temperature-dependent zeta-potential measurements could reveal the stabilizing effect of carboxylic groups. Nonetheless, these effects are very likely to be overshadowed by the stabilizing effects of the temperature-responsive chain segments.

The partially regained responsiveness of the polymer shell, as evidenced by increasing the molecular weight of the stabilizing polymer and its P(NiPAM) content, indicated that the polymers require a specific degree of freedom for temperature-induced reorganization. Obviously, this is not a new conclusion for such a system. From the simulation of thermoresponsive free polymer chains, it is known that in order to show temperature-responsive behavior, a minimum of repeating monomer units in the polymer is necessary.[219–221,285] Transferred to this hybrid, this would mean that in order to show thermoresponsive behavior, the P(NiPAM) segments must form large slopes that reach through the inner shell section into the outer "fuzzy" region of the polymer shell. This assumption could also explain the following two open questions.

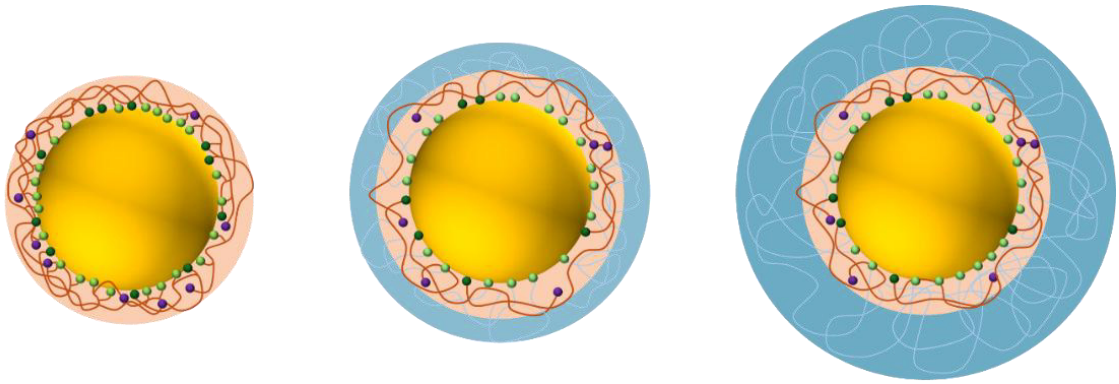


Figure 68. Illustration of the assumed polymer-shell assimilation around the Au core nanoparticle (yellow sphere). The different chain segments are color-coded with orange lines as the P(OEGMA) and light blue as the P(NiPAM) chain segments. The small spheres are the respective end functionalities, with dark green as the dTTC-head group of the backbone, light green as the TTC functionalities of the side chains, and purple as the carboxylic end group of the backbone. The circles illustrate the different regions of the polymer shell.

Why is the temperature-induced reaction of the polymer changing from a rapid response at a distinct transition temperature to a gradual response with no significant transition temperature when it is fixed on a particle surface? Also, is it possible to regain that rapid hydrophilic/hydrophobic transition by increasing the molecular weight of the stabilizing polymer?

Considering the given data and the fact that a minimal number of "free" repeating units is needed for a sharp transition, the fuzzy sphere model can give a first insight into the observed linear-like responsive behavior. The experience gained from GNS@B03 shows that by adding an anchoring point along the chain, the polymer tends to be closely packed around the particle surface, which significantly limits the responsive character. Since the hybrid systems described in Section 5.4.1, especially with the Au@P(DMAEMA)$_n$ systems, show comparable behavior to that of the GNS@B03 hybrid suspension, this is a clear indicator of such stabilization. Assuming that the gold particle surface first must be saturated by suitable anchoring groups before a distinct fuzziness of the shell can be formed, and that a distinct fuzziness is required to show thermoresponsive character, would explain why it is common for GNP@polymer hybrids not to show a rapid, responsive transition. The results from **Figure 67** and **Figure 68** also indicate that this behavior can be overcome when the system's fuzziness, or the slope formation in the outer shell region, is increased, for example, by increasing the molecular weight, which equals a reduced crosslink density for this system. The literature indicates that a decreasing *h*-value relates to an increasing fuzziness of the hybrids, which also depends on the crosslinking density.[10] Therefore, the decreasing *h*-values with increasing P(NiPAM) segment length can be equally interpreted as such.

These observations show that in order to obtain a highly responsive hybrid system, the stabilizing polymer must have a sufficient number of non-attached (mobile) repeating units along its chain. This is especially critical for P(DMAEMA)$_n$ stabilizers because the amine groups in the side chain show a strong affinity to positively charged gold surfaces. To create P(DMAEMA)-based GNS hybrids with a sharp, temperature-dependent transition, adding other chain segments that show a higher affinity for the respective particle surface than DMAEMA's amine groups could be a beneficial approach to increase the mobility of P(DMAEMA) segments.
This leads to the last question about the temperature-responsive optical behavior based on interparticle coupling:

Is it possible to control interparticle distances in the area of the critical coupling distance by using a responsive polymer shell? And if so, is this process reversible?

With the knowledge about how to trigger rapid thermoresponsive transitions in NP@polymer hybrids, it remains questionable if, under the given conditions, interparticle distances can be reached that allow the coupling of two plasmonic modes from different particles—taking the measures from **Figure 11** (Page 29) as guidance means that for GNS with a diameter around 13 nm, the distance between two particles must be 32.5 nm or less, to enable interparticle plamon coupling. Assuming a stimuli-responsive polymer shell should control the coupling of two identical core-shell particles, the shell thickness around each particle cannot exceed 16.3 nm in a collapsed state. To keep it short, only GNS@B03 and GNS@GN01 have sufficiently low hydrodynamic radii (compare **Figure 67** and **Figure 68**) to support interparticle LSPR coupling in suspension. It should also be noted that the 2.5-times the particle diameter assumption describes fixed particles on an ITO surface. As indicated by Equations (4.1) and (4.2), the dielectric constant of the surrounding medium (ε_0) has a crucial role in the resulting plasmon resonance of single particles. It is also known that ε_0 significantly influences the strength of the plasmon coupling, as shown by P. K. Jain and coworkers.[143] For similar particle hybrids, the near-field coupling distance at which a noticeable visual change in the sample's color can be well below the 2.5-times particle mark, as H. Lange et al. have shown.[268]

$$\lambda_{max}(T) = \lambda_{end} + \frac{\lambda_{ini} - \lambda_{end}}{1 + \exp\left(\frac{T - T_c}{h}\right)}$$

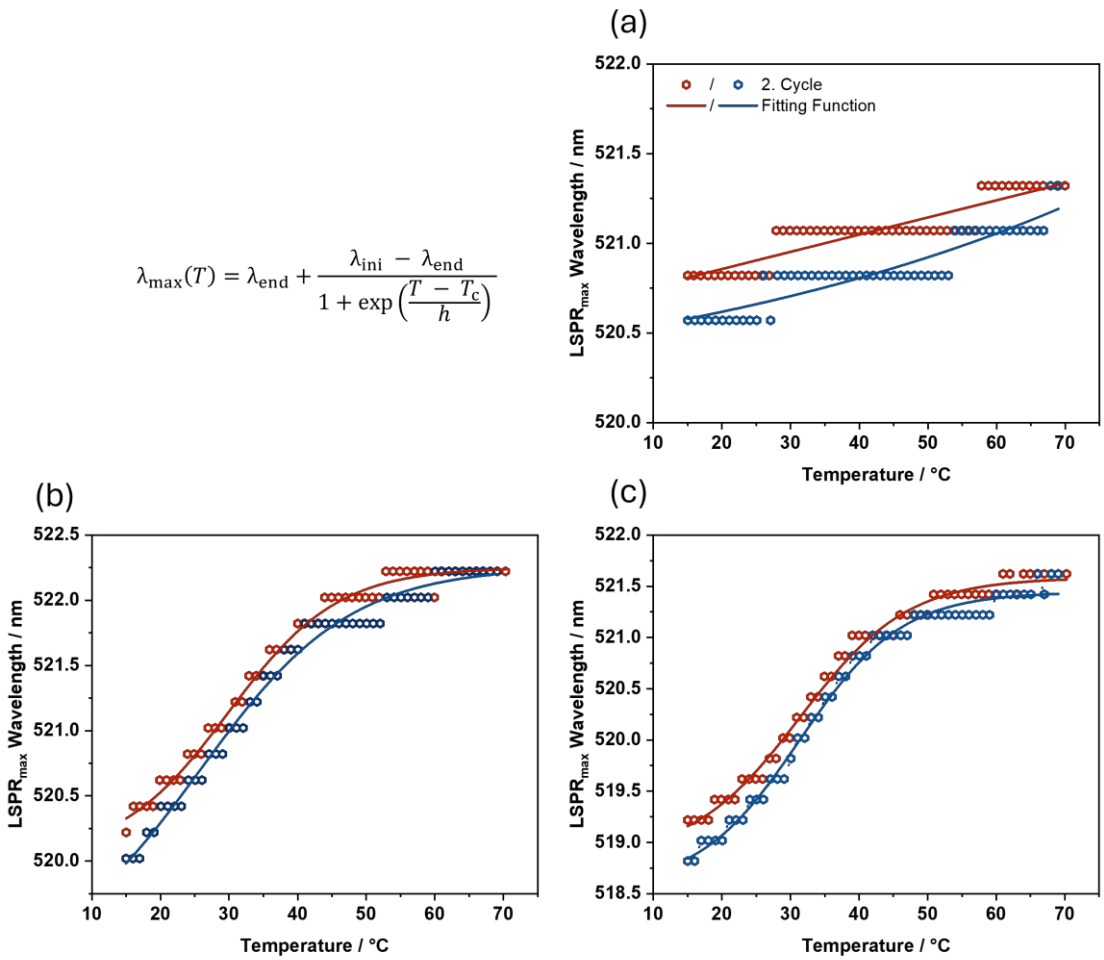


Figure 69. Temperature-responsive LSPR measurement results of aqueous GNS@polymer hybrid suspensions prepared via the optimized stepwise centrifugation protocol. Plotted are the suspensions λ_{max} values against the suspension temperature for the hybrids GNS@B03 (a), GNS@GN01 (b), and GNS@GN02 (c). The red λ_{max} values represent the λ_{max} obtained from the second cycle's heating curve. The blue values represent the cooling curves. The solid lines represent the fitted functions for the heating (red) and cooling (blue) curves.

Table 7: Concluded values obtained from the non-linear fits shown in **Figure 69**. The theoretical molecular weight average of the stabilizing polymer used in the hybrid ($M_{n,th}$) and the percentage weight content of P(NiPAM) in the polymer are included. This table includes the fitting values for the heating and cooling curve of the second temperature cycle. The fitted values for the maximum (λ_{ini}) and minimum (λ_{end}) of λ_{max}, the center Temperature (T_c), the transition stepness h, and the reduced R^2 are provided.

hybrid	$M_{n,th}$ / kDa	%$_{NiPAM}$ (*w/w*)	curve	λ_{ini} / nm	λ_{end} / nm	T_c[a] / °C	h / °C	*red.* R^2 /
GNS@B03	69.9	-	heat	-	-	-	-	0.822
			cool	-	-	-	-	0.843
GNS@GN01	115	37 %	heat	520 ± 0	522 ± 0	29.9 ± 0.8	8.0 ± 0.6	0.991
			cool	519 ± 0	522 ± 0	25.7 ± 2.2	10.9 ± 1.2	0.987
GNS@GN02	138	46 %	heat	519 ± 0	522 ± 0	31.4 ± 0.7	7.9 ± 0.5	0.991
			cool	519 ± 0	521 ± 0	31.3 ± 10.7	7.4 ± 0.5	0.991

Figure 69 indicates the respective fits of the λ_{LSRP} temperature-dependency. The fitting values are summarized in **Table 8**. As expected from **Figure 67**, the λ_{LSRP} for GNS@GN01 and GNS@GN02 roughly follows the dependency ascribed to the fuzzy sphere model. For GNS@GN01 and GNS@GN02, the applied fitting function converged well with the temperature-dependent $\lambda_{max,}$ and the obtained values for the T_c and the h are comparable with the results obtained from fitting the temperature-dependent R_H.

Due to multiple data processing steps to achieve the respective λ_{max} values from the original UV–Vis extinction measurements, the observed $\Delta\lambda_{LSPR}$ for GNS@B03 is nearly insignificant. Therefore, it is not surprising that, for GNS@B03, the applied fitting function did not converge, unlike the R_H values for this nanohybrid.

The fact that for GNS@GN02, no signs of plasmon coupling-based $\Delta\lambda_{LSPR}$ were observed can be explained by the polymer shell around the gold core particles, which is too large to allow the plasmon modes of the gold cores to overlap sufficiently to cause noticeable plasmon-coupling effects.

Following the argument of the critical coupling distance from **Figure 11**, the hybrids GNS@B03 and GNS@GN01 should, in theory, be capable of showing interparticle plasmon coupling. Especially, for GNS@GN01, there should be a switch between a non-coupling state at lower sample temperatures and a coupling state at temperatures above the shells' transition temperature. However, none of the described hybrids exhibit significant interparticle plasmon coupling. The LSPR shifts described in **Figure 69** are in the same single-digit region for all three samples, meaning that the observed shifts are more likely described by refractive index changes of the polymer medium in proximity to the single particle surfaces. As described earlier in this work, interparticle plasmon coupling would cause a stronger $\Delta\lambda_{LSPR}$ in the double-digit nanometer region. This behavior can be explained by the measurement setup and the nature of the samples. Since the measurement was conducted in suspension, it is required that two particles first encounter one another and form a stable dimer. Additionally, in order to detect the coupling particle-mer, they must feature sufficient stability in suspension to be detectable by the UV–Vis instrument, which can be a challenge. An insufficient stabilization would be evident by a significant irreversible decrease of the absorbance band in the UV–Vis extinction spectrum as observed in Section 5.4.2. The small $\Delta\lambda_{LSPR}$ observed for the three hybrids, GNS@B03, GNS@GN01, and GNS@GN02, limits their applicability as optical sensors in suspended form. Combining them by crosslinking them into a hydrogel by following the post-polymerization functionalization procedure described by J. Xu and V. Abetz[1,9] could overcome this limitation, because, bound within a hydrogel, the particles are naturally closer to each other than in suspension. This applicability could also be adjusted in a layer-by-layer structure, using larger particles with longer coupling ranges.

Nevertheless, the hybrids have proven themselves to be interesting research materials for investigating the optical behavior of stimuli-responsive nanoparticle@polymer hybrids in general.

Referring back to the initial question, if it is possible to control interparticle distances reversibly, the results from **Figure 69** confirm reversible optical behavior over several temperature cycles. However, the observed $\Delta\lambda_{LSPR}$ at different temperatures is not within the scale of interparticle coupling for all three hybrid suspensions. Their similarity to the described fuzzy-sphere model strongly indicates a shift driven by the changing refractive index of the polymer shell. In principle, it is possible to prepare samples that show temperature-induced interparticle coupling (see **Figure 65**, Page 130). However, in suspension, this behavior was always accompanied by the irreversible destabilization of the investigated suspensions.

6. Achievements and Future Perspectives

Chapter 5 presented three individual nanohybrid systems. The development of each of these systems came with its own challenges and motivations. However, there are undeniable subjects that place the gold nanohybrid materials from Sections 5.2, 5.3, and 5.4 in a common, joint perspective as already emphasized in Section 5.1. Obviously, gold was chosen as the inorganic core material for all hybrids. Due to their well-established theoretical background, particularly in plasmonic behavior, gold particles were considered an ideal model for investigating NP@polymer hybrids. Another recurring topic of this thesis is the tailoring of polymer stabilizers via photoinferter RAFT polymerization and, moreover, the iterative increase in reaction scale, which is counted among the major achievements of this work. The progressive increase in the scale of RAFT polymerization reactions ranges from a ~12 mL setup to a ~500 mL setup, without significant loss in the product quality of the resulting thermoresponsive polymers. In comparison to polymers synthesized at smaller scales, properties such as the $Đ \leq 1.6$ and the maintenance of the temperature-responsive properties of the polymers P(DMAEMA)$_n$, P(OEGMA$_n$-*r*-BTPEMA$_m$), and their follow-up products indicate a successful scale-up.

Nevertheless, this scale-up still has room for further development. Originating from the described 500 mL polymerization setup for B03, one possible improvement could be to increase the solid content (RAFT agents plus monomers) during polymerization. This content was kept at 20 % because of the limited mixing efficiency caused by the stirring setups (magnetic stirring bar) at setups smaller than the double-walled glass reactor setup. Given the improved mixing setup with an anchor mixing unit, this limitation becomes less of a concern, and higher solid contents during polymerization can be considered in the future. This optimization would also positively affect the environmental aspects of the polymerization setup, reducing the amount of 1,4-dioxane, a critical component within polymerization.

Based on their preparation method, the nanohybrids Au@P(DMAEMA)$_n$ and the polymer-stabilized GNR hybrids can be described as polymer-assisted particle synthesis. Emphasizing the polymers' stabilizing effects during and after particle growth. In this work, it was shown that RAFT polymerization using the iniferter mechanism is an excellent tool for tailoring polymer structures that cover highly specified tasks. The most striking example of this statement is the triggering of anisotropic growth of GNRs using RAFT polymers with a potential approaching that of CTAB, a highly concerning compound for biomedical applications.

In chronological order, the *in situ* synthesis of Au@P(DMAEMA)$_n$ was the first hybrid material developed (Section 5.2). Amongst several others, the effects of varying TTC-endgroup functionalizations were investigated. Showing a significant influence on the hydrophilic behavior of the achieved hybrid when the character of the endgroup is changed. However, this topic's advanced reproducibility and intriguing responsive properties (discussed in section 5.4.1) made the Au@P(DMAEMA)$_n$ hybrids an interesting material for different applications. For instance, these hybrids were used as additives in polyionic liquid (PIL) films.[14] Adding the Au@P(DMAEMA)$_n$ hybrid into the PIL material improved the material's mechanical properties and thermal resilience, and added responsive properties to the films' electrical properties compared to PIL films synthesized without the Au@P(DMAEMA)$_n$ additive. This work demonstrates the success and usability of the Au@P(DMAEMA)$_n$ nanohybrids for a broad range of new materials. It was shown that the polymer-assisted approach using a strong reducing agent and THF as solvent with a TTC-based RAFT polymer is a suitable option for this protocol. Therefore, this work significantly broadens the range of polymers applicable to the procedure described in the literature[2], opening new possibilities for the future. It was additionally shown that, using the nucleophilic character of the amine functions within the stabilizing P(DMAEMA)$_n$ matrix, the hybrids were successfully transferred into a crosslinked gel structure.

The post-polymerization functionalization of the P(DMAEMA) matrix served as the foundation for polymer-assisted anisotropic growth of GNRs (Section 5.3), which followed this work. With the focus on substituting CTAB in water-based seeded growth synthesis of GNR and improving the applicability of GNR for biological and medical use, several polymer architectures were tested as possible CTAB substitutes. Finally, a thermoresponsive diblock copolymer (qBCP02) was introduced, based on a P(DEGMA)-block as the temperature-responsive, water-soluble component and a post-polymerization functionalized P(DMAEMA)-block that mimics the facet-selective behavior of CTAB. qBCP02 showed great potential to assist anisotropic growth. After optimization of reaction parameters, qBCP02 showed a growth-directing potential similar to that of CTAB, with reduced toxicity in cell culture tests. Whether these are impressive achievements, there is still room for improvement in the future. One major limiting factor that needs to be addressed in the future is the solution's viscosity at higher polymer concentrations.

To maintain sufficient seed dispersion after adding them to the monomer solution, the concentration of the polymer precursor had to be kept well below the equivalent CTAB operation concentration in the conventional seeded-growth protocol. This lower amine concentration limited the achievable aspect ratios and the shape selectivity of the polymer-assisted synthesis. In the future, to overcome this limitation, the polymer's architecture needs further development. One open question in this regard is whether the described functionalization of DMAEMA’s aminofunctions with BHD could be substituted by shorter-chained bromoalkanes without significantly losing the facet-directed behavior. Also, substituting the P(DEGMA) block with

another water-soluble block, such as poly(methacrylic acid) (PMAA), can significantly enhance the chains' solubility, allowing shorter chain lengths for this block. This reduced chain length should lower the solution's viscosity at higher polymer mass concentrations compared with qBCP02. Using PMAA as a stabilizing block would also enable a less toxic synthesis route, because it can be polymerized in water. Another possibility to improve the anisotropic yield of the reactions and overcome the limited polymer concentration could be a reduced concentration of inorganic precursors in the growth solution. However, for the described thermoresponsive qBCP02, the question remains: *how does the polymer's temperature-responsive behavior interact with its facet-directed behavior?* The results shown in Sections 5.3.1 and 5.3.2 clearly indicate an interplay between the two characteristics. The extent to which the facet-directing property benefits from temperature-dependent chain rearrangements remains to be demonstrated.

Given the nature of their stabilizers, the GNP@polymer hybrids presented in Sections 5.2 and 5.3 show thermoresponsive behavior. However, some of this behavior was unexpected, especially when compared with the thermoresponsive behavior of the stabilizing polymers. For example, in contrast to their P(DMAEMA) stabilizers, the Au@P(DMAEMA)$_n$ nanohybrids showed no distinct transition temperature (**Figure 56**). The products of the qBCP02-assisted GNR synthesis showed significant differences in their optical behavior when longitudinal and transversal signals are compared (**Figure 57**). This unexpected behavior led to several open questions formulated at the end of Section 5.4.1. To address these questions, a reliable ligand-exchange-based preparation procedure was developed, which is described in Section 5.4.2 in more detail. This protocol remarks the second class of nanohybrid preparation used in this work.

In contrast to polymer-assisted preparation protocols, this protocol involves the separate synthesis of GNPs and the ligand. These protocols enable a more flexible, tailored design of nanohaybrids. After optimization, a reliable, well-reproducible procedure was developed, enabling the synthesis of three GNS nanohybrids. The goal of this development was to answer two of the questions mentioned in Section 5.4.3. *Explicitly, this topic focused on the general model for describing thermoresponsive nanohybrid materials and on the loss and recovery of rapid responsiveness.*

The working hypothesis on the loss of the rapid thermoresponsive behavior of the Au@P(DMAEMA) was that due to the amine functions of P(DMAEMA), the chain loses its mobility, given the fact that these amine functions are bound on the GNPs surface. With the hybrid GNS@B03, this hypothesis was investigated. By adding TTC functions randomly in a P(OEGMA) chain (by randomly copolymerizing the monomer BTPEMA), a dense connection to a GNS surface of a P(DMAEMA) chain was recreated. As a result, the thermoresponsive behavior of GNS@B03 is comparable to that of the Au@P(DMAEMA) hybrids, which supported the theory of limited chain mobility.

The hybrids, GNS@GN01 and GNS@GN02, further showed that increasing the chain length between the attachable TTC functions results in greater temperature-induced response. This regained response supported the mentioned hypothesis and, at the same time, showed a close relationship with the fuzzy sphere model described in the literature by E. Ponomareva, B. Tadgell, et al.[10–12] The results in Section 5.4.3 show that the more chain flexibility is achieved, the better the data fit the criteria of this model. However, more information is needed to determine the boundaries of the fuzzy sphere model assigned to the GNS@polymer system. W*hether there is a molecular weight dependence for one of the fitting parameters associated with the functions used in Section 5.4.3 remains to be proven*.

Another aspect of the research presented in Section 5.4 was the investigation of the LSPR and its temperature dependency. The idea was that adjusting the shell thickness via temperature LSPR coupling should be triggered. In this matter, GNS@GN01 was a promising material because of its varying shell thicknesses: outside the LSPR range in a swollen state and inside the LSPR range in a collapsed state (by assuming the formation of particle-mers). However, for all three hybrids suspended in water, only a $\Delta\lambda_{LSPR}$ in the range of a few nanometers was observed. This small $\Delta\lambda_{LSPR}$ limits their potential applicability in suspended form, for example, as optical sensors. To improve plasmonic behavior, several possible solutions involving crosslinking of the polymer matrix can be tested. For future development, following the procedure described by J. Xu and V. Abetz[1,9], a hydrogel could be formed from the core-shell particles. Incorporated in such a material, the GNS cores are naturally closer to each other than in suspension, which could, especially for GNS@GN01, result in a hydrogel with temperature-controlled plasmonic behavior. In this context, also a combination of grafted copolymer-stabilized particles with particles stabilized, for instance, by a thiol/dithiol ligand mixture in a layer-by-layer structure would be a promising approach. In a recent project, it was demonstrated that crosslinking particles stabilized by comparable copolymers is a feasible option.[13] This work is a further step towards highly responsive plasmonic materials based on the controlled adjustment of the interparticle spaces utilizing a temperature-responsive polymer matrix.

For the presented word, the primary focus was on the successful preparation and the development of well-reproducible synthetic routines. Using these routines, further investigations should be well-equipped to prepare highly interesting, highly potent hybrid nanomaterials. With the work on the tailored design of RAFT (co-)polymers and the provided results, for the photoRAFT polymerizations scale-up, also the groundwork for the scale-up of polymer-stabilized nanoparticle hybrid synthesis is set. Future development will show whether the polymer-assisted GNP synthesis meets the high standards for particle quality, especially for GNRs. However, with the successful preparation of GNR using polymers to facilitate anisotropic growth, a new possibility emerged in the field of seeded-growth-based GNR synthesis. The results in Section 5.4 on the temperature-responsive behavior of polymer-stabilized GNS provide a further perspective on the

versatility that RAFT polymers can contribute to nanoscience. Although the investigated particle suspensions did not exhibit significant particle-particle plasmon coupling, the close relationship to the fuzzy sphere model provides a solid theoretical foundation for further improvement of the GNS@graft polymer hybrids from Section 5.4. This foundation also serves as a tool for more efficiently designing follow-up products based on the described GNS@polymer hybrids.

7. Experimental Methods

This chapter covers the preparatory and analytical methods of this thesis. To draw a complete image of this thesis, the preparation methods from References [3] and [8] are included, with minor additions.

7.1. Used Chemicals

The chemicals used for this thesis are reported in the following sections 7.1.1 and 7.1.2. To provide a clear overview, it is separated into chemicals explicitly used for particle synthesis and for polymerization. If compounds are used for both, they are listed in both sections individually to avoid misconceptions.

7.1.1. Chemicals and Materials Used for RAFT Polymerization

Solvents: All technical-grade solvents, including acetone, ethyl acetate (EA), and methylene dichloride (DCM), were distilled under reduced pressure before use. 1,4-Dioxane (Grüssing, 99 %) was stored over potassium hydroxide to remove hydroxides from the solution. Before using 1,4-dioxane, it was filtered to remove the solids. Cyclohexane (Grüssing; 99.5 %), *N*,*N*-dimethylformamide (DMF, VWR Chemicals, 99 %), diethyl ether (Grüssing, 99 %), *n*-hexane (Grüssing; >99 %), and water (milli-Q 18.1 MΩ·cm^{-1} @25 °C) were used without additional purification.

Monomers: NiPAM (TCI, 98 %) was recrystallized twice from n-hexane and stored in the dark at 0 °C in a closed round-bottom flask. Before using the following monomers, they were filtered over an activated basic aluminum oxide column to remove included stabilizers: 2-(dimethylamino)ethyl methacrylate (DMAEMA; Sigma, 98 %), diethyleneglycolmethacrylate (DEGMA; Sigma-Aldrich, 95 %), OEGMA (Sigma Aldrich, M_n = 300 g/mol). BTPEMA was synthesized according to the literature.[187]

Other Chemicals: Carbon disulfide (Merck, 99 %), 4,4'-azobis-(4-cyanovaleric acid) (ACVA; Aldrich, 98 %), 4-Cyano-4-(dodecyl sulfanyl thiocarbonyl)sulfanyl pentanoic acid (dTTC; ABCR, 97 %), 1,5-dibromopentane (DBP; Thermo Scientific, 98 %)

7.1.2. Chemicals Used for Particle Preparation

Solvents: Tetrahydrofuran (THF; from VWR Chemicals; 99.7 % and Acros Organics; 99.5 %, extra dry over a molecular sieve), and water (milli-Q 18.1 $M\Omega \cdot cm^{-1}$ @25 °C), were used without additional purification.

Inorganic precursors: Gold(III) chloride trihydrate ($HAuCl_4 \cdot 3H_2O$; Sigma Aldrich, 99.9%) was transferred into a Schlenk tube and stored under a nitrogen atmosphere. Silver nitrate ($AgNO_3$; Sigma Aldrich, 99 %) was used directly from the original container.

Reducing agents and ligands: The following agents are used without further purification: 1.0 M lithium triethyl borohydride in THF (superhydrid© (SH); Aldrich), citric acid monohydrate (CA; Sigma Aldrich, 99 %), trisodium citrate dihydrate (TCA; Honeywell, 100 %), sodium borohydride ($NaBH_4$; Honeywell, 99 %), trisodium EDTA (Sigam-Aldrich, >95 %), and cetyltrimethylammonium bromide (CTAB; Sigma, ≥99 %).

7.2. Preparative Methods

7.2.1. Organic Synthesis of The RAFT Agents

Synthesis of the CTA 4-Cyano-4-(propyl sulfanyl thio carbonyl)sulfanyl pentanoic acid (pTTC):

The described procedure for the synthesis of pTTC is performed according to the literature[286] and was reproduced from Ref. [3]. The synthesis of pTTC is a two-step reaction. Both steps were performed under an inert nitrogen atmosphere to avoid oxidation of the sulfur compounds used in this protocol.

The reaction started by dissolving 3.9 g (70 mmol) of potassium hydroxide in 20.0 mL of deionized water, then adding 4.2 g (55 mmol) of propane thiol dropwise to the solution at room temperature. 4.2 g (55 mmol) of carbon disulfide was added to the solution. The obtained solution was stirred at 20 °C for 30 min. Afterward, the solution was cooled to 0 °C, and a second solution containing 28 mL of acetone and 5.3 g (28 mmol) *p*-tosyl chloride was added dropwise over 20 min. After two hours of stirring at 0 °C, acetone was removed under reduced pressure. The remaining aqueous solution was extracted with 20.0 mL of dichloromethane. The organic phase was stored overnight over magnesium sulfate to remove residual water. The solid compounds were removed by filtration. After the remaining organic solvent was removed under reduced pressure, 7.0 g (23 mmol; yield 82 %) of bis(propyl sulfanyl thiocarbonyl) disulfide (BIS) was obtained as a red oil.

For the second reaction step, 2.4 g (7.9 mmol) of BIS and 4.8 g (17 mmol) of ACVA were dissolved in 110 mL of ethyl acetate. Under a nitrogen atmosphere, the solution was heated to 85 °C for 48 hours. The remaining volatiles were removed under reduced pressure. The crude was purified by column chromatography using a mixture of ethyl acetate and n-hexane (1:3) as the mobile phase. After the purification, 3.0 g (10 mmol; yield 63%) of pTTC was obtained as a solid orange product.

7.2.2. Photo RAFT-Polymerization of Polymer Stabilizers

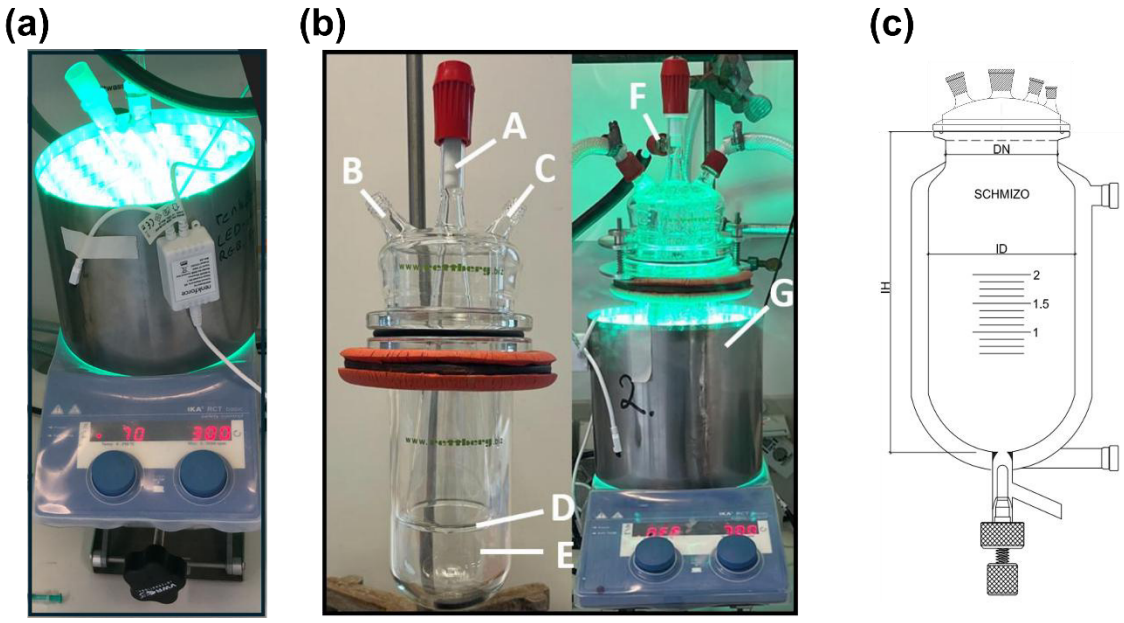


Figure 70. Images of the differently scaled reaction setups used for photoRAFT polymerization in this work. In **(a),** the initial reaction setup is using a modified 100 mL Schlenk tube. This setup was used for reactions up to a reaction volume of ~30 mL. This image is taken with permission from *Macromol. Chem. Phys.* **2022**, 2200355. Copyright 2022 The Authors. Macromolecular Chemistry and Physics, published by Wiley-VCH GmbH.[3] Image **(b)** shows the second polymerization setup using a sublimation reactor from Gebr. Rettberg for reaction scales between 200 mL and 250 mL reaction volumes. Image (b) is taken with permission from *Adv. Funct. Mater*. **2024**, 2400995, without adaptation. Copyright 2024 The Authors. Advanced Functional Materials, published by Wiley-VCH GmbH.[8] Image (c) shows a scheme of a 500 mL double-walled glass reactor with a DN 100 flange from Schmizo AG. This setup was used for reaction scales ≥250 mL.

The RAFT synthesis of the polymer stabilizer/precursors evolved during this project, especially regarding the reaction scale. Four different reaction vessel scales were used. Starting with 12 mL screw-capped vials, to a 50 mL Schlenk tube[3], to a repurposed sublimation reactor with a reaction volume of about 200 mL[8], which was followed by a 500 mL glass reactor setup. Commercially available LED stripes used as the light source were attached inside a metal tube with a diameter of 16.5 cm. In the center of this tube, the respective reaction vessel was placed for the setups (a) and (b); a magnetic stirring bar was used for mixing the solution. In setup (c), a CAT R20 60 W agitator, connected to a PTFE anchor mixer with a 54 mm diameter, was used to mix the reaction solution. Heating the reaction in the setups (b) and (c) was provided via a continuous flow of heated water through the sublimation cone (in (b)) and the outer mantle (in (c)), respectively. In setup (a), heating the reaction was provided by a silicon oil in which the Schlenk tube was placed.

Polymerization of pTTC-P(DMAEMA) and dTTC-P(DMAEMA) macroRAFT homopolymers:

All polymerizations were performed in a Schlenk tube under a nitrogen atmosphere in a photo reactor setup (**Figure 70** setup (A)). The tubular geometry of the reactor volume maintained a constant cross-section, even after several NMR samplings, providing uniform light irradiation throughout the polymerization. Except for the polymerizations discussed in **Figure 21** on Page 60, the photoiniferter mechanism was initiated using the green light LED (513 nm, 0.60 $mW \cdot cm^{-2}$). The following procedure is described based on the synthesis of pTTC-$P(DMAEMA)_{39}$ and can be transferred to other polymerizations using the respective amounts of substances listed in **Table 8**. The polymerization results are summarized in the Appendix **Table A1**.

3.00 g (19.1 mmol) of DMAEMA was dissolved in 12.7 g of 1,4-dioxane. 0.117 g (0.422 mmol) pTTC and 200 µL DMF were added to the monomer solution. By purging the obtained yellow solution with nitrogen gas for 15 min at room temperature, oxygen was removed. After purging, it was heated to 70 °C using a pre-heated silicon oil bath. The reaction was initiated by turning on the green light source. The monomer conversion was tracked by 1H-NMR sampling, as shown in **Figure A1**. After reaching the desired monomer conversion, the light source was turned off, and the reaction was quenched by cooling in an ice bath until the solution froze and was exposed to air. After reaching room temperature again, the reaction solution was diluted with THF and slowly added dropwise to a cooled cyclohexane bath to isolate the pTTC-P(DMAEMA) product by precipitation. The achieved yellow oil was dissolved in THF, and the precipitation process was repeated twice. After the third precipitation, the solvent was removed under reduced pressure at room temperature, yielding an orange product, which was stored in the dark at 0 °C until further use.

Table 8: Concluded pTTC/dTTC-P(DMAEMA) reaction conditions and substance amounts for the discussed P(DMAEAM)$_n$ precursors discussed in Section 5.2. For the respective polymers, the consecutive number (CN) used in the lab journal, the used CTA, the volume of the solvent 1,4-Dioxane (V_{Dox}), of the DMF (V_{DMF}) used as the internal ^{1}H-NMR standard, the amounts of substance of DMAEMA (n_D), and the CTA (n_{CTA}), the reaction temperature (T), and the final monomer conversion (p_m) after a reaction time (t).

Polymer	**CN**	**CTA**	V_{Dox} / g	V_{DMF} / µL	n_D / mmol	n_{CTA} / mmol	T / °C	p_m / %	t / min
pTTC-P(DMAEMA)$_{48}$	P_P1	pTTC	5.04	100	12.76	0.191	80	72	152
pTTC-P(DMAEMA)$_{110}$	P_P2	pTTC	4.91	100	12.75	0.098	75	85	259
pTTC-P(DMAEMA)$_{37}$	P_P5	pTTC	5.09	100	12.75	0.254	75	74	148
pTTC-P(DMAEMA)$_{72}$	P_P6	pTTC	5.09	100	12.79	0.127	75	73	152
pTTC-P(DMAEMA)$_{39}$	P11	pTTC	12.74	200	19.11	0.422	70	86	481
pTTC-P(DMAEMA)$_{92}$	P18	pTTC	11.13	200	19.09	0.149	70	71	411
dTTC-P(DMAEMA)$_{41}$	P14	dTTC	12.41	200	19.09	0.424	70	92	510
dTTC-P(DMAEMA)$_{91}$	NM-P01	dTTC	12.30	200	19.20	0.162	70	76	239
pTTC-P(DMAEMA)$_{21}$	P10-05	pTTC	12.07	100	19.13	0.423	70	48	300
pTTC-P(DMAEMA)$_{30}$	P10-06							67	423
pTTC-P(DMAEMA)$_{34}$	P10-07							76	515
pTTC-P(DMAEMA)$_{44}$	P10-09							98	1505
pTTC-P(DMAEMA)$_{63}$-An	P8An	pTTCAn	4.89	100	12.87	0.126	70	62	120
pTTC-P(DMAEMA)$_{30}$-An	AP4An	pTTCAn	4.48	100	6.39	0.098	70	46	154

PhotoRAFT-polymerization of the P(OEGMA-r-BTPEMA) Backbones and P(DEGMA) macroRAFT Agent:

The scale-up of the synthesis was developed using the example of the known synthesis of P(OEGMA-*r*-BTPEMA). This is why two different setups were applied (Figure 70, setups (B) and (C)) for the polymerization of the respective polymer system.

The exact amount of substances used, including those used for the polymerization of $P(DEGMA)_{244}$, can be taken from **Table 9**. The results of the polymerization are concluded in **Table A2**. The polymerization using the sublimation setup is also discussed in Reference [8]. The 500 mL double-walled glass reactor setup is the point of this thesis, which has not yet been published.

First, a polymerization solution is prepared by dissolving the CTA, the monomer OEGMA, and the inimer BTPEMA in 1,4-dioxane. As a ^{1}H-NMR reference, DMF was added to this solution. The solution was transferred into the reaction vessel and purged for at least 15 minutes using N_2 gas. Purging was performed using a 15 cm metal syringe for the sublimation setup. A glass-made gas inlet attachment was used for the double-walled glass reactor. For both setups, the purging was accompanied by continuous solution mixing. The reaction is heated in this setup through the sublimation inlet immersed in the solution. Parallel to the purging process, the reaction was heated to 70 °C in both setups. The sublimation inlet and the reactor mantle are attached to a flow water heater. After reaching 70 °C, a ^{1}H-NMR sample was taken as a reference for monomer conversion monitoring, using DMF as an internal standard. For the 500 mL glass reactor setup, sampling was accomplished by opening the bottom outlet. For the sublimation setup, the conditioned 15 cm syringe was used.

After the t_0-sample was taken, the green light source (513 nm; 0.60 mW cm^{-2}) was switched on to initiate the polymerization. After reaching the desired monomer conversion, the reaction was stopped by cooling the solution to room temperature and turning off the light source. The resulting P(OEGMA-*r*-BTPEMA) product was purified by precipitating the product solution in a four-fold excess of *n*-hexane. For the first precipitation cycle, the polymerization solution was diluted to half the initial concentration using THF. For the precipitation cycles, four times the volume of non-solvent was used relative to the volume of solvent used for dissolving the polymer. The precipitate was dried for several days under reduced pressure. Using ^{1}H-NMR, the polymer product was tested for traces of residual monomer before further use. The incorporated amount of BTPEMA in the polymer was determined by ^{1}H-NMR spectroscopy, following the procedure described in the literature.[1,9]

Although the polymerization scale-up to 200 mL using the sublimation glass reactor setup was successful, the setup lacked practicality. Examples such as purging the reaction solution, closing the reactor without creating an overpressure that causes the spilling of the reaction solution, and removing the solution from the reactor, including cleaning, are to be named here. These issues were addressed and fixed with the 500 mL reactor setup by adding additional access points at the reactor lid. The solution mixing benefited greatly from the use of an electrically driven, core-drawn, precision glass stirrer attached to an anchor mixing unit. Using this unit, handling reactions with higher viscosity is also possible in future setups, including polymerizations with solid contents (CTA and monomers) above 20 %. The included drain at the bottom of the glass reactor made it possible to start the precipitation directly from the reaction vessel. As described in Section 5.4.2.1, the results from the polymerization are also very positive, making this setup the most favorable among the presented polymerization setups.

Table 9: Concluded reaction conditions and substance amounts for synthesis of the 250 mL-scaled GNR polymer precursors discussed in Section 5.3. For the respective polymers, the consecutive number (CN), the used chain transfer agent (CTA), the volume of the solvent 1,4-Dioxane (V_{Dox}), the volume of the used internal standard DMF (V_{DMF}), the amount of monomer (n_m), the CTA amount (n_{CTA}), the reaction temperature (T), and the final monomer conversion (p_m) are provided.

Polymer	CN	CTA	V_{Dox} / mL	V_{DMF} / mL	n_m / mmol	n_{CTA} / mmol	T / °C	p_m / %
P(OEGMA)$_{230}$-*r*-P(BTPEMA)$_6$	B01	dTTC	220	2	190 7.1	0.479	70	58.6
P(DEGMA)$_{222}$-*r*-P(BTPEMA)$_8$	B04[a]	dTTC	200	1.5	220 7.8	0.581	70	60.2
P(DEGMA)$_{244}$	B02	dTTC	200	2.5	240	0.393	70	39.6
P(OEGMA)$_{233}$-*r*-P(BTPEMA)$_{11}$	B03	dTTC	350	20	300 13.7	0.820	70	65.9

[a]The consecutive number used in the lab journal is B02.

Photo-iniferter RAFT Polymerization of DMAEMA for Chain Extending the macroRAFT Agents B01 and B02:

As found in this project, the principle of conducting a "well-controlled" RAFT polymerization in a batch setup is independent of the scale of the polymerization. The ability to use nearly any TTC-functionalized polymer as an RAFT agent is one of the key factors that make RAFT polymerization a powerful tool for designing highly specialized, tailored polymers. Different light sources were used to synthesise copolymers with P(DMAEMA) segments with $P(OEGMA)_{230}$-*r*-$P(BTPEMA)_6$ (B01) macroRAFT agent. Since the final copolymers are expected to serve as anisotropic growth-directing agents in GNR synthesis, a high DMEMA content was targeted. To increase the probability of DMAEMA addition onto B01, the blue RGB light source was used for the synthesis of the first generation of anisotropic growth directing polymer prototypes (Gen1) (discussed in Section 5.3.1). For the second generation of anisotropic growth-directing DMAEMA-based polymers (Gen2) from Section 5.3.2, the polymerization of DMAEMA onto B01 was initiated using a green RGB-LED light source. In the latest generation, GNR growth directing polymers (Gen3) B01 were replaced by B02. For this polymerization, green light was used to prevent auto-polymerization of DMAEMA. For all three generations, the same setup was used for polymerization, identical to that used for the advanced DMAEMA polymerization described at the beginning of this section (6.2.2). Since the syntheses of GD01, GD02, BCP01, and BCP02 differ only in the source of light and the macroRAFT agents used, the synthesis is described using BCP02 as a successful example. BCP02 has proven to be the polymer with the greatest potential for future advances in polymer-assisted anisotropic growth. The amount of substances used for each polymerization is documented in **Table 10**.

For the synthesis of the $P(DEGMA)_{244}$-*b*-$P(DMAEMA)_{65}$ block copolymer (BCP02), the polymerization solution was prepared by first dissolving 6.31 g (0.136 mmol) of the makroRAFT agent B02 in 32 mL of 1,4-dioxane and adding the solution to the reaction Schlenk tube reaction vessel. To the solution, 3.23 g (20.5 mmol) of DMAEMA and 0.50 mL of DMF were added. Under a nitrogen atmosphere, the solution was purged for 15 minutes to remove oxygen. In the following, the solution was heated with a silicon oil bath to 70 °C. After reaching 70 °C, a ^{1}H-NMR spectrum was acquired as a reference to determine the initial DMAEMA acryl signal intensity, using the distinct DMF signal as the internal standard. Afterwards, the RGB light source was switched on to initiate the photoRAFT polymerization. During the polymerization, the DMAEMA conversion was tracked by conducting ^{1}H-NMR measurements of the reaction solution at different points of the reaction. After reaching a DMAEMA conversion of 43% the polymerization was stopped by turning off the light source and cooling the reaction. The polymer was isolated via precipitation in *n*-hexane at least three times until the ^{1}H-NMR of the vacuum-dried product showed no residual monomer signal.

Table 10: Concluded reaction conditions and substance amounts of the DMAEMA photoRAFT polymerization using different macroRAFT agents for the precursor synthesis of the anisotropic growth-assisting copolymers, discussed in Section 5.3. For the respective polymers, the consecutive number (CN), the used macroRAFT agent (CTA), the volume of the solvent 1,4-Dioxane (V_{Dox}), the volume of the used internal standard DMF (V_{DMF}), the amount of monomer (n_m), the CTA amount (n_{CTA}), the reaction temperature (T), the final monomer conversion (p_m), and the used LED-light source are provided.

Polymer	CN	CTA	V_{Dox} / mL	V_{DMF} / mL	n_D / mmol	n_{CTA} / mmol	T / °C	p_m / %	LED-source
P(O_{229}-*g*-(D_{38})$_6$)-*b*-P(D)$_{38}$	GDP01	B01	52	0.50	38.38	0.0818	70	51	blue
P(O_{229}-*g*-(D_{14})$_6$)-*b*-P(D)$_{14}$	GDP02	B01	55	0.50	25.67	0.1061	70	38	nlue
P(O_{229}-*r*-B_6)-*b*-P(D)$_{61}$	BCP01	B01	36	1.50	11.45	0.0755	70	40	green
P(O_{229}-*r*-B_6)-*b*-P(D)$_{61}$	BCP1.2	B01	30	1.50	10.05	0.0668	70	45	green
P(DEGMA)$_{244}$-*b*-P(D)$_{65}$	BCP2	B02	32	0.50	20.55	0.1360	70	43	green

Photo-iniferter RAFT grafting Polymerization of NiPAM Using P(OEGMA-r-BTPEMA) macroRAFT Agents as Precursor:

In the following, the photoRAFT syntheses of the graft-copolymers GN01 and GN02 are described. The exact polymerization parameters of GN01, GN02, and other NiPAM-based copolymers mentioned in Section 5.4.2 are listed in **Table 11**. The following grafting polymerization is explained using the example of the synthesis of GN01.

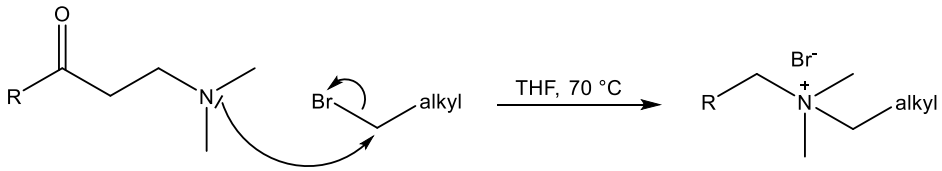
5.51 g (48.7 mmol) of recrystallized NiPAM was dissolved in 42.2 mL of 1,4-dioxane. 5.24 g (0.0707 mmol) B03 and 1.5 mL DMF were added to the monomer solution. The solution was purged with nitrogen gas for 15 min at room temperature to remove dissolved oxygen. The solution was heated to 70 °C using a pre-heated silicon oil bath, and an initial ^{1}H-NMR sample was taken. The reaction was initiated by turning on the blue LED. The monomer conversion was tracked using ^{1}H-NMR according to the literature.[1] At a monomer conversion of 53 %, the light source was turned off, and the reaction was quenched by cooling with an ice bath and exposed to air. The reaction solution was diluted with 40 mL of THF and was slowly added dropwise to a diethyl ether bath. The precipitate was isolated by filtration, redissolved, and precipitated twice more to remove unreacted NiPAM from the copolymer product GN01. Residual solvent was removed from the pale-yellow solid under reduced pressure at room temperature.

Table 11: Concluded reaction conditions and substance amounts for the synthesis of double thermoresponsive graft copolymers discussed in Section 5.4.3. For the respective polymers, the consecutive number (CN), the used chain transfer agent (CTA), the volume of the solvent 1,4-Dioxane (V_{Dox}), and of the DMF (V_{DMF}) used as the internal ^{1}H-NMR standard, the amounts of substance of DMAEMA (n_D), and the CTA (nCTA), the reaction temperature (T), and the final monomer conversion (p).

Polymer	CN	CTA	V_{Dox} / mL	V_{DMF} / mL	n_{mon} / mmol	n_{CTA} / mmol	T / °C	p_m / %
(POEGMA$_{233}$-*r*-P(NiPAM$_{34}$)$_{11}$)-*b*-P(NiPAM)$_{34}$	GN01	B03	42.15	1.0	47.73	0.071	70	53
(POEGMA$_{233}$-*r*-P(NiPAM$_{49}$)$_{11}$)-*b*-P(NiPAM)$_{49}$	GN02	B03	39.61	1.0	53.11	0.051	70	55

7.2.2.1. Post-Polymerization Functionalization

In this work, the nucleophilic character of DMAEMA's amine function was taken advantage of. Therefore, the nucleophilic substitution reaction (S_N2) mechanism was applied for the two relevant functionalizations described in Sections 5.2 and 5.3.



Scheme 8: S_N2 reaction mechanism of the formation of the quaternized amine function within the DMAEMA side chain.

Formation of Au@P(DMAEMA)$_n$ and P(DMAEMA)$_n$ Gel Networks via Aminie Quaternization

To crosslink the P(DMAEMA)-macroTTCs, a 1.0%(*w*/*w*) THF solution of the polymer was prepared. Afterward, 1.00 g of this solution was transferred into a 4.0 mL screw-capped flask. Based on the amount of amine functions in the solution, calculated from the degree of Polymerization of the dissolved polymer, 0.5 equivalents of DBrP were added to the solution. Afterwards, the flask was sealed and placed in a preheated silicon oil bath at 55 °C. Without stirring, the solution was stored for 72 hours in this setup. The obtained free-standing gel structure was investigated optically (**Figure 36**) and was not further analyzed.

To crosslink the Au@P(DMAEMA) hybrid THF suspensions, the concentrations of amines were calculated from TGA results. To the particle THF suspension with a volume of about 1.0 mL, 0.5 equivalents of DBrP were added. The screw-capped flask was sealed, and the suspension was mixed by shaking the flask by hand for a few seconds. Afterwards, the closed flask was heated with a silicon oil bath to 55 °C for 72 h. The obtained free-standing hybrid gel was investigated optically (**Figure 36**).

Formation of Quaternized P(DMAEMA)$_n$-Based Copolymer Precursors using them as CTAB Substitutes in the GNR Synthesis

Based on the experience from the previous paragraph, the post-polymerization functionalization of the tertiary amine is straightforward. Several pre-tests were performed to find the ideal way for the preparation of quaternized P(DMAEMA)$_n$-based polymer precursors. Amongst others, it was tested to prepare the qDMAEMA monomer via functionalization of the amine function of DMAEMA with BHD. However, these trials were unsuccessful because DMAEMA tends to form a colorless solid that is insoluble in common solvents such as water, THF, 1,4-dioxane, and dichloromethane (DCM). For this reason, post-polymerization functionalization was chosen as the most promising approach, as it has already demonstrated good results for the Au@P(DMAEMA) hybrids.

The reaction conditions for the copolymer functionalization were kept as simple as possible. The respective amounts of the used substances are concluded in **Table 12**. The respective P(DMAEMA) copolymer was dissolved together with a molar excess of 1-bromohexadecane (BHD) in DMF. The obtained solution was heated to 70 °C. To ensure complete conversion of the P(DMAEMA) blocks, amine functions, ^{1}H-NMR spectroscopy was used (compare **Figure 41**). For qBCP02, an investigation via FTIR spectroscopy was pursued, as shown in **Figure A5**.

Table 12: List of the chemical amounts and reaction time (t) at 70 °C used to functionalize DMAEMA units: mass of polymer (m_{poly}), mass of BHD (m_{BHD}), and volume of DMF (V_{DMF}).

Polymer	m_{poly} / g	m_{BHD} / g	V_{DMF} / mL	t / h
qGDP01	1.01	0.636	20	2
qGDP02	1.03	0.462	10	17
qBCP1	0.749	0.256	10	2
qBCP1.2	1.390	0.523	50	2.5
qBCP2	3.528	2.001	40	14

7.2.3. GNP Hybrid Material Preparation

This work covers different approaches to synthesizing GNP@Polymer hybrid materials. This chapter covers the three ways of particle preparation, following the order covered in Chapter 5. As mentioned earlier, parts of this work have already been published. Therefore, the following subsections are strongly related to the already published version, with minor adjustments in phrasing and some additional information.[3,8]

7.2.3.1. Synthesis of the Au@P(DMAEMA)$_n$ Hybrid System

The reaction conditions can vary slightly for the different hybrid products. The varying amounts of substance are listed in **Table 13**. The reaction was conducted under an inert gas (N_2) atmosphere. The synthesis of the described Au@P(DMAEMA)$_n$ hybrids was carried out as follows. 20 mL of a $HAuCl_4$-solution (c_{HAuCl4} = 3.5 mmol·L^{-1}) in dried THF was prepared. The freshly prepared solution was filled into a 250 mL three-necked round-bottom flask. The solution was stirred at 400 rpm with an oval magnetic stirring bar (35 mm). The reaction solution was cooled to 0 °C and maintained at this temperature throughout the reaction. A second solution containing 0.0070 mmol of the respective p/dttc-P(DMAEMA)$_n$ macroTTC and 20 mL of dry THF was added dropwise over 5 min to the cooled $HAuCl_4$ solution. After the addition, a turbid yellow solution was obtained. The solution was mixed for 30 min until 0.45 mL of the superhydrid® ($LiBH_4$ in THF c = 0.1 M) was rapidly injected into the solution using a conditioned syringe. During the addition of the reducing agent, the solution immediately turned brown. The solution was stirred at 0 °C for 3 hours. To quench the reduction process, milli-Q water (in an equal volume to the superhydride solution) was added, and the reaction solution was exposed to air.

At 40 °C, the reaction solution was reduced in volume to about 10 mL under reduced pressure. Several purification steps were followed. In the first step, the solution was added dropwise into 120 mL of cyclohexane. The turbid solution was then centrifuged for 6 min at 15 °C and 3820xG. After removing the supernatant, the residue was redispersed in 15 mL of DCM. Occasionally, redispersion was achieved by using ultrasonic sound. The obtained dispersion was filtered to remove larger agglomerates and side products. The residue in the filter was washed with additional DCM. Again, the filtrate volume was reduced to a volume of about 5 mL under reduced pressure at 40 °C. The precipitation process using cyclohexane and the subsequent centrifugation step were repeated. After removing the supernatant, the residue was dispersed in 5 mL THF and was stored in the dark at 0 °C until further use.

Table 13: Reaction conditions for the synthesis of the different Au@P(DMAEMA)$_n$ hybrids. This table summarizes the polymer amounts used (n_{poly}), their respective theoretical molecular weights ($M_{theo,poly}$), and the reaction times (t) for the Au@P(DMAEMA) hybrid synthesis, along with their consecutive numbers (CN).

Hybrid	CN	Polymer	$M_{theo,poly}$ / kDa	n_{poly} / mmol	t / min
Au@P(DMAEMA)$_{39}$	H1	pTTC-P(DMAEMA)$_{39}$	6.4	0.0070	180
Au@P(DMAEMA)$_{92}$	H2	pTTC-P(DMAEMA)$_{92}$	14.7	0.0070	180
Au@P(DMAEMA)$_{41}$	H3	dTTC-P(DMAEMA)$_{41}$	6.9	0.0070	180
Au@P(DMAEMA)$_{91}$	H4	dTTC-P(DMAEMA)$_{91}$	14.6	0.0069	180
Au@P(DMAEMA)$_{48}$	P_Au2	pTTC-P(DMAEMA)$_{48}$	7.9	0.0072	210
Au@P(DMAEMA)$_{48}$	P_Au3	pTTC-P(DMAEMA)$_{48}$	7.9	0.0074	210
Au@P(DMAEMA)$_{110}$	P_Au4	pTTC-P(DMAEMA)$_{110}$	17.5	0.0066	210
Au@P(DMAEMA)$_{37}$	P_Au5	pTTC-P(DMAEMA)$_{37}$	6.1	0.0072	210
Au@P(DMAEMA)$_{110}$	P_Au7	pTTC-P(DMAEMA)$_{110}$	17.5	0.0066	210
Au@P(DMAEMA)$_{110}$	P_Au8	pTTC-P(DMAEMA)$_{110}$	17.5	0.0066	1080
Au@P(DMAEMA)$_{72}$	P_Au10	pTTC-P(DMAEMA)$_{72}$	11.7	0.0070	210
Au@P(DMAEMA)$_{72}$	P_Au11	pTTC-P(DMAEMA)$_{72}$	11.7	0.0035	210
Au@P(DMAEMA)$_{72}$	P_Au12	pTTC-P(DMAEMA)$_{72}$	11.7	0.0141	210
Au@P(DMAEMA)$_{72}$	P_Au13	pTTC-P(DMAEMA)$_{72}$	11.7	0.0035	210
Au@P(DMAEMA)$_{72}$	P_Au14	pTTC-P(DMAEMA)$_{72}$	11.7	0.0140	210
Au@P(DMAEMA)$_{72}$	P_Au15	pTTC-P(DMAEMA)$_{72}$	11.7	0.0070	210
Au@P(DMAEMA)$_{72}$	P_Au16	pTTC-P(DMAEMA)$_{72}$	11.7	0.0053	210
Au@P(DMAEMA)$_{72}$	P_Au17	pTTC-P(DMAEMA)$_{72}$	11.7	0.0053	210
Au@P(DMAEMA)$_{72}$	P_Au18	pTTC-P(DMAEMA)$_{72}$	11.7	0.0026	210
Au@P(DMAEMA)$_{72}$	P_Au19	pTTC-P(DMAEMA)$_{72}$	11.7	0.0023	210
Au@P(DMAEMA)$_{110}$	P_Au20	pTTC-P(DMAEMA)$_{110}$	17.5	0.0066	300
Au@P(DMAEMA)$_{110}$	P_Au21	pTTC-P(DMAEMA)$_{110}$	17.5	0.0066	300
Au@P(DMAEMA)$_{72}$	P_Au22	pTTC-P(DMAEMA)$_{72}$	11.7	0.0071	1440
Au@P(DMAEMA)$_{72}$	P_Au23	pTTC-P(DMAEMA)$_{72}$	11.7	0.0027	1440

7.2.3.2. CTAB and Polymer-based GNR Synthesis: A Step Toward More Biocompatible Procedures

Before starting the GNR synthesis, it is recommended to prepare essential reagent stock solutions and keep them available during the procedure. As already mentioned in the literature and from experience in this work, the consistent quality of the used solutions and the precise timing of their addition to the reaction are essential for the success of the synthesis. The importance of the quality and the right timing cannot be stressed enough here (see Section 4.1.2.2 for more information).
A second recommendation is to prepare the seed solution prior to the preparation of the monomer solution. Since the seed solution shows limited stability, it must be prepared fresh before the reaction. For all solutions, water (milli-Q 18.1 MΩ·cm^{-1} @25 °C) was used as the solvent.
For the preparation of the seed solution and the monomer solution, a $CTAB_{(aq)}$ (c = 0.1 M) is needed. The second solution needed in both steps of the reaction is a $HAuCl_{4\,(aq)}$ (c = 50 mM) solution. Both stock solutions were prepared, sealed, and stored in the dark at 0 °C for several weeks (three months maximum). They were used in several GNR batches. Before use, the CTAB stock solution was heated to 30 °C to redissolve the precipitated CTAB. Since the actual amount of the polymer CTAB substitutes was limited, the stabilizing polymer solutions were prepared in the needed amounts for about three or five batches of polymer-based GNR synthesis. The concentration of CTAB-equivalent groups in these solutions varied with the nature of the polymer.
To reduce Au(III) ions during Au seed preparation, a strong reducing agent is used. Therefore, 10 mL of a 0.1 mM $NaBH_{4\,(aq)}$ solution was prepared five minutes before use and was cooled continuously in an ice bath until use because of the reactivity of $NaBH_4$ in water.
For the preparation of the monomer solution, two additional solutions are required: A 5 mM silver nitrate solution and a 0.1 M ascorbic acid solution. The $AgNO_{3\,(aq)}$ (c = 5 mM) was prepared as a stock solution, but, unlike the $HAuCl_4$ solution, it was stored for a maximum of one week in the dark at 0 °C. The 0.1 M ascorbic acid solution was freshly prepared before use and was consumed on the same day as its preparation.

Preparation of the CTAB Stabilized Seed (GNS@CTAB) Suspensions:

The following synthesis of the GNS@CTAB precursor used for the GNR synthesis has already been reported in the literature and is included here to provide all the information needed to reproduce the reported results in a single work.[8] Therefore, certain overlaps with the given literature can not be excluded. The base for the CTAB-stabilized seed suspensions is the procedure described by Scarabelli and coworkers.[7] Since the quality of the seed solution has a critical influence on the outcome of the GNR synthesis, every seed solution was tested in a regular CTAB-based GNR synthesis.

Prior to seed synthesis, the glassware and magnetic stirring bar were cleaned with aqua regia. All reactions were conducted in a 12 mL screw-capped glass flask. The magnetic stirring bar used for the reactions measured 5 mm in diameter and 20 mm in length. 4.7 mL of the CTAB stock solution was transferred into the glass flask, along with the stirring bar, and heated in an external water bath preheated to 30 °C. After reaching 30 °C, 25 µL of 0.5 mM $HAuCl_{4\,(aq)}$ stock solution was added to the CTAB solution. At this point, the solution turned yellow and usually became cloudy. At 600 rpm, the obtained solution was stirred until it appeared clear. When no more turbidity was observed optically, 300 µL of the $NaBH_{4\,(aq)}$ solution was injected rapidly into the reaction solution. During the whole process, the solution was constantly stirred at 600 rpm and kept at 30 °C. A few seconds after the addition of the reducing agent, the reduction of the Au(III) precursor became noticeable by a change to a brown color. The reaction solution was stored at 30 °C for up to 2 hours under continuous stirring, then used without further purification.

For the synthesis of CTAB-free Au seeds, instead of the 0.1 M CTAB stock solution, a qBCP02 stock solution with an amine concentration of 0.01 M was used.

Anisotropic growth: Seeded Growth of GNR:

Both procedures, the original CTAB-based GNR syntheses and the polymer-based GNR growth, are strongly related to the protocol by Nikoobakht and El-Sayed.[90] As for the Au@CTAB seed preparation, the procedure for GNR preparation is added to this work to provide all necessary information for reproducing the results. Since these results are already published, there will be significant overlaps with our publication.[8] Varying amounts of substances between each GNR batch are listed in **Table 14**. Each synthesis was performed in a 50 mL round-bottom flask. It was ensured that all flasks had the exact dimensions for optimal reproducibility. Additionally, it was ensured that all magnetic stirring bars used for mixing had the exact dimensions (20 mm × 5 mm). The used glassware and magnetic stirring bar were pre-cleaned with aqua regia to remove any residual particle impurities left on the equipment.

As shown in **Figure 6** on Page 20, the Au(I) monomer solution must first be prepared. Therefore, 10 mL of the 0.1 M CTAB solution was filled into the rinsed 50 mL round-bottom flask and was heated to 30 °C using a water bath. The solution was stirred at 600 rpm until it was clear. Afterwards, 100 µL of the $HAuCl_4$ stock solution was added to the CTAB solution. The addition caused an immediate color change from colorless to yellow. The solution was stirred for two minutes at a constant rate to ensure the complexation of the CTAB with the gold salt. If the solution appeared turbid, it was mixed until it seemed transparent. 75 µL of the ascorbic acid solution was added to the yellow solution to reduce the Au(III) ions to Au(I) ions. A decolorization of the yellow solution accompanies this reduction.

Immediately after the decolorization, 80 µL of a 5 mM $AgNO_{3\,(aq)}$ solution was added to obtain the precursor solution. The mixture was stirred for a few seconds before 120 µL of the previously prepared seed solution was rapidly injected directly into the precursor solution. After adding the seed solution, the reaction mixture was stirred for 20 s. *To support the mixing process, the solution can also be shaken by hand for a few seconds.* Afterward, the solution was left undisturbed for 30 min at 30 °C. Then, a UV–vis absorbance spectrum of the reaction solution was measured, and the solution was centrifuged at 30 °C for 75 min at 10,000xG. The supernatant was removed carefully with a pipette, and the precipitate was redispersed in 20 mL of water. The centrifuge cycle was performed a second time, and the final precipitate was redispersed in 5 mL of water (milli-Q 18.1 $M\Omega \cdot cm^{-1}$ @25 °C).

As a side note, the CTAB-based synthesis has a cation concentration of 0.1 M, while the cation concentration of the polymer-based approaches does not exceed 0.02 M. The change in viscosity of the monomer solution at high polymer concentrations prohibited achieving cation concentrations above 0.02 M. Additionally, for the grafted polymer structures, their insolubility significantly accounts for the lower anisotropic growth-directing cation concentration.

The copolymer-based NR synthesis followed the described protocol, substituting CTAB in the growth solution with the quaternized copolymer. The exact amounts of copolymer and the varying conditions are listed in **Table 14**.

Table 14: Reaction conditions for the synthesis of the different GNR-batches that are directly addressed in Section 5.3. This table includes the GNR nomenclature based on its stabilization, the consecutive number used in the related publication[8] (CN), the stabilizing ligand used for the synthesis, the amine concentration whtin the monomer solution (c_{amine}), the monomer solutions concetration of silver nitrate (c_{AgNO3}), the reaction temperature (T), and the reaction/growth time before the reaction was quenched.

GNR	CN	Ligand	c_{amine} / mol·L^{-1}	c_{AgNO3} / mmol·L^{-1}	T / °C	t / min
GNR@CTAB	NR1-CTAB	CTAB	0.1	5	30	30
GNR@qGDP01	NR1-30	qGDP01	<0.01	5	30	30
GNR@qGDP01	NR1-60	qGDP01	<0.01	5	30	60
GNR@qGDP01	NR1-120	qGDP01	<0.01	5	30	120
GNR@CTAB	-	CTAB	0.1	5	30	30
GNR@qGDP02	-	qGDP02	<0.01	5	27	30
GNR@qGDP02	-	qGDP02	<0.01	5	70	30
GNR@CTAB	NR3-CTAB	CTAB	0.1	5	30	30
GNR@qBCP01	NR3-30	qBCP01	0.01	5	30	30
GNR@qBCP01	NR3-70	qBCP01	0.01	5	70	30
GNR@CTAB	NR4-0.1	CTAB	0.1	5	30	30
GNR@CTAB	NR4-0.01	CTAB	0.01	5	30	30
GNR@qBCP02	NR7-0.01-30	qBCP02	0.01	10	27	30
GNR@qBCP02	NR7-0.02-30	qBCP02	0.02	10	27	30
GNR@qBCP02	NR8-30	qBCP02	0.05	10	27	30
GNR@qBCP02	NR9-45	qBCP02	0.01	10	45	30

7.2.3.3. Highly Reproducible Preparation of the GNS@Graft-Polymer Hybrids:

To produce GNS@GRAFT-Polymer hybrids, this work establishes the following procedure based on the grafting-to protocol first described by P. Vana and his coworkers.[247] The procedure started with the synthesis of monodispersed GNS@citrate based on the optimized reversed Truckevich synthesis from F. Schulz and coworkers.[63]

GNS synthesis: inversed Turkevich

Before the synthesis, the glassware was rinsed with aqua regia to remove any residual GNS from the inner surface of the used 2000 mL Erlenmeyer flask. For the reaction, two solutions were prepared. The first solution was prepared by dissolving 320 mg of $HAuCl_4$ $3H_2O$ in 1000 mL of water (cAu = 813 µM). This solution was later used as a stock solution for further batches. A second solution containing 487 mg (1.66 mmol) of TCA, 107 mg (0.509 mmol) of CA, and 800 mL of water was prepared. In a 2000 mL Erlenmeyer flask, the TCA/CA solution was heated to the boiling point. Under continuous mixing and heating, 6 mg (0.02 mmol) trisodium EDTA was added to the solution.
Meanwhile, 200 mL of the gold solution was heated to a temperature just below the boiling temperature. The hot Au precursor solution was rapidly added to the boiling TC/SC solution. The resulting reaction solution was stirred for 20 minutes. Afterwards, the heating was turned off, and the solution was slowly cooled to approximately 60 °C before being transferred into a room-temperature, brown glass, screw-capped flask. The solution was stored at room temperature in the dark. The solution was characterised using TEM and UV–Vis spectroscopy.

Preparation of the Au@Polymer Hybrids: Ligand Exchange

Preparing the Au@Polymer hybrids followed the protocol described by P. Vana and coworkers.[247] The procedure from the literature was stepwise adjusted, and a protocol was developed as a reliable method for preparing RAFT-polymer-stabilized GNS, which was transferable across different graft-polymer compositions.
First, a 1.0 $\%^{wt}$ solution of the graft copolymers was prepared. 80 mL of this solution was added to 80 mL of the GNS@citrate dispersion. The mixture was stirred for 1 hour and then stored undisturbed at 0°C in the dark for 72 hours. The sample was purified using three centrifuge cycles to remove excess citrate and unbound polymer. For the first cycle, the solution was transferred and separated into four 50 mL conical polypropylene centrifuge tubes, which were centrifuged at 0 °C at 8600xG for 8 hours. The colourless solvent was carefully removed from the red precipitate using a glass pipette. To reduce the loss of GNS, at least 4 mL of the solvent was left in each tube. Each tube was refilled to a volume of 20 mL with methanol, and the residue was redispersed. All

four dispersions were centrifuged at -5 °C and 8600xG for 8 hours. The colorless supernatant was carefully removed from the precipitate using a glass pipette. The centrifugation was repeated once, and the obtained precipitates were redispersed in 10 mL of water each. The dispersions were collected in one tube, which was centrifuged at 0 °C and 9500xG for 8 hours. The precipitate of that centrifugation was collected and dispersed in 30 mL of water. The final solution was characterized using TEM and UV–Vis absorbance spectroscopy.

This procedure was applied for the hybrid materials GNS@B03, GNS@GN01, and GNS@GN02. In the context of this work, several minor adjustments to the centrifugation cycle intensities and the polymer concentration of the initial polymer solution were tested. However, the presented method provided the most reliable results for particle assemblies, TEM imaging, and the temperature-responsive behavior of the hybrid materials. The described protocol offers some flexibility regarding polymer concentration in individual cases. However, to ensure comparable results, it is recommended not to use polymer concentrations below 1 %(*w*/*w*) in the initial solution. It is also worth noting that the volume scale of this method was limited by the centrifuge used. Using a larger scale for the ligand exchange could be beneficial for the process, because minor preparative inaccuracies and batch variations can be compensated for more effectively.

Table 15: Reaction conditions for the synthesis of the different GNS@graft-polymer batches discussed in Section 5.4. Listed are the hybrids with the respective polymer used for ligand exchange. This table includes the mass concentration of the prepared polymer solution (c_{Ligand}), the volume of the polymer solution used (V_{Ligand}), the Volume of the GNS@citrate suspension, and the ligand exchange time (t_{exc}), which corresponds to the time the combined solution was stored at 0 °C in the dark.

Hybrid	Ligand	c_{Ligand} / %(*w*/*w*)	V_{Ligand} / mL	V_{GNS} / mL	t_{exc} / h	procedure
GNS@BB03	BB03	1.0	80	80	72	centrifugation
GNS@GN01	GN01	1.0	80	80	72	centrifugation
GNS@GN02	GN02	1.0	80	80	72	centrifugation
GNS@TB-GN1	TB-GN1	0.15	20	20	~220	dialysis against 5 L
GNS@TB-GN1	TB-GN1	0.15	20	20	15	centrifugation
GNS@TB-GN2	TB-GN2	0.15	20	20	15	centrifugation

7.3. Analytical Methods

7.3.1. Basic Analytical Methods

Analytical methods that are considered basic methods are described in the appendix. To characterize the polymer products, the primary analytical methods used were ^{1}H-NMR spectroscopy and size-exclusion chromatography. Depending on the respective task, FTIR spectroscopy was employed, usually for a qualitative verification of the post-polymerization functionalization of P(DMAEMA)s' amine functions. See Appendix Section 9.1 for more detailed information. For the particle size evaluation of the Au-NP core of the different hybrids, TEM was used. The sample preparation, measurement, and evaluation of the TEM images are described in the appendix in Section 8.2

7.3.2. Temperature-Dependent Analytics

This section covers the temperature-dependent characterization methods for the RAFT polymers and for the GNP-hybrids described in Section 5.4. It includes the procedures for UV–Vis spectroscopy and DLS experiments, which are used in this work as standard analytical methods for temperature-responsive behaviour.

7.3.2.1. UV-Vis Spectroscopy

The Mettler Toledo UV5 was used for the UV–Vis measurements of the particle and polymer solutions. All measurements were conducted in a 10 mm quartz cuvette, at a measuring time of 60 seconds. To control the sample's temperature, a CuveT temperature element with an inlet temperature sensor was used. To measure their temperature-responsive properties, all polymers were dissolved in water (milli-Q 18.1 MΩ·cm^{-1} @25 °C), and a polymer concentration of 1.0 %(*w*/*w*) was set. For the GNS@polymer hybrids discussed in Section 5.4.2.2 and Section 5.4.3, the particle concentration was adjusted to a maximum absorbance of the plasmon signal between 2.5 and 3.0 before the temperature-dependent sequence was started. The preparation of the Au@P(DMAEMA)$_n$ hybrids is discussed in Section 5.4.1. The GNR@polymer hybrid was measured directly from the purified product suspension.

All solutions were measured in at least two heating–cooling cycles. The temperature range of the cycles was adjusted according to the expected transition temperatures of the sample. The temperature step size was 1 °C, and the temperature tolerance was 0.2 °C. At each temperature step, one absorbance spectrum was recorded for the sample. To avoid measuring the sample in a non-equilibrated state, an equilibration time between reaching each temperature step and taking the measurement was set to 30 seconds. This procedure was continuously adjusted throughout the project. For the P(DMAEMA)$_n$ and their respective Au@P(DMAEMA)$_n$ hybrids, the following cycles were conducted with an equilibration time of 10 minutes. Several experiments showed that this equilibration period could be readjusted down to 5 minutes without significant influence.

For the following two projects, the equilibration time of 5 minutes was used. This adjustment allowed a more time-effective characterization without losing its comparability to the DLS temperature-dependent experiments.

To evaluate the obtained data, OriginPro (64-bit; Version: 9.6.0.172) was used. The turbidity plots of the polymer solutions were calculated from the absorbance values of the UV–Vis spectra at the respective temperatures, measured at a wavelength of 800 nm. To evaluate the shift of the plasmonic maxima, the obtained UV–Vis spectra were plotted with a polynomial fit (9th Order) around the plasmonic band to determine the wavelength with the maximal plasmonic absorption.

7.3.2.2. Dynamic Light Scattering (DLS) Experiments

All DLS measurements were performed on an ALV CGS-3 with a He-Ne laser (633 nm wavelength). The DLS experiments of the Au-hybrid suspensions were conducted at the same concentration as the UV–Vis measurements. The aqueous polymer solution measurements were conducted at a polymer concentration of 0.1 %(*w*/*w*) in water.

All DLS measurements were conducted according to the following procedure. The detector was aligned at a 90° angle to the incident laser. For all measurements, a correlation time of 60 seconds was applied. For all samples, the temperature range was set from 20 °C to 70 °C. The temperature step size was set to 2 °C. The temperature tolerance for each step was set to 1.0 °C. The long correlation time and the high-temperature tolerance resulted in approximately one DLS measurement every 1 °C steps with a nearly continuous heating/cooling rate.

A tailor-made Python® script, programmed by Felix Lauterbach,[287] was used for evaluating the correlation function obtained from the DLS measurements. This program uses a cumulative fitting of the correlation function to determine the average hydrodynamic radius within the aqueous suspension.

7.3.2.3. Zeta potential

Zeta potential measurements were used for optimizing the polymer-assisted GNR synthesis. For these measurements, a Malvern Zetasizer Pro was used. Zeta potential measurements were applied only to the GNR for fundamental analysis. These measurements were conducted after the temperature-dependent turbidity measurements. Therefore, the temperature range of the measurement was adjusted to encompass the transition temperature of the respective polymer, typically from 20°C to 50°C, for a more time-efficient procedure. Around the transition temperature (±5.0 °C) of the polymer, the zeta potential was determined in steps of 1.0 °C; below and above this region, 5 °C steps were applied—the equilibration time after reaching the next temperature value before the subsequent measurement was set to 180 s.

8. References

[1] J. Xu, V. Abetz, *Soft Matter* **2022**, *18*, 2082–2091.

[2] J. Shan, M. Nuopponen, H. Jiang, E. Kauppinen, H. Tenhu, *Macromolecules* **2003**, *36*, 4526–4533.

[3] S. B. Lemich, N. Sobania, N. Meyer, P. Schütz, B. Hankiewicz, V. Abetz, *Macromol. Chem. Phys.* **2023**, *224*, 2200355.

[4] L. Vigderman, P. Manna, E. R. Zubarev, *Angew. Chemie - Int. Ed.* **2012**, *51*, 636–641.

[5] C. Kinnear, H. Dietsch, M. J. D. Clift, C. Endes, B. Rothen-Rutishauser, A. Petri-Fink, *Angew. Chemie - Int. Ed.* **2013**, *52*, 1934–1938.

[6] S. Wang, W. Lu, O. Tovmachenko, U. S. Rai, H. Yu, P. C. Ray, *Chem. Phys. Lett.* **2008**, *463*, 145–149.

[7] L. Scarabelli, A. Sánchez-Iglesias, J. Pérez-Juste, L. M. Liz-Marzán, *J. Phys. Chem. Lett.* **2015**, *6*, 4270–4279.

[8] S. B. Lemich, S. Soltau, M. Weißpflog, V. R. Schulze, N. Feliu, B. Hankiewicz, V. Abetz, *Adv. Funct. Mater.* **2024**, *34*, 1–9.

[9] J. Xu, V. Abetz, *Macromol. Chem. Phys.* **2022**, *223*, 2200058.

[10] E. Ponomareva, B. Tadgell, M. Hildebrandt, M. Krüsmann, S. Prévost, P. Mulvaney, M. Karg, *Soft Matter* **2022**, *18*, 807–825.

[11] B. Tadgell, E. Ponomareva, M. Karg, P. Mulvaney, *J. Phys. Chem. C* **2022**, *126*, 15336–15347.

[12] B. Tadgell, E. Ponomareva, M. Karg, P. Mulvaney, *J. Phys. Chem. C* **2022**, *126*, 4118–4131.

[13] P. Schütz, S. B. Lemich, M. Weißpflog, P. Körner, V. Abetz, B. Hankiewicz, *Nano Trends* **2025**, *10*, 100113.

[14] C.-W. Chang, S. B. Lemich, P. Schütz, S. Weerathaworn, M. Weißpflog, C.-T. Wu, Y.-H. Tseng, C.-T. Chang, B. Hankiewicz, V. Abetz, et al., *ACS Appl. Mater. Interfaces* **2024**, *16*, 61096–61104.

[15] H. Xia, G. Su, D. Wang, *Angew. Chemie* **2013**, *125*, 3814–3818.

[16] Y. Cai, W. Peng, P. Vana, *Nanoscale Adv.* **2022**, *4*, 2787–2793.

[17] F. Schulz, T. Vossmeyer, N. G. Bastús, H. Weller, *Langmuir* **2013**, *29*, 9897–9908.

[18] C. H. Su, H. L. Chiu, Y. C. Chen, M. Yesilmen, F. Schulz, B. Ketelsen, T. Vossmeyer, Y. C. Liao, *Langmuir* **2019**, *35*, 3256–3264.

[19] M. A. Garcia, *J. Phys. D. Appl. Phys.* **2012**, *45*, 389501.

[20] L. Jauffred, A. Samadi, H. Klingberg, P. M. Bendix, L. B. Oddershede, *Chem. Rev.* **2019**, *119*, 8087–8130.

[21] M. Faraday, *Philos. Trans. R. Soc. London* **1857**, *147*, 145–181.

[22] H. Siedentopf, R. Zsigmondy, *Ann. Phys.* **1902**, *315*, 1–39.

[23] A. Einstein, *Ann. Phys.* **1905**, *322*, 549–560.

[24] G. Mie, *Ann. Phys.* **1908**, *330*, 377–445.

[25] M. I. Mishchenko, *J. Quant. Spectrosc. Radiat. Transf.* **2009**, *110*, 1210–1222.

[26] C. Li, S. R. Grobmyer, N. Massol, X. Liang, Q. Zhang, L. Chen, L. L. Fajardo, H. Jiang, *Med. Phys.* **2008**, *35*, 2493–2501.

[27] J. A. Lock, G. Gouesbet, *J. Quant. Spectrosc. Radiat. Transf.* **2009**, *110*, 800–807.

[28] R. Gans, *Ann. Phys.* **1912**, *342*, 881–900.

[29] J. Turkevich, P. C. Stevenson, J. Hillier, *Discuss. Faraday Soc.* **1951**, *11*, 55–75.

[30] G. FRENS, *Nat. Phys. Sci.* **1973**, *241*, 20–22.

[31] G. Schmid, R. Pfeil, R. Boese, F. Bandermann, S. Meyer, G. H. M. Calis, J. W. A. van der Velden, *Chem. Ber.* **1981**, *114*, 3634–3642.

[32] M. Brust, M. Walker, D. Bethell, D. J. Schiffrin, R. Whyman, *J. Chem. Soc., Chem. Commun.* **1994**, 801–802.

[33] X. L. Deán-Ben, S. Gottschalk, B. Mc Larney, S. Shoham, D. Razansky, *Chem. Soc. Rev.* **2017**, *46*, 2158–2198.

[34] X. Huang, I. H. El-Sayed, W. Qian, M. A. El-Sayed, *J. Am. Chem. Soc.* **2006**, *128*, 2115–2120.

[35] J. Wu, W. Li, G. Hajisalem, A. Lukach, E. Kumacheva, F. Hof, R. Gordon, *Biomed. Opt. Express* **2014**, *5*, 4101.

[36] E. C. Dreaden, M. A. Mackey, X. Huang, B. Kang, M. A. El-Sayed, *Chem. Soc. Rev.* **2011**, *40*, 3391.

[37] S. Hwang, J. Nam, S. Jung, J. Song, H. Doh, S. Kim, *Nanomedicine* **2014**, *9*, 2003–2022.

[38] Y. Chen, X. Feng, *Int. J. Pharm.* **2022**, *625*, 122122.

[39] S. Yook, Z. Cai, Y. Lu, M. A. Winnik, J.-P. Pignol, R. M. Reilly, *J. Nucl. Med.* **2016**, *57*, 936–942.

[40] Y. Bae, W.-D. Jang, N. Nishiyama, S. Fukushima, K. Kataoka, *Mol. Biosyst.* **2005**, *1*, 242.

[41] L. S. Ardekani, P. W. Thulstrup, *Nanomaterials* **2022**, *12*, 1–17.

[42] R. E. Ionescu, *Int. J. Mol. Sci.* **2023**, *24*.

[43] O. I. Guliy, L. A. Dykman, *Biosens. Bioelectron. X* **2024**, *17*, 100457.

[44] M. Comotti, C. Della Pina, M. Rossi, *J. Mol. Catal. A Chem.* **2006**, *251*, 89–92.

[45] M. H. Rashid, T. K. Mandal, *Adv. Funct. Mater.* **2008**, *18*, 2261–2271.

[46] P. Zijlstra, J. W. M. Chon, M. Gu, *Nature* **2009**, *459*, 410–413.

[47] Y. Joseph, B. Guse, A. Yasuda, T. Vossmeyer, *Sensors Actuators, B Chem.* **2004**, *98*, 188–195.

[48] B. Shan, Y. Y. Broza, W. Li, Y. Wang, S. Wu, Z. Liu, J. Wang, S. Gui, L. Wang, Z. Zhang, et al., *ACS Nano* **2020**, *14*, 12125–12132.

[49] A. Choe, J. Yeom, R. Shanker, M. P. Kim, S. Kang, H. Ko, *NPG Asia Mater.* **2018**, *10*, 912–922.

[50] L. Chang, Y. Khan, L. Li, N. Yang, P. Yin, L. Guo, *RSC Adv.* **2017**, *7*, 13896–13903.

[51] E. Cao, W. Lin, M. Sun, W. Liang, Y. Song, *Nanophotonics* **2018**, *7*, 145–167.

[52] P. Biagioni, J. S. Huang, B. Hecht, *Reports Prog. Phys.* **2012**, *75*.

[53] L. Novotny, N. Van Hulst, *Nat. Photonics* **2011**, *5*, 83–90.

[54] C. Daruich De Souza, B. Ribeiro Nogueira, M. E. C. M. Rostelato, *J. Alloys Compd.* **2019**, *798*, 714–740.

[55] E. Boisselier, D. Astruc, *Chem. Soc. Rev.* **2009**, *38*, 1759.

[56] I. Ojea-Jiménez, F. M. Romero, N. G. Bastús, V. Puntes, *J. Phys. Chem. C* **2010**, *114*, 1800–1804.

[57] M. K. Chow, C. F. Zukoski, *J. Colloid Interface Sci.* **1994**, *165*, 97–109.

[58] P. W. Chung, R. Kumar, M. Pruski, V. S. Y. Lin, *Adv. Funct. Mater.* **2008**, *18*, 1390–1398.

[59] J. Polte, T. T. Ahner, F. Delissen, S. Sokolov, F. Emmerling, A. F. Thünemann, R. Kraehnert, *J. Am. Chem. Soc.* **2010**, *132*, 1296–1301.

[60] Y. Mikhlin, A. Karacharov, M. Likhatski, T. Podlipskaya, Y. Zubavichus, A. Veligzhanin, V. Zaikovski, *J. Colloid Interface Sci.* **2011**, *362*, 330–336.

[61] I. Ojea-Jiménez, J. M. Campanera, *J. Phys. Chem. C* **2012**, *116*, 23682–23691.

[62] P. Zhao, N. Li, D. Astruc, *Coord. Chem. Rev.* **2013**, *257*, 638–665.

[63] F. Schulz, T. Homolka, N. G. Bastús, V. Puntes, H. Weller, T. Vossmeyer, *Langmuir* **2014**, *30*, 10779–10784.

[64] C. B. Whitehead, S. Özkar, R. G. Finke, *Chem. Mater.* **2019**, *31*, 7116–7132.

[65] B. K. Pong, H. I. Elim, J. X. Chong, W. Ji, B. L. Trout, J. Y. Lee, *J. Phys. Chem. C* **2007**, *111*, 6281–6287.

[66] X. Ji, X. Song, J. Li, Y. Bai, W. Yang, X. Peng, *J. Am. Chem. Soc.* **2007**, *129*, 13939–13948.

[67] K. Zabetakis, W. E. Ghann, S. Kumar, M. C. Daniel, *Gold Bull.* **2012**, *45*, 203–211.

[68] S. Kumar, K. S. Gandhi, R. Kumar, *Ind. Eng. Chem. Res.* **2007**, *46*, 3128–3136.

[69] H. Xia, S. Bai, J. Hartmann, D. Wang, *Langmuir* **2010**, *26*, 3585–3589.

[70] F. Wang, V. N. Richards, S. P. Shields, W. E. Buhro, *Chem. Mater.* **2014**, *26*, 5–21.

[71] N. T. K. Thanh, N. Maclean, S. Mahiddine, *Chem. Rev.* **2014**, *114*, 7610–7630.

[72] I. Ojea-Jiménez, N. G. Bastús, V. Puntes, *J. Phys. Chem. C* **2011**, *115*, 15752–15757.

[73] S. K. Sivaraman, S. Kumar, V. Santhanam, *J. Colloid Interface Sci.* **2011**, *361*, 543–547.

[74] M. Wuithschick, A. Birnbaum, S. Witte, M. Sztucki, U. Vainio, N. Pinna, K. Rademann, F. Emmerling, R. Kraehnert, J. Polte, *ACS Nano* **2015**, *9*, 7052–7071.

[75] J. Polte, *CrystEngComm* **2015**, *17*, 6809–6830.

[76] F. Kettemann, A. Birnbaum, S. Witte, M. Wuithschick, N. Pinna, R. Kraehnert, K. Rademann, J. Polte, *Chem. Mater.* **2016**, *28*, 4072–4081.

[77] A. Gole, C. J. Murphy, *Chem. Mater.* **2004**, *16*, 3633–3640.

[78] C. J. Johnson, E. Dujardin, S. A. Davis, C. J. Murphy, S. Mann, *J. Mater. Chem.* **2002**, *12*, 1765–1770.

[79] S. Barbosa, A. Agrawal, L. Rodríguez-Lorenzo, I. Pastoriza-Santos, R. A. Alvarez-Puebla, A. Kornowski, H. Weller, L. M. Liz-Marzán, *Langmuir* **2010**, *26*, 14943–14950.

[80] D. Sun, F. Ben Romdhane, A. Wilson, M. Salmain, S. Boujday, *ACS Appl. Nano Mater.* **2024**, *7*, 5093–5102.

[81] S. Ye, A. A. Azad, J. E. Chambers, A. J. Beckett, L. Roach, S. C. T. Moorcroft, Z. Aslam, I. A. Prior, A. F. Markham, P. L. Coletta, et al., *Small* **2020**, *16*.

[82] C. Schönenberger, B. M. I. Van Der Zande, L. G. J. Fokkink, M. Henny, C. Schmid, M. Krüger, A. Bachtold, R. Huber, H. Birk, U. Staufer, *J. Phys. Chem. B* **1997**, *101*, 5497–5505.

[83] C. Gao, Q. Zhang, Z. Lu, Y. Yin, *J. Am. Chem. Soc.* **2011**, *133*, 19706–19709.

[84] A. V. Alekseeva, V. A. Bogatyrev, B. N. Khlebtsov, A. G. Mel'nikov, L. A. Dykman, N. G. Khlebtsov, *Colloid J.* **2006**, *68*, 661–678.

[85] W. Niu, L. Zhang, G. Xu, *Nanoscale* **2013**, *5*, 3172–3181.

[86] C. J. Murphy, L. B. Thompson, D. J. Chernak, J. A. Yang, S. T. Sivapalan, S. P. Boulos, J. Huang, A. M. Alkilany, P. N. Sisco, *Curr. Opin. Colloid Interface Sci.* **2011**, *16*, 128–134.

[87] A. Chhatre, R. Thaokar, A. Mehra, *Cryst. Growth Des.* **2018**, *18*, 3269–3282.

[88] E. Carbó-Argibay, B. Rodríguez-González, S. Gómez-Graña, A. Guerrero-Martínez, I. Pastoriza-Santos, J. Pérez-Juste, L. M. Liz-Marzán, *Angew. Chemie Int. Ed.* **2010**, *49*, 9397–9400.

[89] J. Mosquera, D. Wang, S. Bals, L. M. Liz-Marzán, *Acc. Chem. Res.* **2023**, *56*, 1204–1212.

[90] B. Nikoobakht, M. A. El-Sayed, *Chem. Mater.* **2003**, *15*, 1957–1962.

[91] J. Pérez-Juste, L. M. Liz-Marzán, S. Carnie, D. Y. C. Chan, P. Mulvaney, *Adv. Funct. Mater.* **2004**, *14*, 571–579.

[92] C. Oliveira, C. R. Chaves, P. Bargiela, M. da G. C. da Rocha, A. F. da Silva, J. F. D. Chubaci, M. Boström, C. Persson, M. Malta, *J. Mater. Res. Technol.* **2021**, *15*, 768–776.

[93] M. J. Walsh, W. Tong, H. Katz-Boon, P. Mulvaney, J. Etheridge, A. M. Funston, *Acc.*

Chem. Res. **2017**, *50*, 2925–2935.

[94] Y. Xia, X. Xia, H. C. Peng, *J. Am. Chem. Soc.* **2015**, *137*, 7947–7966.

[95] J. Zheng, X. Cheng, H. Zhang, X. Bai, R. Ai, L. Shao, J. Wang, *Chem. Rev.* **2021**, *121*, 13342–13453.

[96] B. Nikoobakht, M. A. El-Sayed, *Langmuir* **2001**, *17*, 6368–6374.

[97] C. J. Murphy, T. K. Sau, A. M. Gole, C. J. Orendorff, J. Gao, L. Gou, S. E. Hunyadi, T. Li, *J. Phys. Chem. B* **2005**, *109*, 13857–13870.

[98] T. K. Sau, C. J. Murphy, *Langmuir* **2005**, *21*, 2923–2929.

[99] M. Sethi, G. E. Joung, M. R. Knecht, *Langmuir* **2009**, *25*, 317–325.

[100] D. W. Taylor, T. A. Nieman, *Anal. Chem.* **1984**, *56*, 593–595.

[101] S. Tiwari, C. Mall, P. P. Solanki, *Surfaces and Interfaces* **2020**, *18*, 100427.

[102] S. Chandravanshi, S. K. Upadhyay, *Color. Technol.* **2012**, *128*, 300–305.

[103] M. T. Anderson, J. E. Martin, J. G. Odinek, P. P. Newcomer, *Chem. Mater.* **1998**, *10*, 1490–1500.

[104] N. R. Jana, *Chem. Commun.* **2003**, *3*, 1950.

[105] M. Sethi, G. E. Joung, M. R. Knecht, *Langmuir* **2009**, *25*, 1572–1581.

[106] K. Liu, N. Zhao, E. Kumacheva, *Chem. Soc. Rev.* **2011**, *40*, 656–671.

[107] L. Vigderman, B. P. Khanal, E. R. Zubarev, *Adv. Mater.* **2012**, *24*, 4811–4841.

[108] X. Huang, S. Neretina, M. A. El-Sayed, *Adv. Mater.* **2009**, *21*, 4880–4910.

[109] Z. L. Wang, M. B. Mohamed, S. Link, M. A. El-Sayed, *Surf. Sci.* **1999**, *440*.

[110] M. Grzelczak, J. Pérez-Juste, P. Mulvaney, L. M. Liz-Marzán, *Chem. Soc. Rev.* **2008**, *37*, 1783.

[111] Y. Xu, L. Chen, X. Ye, X. Wang, J. Yu, Y. Zhao, M. Cao, Z. Xia, B. Sun, Q. Zhang, *Nano Res.* **2017**, *10*, 2146–2155.

[112] F. Hubert, F. Testard, O. Spalla, *Langmuir* **2008**, *24*, 9219–9222.

[113] N. Almora-Barrios, G. Novell-Leruth, P. Whiting, L. M. Liz-Marzán, N. López, *Nano Lett.* **2014**, *14*, 871–875.

[114] J. A. Edgar, A. M. McDonagh, M. B. Cortie, *ACS Nano* **2012**, *6*, 1116–1125.

[115] Z. Zhang, M. Lin, *RSC Adv.* **2014**, *4*, 17760–17767.

[116] M. Tebbe, C. Kuttner, M. Männel, A. Fery, M. Chanana, *ACS Appl. Mater. Interfaces* **2015**, *7*, 5984–5991.

[117] X. Ye, L. Jin, H. Caglayan, J. Chen, G. Xing, C. Zheng, V. Doan-Nguyen, Y. Kang, N. Engheta, C. R. Kagan, et al., *ACS Nano* **2012**, *6*, 2804–2817.

[118] X. Ye, C. Zheng, J. Chen, Y. Gao, C. B. Murray, *Nano Lett.* **2013**, *13*, 765–771.

[119] M. G. Blaber, M. D. Arnold, M. J. Ford, *J. Phys. Condens. Matter* **2010**, *22*.

[120] V. Amendola, R. Pilot, M. Frasconi, O. M. Maragò, M. A. Iatì, *J. Phys. Condens. Matter* **2017**, *29*.

[121] K. A. Willets, R. P. Van Duyne, *Annu. Rev. Phys. Chem.* **2007**, *58*, 267–297.

[122] S. Eustis, M. A. El-Sayed, *Chem. Soc. Rev.* **2006**, *35*, 209–217.

[123] K. M. Mayer, J. H. Hafner, *Chem. Rev.* **2011**, *111*, 3828–3857.

[124] X. Cui, Q. Ruan, X. Zhuo, X. Xia, J. Hu, R. Fu, Y. Li, J. Wang, H. Xu, *Chem. Rev.* **2023**, *123*, 6891–6952.

[125] M. L. Brongersma, N. J. Halas, P. Nordlander, *Nat. Nanotechnol.* **2015**, *10*, 25–34.

[126] M. Bernardi, J. Mustafa, J. B. Neaton, S. G. Louie, *Nat. Commun.* **2015**, *6*.

[127] S. Link, M. A. El-Sayed, *J. Phys. Chem. B* **1999**, *103*, 4212–4217.

[128] N. G. Khlebtsov, *Anal. Chem.* **2008**, *80*, 6620–6625.

[129] S. Link, M. A. El-Sayed, *Int. Rev. Phys. Chem.* **2000**, *19*, 409–453.

[130] L. B. Scaffardi, N. Pellegri, O. De Sanctis, J. O. Tocho, *Nanotechnology* **2005**, *16*, 158–163.

[131] R. Yu, L. M. Liz-Marzán, F. J. García De Abajo, *Chem. Soc. Rev.* **2017**, *46*, 6710–6724.

[132] H. Chen, L. Shao, Q. Li, J. Wang, *Chem. Soc. Rev.* **2013**, *42*, 2679–2724.

[133] H. Okamoto, K. Imura, *J. Mater. Chem.* **2006**, *16*, 3920–3928.

[134] N. Verellen, F. López-Tejeira, R. Paniagua-Domínguez, D. Vercruysse, D. Denkova, L. Lagae, P. Van Dorpe, V. V. Moshchalkov, J. A. Sánchez-Gil, *Nano Lett.* **2014**, *14*, 2322–2329.

[135] Q. Ruan, L. Shao, Y. Shu, J. Wang, H. Wu, *Adv. Opt. Mater.* **2014**, *2*, 65–73.

[136] A. M. Alkilany, C. J. Murphy, *J. Nanoparticle Res.* **2010**, *12*, 2313–2333.

[137] M. Liang, I. C. Lin, M. R. Whittaker, R. F. Minchin, M. J. Monteiro, I. Toth, *ACS Nano* **2010**, *4*, 403–413.

[138] S. Link, M. B. Mohamed, M. A. El-Sayed, *J. Phys. Chem. B* **1999**, *103*, 3073–3077.

[139] A. Liu, G. Wang, F. Wang, Y. Zhang, *Coord. Chem. Rev.* **2017**, *336*, 28–42.

[140] N. J. Halas, S. Lal, W.-S. Chang, S. Link, P. Nordlander, *Chem. Rev.* **2011**, *111*, 3913–3961.

[141] K. H. Su, Q. H. Wei, X. Zhang, J. J. Mock, D. R. Smith, S. Schultz, *Nano Lett.* **2003**, *3*, 1087–1090.

[142] W. Rechberger, A. Hohenau, A. Leitner, J. R. Krenn, B. Lamprecht, F. R. Aussenegg, *Opt. Commun.* **2003**, *220*, 137–141.

[143] P. K. Jain, W. Huang, M. A. El-Sayed, *Nano Lett.* **2007**, *7*, 2080–2088.

[144] C. Tabor, D. Van Haute, M. A. El-Sayed, *ACS Nano* **2009**, *3*, 3670–3678.

[145] P. K. Jain, M. A. El-Sayed, *Nano Lett.* **2007**, *7*, 2854–2858.

[146] L. Gunnarsson, T. Rindzevicius, J. Prikulis, B. Kasemo, M. Käll, S. Zou, G. C. Schatz, *J. Phys. Chem. B* **2005**, *109*, 1079–1087.

[147] K. G. Thomas, S. Barazzouk, B. I. Ipe, S. T. S. Joseph, P. V. Kamat, *J. Phys. Chem. B* **2004**, *108*, 13066–13068.

[148] S. T. Shibu Joseph, B. I. Ipe, P. Pramod, K. G. Thomas, *J. Phys. Chem. B* **2006**, *110*, 150–157.

[149] P. K. Jain, S. Eustis, M. A. El-Sayed, *J. Phys. Chem. B* **2006**, *110*, 18243–18253.

[150] L. S. Slaughter, Y. Wu, B. A. Willingham, P. Nordlander, S. Link, *ACS Nano* **2010**, *4*, 4657–4666.

[151] B. Luk'Yanchuk, N. I. Zheludev, S. A. Maier, N. J. Halas, P. Nordlander, H. Giessen, C. T. Chong, *Nat. Mater.* **2010**, *9*, 707–715.

[152] K. C. Woo, L. Shao, H. Chen, Y. Liang, J. Wang, H. Q. Lin, *ACS Nano* **2011**, *5*, 5976–5986.

[153] L. Shao, C. Fang, H. Chen, Y. C. Man, J. Wang, H.-Q. Lin, *Nano Lett.* **2012**, *12*, 1424–1430.

[154] S. Perrier, *Macromolecules* **2017**, *50*, 7433–7447.

[155] K. Matyjaszewski, *Macromolecules* **2012**, *45*, 4015–4039.

[156] H. R. Lamontagne, B. H. Lessard, *ACS Appl. Polym. Mater.* **2020**, *2*, 5327–5344.

[157] A. D. Jenkins, R. G. Jones, G. Moad, *Pure Appl. Chem.* **2009**, *82*, 483–491.

[158] G. Moad, E. Rizzardo, S. H. Thang, *Polym. Int.* **2011**, *60*, 9–25.

[159] I. Blakey, T. L. Schiller, Z. Merican, P. M. Fredericks, *Langmuir* **2010**, *26*, 692–701.

[160] H. Zhu, D. M. Coleman, C. J. Dehen, I. M. Geisler, D. Zemlyanov, J. Chmielewski, G. J. Simpson, A. Wei, *Langmuir* **2008**, *24*, 8660–8666.

[161] C. Boyer, M. R. Whittaker, K. Chuah, J. Liu, T. P. Davis, *Langmuir* **2010**, *26*, 2721–2730.

[162] B. Ebeling, P. Vana, *Macromolecules* **2013**, *46*, 4862–4871.

[163] W. Peng, C. Rossner, V. Roddatis, P. Vana, *ACS Macro Lett.* **2016**, *5*, 1227–1231.

[164] J. Chiefari, Y. K. B. Chong, F. Ercole, J. Krstina, J. Jeffery, T. P. T. Le, R. T. A. Mayadunne, G. F. Meijs, C. L. Moad, G. Moad, et al., *Living Free-Radical Polymerization by Reversible Addition−Fragmentation Chain Transfer: The RAFT Process*, **1998**.

[165] P. Corpart, D. Charmot, S. Z. Zard, T. Biadatti, D. Michelet, *Method for Block Polymer Synthesis by Controlled Radical Polymerisation*, **1998**.

[166] L. Tam Phuong, G. Moad, E. Rizzardo, T. San Hoa, *Polymerization with Living Characteristics*, **1998**.

[167] M. Semsarilar, V. Abetz, *Macromol. Chem. Phys.* **2021**, *222*.

[168] G. Moad, E. Rizzardo, S. H. Thang, *Aust. J. Chem.* **2012**, *65*, 985.

[169] A. E. Smith, X. Xu, C. L. McCormick, *Prog. Polym. Sci.* **2010**, *35*, 45–93.

[170] D. J. Keddie, G. Moad, E. Rizzardo, S. H. Thang, *Macromolecules* **2012**, *45*, 5321–5342.

[171] F. Lauterbach, V. Abetz, *Macromol. Rapid Commun.* **2020**, *2000029*, 2000029.

[172] S. Weerathaworn, V. Abetz, *Macromol. Chem. Phys.* **2022**, *2200248*.

[173] S. Eggers, T. Eckert, V. Abetz, *J. Polym. Sci. Part A Polym. Chem.* **2018**, *56*, 399–411.

[174] I. Oral, L. Grossmann, E. Fedorenko, J. Struck, V. Abetz, *Polymers (Basel).* **2021**, *13*, 3675.

[175] F. Lauterbach, V. Abetz, *Soft Matter* **2020**, *16*, 2321–2331.

[176] M. Hartlieb, *Macromol. Rapid Commun.* **2022**, *43*.

[177] G. Moad, E. Rizzardo, S. H. Thang, *Aust. J. Chem.* **2009**, *62*, 1402–1472.

[178] G. Gody, T. Maschmeyer, P. B. Zetterlund, S. Perrier, *Macromolecules* **2014**, *47*, 639–649.

[179] P. Derboven, P. H. M. Van Steenberge, J. Vandenbergh, M. Reyniers, T. Junkers, D. R. D'hooge, G. B. Marin, *Macromol. Rapid Commun.* **2015**, *36*, 2149–2155.

[180] M. H. Stenzel, *Macromol. Rapid Commun.* **2009**, *30*, 1603–1624.

[181] T. Otsu, *J. Polym. Sci. Part A Polym. Chem.* **2000**, *38*, 2121–2136.

[182] H. Wang, Q. Li, J. Dai, F. Du, H. Zheng, R. Bai, *Macromolecules* **2013**, *46*, 2576–2582.

[183] T. G. McKenzie, Q. Fu, M. Uchiyama, K. Satoh, J. Xu, C. Boyer, M. Kamigaito, G. G. Qiao, *Adv. Sci.* **2016**, *3*, 1–9.

[184] T. G. McKenzie, Q. Fu, E. H. H. Wong, D. E. Dunstan, G. G. Qiao, *Macromolecules* **2015**, *48*, 3864–3872.

[185] J. Phommalysack-Lovan, Y. Chu, C. Boyer, J. Xu, *Chem. Commun.* **2018**, *54*, 6591–6606.

[186] L. Hub, J. Koll, M. Radjabian, V. Abetz, *Polym. Chem.* **2023**, *14*, 3063–3074.

[187] S. Shanmugam, J. Cuthbert, T. Kowalewski, C. Boyer, K. Matyjaszewski, *Macromolecules* **2018**, *51*, 7776–7784.

[188] S. Kitano, Y. Koyama, K. Kataoka, T. Okano, Y. Sakurai, *J. Control. Release* **1992**, *19*, 161–170.

[189] S. V. Walter, F. Ennen-Roth, D. Büning, D. Denizer, M. Ulbricht, *ACS Appl. Bio Mater.* **2019**, *2*, 2464–2480.

[190] A. Ali, S. Saroj, S. Saha, S. K. Gupta, T. Rakshit, S. Pal, *ACS Appl. Mater. Interfaces* **2023**, *15*, 32240–32250.

[191] M. R. Islam, Y. Gao, X. Li, M. J. Serpe, *J. Mater. Chem. B* **2014**, *2*, 2444–2451.

[192] I. Park, K. Singha, R. B. Arote, Y. Choi, W. J. Kim, C. Cho, *Macromol. Rapid Commun.* **2010**, *31*, 1122–1133.

[193] A. Darabi, P. G. Jessop, M. F. Cunningham, *Chem. Soc. Rev.* **2016**, *45*, 4391–4436.

[194] G. Kocak, C. Tuncer, V. Bütün, *Polym. Chem.* **2017**, *8*, 144–176.

[195] S. Eggers, B. Fischer, V. Abetz, *Macromol. Chem. Phys.* **2016**, *217*, 735–747.

[196] T. Xiang, T. Lu, W.-F. Zhao, C.-S. Zhao, *Langmuir* **2019**, *35*, 1146–1155.

[197] J. P. Magnusson, A. Khan, G. Pasparakis, A. O. Saeed, W. Wang, C. Alexander, *J. Am. Chem. Soc.* **2008**, *130*, 10852–10853.

[198] P.-H. Hsu, A. Almutairi, *J. Mater. Chem. B* **2021**, *9*, 2179–2188.

[199] S. Fu, C. M. Rempson, V. Puche, B. Zhao, F. Zhang, *Methods* **2022**, *199*, 67–79.

[200] F. D. Jochum, P. Theato, *Chem. Soc. Rev.* **2013**, *42*, 7468–7483.

[201] O. Bertrand, J.-F. Gohy, *Polym. Chem.* **2017**, *8*, 52–73.

[202] G. Stoychev, A. Kirillova, L. Ionov, *Adv. Opt. Mater.* **2019**, *7*.

[203] A. Gafiullina, B. P. Ladewig, J. Zhang, *ACS Appl. Polym. Mater.* **2023**, *5*, 1–30.

[204] A. F. Kanaan, A. P. Piedade, *Mater. Adv.* **2022**, *3*, 2337–2353.

[205] E. Yarali, M. Baniasadi, A. Zolfagharian, M. Chavoshi, F. Arefi, M. Hossain, A. Bastola, M. Ansari, A. Foyouzat, A. Dabbagh, et al., *Appl. Mater. Today* **2022**, *26*, 101306.

[206] Y. Itoh, D. Morishita, *Polym. J.* **2023**, *55*, 1035–1048.

[207] T. Manouras, M. Vamvakaki, *Polym. Chem.* **2017**, *8*, 74–96.

[208] A. Feng, C. Zhan, Q. Yan, B. Liu, J. Yuan, *Chem. Commun.* **2014**, *50*, 8958.

[209] D. Selianitis, S. Pispas, *J. Polym. Sci.* **2020**, *58*, 1867–1880.

[210] J. Xu, V. Abetz, *Macromol. Rapid Commun.* **2021**, *42*.

[211] B. Karagoz, L. Esser, H. T. Duong, J. S. Basuki, C. Boyer, T. P. Davis, *Polym. Chem.* **2014**, *5*, 350–355.

[212] S. Agarwal, Y. Zhang, S. Maji, A. Greiner, *Mater. Today* **2012**, *15*, 388–393.

[213] J. I. Clodt, V. Filiz, S. Rangou, K. Buhr, C. Abetz, D. Höche, J. Hahn, A. Jung, V. Abetz, *Adv. Funct. Mater.* **2013**, *23*, 731–738.

[214] Y. T. Shieh, Y. C. Yeh, C. C. Cheng, *ACS Omega* **2019**, *4*, 15479–15487.

[215] T. Eckert, V. Abetz, *J. Polym. Sci.* **2020**, *58*, 3050–3060.

[216] G. M. Kontogeorgis, N. von Solms, in *Handb. Surf. Colloid Chem.*, CRC Press, **2015**, pp. 214–288.

[217] X. Wang, X. Qiu, C. Wu, *Macromolecules* **1998**, *31*, 2972–2976.

[218] Y. Maeda, T. Nakamura, I. Ikeda, *Macromolecules* **2001**, *34*, 8246–8251.

[219] S. A. Deshmukh, S. K. R. S. Sankaranarayanan, K. Suthar, D. C. Mancini, *J. Phys. Chem. B* **2012**, *116*, 2651–2663.

[220] S. A. Deshmukh, Z. Li, G. Kamath, K. J. Suthar, S. K. R. S. Sankaranarayanan, D. C. Mancini, *Polymer (Guildf).* **2013**, *54*, 210–222.

[221] S. A. Deshmukh, S. K. R. S. Sankaranarayanan, D. C. Mancini, *J. Phys. Chem. B* **2012**, *116*, 5501–5515.

[222] L. Tavagnacco, E. Zaccarelli, E. Chiessi, *J. Phys. Chem. B* **2022**, *126*, 3778–3788.

[223] Y. Zhang, S. Furyk, D. E. Bergbreiter, P. S. Cremer, *J. Am. Chem. Soc.* **2005**, *127*, 14505–14510.

[224] D. G. Mintis, M. Dompé, M. Kamperman, V. G. Mavrantzas, *J. Phys. Chem. B* **2020**, *124*, 240–252.

[225] D. Fournier, R. Hoogenboom, H. M. L. Thijs, R. M. Paulus, U. S. Schubert, *Macromolecules* **2007**, *40*, 915–920.

[226] P. Van De Watering, N. J. Zuidam, M. J. Van Steenbergen, O. A. G. J. Van Der Houwen, W. J. M. Underberg, W. E. Hennink, *Macromolecules* **1998**, *31*, 8063–8068.

[227] V. Bütün, S. P. Armes, N. C. Billingham, *Polymer (Guildf).* **2001**, *42*, 5993–6008.

[228] M. F. Cunningham, P. G. Jessop, *Eur. Polym. J.* **2016**, *76*, 208–215.

[229] O. Samsonova, C. Pfeiffer, M. Hellmund, O. M. Merkel, T. Kissel, *Polymers (Basel).* **2011**, *3*, 693–718.

[230] D. W. Lim, Y. Il Yeom, T. G. Park, *Bioconjug. Chem.* **2000**, *11*, 688–695.

[231] H. Liu, S. Lin, Y. Feng, P. Theato, *Polym. Chem.* **2017**, *8*, 12–23.

[232] C. Roosen, M. Ansorge-Schumacher, T. Mang, W. Leitner, L. Greiner, *Green Chem.* **2007**, *9*, 455–458.

[233] J. D. Holmes, K. J. Ziegler, M. Audriani, C. T. Lee, P. A. Bhargava, D. C. Steytler, K. P. Johnston, *J. Phys. Chem. B* **1999**, *103*, 5703–5711.

[234] K. L. Toews, R. M. Shroll, C. M. Wai, N. G. Smart, *Anal. Chem.* **1995**, *67*, 4040–4043.

[235] J. Y. Quek, T. P. Davis, A. B. Lowe, *Chem. Soc. Rev.* **2013**, *42*, 7326–7334.

[236] J. Y. Quek, P. J. Roth, R. A. Evans, T. P. Davis, A. B. Lowe, *J. Polym. Sci. Part A Polym.*

Chem. **2013**, *51*, 394–404.

[237] D. Zhang, Y. Fan, H. Chen, S. Trépout, M. H. Li, *Angew. Chemie - Int. Ed.* **2019**, *100029*, 10260–10265.

[238] B. Yan, D. Han, O. Boissière, P. Ayotte, Y. Zhao, *Soft Matter* **2013**, *9*, 2011.

[239] M. Li, L. Lei, Q. Zhang, S. Zhu, *Macromol. Rapid Commun.* **2016**, *37*, 957–962.

[240] M. F. Cunningham, P. G. Jessop, *Macromolecules* **2019**, acs.macromol.9b00914.

[241] M. Kampferbeck, T. Vossmeyer, H. Weller, *Langmuir* **2019**, *35*, 8790–8798.

[242] M. U. Witt, S. Hinrichs, N. Möller, S. Backes, B. Fischer, R. Von Klitzing, *J. Phys. Chem. B* **2019**, *123*, 2405–2413.

[243] M. U. Witt, J. Landers, S. Hinrichs, S. Salamon, J. Kopp, B. Hankiewicz, H. Wende, R. Von Klitzing, *Soft Matter* **2022**, *18*, 1089–1099.

[244] P. Haida, G. Signorato, V. Abetz, *Polym. Chem.* **2021**.

[245] P. Haida, S. Chirachanchai, V. Abetz, *ACS Sustain. Chem. Eng.* **2023**, *11*, 8350–8361.

[246] A. S. Duwez, P. Guillet, C. Colard, J. F. Gohy, C. A. Fustin, *Macromolecules* **2006**, *39*, 2729–2731.

[247] C. Rossner, B. Ebeling, P. Vana, *ACS Macro Lett.* **2013**, *2*, 1073–1076.

[248] L. Upadhyaya, M. Semsarilar, S. Nehache, D. Cot, R. Fernández-Pacheco, G. Martinez, R. Mallada, A. Deratani, D. Quemener, *Macromolecules* **2016**, *49*, 7908–7916.

[249] L. Upadhyaya, C. Egbosimba, X. Qian, R. Wickramasinghe, R. Fernández-Pacheco, I. M. Coelhoso, C. A. M. Portugal, J. G. Crespo, D. Quemener, M. Semsarilar, *Macromol. Rapid Commun.* **2019**, *40*, 1800333.

[250] S. K. Kumar, B. C. Benicewicz, R. A. Vaia, K. I. Winey, *Macromolecules* **2017**, *50*, 714–731.

[251] M. Nuopponen, H. Tenhu, *Langmuir* **2007**, *23*, 5352–5357.

[252] C. Said-Mohamed, J. Niskanen, M. Karesoja, P. Pulkkinen, H. Tenhu, M. Daoud, L. T. Lee, *Soft Matter* **2011**, *7*, 7112–7122.

[253] J. Shan, M. Nuopponen, H. Jiang, T. Viitala, E. Kauppinen, K. Kontturi, H. Tenhu, *Macromolecules* **2005**, *38*, 2918–2926.

[254] A. B. Lowe, B. S. Sumerlin, M. S. Donovan, C. L. McCormick, *J. Am. Chem. Soc.* **2002**,

124, 11562–11563.

[255] J. Shan, Y. Zhao, N. Granqvist, H. Tenhu, *Macromolecules* **2009**, *42*, 2696–2701.

[256] E. GIL, S. HUDSON, *Prog. Polym. Sci.* **2004**, *29*, 1173–1222.

[257] F. Yang, Z. Cao, G. Wang, *Polym. Chem.* **2015**, *6*, 7995–8002.

[258] C. Rossner, Q. Tang, O. Glatter, M. Müller, P. Vana, *Langmuir* **2017**, *33*, 2017–2026.

[259] C. Rossner, T. A. F. König, A. Fery, *Adv. Opt. Mater.* **2021**, *9*.

[260] L. Lorbeer, M. Alaghemandi, E. Spohr, *J. Mol. Liq.* **2014**, *189*, 57–62.

[261] S. Balamurugan, S. Mendez, S. S. Balamurugan, M. J. O'Brien, G. P. López, *Langmuir* **2003**, *19*, 2545–2549.

[262] J. Shan, J. Chen, M. Nuopponen, H. Tenhu, *Langmuir* **2004**, *20*, 4671–4676.

[263] L. M. Liz-Marzán, M. Giersig, P. Mulvaney, *Langmuir* **1996**, *12*, 4329–4335.

[264] R. Contreras-Cáceres, A. Sánchez-Iglesias, M. Karg, I. Pastoriza-Santos, J. Pérez-Juste, J. Pacifico, T. Hellweg, A. Fernández-Barbero, L. M. Liz-Marzán, *Adv. Mater.* **2008**, *20*, 1666–1670.

[265] J. Raula, J. Shan, M. Nuopponen, A. Niskanen, H. Jiang, E. I. Kauppinen, H. Tenhu, *Langmuir* **2003**, *19*, 3499–3504.

[266] F. Liu, S. Agarwal, *Macromol. Chem. Phys.* **2015**, *216*, 460–465.

[267] C. Boyer, M. R. Whittaker, M. Luzon, T. P. Davis, *Macromolecules* **2009**, *42*, 6917–6926.

[268] H. Lange, B. H. Juárez, A. Carl, M. Richter, N. G. Bastús, H. Weller, C. Thomsen, R. Von Klitzing, A. Knorr, *Langmuir* **2012**, *28*, 8862–8866.

[269] M. Tagliazucchi, M. G. Blaber, G. C. Schatz, E. A. Weiss, I. Szleifer, *ACS Nano* **2012**, *6*, 8397–8406.

[270] F. Lauterbach, M. Rubens, V. Abetz, T. Junkers, *Angew. Chemie - Int. Ed.* **2018**, *57*, 14260–14264.

[271] T. Eckert, F. C. Klein, P. Frieler, O. Thunich, V. Abetz, *Polymers (Basel).* **2021**, *13*.

[272] M. K. Corbierre, N. S. Cameron, R. B. Lennox, *Langmuir* **2004**, *20*, 2867–2873.

[273] W. Shen, Y. Chang, G. Liu, H. Wang, A. Cao, Z. An, *Macromolecules* **2011**, *44*, 2524–2530.

[274] A. Nouri, R. Castro, V. Kairys, J. L. Santos, J. Rodrigues, Y. Li, H. Tomás, *J. Mater. Sci. Mater. Med.* **2012**, *23*, 2967–2980.

[275] X. Sun, M. Gamal, P. Nold, A. Said, I. Chakraborty, B. Pelaz, F. Schmied, K. von Pückler, J. Figiel, Y. Zhao, et al., *Appl. Mater. Today* **2019**, *15*, 267–279.

[276] D. Zhu, L. Feng, N. Feliu, A. H. Guse, W. J. Parak, *Adv. Mater.* **2021**, *33*.

[277] H. Schlicke, S. C. Bittinger, T. Vossmeyer, *ACS Appl. Electron. Mater.* **2020**, *2*, 3741–3748.

[278] H. Schlicke, J. H. Schröder, M. Trebbin, A. Petrov, M. Ijeh, H. Weller, T. Vossmeyer, *Nanotechnology* **2011**, *22*.

[279] H. Schlicke, S. C. Bittinger, H. Noei, T. Vossmeyer, *ACS Appl. Nano Mater.* **2021**, *4*, 10399–10408.

[280] K. Schaefer, C. Y. Liu, A. Meyer, H. Schlicke, T. Vossmeyer, C. Herrmann, *J. Phys. Chem. C* **2024**, *128*, 3994–4008.

[281] S. T. Jones, Z. Walsh-Korb, S. J. Barrow, S. L. Henderson, J. Del Barrio, O. A. Scherman, *ACS Nano* **2016**, *10*, 3158–3165.

[282] K. Shimoda, T. Fujigaya, N. Nakashima, Y. Niidome, *Chem. Lett.* **2013**, *42*, 1247–1249.

[283] M. H. Stenzel, C. Barner-Kowollik, *Mater. Horizons* **2016**, *3*, 471–477.

[284] S. Eggers, F. Lauterbach, V. Abetz, *Polymer (Guildf).* **2016**, *107*, 357–367.

[285] S. H. Min, S. K. Kwak, B. S. Kim, *Soft Matter* **2015**, *11*, 2423–2433.

[286] X. Xu, A. E. Smith, S. E. Kirkland, C. L. McCormick, *Macromolecules* **2008**, *41*, 8429–8435.

[287] Felix Lauterbach, *Advances in RAFT Polymerization Process Design and Analysis, Dissertation*, University Of Hamburg, **2020**.

9. Appendix

9.1. Polymerization Conditions and Polymer Characterization Results

9.1.1. NMR-Spectroscopy

As a standard method in chemical analytics, NMR spectroscopy was frequently used in this work. ^{1}H-NMR spectroscopy was used to determine monomer conversion during polymerization. Therefore, DMF was used as a constant reference signal to calculate the amount of consumed methacrylate monomers. For the measurement, a Bruker Fourier 300 NMR spectrometer was used. ^{1}D-chloroform ($CDCl_3$) was used as the solvent for all polymerization solutions and purified polymer products.

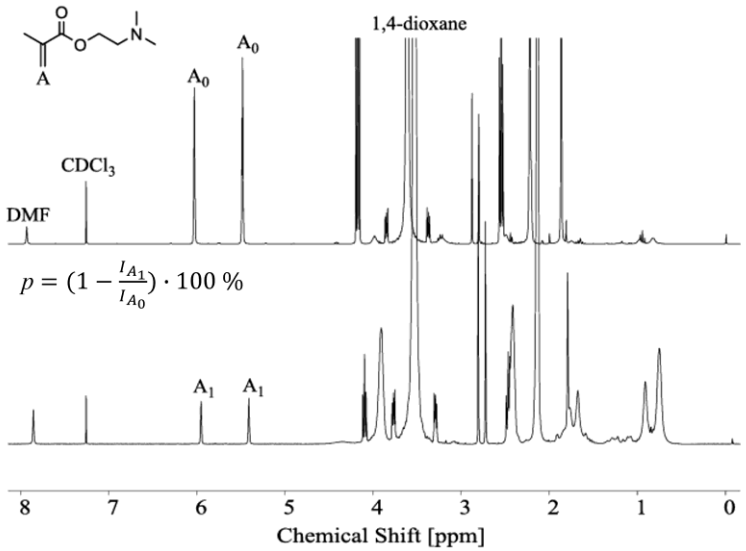


Figure A1. ^{1}H-NMR spectra of the polymerization solution before initiation (t = 0 min; upper spectrum) and after eight hours of polymerization (spectrum on the bottom). The classification of the respective acryl proton signals and the equation for calculating the monomer conversion p are included. The NMR spectra are taken with permission from *Macromol. Chem. Phys.* **2022**, 2200355. Copyright 2022 The Authors. Macromolecular Chemistry and Physics, published by Wiley-VCH GmbH.[3]

The monomer conversion (p) was calculated according to the literature, following the equation shown in **Figure A1**. The calculation of p assumes that the DMF signal remains constant throughout polymerization and can therefore be used as a fixed reference for signal integration. Based on the calculation of p, the theoretical average molecular weight ($M_{n,th}$) and the degree of polymerization (DP) of the respective monomer were calculated using Equation (4.6). Equation (4.6) is only valid if the discomposure of the CTA functionality can be neglected, and under the assumption that every CTA molecule forms an individual polymer chain. Using this equation, the values concluded in **Table A1** are obtained.

9.1.2. Size Exclusion chromatography (SEC)

To determine the *Đ* of the synthesized polymers via SEC, an Agilent 1260 Infinity system was used. Depending on the analyzed polymer system, different combinations of mobile and stationary phases were used. For the determination of the molecular masses and the *Đ*, a narrowly distributed polystyrene (PS) standard was used.

To analyze the P(DMAEMA)$_n$ RAFT-homopolymers from Section 5.2 N, N-dimethylacetamide (DMAc) with 0.1 M LiCl and a flow rate of 1.0 mL·min^{-1} at 30 °C was used as the mobile phase. The measurement was conducted using a PSS Gram column set (3,000–100,000 Å) and a VWR LaChrom L-2490 RI-detector. The same analytical setup was applied to measure B02 and BCP02. The same column set, with DMF (0.1 m LiCl) as the mobile phase, was used to measure GD01, GD02, BCP01, GN01, and GN02 at a column temperature of 50 °C. The flow rate was adjusted to 0.8 mL·min^{-1}. For B01 and B03 THF with a flow rate of 1.0 mL·min^{-1} was used as mobile phase. For this measurement, a PSS SDV column set (1000–1 000 000 Å) with a column temperature of 30 °C was used as the stationary phase.

9.1.3. Analytical Results and Kinetics

Table A1: Concluded pTTC/dTTC-P(DMAEAM)$_n$ precursors characterization results discussed in Section 5.2.

Polymer	DP_{DMAEMA}	$M_{n.th}$ / kg/mol	$\bar{M}_n$ / kg/mol	$Đ$ /	T_{cp} / °C
pTTC-P(DMAEMA)$_{48}$	48	7.9	8.1	1.17	43–45
pTTC-P(DMAEMA)$_{110}$	110	17.5	16.7	1.20	40–42
pTTC-P(DMAEMA)$_{37}$	37	6.1	6.7	1.18	44–45
pTTC-P(DMAEMA)$_{72}$	72	11.4	11.7	1.11	-
pTTC-P(DMAEMA)$_{39}$	39	6.4	6.5	1.20	46–49
pTTC-P(DMAEMA)$_{92}$	92	14.7	15.4	1.15	38–42
dTTC-P(DMAEMA)$_{41}$	41	6.9	7.1	1.22	49–51
dTTC-P(DMAEMA)$_{91}$	91	14.6	14.4	1.16	40–42

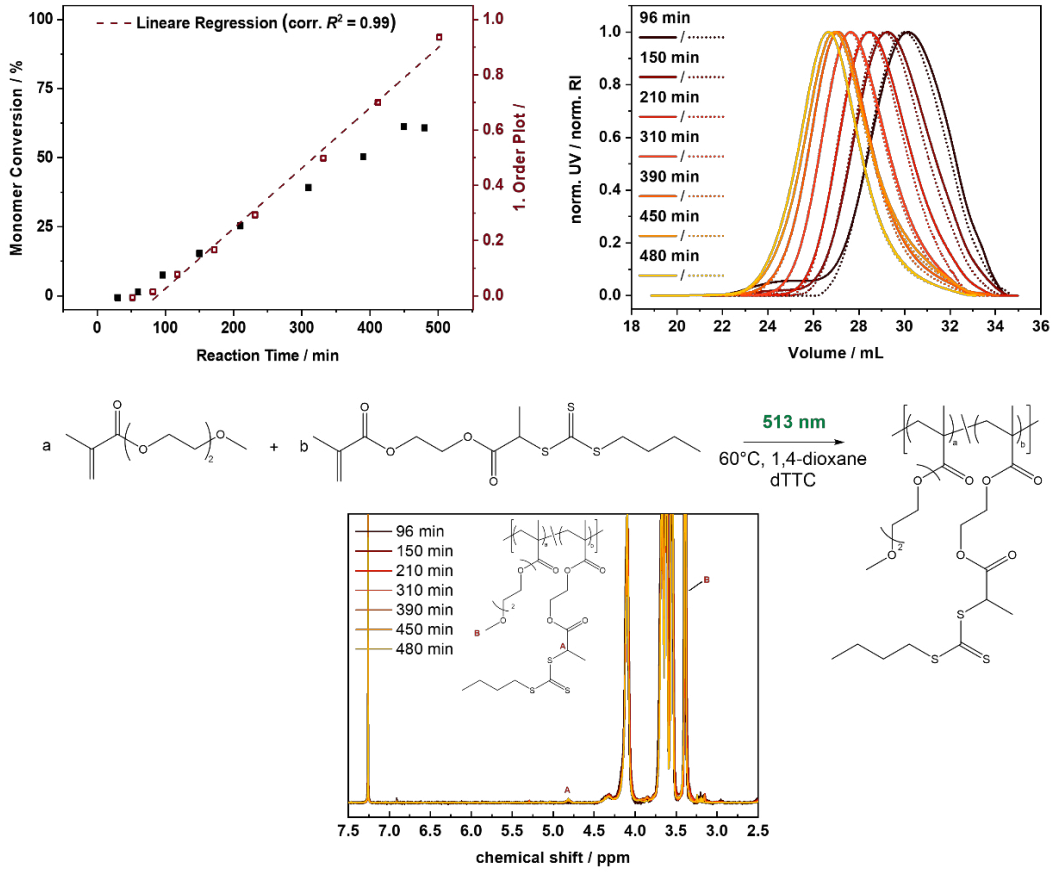


Figure A2. Polymerization kinetic results of the DEGMA/BTPEMA copolymerization using the 250 mL-scaled sublimation reactor setup for the green light-initiated photoRAFT polymerization.

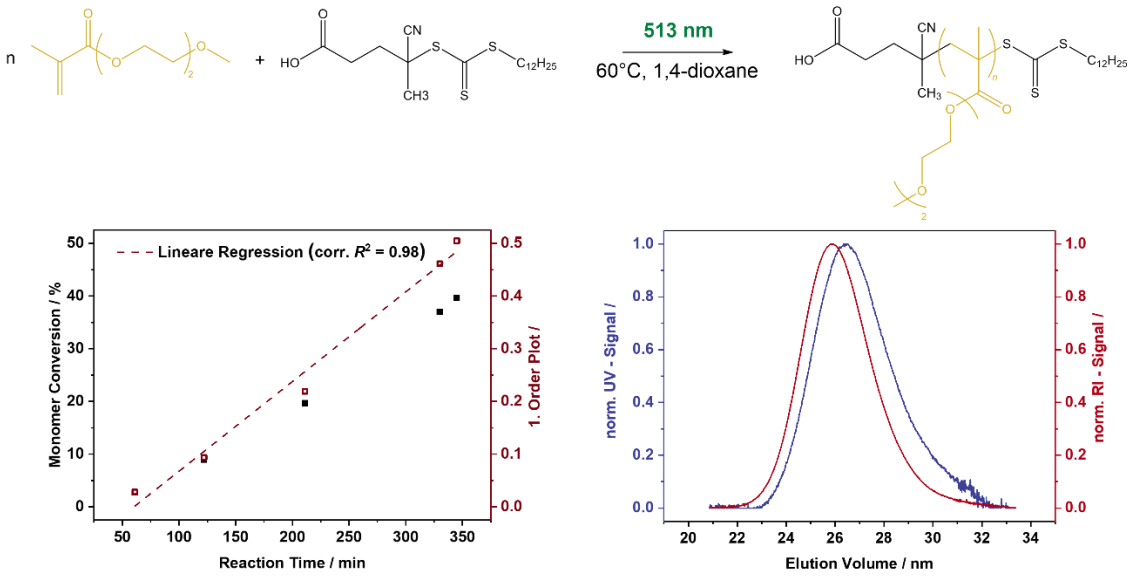


Figure A3. Polymerization kinetic results of the DEGMA homopolymerization using the 250 mL-scaled sublimation reactor setup for the green light-initiated photoRAFT polymerization. At the top, the reaction scheme of the respective polymerization is provided. The graphic at the bottom left shows the kinetic plot based on 1H-NMR spectra collected during polymerization. The plots on the right-hand side show the size-exclusion diagrams for the $P(DEGMA)_{244}$ polymer product (BCP02).

Table A2: Concluded polymerization results for the LCST polymer backbones investigated following the GNR research topic discussed in Section 5.3.

Polymer	CN	DP_{Mon} /	$M_{n.th}$ / kg/mol	$\bar{M}_n$ / kg/mol	$Đ$ /
$P(OEGMA)_{230}$-*r*-$P(BTPEMA)_6$	B01	230 6	72.4	50	1.4
$P(DEGMA)_{222}$-*r*-$P(BTPEMA)_8$	-[a]	222 8	45.1	32	1.6
$P(DEGMA)_{244}$	B02	244	46.4	23	1.5
$P(OEGMA)_{233}$-*r*-$P(BTPEMA)_{11}$	B03	233 11	76.7	41	1.5

[a]consecutive number used in the lab journal was B02.

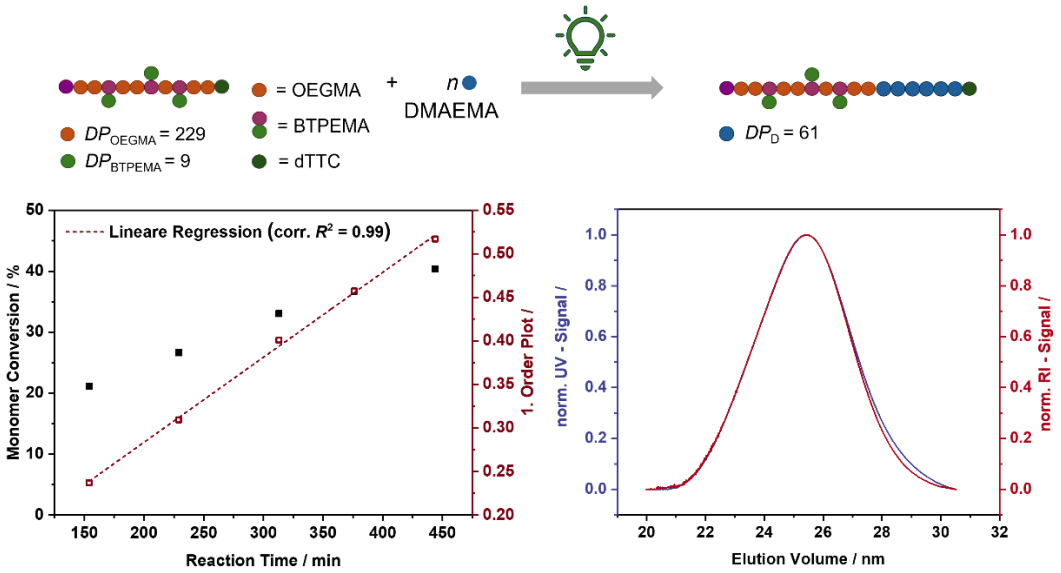


Figure A4. This figure shows the polymerization results for the BCP01 synthesis using B02 as the macroRAFT agent for the photoRAFT polymerization of DMAEMA, initiated by green light. Shown are the kinetic results obtained by ^{1}H-NMR spectroscopy and the corresponding 1. Order plot with a correlated $R^2 = 0.99$ on the left and the size exclusion chromatograms of the product BCP01 on the right.

9.1.4. ATR-FTIR Spectroscopy

A BRUKER VERTEX70/70 FTIR with a diamond attenuated total reflection (ATR) unit was used to measure FTIR analysis. The dried polymers were measured for 60 s at room temperature. The measuring range was between 7500 cm^{-1} and 400 cm^{-1} at a resolution of 4 cm^{-1}.

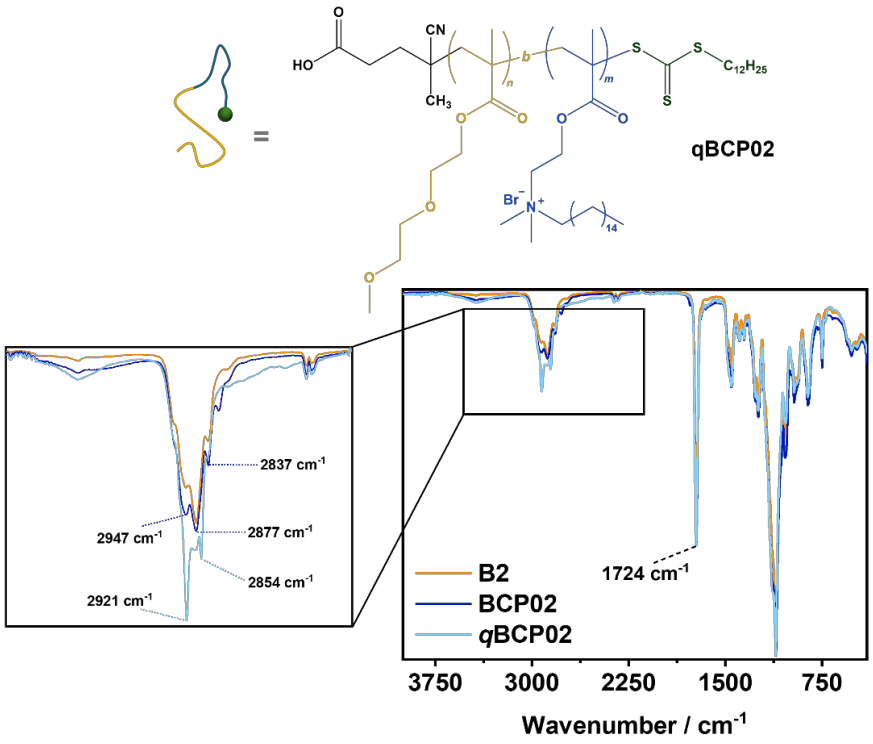


Figure A5. Compareson of the IR spectra of P(DEGMA)$_{244}$ (B02), P(DEGMA)$_{244}$-*b*-P(DMAEMA)$_{65}$ (BCP02), and P(DEGMA)$_{244}$-*b*-P(qDMAEMA)$_{65}$ (qBCP02). The FTIR data were taken with permission from the SI of the open-access article *Adv. Funct. Mater*. **2024**, 2400995, with optical adaptations. Copyright 2024 The Authors. Advanced Functional Materials, published by Wiley-VCH GmbH.[8]

9.2. Particle Results: TEM Images, TEM Evaluation, and Thermoresponsive Properties

9.2.1. TEM Sample Preparation, Measurement, and Image Evaluation

To prepare a TEM sample, the respective suspension was drop-cast onto a carbon-coated copper grid (200 mesh) and placed under a cover to shield the sample from dust contamination during drying. To drop a sample suspension onto the grid, the suspension was taken up with a glass pipette using capillary force. The optimal particle concentration on the grid surface varied among samples and was determined for each sample individually. As a general rule, each sample was diluted by adding at least twice the original volume of solvent.

After drying the grid for at least 10 hours, depending on the solvent, the samples were measured in the TEM. The Au@P(DMAEMA)$_n$ hybrid suspensions were measured by using the FEI/Tecnai G2 Spirit Twin cryo-TEM in bright field mode with an acceleration voltage of 120 kV. The camera used for the detection was an Eagle 4K HS. The measurements of the GNR and grafted GNS samples were conducted on a JeolJem 1011 with a LaB_6 cathode at an acceleration voltage of 100 kV. The imaging camera was a SIS CCD (1376 × 1032 pixels).

The evaluation of particle diameters was performed manually using the evaluation software tool ImageJ (version 1.51f). For the evaluation of each sample, several TEM images of the respective sample were measured. For the evaluation of the Au@P(DMAEMA)$_n$ samples, the diameters of at least 700 particles were measured. To evaluate the GNR dimensions, the length and the width of the NRs were measured for at least 300 individual particles. The results were later plotted using the software OriginPro 2025 (10.2.0.188). The evaluation process of the GNS@graft-Polymer hybrids from Sections 5.4.2 and 5.4.3 was similar to the evaluation of the Au@P(DMAEMA)$_n$ hybrids.

9.2.2. Additional TEM Images and Evaluation Results

Table A3: Results of the particle synthesis at 30 °C using qBCP02: amine concentration (c_{amine}), reaction time (t), average particle length (l), average width (w), and average aspect ratio (a_r), median of the particle length (L), and width (W), aspect ratio (A_R), maximum aspect ratio ($a_{r,max}$), and number of measured particles (N). The data are taken with permission from *Adv. Funct. Mater*. **2024**, 2400995. Copyright 2024 The Authors. Advanced Functional Materials, published by Wiley-VCH GmbH.[8]

c_{amine} / mol·L^{-1}	T / min	l / nm	w / nm	ar /	L / nm	W / nm	AR /	$armax$ /	N /
0.005	30	16±3	13±2	1.3±0.3	16.1	5.7	1.2	3.8	620
0.005	60	16±4	13±2	1.3±0.3	16.1	12.6	1.2	3.4	734
0.005	130	17±4	13±2	1.3±0.3	17.9	13.2	1.2	3.4	670
0.01	30	16±3	9±1	1.9±0.5	15.6	8.7	1.8	4.2	876
0.01	60	16±3	9±1	1.8±0.6	15.3	9.0	1.7	5.5	912
0.01	130	16±4	9±2	1.9±0.7	15.7	9.1	1.7	4.9	452
0.02	30	13±2	9±1	1.5±0.3	12.8	8.9	1.4	2.9	817
0.02	60	14±2	10±1	1.4±0.3	13.5	10.1	1.3	3.2	1010
0.02	130	14±2	9±1	1.5±0.3	13.9	9.5	1.5	3.3	809

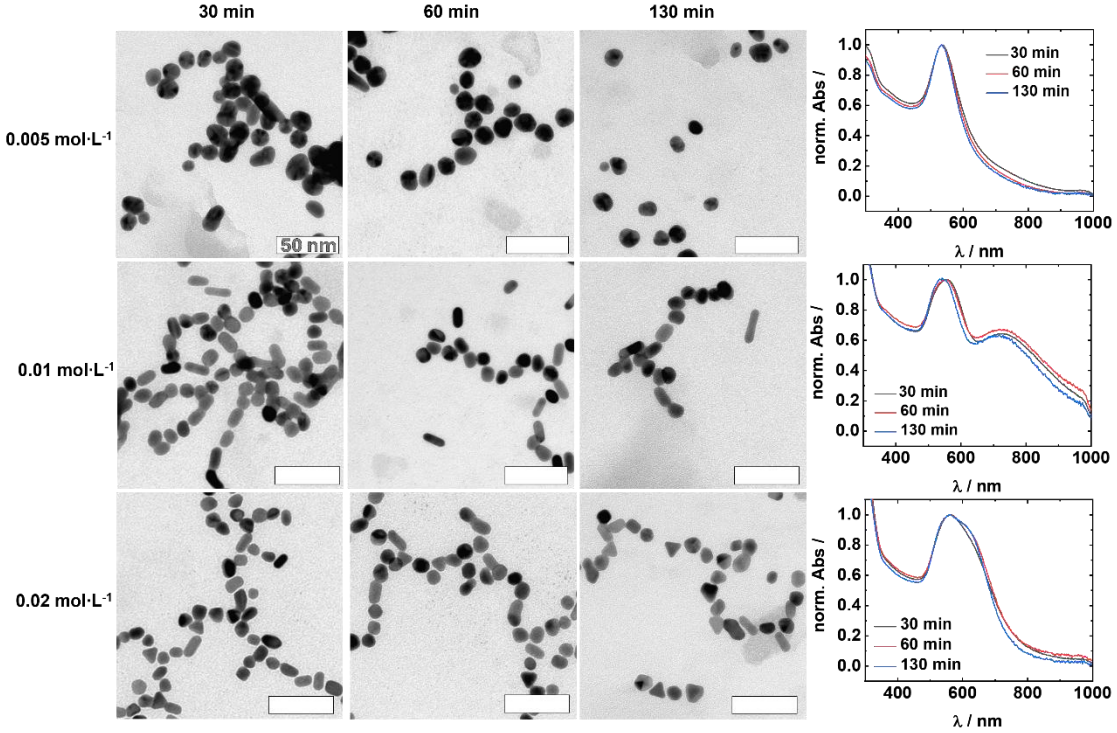


Figure A6. TEM images of the product solutions after one cycle of centrifugation for the qBCP2-based GNR synthesis at varying quaternized amine concentrations from 0.005 to 0.02 mol L−1 and different growth times. The scale bars are 50 nm. The right column shows the UV–vis absorbance spectra of diluted (half the initial concentration) reaction solutions. This figure was taken with permission from *Adv. Funct. Mater*. **2024**, 2400995 without adaptation. Copyright 2024 The Authors. Advanced Functional Materials, published by Wiley-VCH GmbH.[8]

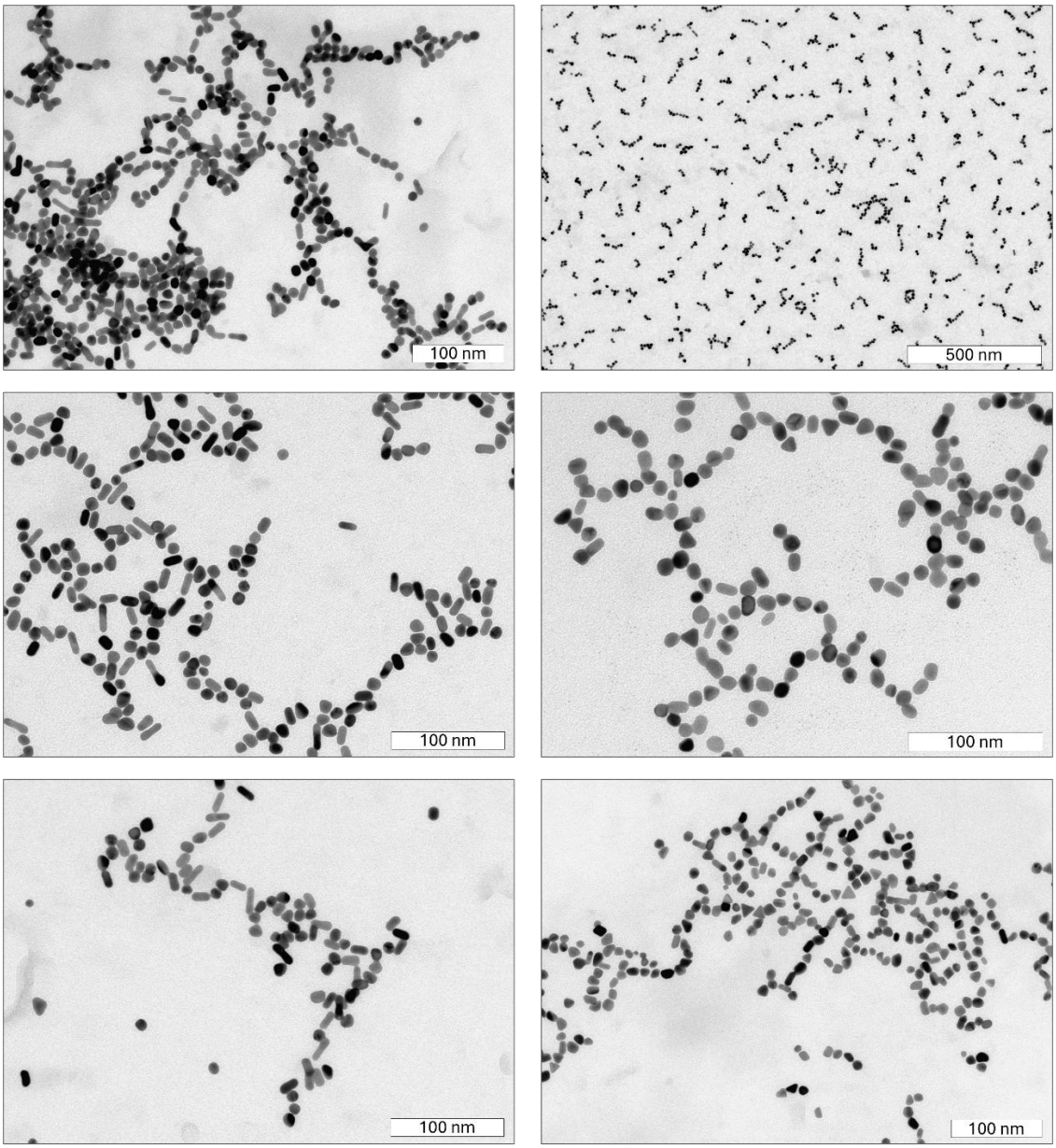


Figure A7. TEM images of the qBCP02-based GNR samples synthesized with camine = 0.01 mol/L (left column) and camine = 0.02 mol·L^{-1} (right column). Shown are images of samples prepared after a reaction time of 30 min, 60 min, and 130 min from top to bottom.

9.3. Additional Analytics for the Temperature-Dependent Behavior of GNP@Polymer Hybrids and Their Polymer Stabilizers

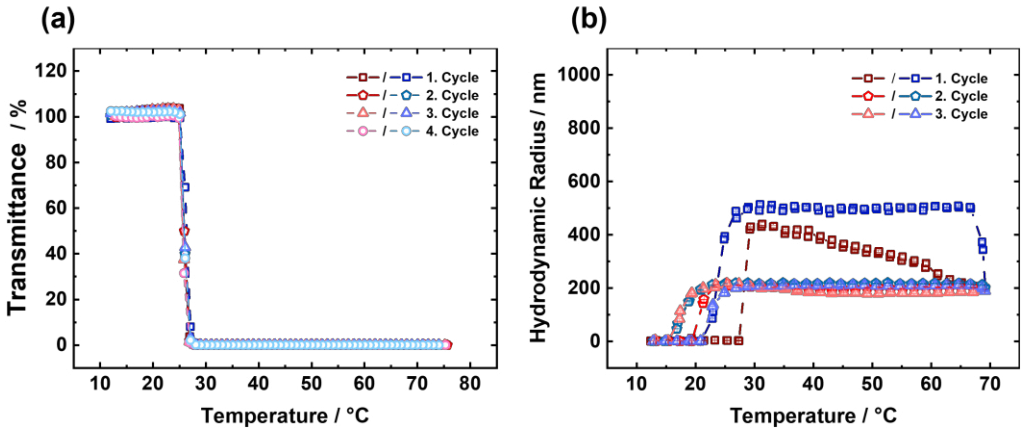


Figure A8. Temperature-dependent measurements of qBCP02. In (a), the transmittance at 800 nm obtained via UV–Vis absorbance spectroscopy is plotted against the sample temperature. Graph (b) shows the hydrodynamic radius obtained by DLS experiments plotted against the qBCP02 sample temperature.

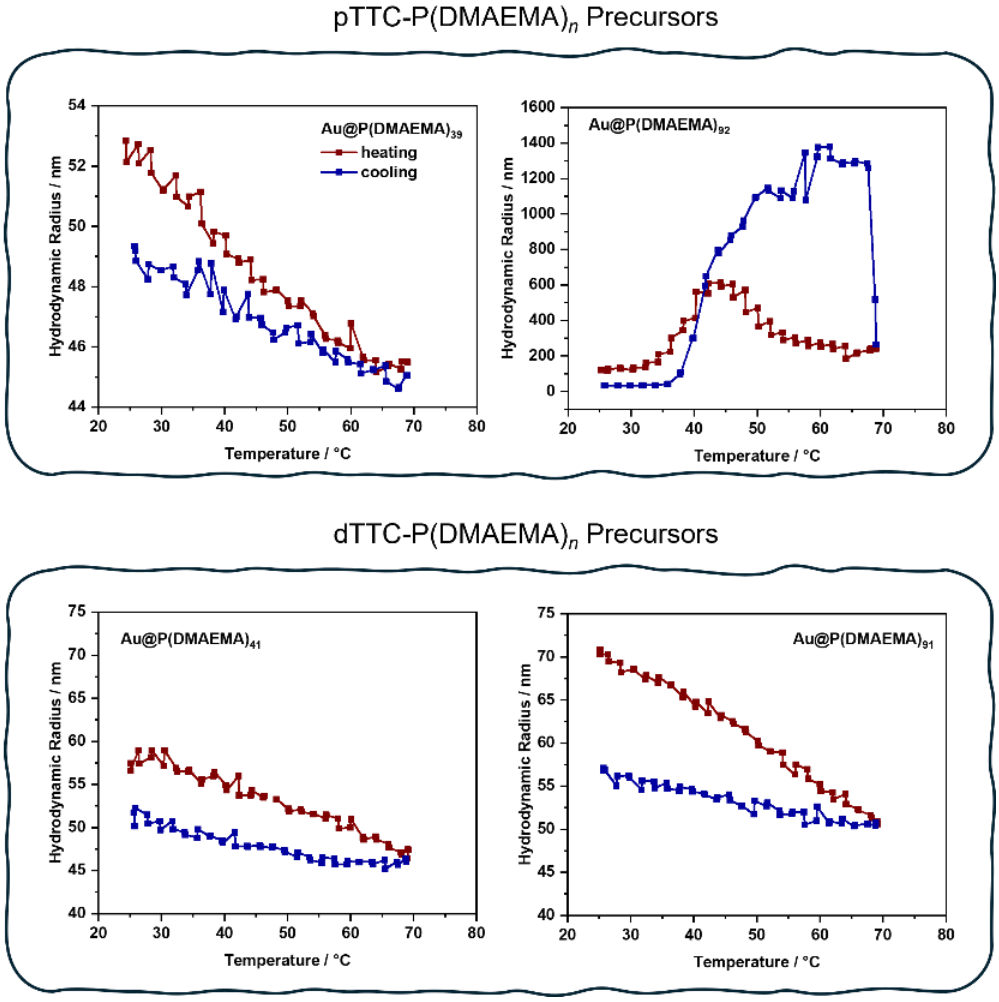


Figure A9. Results of the first temperature cycles of temperature-dependent DLS measurements of the Au@P(DMAEMA)$_n$ hybrids are presented and discussed in **Figure 56**.

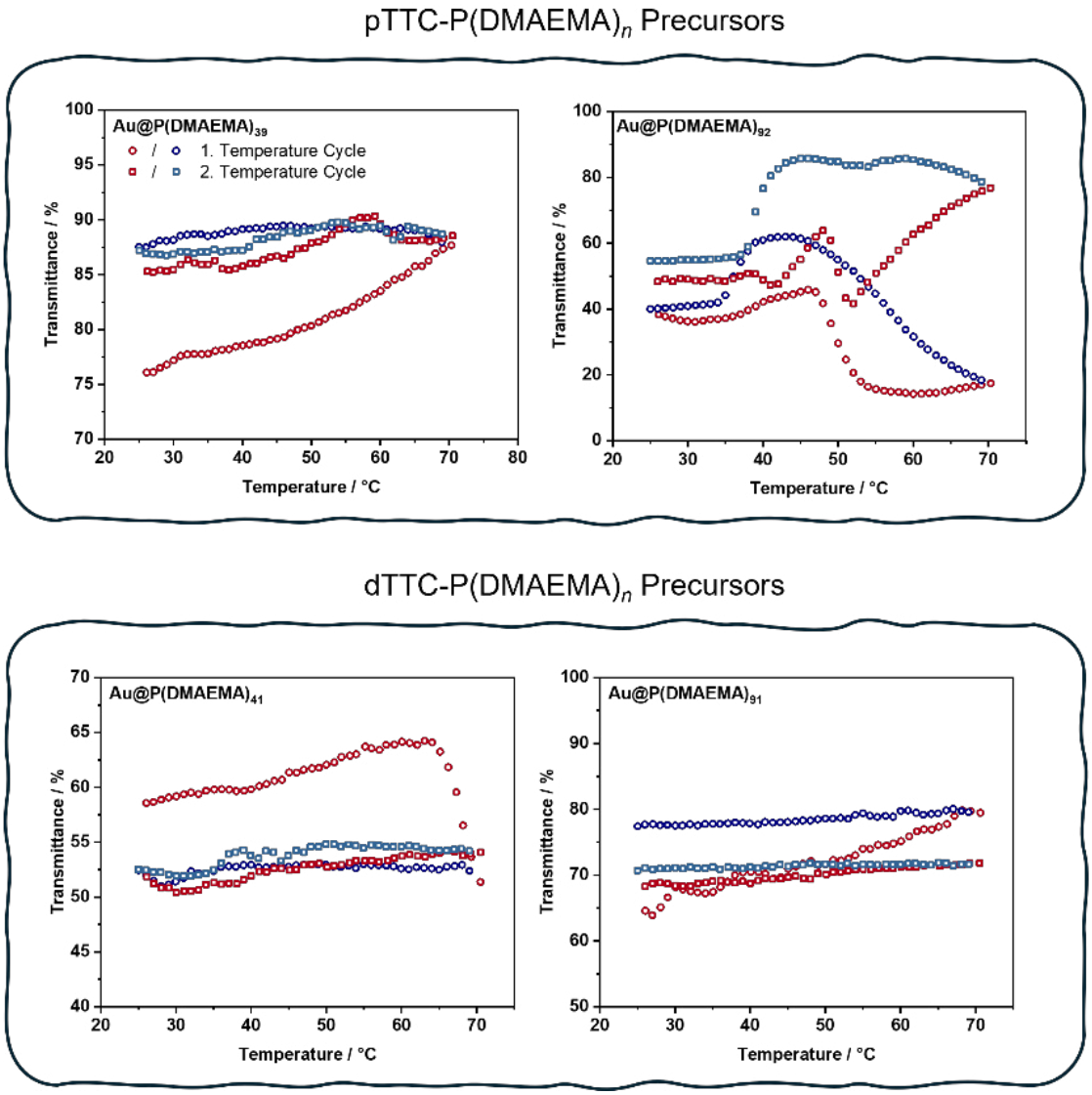


Figure A10. Temperature-dependent transmittance (at 800 nm) plots of pTTC- and dTTC-P(DMAEMA)$_n$ based Au@P(DMAEMA)$_n$ nanohybrids with different DMAEMA-chain lengths. The data for the four plots shown are taken with permission from *Macromol. Chem. Phys. 2022, 2200355*, without adaptation.[3] Copyright 2022 The Authors. Macromolecular Chemistry and Physics published by Wiley-VCH GmbH.

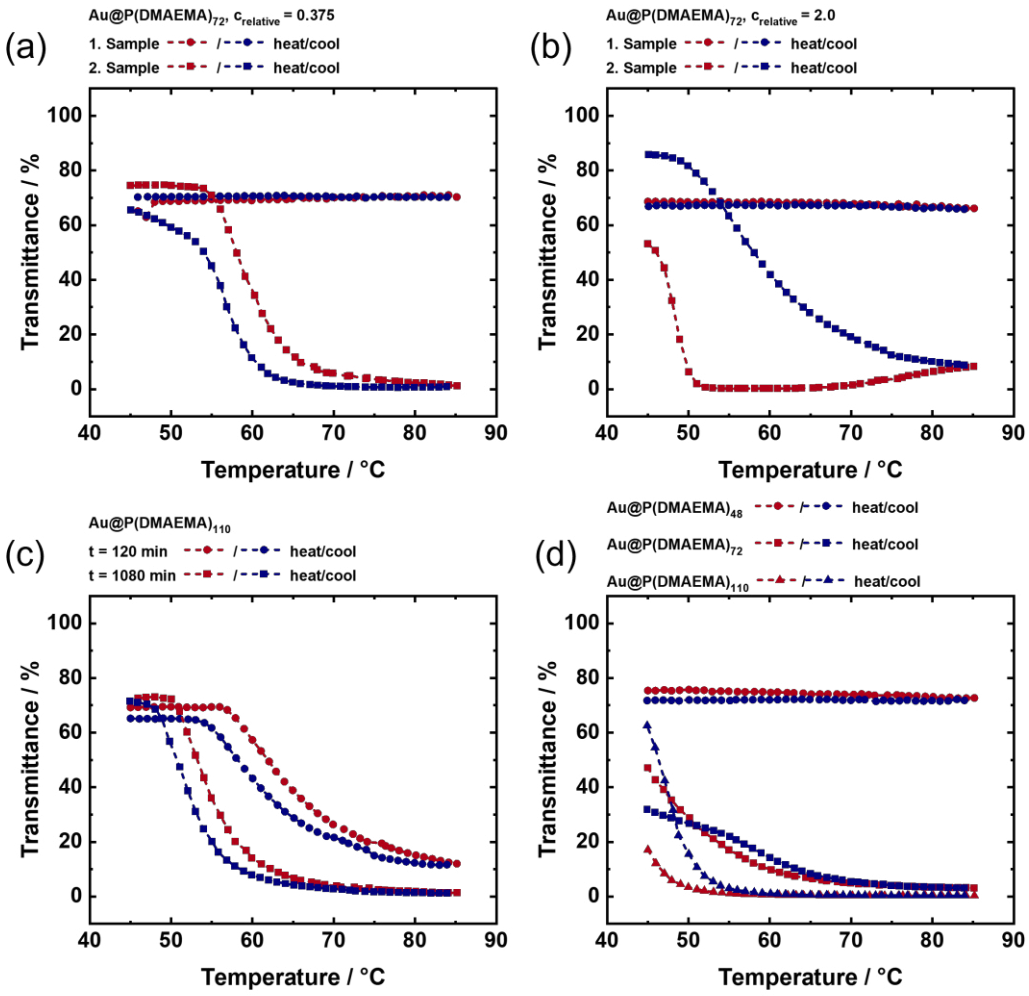


Figure A11. Temperature-dependent transmittance (@ 800 nm wavelength) plots of pTTC-P(DMAEMA)$_n$ based Au@P(DMAEMA)$_n$ nanohybrids. In (a) and (b), the transmittance plots of the Au@P(DMAEMA)$_{72}$ hybrids are shown, with a relative polymer concentration (to the standard synthesis) at the reaction c_{relative} of 0.375 for (a) and 2.0 for (b). In (c), the thermoresponsive behavior of Au@P(DMAEMA)$_{110}$ hybrids synthesized with different reaction times is plotted. In (d), the temperature-responsive behavior of Au@P(DMAEMA)$_n$ hybrids based on pTTC-p(DMAEMA)$_n$ precursors with varying DP_{D} is plotted.

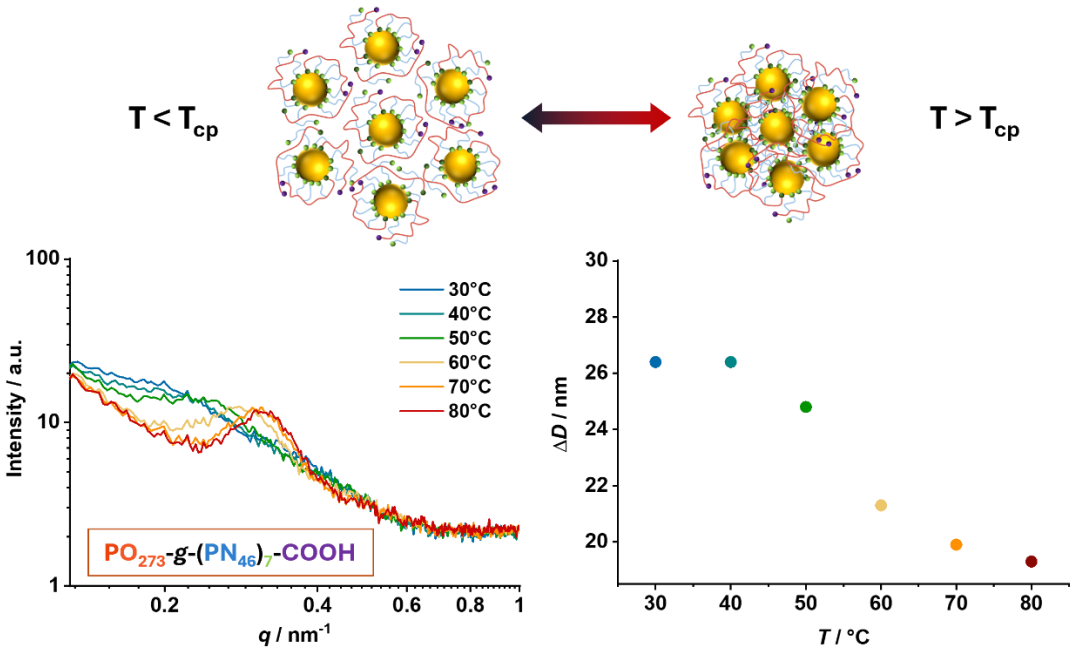


Figure A12. Temperature-dependent SAXS measurements of GNS@ TB-GN2. Showing the SAXS scattering vector (q) plots (bottom left graph) at different sample temperatures and the resulting core-to-core distances as a function of the temperature (bottom right graph) obtained from the q-plots.

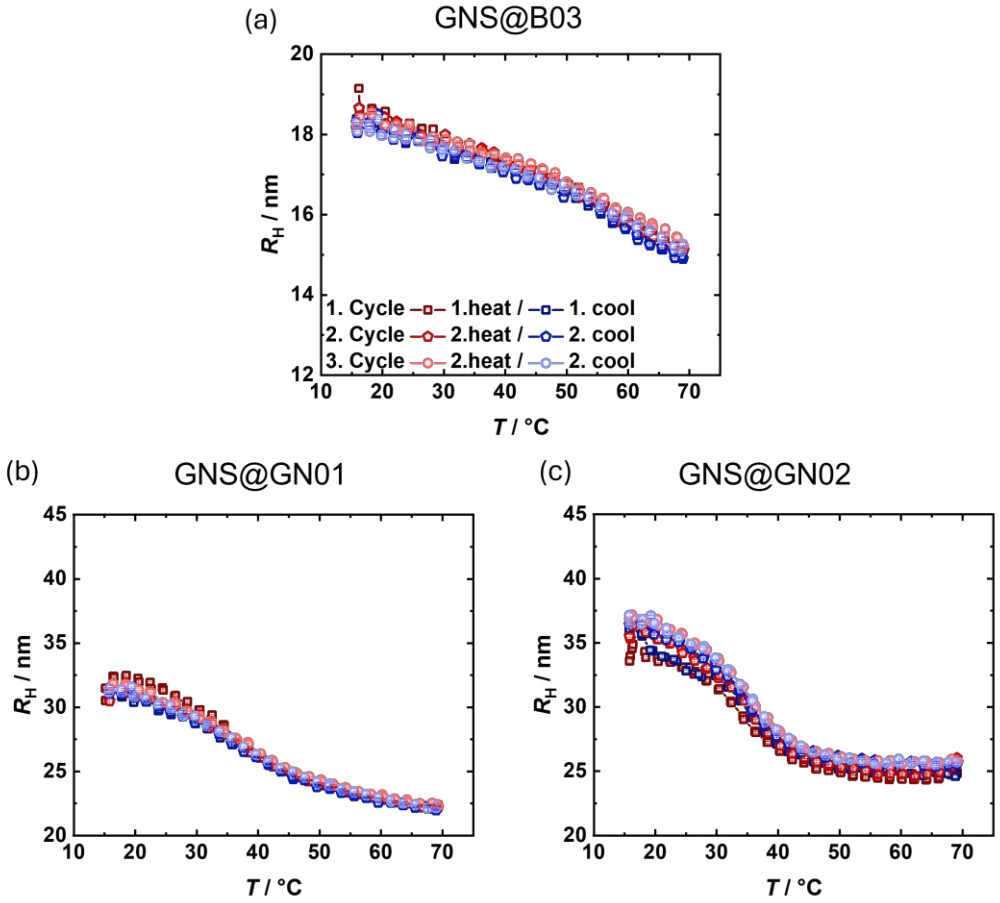


Figure A13. Temperature-dependent R_H-plots of the hybrids GNS@B03 (a), GNS@GN01(b), and GNS02(c) during three consecutive temperature cycles. The results are obtained by consecutively performing DLS experiments by fitting the intensity correlation function with a single decay.

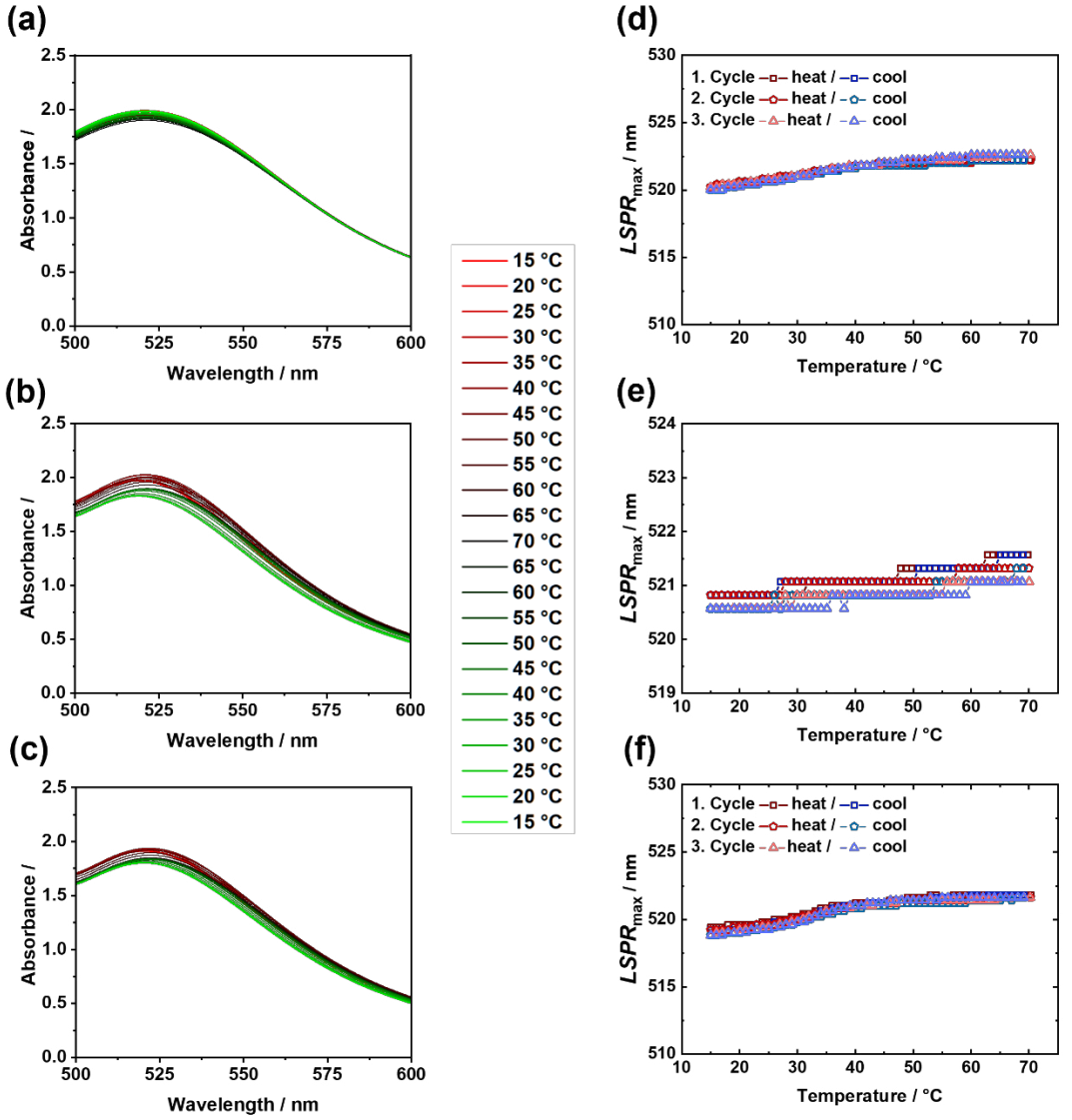


Figure A14. The left column shows the fitted functions of the UV–Vis absorbance measurements at varying temperatures of the hybrids GNS@B03 (a), GNS@GN01 (b), and GNS02 (c) during the second temperature cycle, starting at 15 °C (red) and ending at 15 °C (light green). In the right column, the respective temperature-dependent λ_{LSPR} plots for all three cycles are shown for GNS@B03 (d), GNS@GN01 (e), and GNS02 (f).

9.4. Hazardous Substances According to the Globally Harmonised System (GHS)

Table 16: Listed hazardous substances according to GHS.

Subtance	GHS-Symbol	Hazard Statements	Precautionary Statements
acetone		*H225, H319, H336, EUH066*	*P210, P233, P240, P241, P242, P305+P351+P338*
aqua regia		*H272, H314*	*P210, P220, P221, P280, P303+P361+P353, P305+P351+P338+P310*
4,4'-azobis-(4-cyanovaleric acid)		*H242*	*P210, P234, P235, P240, P370+P378, P403*
ethyl acetate		*H225, H319, H336, EUH066*	*P210, P233, P240, P241, P242, P305+P351+P338*
carbon dioxide		*H208*	*P403*
carbon disulfide		*H225, H315, H319, H332, H361fd, H372*	*P201, P210, P303+P361+P353, P304+P340+P312, P305+P351+P338, P308+P313*
cetyltrimethylammonium bromide		*H302, H315, H318, H335, H373, H410*	*P273, P280, P301+P312, P302+P352, P305+P351+P338, P314*
citric acid monohydrate		*H319, H335*	*P261, P264, P271, P280, P304+P340+P312, P305+P351+P338*
4-cyano-4-(dodecyl sulfanyl thiocarbonyl) sulfanyl pentanoic acid		*H302*	*P264, P270, P301+P312+P330 P501*
cyclohexane		*H225, H304, H315, H336, H410*	*P210, P233, P273, P301+P310, P303+P361+P353, P331*
deuterated chloroform		*H302, H315, H319, H331, H336, H361d, H372*	*P202, P301+P352, P304+P340+P311, P305+P351+P338*
dichloromethane		*H315, H319, H336, H351*	*P201, P261, P264, P302+P352, P305+P351+P338, P308+P313*
1,5-dibromopentane		*H315, H319*	*P302+P352, P305+P351+P338*
di(ethylene glycol) methyl ether methacrylate		*H315, H317, H319, H335*	*P261, P264, P271, P280, P302+P352, P305+P351+P338*
diethyl ether		*H224, H302, H336, EUH019, EUH066*	*P210, P233, P240, P241, P301+P312, P403+P233*
2-(dimethylamino) ethyl methacrylate		*H302+H312, H314, H314*	*P261, P272, P280, P301+P312, P303+P361+P353 P350+P351+P338*

Subtance	GHS-Symbol	Hazard Statements	Precautionary Statements
N,N'-dimethylformamide		*H226, H312+H322. H319, H360D*	*P210, P280, P303+P361+P353, P304+P340+P312, P305+P351+P338, P308+P313*
1,4-dioxane		*H225, H319, H335, H350, EUH019, EUH066*	*P202, P210, P233, P240, P305+P351+P338, P308+P313*
ethanol		*H225, H319*	*P210, P233, P240, P241, P242, P305+P351+P338*
gold(III) chloride trihydrate		*H290, H302, H314, H373, H411*	*P260, P273, P280, P303+P361+P353, P305+P351+P338*
n-hexane		*H225, H304, H315, H336. H361f, H372, H411*	*P202, P210, P273, P301+P310, P303+P361+P353, P331*
N-isopropylacrylamide		*H302, H318*	*P264, P270, P280, P301+P312, P305+P351+P338*
lithium triethyl borohydride (superhydrid©)		*H225, H260, H302, H314, H335, H336, H351, EUH014, EUH019*	*P210, P231+P232, P280,P303+P361+P353, P304+P340+P310*
methanol		*H225, H301+H311+H331*	*P210, P233, P280, P301+P310, P303+P361+P353, P304+P340+P311*
potassium hydroxide		*H290, H302, H314*	*P234,P260, P280, P301+P312, P303+P361+P353, P305+P351+P338*
1-propane thiol		*H225, H302, H317, H400, H410*	*P210, P233, P273, P280, P301+P312, P303+P361+P353*
sodium borohydride		*H260, H301, H314, H360FD, EUH014*	*P231+P232, P260, P280, P303+P361+P353, P304+P340+P310, P305+P351+P338*
silver nitrate		*H272, H290, H314, H360D, H410*	*P210, P260, P280, P303+P361+P353, P304+P340+P310 P305+P351+P338*

Subtance	GHS-Symbol	Hazard Statements	Precautionary Statements
tetrahydrofuran		*H225, H302, H319, H335, H336, H351, EUH019*	*P210, P280, P301+P312+P330, P305+P351+P338, P370+P378, P403+P235*
p-tosyl chloride		*H290, H315, H317, H318*	*P234, P261, P280, P302+P352, P305+P351+P338*
trisodium EDTA		*H315, H319, H335*	*P261, P264, P271, P280, P302+P352, P305+P351+P338*

10. Danksagung

Zunächst möchte ich mich in aller Form bei **Prof. Dr. Volker Abetz** und **Prof. Dr. Wolfgang Parak** für die Erstellung der schriftlichen Gutachten bedanken. Ich sehe diese Bereitschaft keineswegs als selbstverständlich an und freue mich daher umso mehr, dass trotz der hohen Arbeitsbelastung und des damit verbundenen Zeitdrucks sich auch hierfür die Zeit genommen wurde. Vielen Dank!

Ebenso möchte ich mich bei **Dr. Christopher Wutz** und **Dr. Tobias Vossmeyer** herzlich für ihre Bereitschaft bedanken, der Prüfungskommission meiner Disputation beizuwohnen.

Bereits im Masterstudium habe ich sehr viel Zeit in der Arbeitsgruppe Abetz verbracht – zunächst als Praktikant bei **Stephan Gleich (geb. Hinrichs)** und später im Rahmen mehrerer Praktika bei **Felix Lauterbach**. Für die hervorragende Betreuung bin ich euch beiden unheimlich dankbar. Ihr habt einen nicht zu unterschätzenden Anteil am Erfolg dieser Arbeit. Auch die Dynamik in der Gruppe zu dieser Zeit war sehr angenehm. So früh, so herzlich in Gruppenaktivitäten eingebunden worden zu sein, war unter anderem ein entscheidender Grund dafür, dass ich in die Arbeitgruppe Abetz wollte.

Natürlich lag die Entscheidung, der Gruppe beizutreten, nicht allein bei mir. In diesem Sinne möchte ich mich von ganzem Herzen bei **Volker** und **Birgit** für diese Chance bedanken. Teil eurer Arbeitsgruppe gewesen zu sein, macht mich sehr stolz. Auch wenn eure Betreuungsstile sehr unterschiedlich sind, hat jeder von euch ein ausgewogenes Verhältnis zwischen fachlichem Freiraum und struktureller Führung gefunden. Eure Anleitung war der initiierende Keim für ein enormes fachliches wie auch persönliches Wachstum meinerseits. Die Freiheit, die ihr mir bei dieser Arbeit gewährt habt, hat mir geholfen, selbstverantwortlicher und zielorientierter zu arbeiten. Sie ermöglichte es mir außerdem, mich mit dem Thema der Arbeit zu identifizieren – ein Prozess, der zugegebenermaßen etwas Zeit in Anspruch genommen hat. Schlussendlich haben mir euer offenes Ohr und eure Hilfsbereitschaft geholfen, diese Arbeit trotz mancher Umstände erfolgreich abzuschließen. Ich bin sehr froh, euch beide als Mentoren gehabt zu haben.

Gerne erinnere ich mich an die ersten zwei Jahre meiner Promotion zurück. Insbesondere die Hilfsbereitschaft von Kollegen wie **Iklima, Philipp, Tilman und Jingcong** war sehr erfrischend und vermittelte ein echtes Teamgefühl. Vor allem die ausführlichen Gespräche nach Dienstschluss sind mir in sehr guter Erinnerung geblieben. An dieser Stelle möchte ich insbesondere **Iklima** und **Philipp** hervorheben. Die privaten und fachlichen Diskussionen auf einer freundschaftlichen Ebene habe ich sehr genossen. Ich denke, wir alle haben von diesen Gesprächen profitiert – als damaliger Neuling in der Runde jedoch vermutlich ich am meisten. Euer Anteil an diesem Projekt war maßgeblich, und ich bin euch sehr dankbar für eure Unterstützung.

Leider war mein Beginn der Promotionszeit – wie für viele andere auch – überschattet vom Ausbruch der Corona-Pandemie und den ersten beiden Lockdowns. Die allgemeine Situation war für alle sehr belastend. Sich lediglich theoretisch auf die Promotionszeit vorbereiten zu können, ohne im Labor arbeiten zu dürfen, stellte für mich eine besondere Herausforderung dar. Umso mehr habe ich die Momente genossen, dem Alltag des reinen Literaturstudiums zu entkommen. Die Gaming-Runden in der Mittagspause mit **Tilman, Stephan** und **Niklas** waren hierbei eine willkommene Abwechslung und halfen, der Situation etwas von ihrem Ernst zu nehmen. An dieses Ritual erinnere ich mich sehr gern zurück, da es auch nach den Lockdowns eine angenehme Pause zwischen den Laborarbeitszeiten darstellte und eine gute Möglichkeit bot, unvermeidbare Wartezeiten im Forschungsalltag sinnvoll zu überbrücken.

Natürlich wäre diese Arbeit in ihrer jetzigen Form nicht möglich gewesen ohne das Zutun meiner **Praktikanten, Bacheloranden und studentischen Hilfskräfte**. Zu Beginn meiner Promotionszeit erhielt ich von Philipp den Ratschlag, meinen Praktikanten Ideen verfolgen zu lassen, für die ich selbst keine Zeit hatte, die ich aber gerne ausprobiert hätte. Diesen Ratschlag habe ich bei meiner Betreuung beherzigt – und definitiv nicht bereut. Viele Ergebnisse dieser Arbeit haben ihren Ursprung in Praktikums- oder Bachelorarbeiten, die ich betreuen durfte. Besonders hervorheben möchte ich an dieser Stelle meine Bacheloranden **Paul Körner** und **Steffen Soltau**. Auch wenn bislang nur eine der beiden Arbeiten in einer Fachzeitschrift veröffentlicht wurde, haben beide Arbeiten mit ihrer Qualität einen maßgeblichen Einfluss auf die fachliche Ausrichtung dieser Arbeit gehabt. Ebenso danke ich **Patrick Schütz** und **Nils Sobania** für ihren Beitrag. Auch wenn ihr als Praktikanten beziehungsweise HiWis vor allem die Fleißarbeiten übernommen habt, war euer Einsatz – insbesondere für die erste Publikation dieser Arbeit – ein entscheidender Faktor.

Ich wünsche euch allen alles Gute für euren weiteren beruflichen Weg. Das Gleiche gilt selbstverständlich für den restlichen aktiven und ehemaligen Teil des **Team Abetz**, der hier nicht mehr namentlich erwähnt werden konnte.
Während meines Chemiestudiums bin ich nicht selten an meine persönlichen Grenzen gestoßen. In solchen Momenten ist es besonders wichtig, Menschen um sich zu haben, die einen unterstützen. Insbesondere meiner Familie, meinen engen Freunden und meinen Wegbegleitern beim Sport bin ich daher unendlich dankbar. Ohne eure Unterstützung wäre ich niemals so weit gekommen. Diese Arbeit ist daher eine echte Teamleistung, bei der sich nun endlich die Ziellinie abzeichnet.

Ich danke euch allen von Herzen.

11. Eidesstattliche Erklärung

Hiermit versichere ich an Eides statt, die vorliegende Dissertationsschrift selbst verfasst und keine anderen als die angegebenen Hilfsmittel und Quellen benutzt zu haben. Sofern im Zuge der Erstellung der vorliegenden Dissertationsschrift generative künstliche Intelligenz (gKI) basierte elektronische Hilfsmittel verwendet wurden, versichere ich, dass meine eigene Leistung im Vordergrund stand und dass eine vollständige Dokumentation aller verwendeten Hilfsmittel gemäß der Guten wissenschaftlichen Praxis vorliegt. Ich trage die Verantwortung für eventuell durch die gKI generierte fehlerhafte oder verzerrte Inhalte, fehlerhafte Referenzen, Verstöße gegen das Datenschutz- und Urheberrecht oder Plagiate.

Hamburg, 21.04.2026 S. Lemich

Ort, Datum Unterschrift

I hereby declare and affirm that this doctoral dissertation is my own work and that I have not used any aid and sources other than those indicated. If electronic resources based on generative artificial intelligence (gAI) were used in the course of writing this dissertation, I confirm that my own work was the main and value-adding contribution and that complete documentation of all resources used is available in accordance with good scientific practice. I am responsible for any erroneous or distorted content, incorrect references, violations of data protection and copyright law or plagiarism that may have been generated by the gAI.

Hamburg, 21.04.2026 S. Lemich

City, date Signature